

COSMOLOGY WITH THE LYMAN ALPHA FOREST

by

Jochen Liske

A thesis submitted in satisfaction of
the requirements for the degree of
Doctor of Philosophy
in the Faculty of Science and Technology.

December 2000

Statement of Originality

I hereby declare that this submission is my own work and to the best of my knowledge it contains no materials previously published or written by another person, nor material which to a substantial extent has been accepted for the award of any other degree or diploma at UNSW or any other educational institution, except where due acknowledgement is made in the thesis. Any contribution made to the research by others, with whom I have worked at UNSW or elsewhere, is explicitly acknowledged in the thesis.

I also declare that the intellectual content of this thesis is the product of my own work, except to the extent that assistance from others in the project's design and conception or in style, presentation and linguistic expression is acknowledged.

(Signed)

Abstract

In this thesis we investigate the large-scale distribution of Ly α forest absorption, the effect of ionizing radiation from QSOs on their surrounding intergalactic medium and the primordial abundance of deuterium.

We develop a new technique for detecting structure on Mpc scales in the Ly α forest. This technique does not rely on identifying individual absorption lines but is rather based on the statistics of the transmitted flux. We demonstrate that the new method is significantly more sensitive to the presence of large-scale structure in the Ly α forest than a two-point correlation function analysis. We apply this method to 2 Å resolution spectra of ten QSOs which cover the redshift range $2.2 < z < 3.4$. The QSOs form a closely spaced group on the sky and are concentrated within a 1-deg² field. We find evidence for large-scale structure in the distribution of Ly α forest absorption at the > 99 per cent confidence level. Along the line of sight we find over-density Ly α absorption on scales of up to 1200 km s⁻¹. There is also strong evidence for correlated absorption across line of sight pairs separated by $< 3 h^{-1}$ Mpc. For larger separations the cross-correlation signal becomes progressively less significant.

Using the same technique and dataset we confirm the existence of the proximity effect. We derive a value for the mean intensity of the extragalactic background radiation at the Lyman limit of $J = 3.6_{-1.3}^{+3.5} \times 10^{-22}$ ergs s⁻¹ cm⁻² Hz⁻¹ sr⁻¹. This value assumes that QSO redshifts measured from high ionization lines differ from the true systemic redshifts by $\Delta v \approx 800$ km s⁻¹. Allowing for *known* QSO variability we find evidence at a level of 2.1σ that the significance of the proximity effect is correlated with QSO Lyman limit luminosity.

From the complete sample we find no evidence for the existence of a foreground proximity effect, implying either that $J > 20 \times 10^{-22}$ ergs s⁻¹ cm⁻² Hz⁻¹ sr⁻¹ or that QSOs emit at least a factor of 1.4 less ionizing radiation in the plane of the sky

than along the line of sight to Earth. We do, however, find one counter-example where a foreground QSO apparently depletes the absorbing gas in *four* surrounding lines of sight.

We discuss the feasibility of pre-selecting absorption systems from low resolution data for a measurement of the primordial deuterium abundance. We present a new, low resolution spectroscopic survey of 101 high redshift QSOs aimed at identifying candidate D/H systems. We further present an echelle spectrum of a Lyman limit system at $z = 2.917$. We find that this system is most likely heavily contaminated and does not yield an interesting limit on D/H.

Contents

Abstract	i
Acknowledgements	vi
Preface	vii
1 Introduction	1
2 A new technique for the detection of LSS in Lyα forest spectra	4
2.1 Introduction	4
2.1.1 Background	4
2.1.2 Detecting LSS in the Ly α forest	7
2.2 Technique	8
2.2.1 The mean Ly α transmission	10
2.2.2 The auto-covariance	11
2.2.3 Instrumental effects	12
2.2.4 Filter matching	14
2.3 Simulations	16
2.3.1 B and q from simulations	17
2.3.2 Comparison of analytical to numerical results	23
2.3.3 Sensitivity	25
2.3.4 Comparison to TPCF	27
2.4 Conclusions	36
3 Analysis of the LSS toward a group of ten QSOs	37
3.1 Introduction	37

3.2	The data	40
3.3	Analysis	42
3.4	Results	44
3.4.1	Single lines of sight	44
3.4.2	Local minima	48
3.4.3	Double lines of sight	52
3.4.4	Correlation with metal lines	59
3.4.5	Triple lines of sight	60
3.5	Uncertainties	63
3.6	Conclusions and discussion	65
4	The cosmological distance and redshift between any two objects	68
4.1	Introduction	68
4.2	The distance between any two objects	69
4.2.1	$\Lambda \neq 0$	74
4.3	Results	75
4.4	Relation to other solutions	80
4.5	Validity of approximation	81
5	The (foreground) proximity effect	84
5.1	Introduction	84
5.2	The data	89
5.3	Analysis	93
5.3.1	Method	93
5.3.2	Incorporating local ionizing sources	93
5.3.3	Further improvements	95
5.4	Results on classical proximity effect	97
5.4.1	Significance	97
5.4.2	Measurement of J	99
5.4.3	Variation with luminosity and redshift	103

5.5	Results on foreground proximity effect	114
5.5.1	Existence of the effect	114
5.5.2	Lower limit on J	117
5.5.3	The Q0042–2639 quadrangle	117
5.6	Uncertainties	120
5.7	Conclusions	125
6	The primordial deuterium abundance	130
6.1	Introduction	130
6.1.1	Big Bang Nucleosynthesis	130
6.1.2	D/H in QSO absorption line systems	142
6.2	Pre-selection of D/H candidates	150
6.2.1	The necessity of pre-selection	150
6.2.2	The ideal D/H absorption system	150
6.2.3	Principles of pre-selection	151
6.2.4	Summary	158
6.3	PD2H: a low resolution spectroscopic QSO survey	159
6.3.1	2.3-m observations	213
6.3.2	WHT observations	218
6.4	D/H towards Q0940–1050	219
6.4.1	Selection of Q0940–1050	219
6.4.2	Echelle spectroscopy	223
6.4.3	An upper limit on D/H	233
6.5	Further work	242
7	Summary	244
	References	248

Acknowledgements

I would like to thank my supervisor, John Webb, for his guidance, support and good humour throughout the course of this project. It has been a pleasure to work with him and his advice has been invaluable.

I am grateful to Gerry Williger, J. Baldwin, C. Hazard, R. McMahon and A. Smette for kindly providing access to the data that was used in Chapters 3 and 5. Thanks also to W. L. W. Sargent and L. Storrie-Lombardi for sharing their respective datasets with me.

It is a pleasure to thank Bob Carswell for stimulating discussions and for passing on some of his observational experience. I would also like to thank him and the Institute of Astronomy for hosting me during two extended visits to Cambridge.

Many thanks go to Simon Driver, Alberto Fernández-Soto and Charlie Lineweaver for many hours of sometimes lively, but always inspiring discussion from which I have benefited enormously.

I gratefully acknowledge the financial support of the German Academic Exchange Service (DAAD) and the Australian Department of Education, Training and Youth Affairs.

A warm thank you goes to the entire Department of Astrophysics at UNSW for providing a friendly and stimulating work environment. For sharing the joys and woes of PhD life with me I thank my fellow postgraduate students and wish them all the best for their future careers. In particular, I wish to thank my various office mates, past and present, for their friendship, humour, insights, arguments and hours of Marshmallow-Man fun.

To the Coogee Gang, John, Sue, Oliver, Nic, Robert, Tamzin and all the others I am eternally grateful for making sure that I still have a life in the 'real world'. A special thanks to the greatest of friends, Kate (PoF), for teaching me about friendship and setting me right when I was wrong. To Tanja a heart-felt thanks for her love, encouragement and faith in me when it was needed most. And finally, I thank my family, who has supported me from afar (and even further), for their unconditional love and trust and a sense of belonging.

Preface

Three chapters of this thesis were originally published as follows:

Chapter 2: Liske J., Webb J. K., Carswell R. F., 1998, MNRAS, 301, 787

Chapter 3: Liske J., Webb J. K., Williger G. M., Fernández-Soto A.,
Carswell R. F., 2000, MNRAS, 311, 657

Chapter 4: Liske J., 2000, MNRAS, 319, 557

Chapter 5 is also intended for publication in MNRAS. Although I have retained the use of the first person plural for this thesis, all of these publications were the product of my own work.

And then there is also a need that each should understand where he came from and what he is – and what will become of him.

Wulfstan, Archbishop of York (1002–1023)

Chapter 1

Introduction

Soon after the discovery of quasi-stellar objects (QSOs) by Schmidt (1963), the absorption line spectra of these objects generated intense interest due to their bewildering complexity. Although some of the lines could be identified as redshifted absorption from a variety of elements (e.g. Burbidge, Lynds, & Burbidge 1966; Stockton & Lynds 1966), a large fraction of them remained unidentified.

Gunn & Peterson (1965) and Bahcall & Salpeter (1965) had first suggested that intergalactic neutral hydrogen (H I) along the line of sight to cosmologically distant objects could be detected by its redshifted ultraviolet (UV) absorption features in the optical spectra of these objects. Lynds (1971) subsequently suggested that the unidentified absorption lines, which lay almost exclusively on the blue side of the QSO Lyman- α emission line, were in fact due to the Ly α transition of intervening H I. Thus he had ‘planted’ the Ly α forest.

Today QSO absorption lines are a valuable tool in extragalactic astronomy and cosmology. They are routinely observed at redshifts of up to ~ 5 and represent a formidable probe of the high redshift Universe. Each QSO spectrum affords us with an unbiased view of the intervening gaseous material, providing information on its distribution, composition, kinematics and physical environment. When placed

into the context of observations of the local Universe and of the Cosmic Microwave Background at $z \approx 1000$, QSO absorption line studies provide a rare constraint on the evolution of the Universe at intermediate epochs.

The term ‘Ly α forest’ refers to the multitude of narrow absorption lines observed in the spectra of all QSOs blueward of the Ly α emission line. Initially, Ly α forest absorbers were thought of as a distinct class of objects (Sargent et al. 1980), differing in their properties from both galaxies and other absorption line classes, such as metal line systems and the higher column density Lyman limit and damped Ly α absorption systems. Although some of these distinctions have become blurred, the original interpretation that the high redshift Ly α forest is due to the intervening intergalactic medium is still prevalent. For a comprehensive review of the Ly α forest, which considers both theoretical and observational aspects, see Rauch (1998).

In this thesis we report the results of three separate investigations. The common ground of these studies is that they address cosmological topics and use observations of the Ly α forest (hence the somewhat unimaginative title of this thesis). We introduce each topic independently at the beginning of its chapter.

In Chapter 2 we consider the problem of detecting large-scale structure (LSS) in the distribution of Ly α forest absorption with a particular view to intermediate resolution data. We develop a new method to detect LSS and show that it is significantly more sensitive than a two-point correlation function analysis.

In Chapter 3 we apply this technique to the spectra of a group of ten QSOs. The QSOs form a closely spaced group on the sky which allows us to probe structures not only along the line of sight but also in the plane of the sky. We find strong evidence for the existence of LSS in the Ly α forest and identify the scale-length of this structure both along and across the line of sight.

In Chapter 4 we briefly digress from the main theme of this thesis. We present a new variant of the known, but surprisingly nearly undocumented solution to the problem of how to calculate the distance between any two cosmological objects given their redshifts and angular separation on the sky. The results of these calculations

find an application in Chapter 5.

The topic of the fifth chapter is the well-known proximity effect, i.e. the underdensity of Ly α forest absorption near the background QSO. Since this is also a large-scale effect, the technique developed in Chapter 2 is well suited to investigate it. Using the same data as in Chapter 3 we measure the intensity of the mean extragalactic background at the Lyman limit and show that the strength of the proximity effect correlates with QSO luminosity. Again exploiting the three-dimensionality of our particular dataset we also address the so-called foreground proximity effect where the Ly α forest of a background QSO may be influenced by the proximity of a nearby foreground QSO.

Finally, we turn to the third main topic of this thesis, the primordial deuterium abundance, in Chapter 6. We discuss the feasibility of selecting candidate absorption systems for a D/H measurement from low and intermediate resolution data. Implementing this selection process in a multi-phased observational programme, we present a new, low resolution spectroscopic survey of 101 high redshift QSOs. We further present an echelle spectrum for one of these objects which was selected for further study on the basis of the low resolution data. We perform a D/H analysis of a Lyman limit absorption system at $z = 2.917$ and show, unfortunately but conclusively, that it does not yield a cosmologically interesting limit on D/H.

Chapter 2

A new technique for the detection of LSS in Ly α forest spectra

2.1 Introduction

2.1.1 Background

The Ly α forest seen in the spectra of distant QSOs may constitute a substantial fraction of the baryonic content of the Universe (Rauch & Haehnelt 1995) and its evolution can be traced over most of the history of the Universe. Every QSO absorption spectrum provides us with a representative, albeit one-dimensional sample of the baryonic matter distribution, unaffected by any luminosity bias. The intimate relationship of the absorbing gas with the thermal, chemical and dynamical history of the Universe makes the Ly α forest a versatile, but not always user-friendly tool in the study of cosmology.

The observational and theoretical advances of the past decade have significantly altered our understanding of the Ly α forest. The advent of HST's UV spectroscopic capabilities led to the first detailed analyses of the low redshift Ly α forest (Morris et al. 1991; Bahcall et al. 1991). Subsequently, using multislit spectroscopy and deep imaging of galaxies in the fields of QSOs, significant numbers of coincidences

between the redshifts of absorption lines and galaxies were found at $z \lesssim 1$. Several groups determined that galaxies have absorption cross-sections of $\sim 200 \text{ h}^{-1} \text{ kpc}$ (Lanzetta et al. 1995; Le Brun, Bergeron, & Boissé 1996; Bowen, Blades, & Pettini 1996). Moreover, Lanzetta et al. (1995), Chen et al. (1998) and Tripp, Lu, & Savage (1998) found an anti-correlation of the Ly α rest equivalent width, W , with the distance of the absorbing galaxy to the line of sight of the QSO as well as a slight correlation with luminosity (Chen et al. 1998). Thus Chen et al. (1998) confirmed earlier results that the extended gaseous halos of galaxies are directly responsible for a significant fraction of the Ly α forest at $z \lesssim 1$. However, there is evidence that this may only be true for stronger lines ($W \gtrsim 0.3 \text{ \AA}$) and that the weaker absorption lines trace the large-scale gaseous structures in which galaxies are presumably embedded (Le Brun & Bergeron 1998; Tripp, Lu, & Savage 1998).

At high redshift, the discovery of measurable amounts of C IV associated with 75 per cent of all Ly α absorbers with column density $N(\text{H I}) > 10^{14.5} \text{ cm}^{-2}$ (Cowie et al. 1995; Songaila & Cowie 1996) in high quality spectra obtained with the HIRES spectrograph on the Keck 10-m telescope has challenged the original notion of the Ly α forest arising in pristine, primordial gas. However, Lu et al. (1998) found almost no associated C IV absorption for systems with $N(\text{H I}) < 10^{14} \text{ cm}^{-2}$ and derived $[\text{C}/\text{H}] < -3.5$, about a factor of ten smaller than inferred by Songaila & Cowie (1996) (see also Davé et al. 1998), suggesting a sharp drop in the metallicity of the Ly α forest at $N(\text{H I}) \approx 10^{14} \text{ cm}^{-2}$. Nevertheless, the metallicity of the higher column density systems raises the possibility of an association of these systems with galaxies at high redshift. Using the same C IV lines to resolve the structure of the corresponding blended Ly α lines, Fernández-Soto et al. (1996) have shown that the clustering properties of these systems are consistent with the clustering of present-day galaxies if the correlation length of galaxies is allowed to evolve rapidly with redshift ($\epsilon \approx 2.4$).

On the theoretical side, models have progressed from the early pressure-confined (Sargent et al. 1980; Ostriker & Ikeuchi 1983; Ikeuchi & Ostriker 1986; Williger

& Babul 1992) and dark matter mini-halo (Rees 1986; Ikeuchi 1986) scenarios to placing the Ly α forest fully within the context of the theory of CDM dominated, hierarchical structure formation. Both semi-analytical (Petitjean, Mücke, & Kates 1995; Bi & Davidsen 1997; Hui, Gnedin, & Zhang 1997; Gnedin & Hui 1998) and full hydrodynamical numerical simulations (Cen et al. 1994; Zhang, Anninos, & Norman 1995; Miralda-Escudé et al. 1996; Hernquist et al. 1996; Wadsley & Bond 1997; Theuns et al. 1998) of cosmological structure formation, which include the effects of gravity, photo-ionization, gas dynamics and radiative cooling, have shown the Ly α forest to arise as a natural by-product in the fluctuating but continuous medium which forms by gravitational growth from initial density perturbations. The simulations are able to match many of the observed properties of the Ly α absorption to within reasonable accuracy (Miralda-Escudé et al. 1996; Zhang et al. 1997; Davé et al. 1997; Davé et al. 1999; Mücke et al. 1996; Riediger, Petitjean, & Mücke 1998; Theuns, Leonard, & Efstathiou 1998). A common feature of all the simulations is that the absorbing structures exhibit a variety of geometries, ranging from low density, sheet-like and filamentary structures to the more dense and more spherical regions where the filaments interconnect and where, presumably, galaxies form. The dividing line between these different geometries lies in the range $10^{14} \text{ cm}^{-2} \lesssim N(\text{HI}) \lesssim 10^{15} \text{ cm}^{-2}$ (Cen & Simcoe 1997; Zhang et al. 1998).

Thus a consistent picture may be emerging: absorption lines with $N(\text{HI}) \gtrsim 10^{14.5} \text{ cm}^{-2}$ are closely associated with the large, spherical outer regions of galaxies, cluster strongly on small velocity scales along the line of sight (Fernández-Soto et al. 1996) and have been contaminated with metals by supernovae from a postulated Population III (e.g. Miralda-Escudé & Rees 1997; Hellsten et al. 1997) or by galaxy mergers (e.g. Gnedin 1998); whereas lower column density lines trace the interconnecting, filamentary structures of the intergalactic medium.

Whatever the case may be, it seems likely that the large-scale distribution of the Ly α absorption holds important clues to its origin. The simulations seem to suggest that Ly α absorbers are a less biased tracer of dark matter than are galaxies. They

are probably fair tracers of the large-scale cosmic density field and should thus be able to constrain structure formation models. This warrants a new investigation into the large-scale clustering properties of the Ly α forest and into the techniques employed in deriving these.

2.1.2 Detecting LSS in the Ly α forest

Fitting individual absorption lines and computing their two-point correlation function (tpcf) is the most commonly adopted approach to clustering analysis of the Ly α forest. Pando & Fang (1996) discussed this and other methods based on line statistics and concluded that a space-scale decomposition is most effective. However, the analysis by Fernández-Soto et al. (1996) demonstrates the difficulty of using any sort of analysis based on the statistics of fitted absorption lines. As will be shown later in this chapter, even in high resolution spectra blending successfully masks even very strong clustering, so that any procedure involving identifying individual absorption lines may severely underestimate the strength and scale of the ‘true’ correlation. Furthermore, it seems somewhat excessive and an inefficient use of telescope time to employ a resolution of, say, 10 km s⁻¹ when one is interested in Mpc-scale structures. Finally, if the aforementioned numerical simulations are more or less correct then at least the low column density forest does not correspond to well-defined individual ‘clouds’ since it arises in a fluctuating but continuous medium with small to moderate overdensities.

Ideally we therefore need a statistical method which does not rely on identifying individual lines and which is free from any systematic effects associated with line counting. In this chapter we introduce a new technique based on the statistical properties of the transmitted flux. The method is a space-scale decomposition and as such retains spatial information. It allows us to locate specific structures in the Ly α forest and assess their significance, as compared to a random distribution. The method is compared to a line counting/tpcf method, and we show that it is substantially more sensitive. Flux statistics have been used previously in other

contexts by Nusser & Haehnelt (2000), Hui (1999), Croft et al. (1999), Zuo & Bond (1994), Zuo & Lu (1993), Press, Rybicki, & Schneider (1993), Press & Rybicki (1993), Webb et al. (1992) and Jenkins & Ostriker (1991).

The organisation of the rest of this chapter is as follows: in Section 2.2 we describe the new analysis and carry out all necessary analytic calculations. In Section 2.3 we use Monte-Carlo simulations to compare the new method with a tpcf analysis. We present our conclusions in Section 2.4.

2.2 Technique

We base our analysis on the null-hypothesis that any Ly α forest spectrum can be fairly well represented by a collection of individual absorption lines (Carswell et al. 1984; Kirkman & Tytler 1997; Lu et al. 1996; Hu et al. 1995) whose parameters are uncorrelated. Usually those lines are taken to be Voigt profiles and we shall adopt this although the exact shape of the profile is not relevant. We also need to adopt the functional form of the distribution of the absorption line parameters, $\eta(z, N, b)$, which we take from observations. We stress that we make *no* assumptions about what causes the absorption lines. Our analysis does not rely on identifying an absorption line with an individual, well-defined absorbing cloud. The composition of a spectrum of individual lines is purely descriptive. We simply use the null-hypothesis to predict integral properties of the absorption caused by the collection of lines.

The general idea of the new analysis then is to use those predictions to identify overdense and underdense regions of absorption as a function of scale and position (space-scale decomposition) and to assess their statistical significance. This is implemented by using a matched filter technique; in order to obtain an estimate of the mean transmission we simply convolve a normalised spectrum (of N_p pixels) with a smoothing function of scale σ_s and repeat this process for all possible scales ($\sigma_s = 1, \dots, N_p$). This smoothing essentially filters out the high frequency ‘noise’ of the individual absorption lines. When plotted in the (λ, σ_s) plane, this procedure

results in the ‘transmission triangle’ of the spectrum. When using a top hat function as the smoothing function the base of the transmission triangle is the spectrum itself (the original spectrum smoothed by a top hat of width $\sigma_s = 1$ pixel) and the tip of the triangle is $1 - D_A$ (Oke & Korycansky 1982) (the original spectrum smoothed by a top hat of width $\sigma_s = N_p$ pixels). Since we are only interested in local fluctuations of the transmission around the mean, we then subtract out the mean as calculated on the basis of our null-hypothesis. Essentially, this removes the global redshift evolution of the optical depth. The statistical significance of any remaining residual fluctuations around zero are then assessed in terms of the expected rms as a function of wavelength and scale.

In the rest of this section we calculate the relevant quantities. The work presented here is developed from earlier calculations carried out by Zuo & Phinney (1993), Zuo (1993) and Zuo & Bond (1994) (but see also Press, Rybicki, & Schneider 1993). For completeness and clarity we reiterate some of their derivations in Section 2.2.1.

When considering the expected mean transmission and its variance it is helpful to introduce the concept of transmission probability. The idea is to view a Ly α forest spectrum as a random stochastic process (Press, Rybicki, & Schneider 1993). Every point in the spectrum is a random variable, $e^{-\tau}$, drawn from the transmission probability density function $f_\lambda(e^{-\tau})$, also known as flux decrement distribution function (Rauch et al. 1997; Kim et al. 1997) or distribution of intensities (Jenkins & Ostriker 1991; Webb et al. 1992). In principle, we have a different probability density function at each wavelength such that e.g. the moments of f_λ are functions of wavelength. There is a small and subtle difference between the transmission probability density function and the distribution of pixel intensities of a spectrum. f_λ should in principle be measured by constructing the frequency distribution of pixel intensities at λ (and only at λ) of many different spectra. Although this is important to note we shall see later that at least the first and second moments of f_λ are only slowly varying functions of λ so that in many calculations we can approximate $e^{-\tau}$ as a stationary stochastic process.

2.2.1 The mean Ly α transmission

Given the distribution of absorption line parameters $d^3\mathcal{N}/dz dN db = \eta(z, N, b)$, what is the mean transmission at a given wavelength? We can define an effective optical depth, τ_{eff} , as a function of observed wavelength, λ , by

$$e^{-\tau_{\text{eff}}(\lambda)} \equiv \langle e^{-\tau(\lambda)} \rangle. \quad (2.1)$$

In the following we will neglect any contribution to τ_{eff} from the classical Gunn-Peterson effect (Gunn & Peterson 1965) which is limited to $\tau_{\text{GP}} \lesssim 0.04$ (Webb et al. 1992). If the number of absorption lines per sight-line is Poisson distributed with a mean of $m = \int_0^\infty \int_0^\infty \int_{z_1}^{z_2} \eta(z, N, b) dz dN db$ then we have

$$e^{-\tau_{\text{eff}}} = \sum_{k=0}^{\infty} p(k; m) \langle e^{-\tau_s} \rangle^k, \quad (2.2)$$

where $p(k; m) = e^{-m} m^k / k!$ and

$$\langle e^{-\tau_s(\lambda)} \rangle = \int_0^\infty \int_0^\infty \int_{z_1}^{z_2} \frac{\eta(z, N, b)}{m} e^{-\tau_s(\lambda_z; N, b)} dz dN db. \quad (2.3)$$

$\tau_s(\lambda_z; N, b)$ is the profile of a single absorption line at z, N, b where $\lambda_z = \lambda/(1+z)$. After some algebra we find

$$\begin{aligned} \tau_{\text{eff}} = m(1 - \langle e^{-\tau_s} \rangle) &= \int \eta(1 - e^{-\tau_s(\lambda_z)}) dz dN db \\ &= \lambda \int_0^\infty \int_0^\infty \int_{\lambda_{z_2}}^{\lambda_{z_1}} \frac{\eta}{\lambda_z^2} (1 - e^{-\tau_s(\lambda_z)}) d\lambda_z dN db \end{aligned} \quad (2.4)$$

If we exclude strongly saturated and damped systems from our analysis then $\tau_s(\lambda_z)$ peaks sharply at $\lambda_z = \lambda_\alpha = 1215.67 \text{ \AA}$ so that

$$\tau_{\text{eff}} \simeq \frac{1 + z_{\text{abs}}}{\lambda_\alpha} \iint \eta(z_{\text{abs}}, N, b) \int_{\lambda_{z_2}}^{\lambda_{z_1}} (1 - e^{-\tau_s(\lambda_z)}) d\lambda_z dN db, \quad (2.5)$$

where $z_{\text{abs}} = \lambda/\lambda_\alpha - 1$. Usually, $z_1 = \lambda_\beta/\lambda_\alpha(1 + z_{\text{em}}) - 1$ where $\lambda_\beta = 1025.72 \text{ \AA}$ and, in the absence of a proximity effect, $z_2 = z_{\text{em}}$. For λ close to $\lambda_\alpha(1 + z_{\text{em}})$, there are fewer than average absorption lines longward of λ . This produces an ‘edge effect’, superimposed on the well-known proximity effect (Weymann, Carswell, & Smith 1981; Cooke, Espey, & Carswell 1997). Similarly, there will be a reverse edge effect

for λ close to $\lambda_\beta(1 + z_{\text{em}})$ because of the additional absorption by Ly β lines. If λ falls well away from these limits then we can extend the upper and lower integration limits in (2.5) to ∞ and 0 respectively because, if λ_z and λ_α are sufficiently far apart, $1 - e^{-\tau_s}$ is zero. Thus we have

$$\tau_{\text{eff}} \simeq \frac{1 + z_{\text{abs}}}{\lambda_\alpha} \int \eta(z_{\text{abs}}, N, b) W(N, b) dN db. \quad (2.6)$$

Observationally η is found to be of the form $\eta(z, N, b) = (1 + z)^\gamma F(N, b)$ (Kim et al. 1997; Lu et al. 1996; Bechtold 1994; Williger et al. 1994; Bahcall et al. 1993). We therefore arrive at

$$\tau_{\text{eff}} = B(1 + z_{\text{abs}})^{\gamma+1} = B \left(\frac{\lambda}{\lambda_\alpha} \right)^{\gamma+1}, \quad (2.7)$$

where

$$B = \frac{1}{\lambda_\alpha} \int_0^\infty \int_0^\infty F(N, b) W(N, b) dN db. \quad (2.8)$$

In practice, we compute B directly from the data for reasons described in Section 2.3. Thus we have

$$\langle e^{-\tau} \rangle = e^{-B \left(\frac{\lambda}{\lambda_\alpha} \right)^{\gamma+1}}. \quad (2.9)$$

2.2.2 The auto-covariance

The auto-covariance function of the transmission is given by

$$\begin{aligned} \gamma_{e^{-\tau}}(\lambda, \lambda') &= \left\langle \left[e^{-\tau(\lambda)} - \langle e^{-\tau(\lambda)} \rangle \right] \left[e^{-\tau(\lambda')} - \langle e^{-\tau(\lambda')} \rangle \right] \right\rangle \\ &= \langle e^{-\tau(\lambda)} e^{-\tau(\lambda')} \rangle - e^{-\tau_{\text{eff}}(\lambda)} e^{-\tau_{\text{eff}}(\lambda')} \\ &\equiv e^{-\Pi(\lambda, \lambda')} - e^{-\tau_{\text{eff}}(\lambda)} e^{-\tau_{\text{eff}}(\lambda')}. \end{aligned} \quad (2.10)$$

Following the same calculations as in the previous section, we find

$$\Pi(\lambda, \lambda') = \int \eta(z, N, b) (1 - e^{-\tau_s(\lambda)} e^{-\tau_s(\lambda')}) dz dN db. \quad (2.11)$$

Let us consider the variance of the transmission given by

$$\sigma_{e^{-\tau}}^2 = \gamma_{e^{-\tau}}(\lambda, \lambda). \quad (2.12)$$

Since $\tau_s(N) \propto N$, we have $2\tau_s(N) = \tau_s(2N)$ and thus we get similarly to equation (2.7)

$$\Pi(\lambda, \lambda) = \tilde{B}(1+z)^{\gamma+1}, \quad (2.13)$$

where

$$\tilde{B} = \frac{1}{\lambda_\alpha} \int_0^\infty \int_0^\infty F(N, b) W(2N, b) dN db. \quad (2.14)$$

Observations have shown that the distribution of column densities can be fairly well represented by a power law, $F(N, b) = N^{-\beta} f(b)$ (Carswell et al. 1984) with $\beta \approx 1.5$ (Kim et al. 1997; Kirkman & Tytler 1997; Lu et al. 1996; Hu et al. 1995). A finite number of absorption lines per line of sight implies that the power law must break off at the low N end at some N_{low} . We also expect a break at the high N end at some N_{hi} . Thus we have

$$\tilde{B} = \frac{2^{\beta-1}}{\lambda_\alpha} \int_0^\infty \int_{2N_{\text{low}}}^{2N_{\text{hi}}} F(N, b) W(N, b) dN db. \quad (2.15)$$

We know that the power law is a good approximation for the range $12 \lesssim \log N \lesssim 22$ (Hu et al. 1995; Petitjean et al. 1993), so that N_{low} and N_{hi} are in the linear and square-root regimes of the curve of growth respectively. Under this assumption it is straightforward to show that \tilde{B} can be well approximated by $2^{\beta-1}B$ for $\beta \lesssim 1.8$, this being the exact result (for all β) if there are no breaks in the power law. Therefore we finally arrive at

$$\sigma_{e^{-\tau}}^2 = \exp \left[-2^{\beta-1}B(1+z)^{\gamma+1} \right] - \exp \left[-2B(1+z)^{\gamma+1} \right]. \quad (2.16)$$

2.2.3 Instrumental effects

So far we have not considered any instrumental effects. There are two classes of such effects: finite spectral resolution and various sources of noise.

Finite resolution

A new stochastic variable X is produced by convolving $e^{-\tau}$ with a line spread function (LSF) L :

$$X(\lambda) = \int_{-\infty}^{\infty} e^{-\tau(\lambda')} L(\lambda - \lambda') d\lambda' \quad (2.17)$$

For the mean of X we get

$$\langle X \rangle = \int_{-\infty}^{\infty} \langle e^{-\tau(\lambda')} \rangle L(\lambda - \lambda') d\lambda'. \quad (2.18)$$

Although it has been stressed that the mean and the variance of $e^{-\tau}$ are functions of λ , we will now approximate $e^{-\tau}$ as a *stationary* stochastic process because both the mean and the variance are smooth, slowly varying functions of λ . Lu & Zuo (1994) have shown this approximation to be valid. Thus we have

$$\langle X \rangle(\lambda) \simeq e^{-\tau_{\text{eff}}(\lambda)} \quad (2.19)$$

since the LSF is normalised to unity. As is intuitively clear, the convolution does not change the mean transmission.

The auto-covariance function of X is given by

$$\begin{aligned} \gamma_X(\lambda_1, \lambda_2) &= \langle (X(\lambda_1) - \langle X \rangle(\lambda_1)) (X(\lambda_2) - \langle X \rangle(\lambda_2)) \rangle \\ &= \int_{-\infty}^{+\infty} \int_{-\infty}^{+\infty} L(\lambda_1 - \lambda'_1) L(\lambda_2 - \lambda'_2) \gamma_{e^{-\tau}}(\lambda'_1, \lambda'_2) d\lambda'_1 d\lambda'_2. \end{aligned} \quad (2.20)$$

Since we consider $e^{-\tau}$ to be a *stationary* process, $\gamma_{e^{-\tau}}$ depends only on $u' = \lambda'_2 - \lambda'_1$ and γ_X depends only on $u = \lambda_2 - \lambda_1$ (Jenkins & Watts 1968). Usually, the LSF can be well approximated as a Gaussian. After some algebra we get

$$\gamma_X(u) = \frac{1}{\sqrt{2\pi}\sigma'_{\text{LSF}}} \int_{-\infty}^{\infty} \gamma_{e^{-\tau}}(u') \exp \left[-\frac{(u - u')^2}{2\sigma'^2_{\text{LSF}}} \right] du', \quad (2.21)$$

where $\sigma'_{\text{LSF}} = \sqrt{2}\sigma_{\text{LSF}}$.

Noise

The noise in optical spectra is mainly due to photon counting statistics, detector read-out noise, dark current, sky subtraction and cosmic rays. As the Poisson statistics of the absorption lines are expected to dominate the variance we have not attempted to model the noise characteristics in great detail. We rather approximate the cumulative effect of all the noise components mentioned above to be Gaussian. Therefore, we define the stochastic variable Y by

$$Y(\lambda) = X(\lambda) + n(X(\lambda)), \quad (2.22)$$

where n is a random variable drawn from a Gaussian with mean zero and variance $\sigma_n^2(X) = X(c_1 - c_2) + c_2$. The constants c_1 and c_2 characterise the photon counting statistics and the sky subtraction plus detector noise ($c_1 > c_2$). For the mean of Y we have

$$\langle Y \rangle = \langle X \rangle + \langle n \rangle = \langle X \rangle = \langle e^{-\tau} \rangle \quad (2.23)$$

and the covariance is given by

$$\gamma_Y(\lambda_1, \lambda_2) = \gamma_X(\lambda_1, \lambda_2) + \gamma_{Xn}(\lambda_1, \lambda_2) + \gamma_{Xn}(\lambda_2, \lambda_1) + \gamma_n(\lambda_1, \lambda_2). \quad (2.24)$$

γ_{Xn} denotes the *cross-covariance* function of X and n . Although X and n are not *independent* they are, by construction, *uncorrelated*, so that $\gamma_{Xn} = 0$. Zuo & Bond (1994) showed that the originally uncorrelated photon noise in different wavelength bins remains uncorrelated after passing through a spectrograph of finite resolution. Therefore $\gamma_n(u)$ must be discontinuous at $u = 0$:

$$\gamma_n(u) = \begin{cases} 0 & u > 0 \\ \int f_X(x) \sigma_n^2(x) dx & u = 0 \end{cases} \quad (2.25)$$

where $f_X(x)$ denotes the pdf of X . The integral reduces to $\sigma_n^2(\langle X \rangle)$. Thus

$$\begin{aligned} \sigma_Y^2 &= \sigma_X^2 + \sigma_n^2(\langle X \rangle) \\ \gamma_Y(u) &= \gamma_X(u) \quad u > 0. \end{aligned} \quad (2.26)$$

2.2.4 Filter matching

In order to develop a method for detecting structures of arbitrary scale, we proceed by convolving the spectrum with a smoothing function of smoothing scale σ_s . The convolution filters out all power on scales smaller than σ_s . By changing the width of the smoothing function we can match the filter width to the scale of any feature and thus maximise its signal. In practice, we perform the convolution successively at all possible smoothing scales. At the largest possible scale ($\sigma_{s,\max}$ = number of pixels in the spectrum) the entire spectrum is compressed into a single number whereas on the smallest scale ($\sigma_{s,\min}$ = 1 pixel) the spectrum remains essentially unchanged.

These two extremes correspond to the tip and the base of the triangle which forms when the successive convolutions of the spectrum are plotted in the (λ, σ_s) plane. In principle, there are many choices for the specific form of the smoothing function but for simplicity we will use a Gaussian, thus constructing a new stochastic variable G :

$$G(\lambda, \sigma_s) = \frac{1}{\sqrt{2\pi} \sigma_s} \int_{-\infty}^{\infty} Y(\lambda') \exp\left(-\frac{(\lambda - \lambda')^2}{2\sigma_s^2}\right) d\lambda'. \quad (2.27)$$

As in Section 2.2.3 we have

$$\langle G \rangle(\lambda) \simeq e^{-\tau_{\text{eff}}(\lambda)} = \exp\left[-B \left(\frac{\lambda}{\lambda_\alpha}\right)^{\gamma+1}\right]. \quad (2.28)$$

Note that the use of a top hat function would yield a variable akin to $1 - D_A$ (and the same result as equation (2.28)), where D_A is the flux deficit parameter (Oke & Korycansky 1982). The observations are consistent with this result (Press, Rybicki, & Schneider 1993; Zuo & Lu 1993; but see also Bi & Davidsen 1997). Similar to equation (2.21) we find

$$\begin{aligned} \gamma_G(u) &= \frac{1}{\sqrt{2\pi} \sigma'_s} \int_{-\infty}^{\infty} \gamma_Y(u') \exp\left[-\frac{(u - u')^2}{2\sigma_s'^2}\right] du' \\ &= \frac{\sigma_n^2(e^{-\tau_{\text{eff}}})}{\sqrt{2\pi} \sigma'_s / ps} e^{-\frac{u^2}{2\sigma_s'^2}} \\ &+ \frac{1}{\sqrt{2\pi} \sqrt{\sigma_s'^2 + \sigma_{\text{LSF}}'^2}} \int_{-\infty}^{\infty} \gamma_{e^{-\tau}}(u'') \exp\left[-\frac{(u - u'')^2}{2(\sigma_s'^2 + \sigma_{\text{LSF}}'^2)}\right] du'' \end{aligned} \quad (2.29)$$

where ps denotes the pixel size in Å. To proceed we need to consider the auto-covariance function of a ‘perfect’ spectrum, $\gamma_{e^{-\tau}}$, in more detail. In principle, it can be calculated from equation (2.11) as was done by Zuo & Bond (1994) for a single Doppler parameter rather than a distribution of b values. The result is a rather unwieldy numerical integral. Here we can take a different approach. As expected, we can see from equation (2.29) that the quantity that we are interested in, $\sigma_G^2 = \gamma_G(0)$, does *not* depend on the exact shape of $\gamma_{e^{-\tau}}$ but rather on the convolution of $\gamma_{e^{-\tau}}$ with a Gaussian. We may therefore hope to be able to use a simpler analytic approximation for $\gamma_{e^{-\tau}}$ since all systematic differences will be somewhat ‘washed out’ by the convolution. Ultimately, this procedure must be

justified by its success. We shall return to this point when we compare the results of this section to simulations. The most obvious (because simplest) approximation for $\gamma_{e^{-\tau}}$ is a Gaussian, especially when considering that unsaturated Voigt profiles are very nearly Gaussian:

$$\gamma_{e^{-\tau}}(u) \simeq \sigma_{e^{-\tau}}^2 e^{-\frac{u^2}{2q^2}}. \quad (2.30)$$

Since we are operating in wavelength space rather than in velocity space the width, q , must be a function of wavelength, because an absorption line with a given Doppler parameter will be wider in wavelength space at higher redshifts than at lower redshifts. This is of course just another reflection of the fact that $e^{-\tau}$ is not a stationary process. But again, q will vary only slowly with wavelength (approximately linearly) so that the stationary approximation is valid. Using this approximation we find

$$\sigma_G^2(\lambda, \sigma_s) = \frac{\sigma_n^2(e^{-\tau_{\text{eff}}(\lambda)})}{2\sqrt{\pi} \sigma_s/pS} + \frac{\sigma_{e^{-\tau}}^2(\lambda)}{\sqrt{2\frac{\sigma_s^2 + \sigma_{\text{LSF}}^2}{q^2(\lambda)} + 1}}. \quad (2.31)$$

Equations (2.28) and (2.31) are the final result of this section.

2.3 Simulations

The motivation for simulations of Ly α forest spectra in this work is threefold. First of all we need to determine the parameters B and q . The normalisation B could be calculated numerically from equation (2.8). However, it is clear that for real data small inaccuracies in the zeroth and first order of the continuum fit will cause an artificial offset of the measured mean transmission from the calculated one. In anticipation of this problem we choose to determine B directly from the data. Since equation (2.30) is only an approximation we cannot *a priori* calculate a precise value for q . We therefore have to measure it from simulations. Secondly, we would like to check the validity of equations (2.28) and (2.31) by comparing the calculations with an analysis of simulated spectra. Thirdly, we would like to compare the sensitivity of the new analysis to the presence of non-random structures to that of the traditional line counting technique. In order to cater for this third need, we employed a more

sophisticated method than simply randomly drawing the parameters of absorption lines from a given distribution $\eta(z, N, b)$. Instead we distribute absorbers in a cosmological volume and take lines of sight through that volume. This provides the flexibility of introducing specific types of clustering models. We assume absorbers to be spherical and prescribe a column density–impact parameter relationship of the form $N(r) = N_0(r/r_0)^{-a}$ which has been observed at low redshift where galaxies are unambiguously associated with Ly α absorbers (Chen et al. 1998; Lanzetta, Webb, & Barcons 1996; Lanzetta et al. 1995; but see also Bowen, Blades, & Pettini 1996). This procedure simply ensures that the column density distribution of the absorption lines will be of the form $N^{-\beta}$ with $\beta = 2/a + 1$. We draw Doppler parameters from a truncated Gaussian. We choose to keep the comoving number density of absorbers constant and thus ascribe their redshift evolution solely to the evolution of their absorption cross-section. This requires a redshift dependence of r_0

$$r_0(z) = r_0(\hat{z}) \frac{(1 + 2q_0z)^{\frac{1}{4}} (1 + z)^{\frac{\gamma-1}{2}}}{(1 + q_0)^{\frac{1}{4}} (1 + \hat{z})^{\frac{\gamma-1}{2}}} \quad (2.32)$$

where we take the normalisation $r_0(\hat{z}) = 1 \text{ h}^{-1} \text{ Mpc}$ at $N_0 = 10^{12} \text{ cm}^{-2}$ from Lanzetta et al. (1995) at $\hat{z} = 0.5$.

2.3.1 B and q from simulations

In order to compare equations (2.28) and (2.31) with simulations we have produced a set of 1000 spectra in the manner described in the previous section with randomly distributed absorbers. The spectra are convolved with a line spread function and noise is added according to equation (2.22). The parameters of the simulation are listed in Table 2.1 (S1). For each spectrum we constructed its transmission triangle using a Gaussian smoothing function. From this set of 1000 triangles we produced the mean and rms transmission triangles which are shown in Figs. 2.1 and 2.2. Before we can go on to compare these results with equations (2.28) and (2.31) we must determine the values of the two parameters B and q . We fix the normalisation

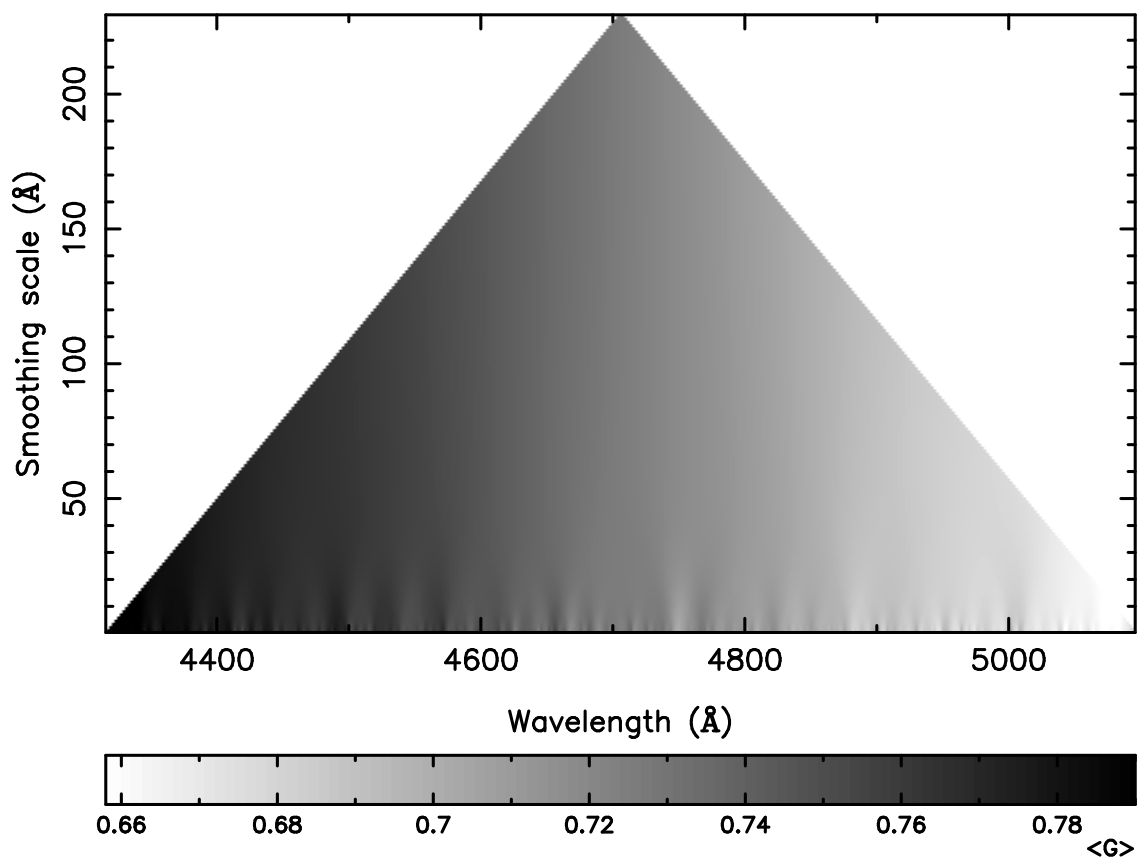


Figure 2.1: Mean transmission triangle produced from 1000 simulated spectra.

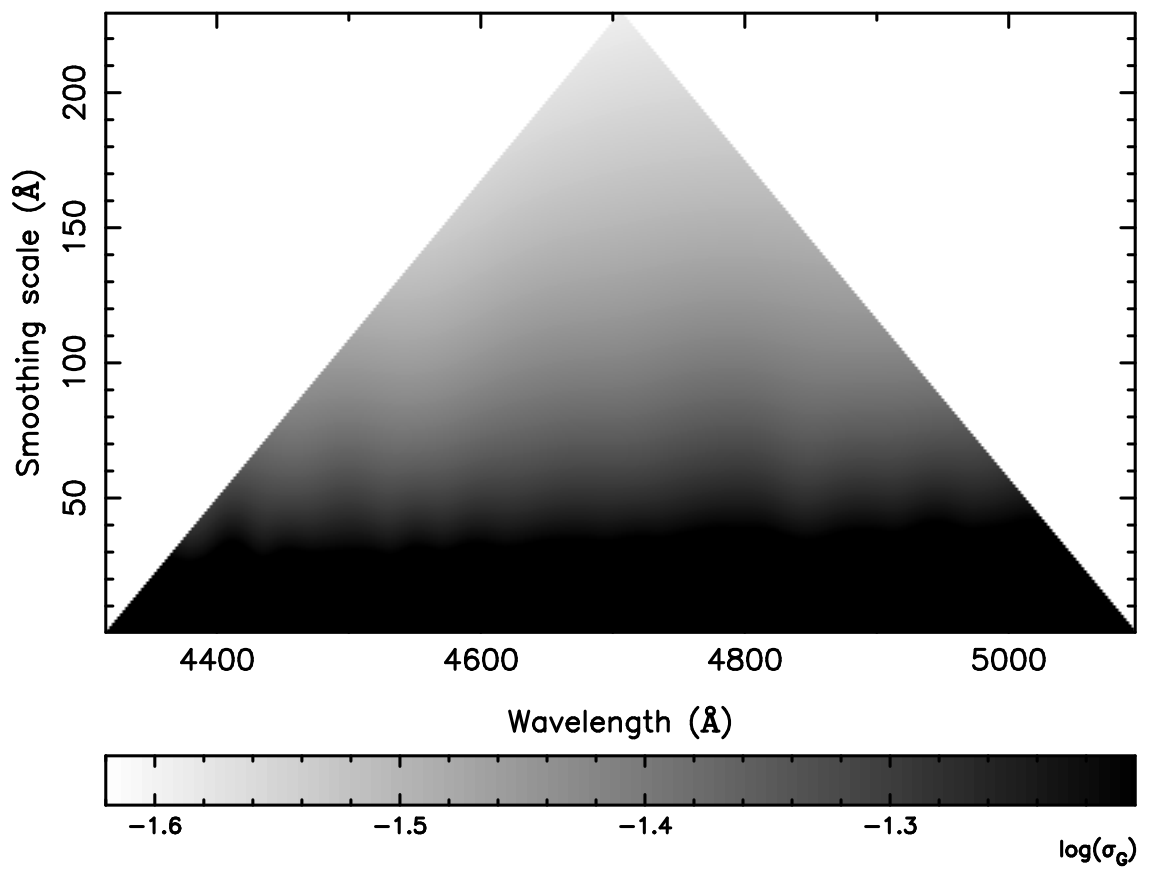


Figure 2.2: Rms transmission triangle produced from 1000 simulated spectra.

Table 2.1: Parameters of simulations.

	γ	β	n_0 ($h^3 \text{ Mpc}^{-3}$)	μ_b (km s^{-1})	σ_b (km s^{-1})	b_{cut} (km s^{-1})	S/N	FWHM_{LSF} (\AA)
S1	2.5	1.5	0.01	30	8	18	20	2
S2	2.5	1.7	0.01	30	8	18	20	2
S3	2.7	1.5	0.01	30	8	18	20	2
S4	2.5	1.5	0.015	30	8	18	20	2
S5	2.5	1.5	0.01	50	8	38	20	2
S6	2.5	1.5	0.01	30	16	18	20	2
S7	2.5	1.5	0.01	30	8	18	20	0.5
S8	2.5	1.5	0.01	30	8	18	5	2

n_0 is the comoving number density of absorbers [normalisation of $\eta(z, N, b)$], μ_b , σ_b and b_{cut} are the mode, width and lower cut-off of the Doppler parameter distribution respectively. For models S1 and S7 we created 1000 spectra, in all other cases we simulated 100 spectra. For all spectra $\langle z \rangle = 2.87$.

B at the tip of the mean transmission triangle by requiring

$$\langle G \rangle(\sigma_{s,\max}, \lambda_c) = e^{-B(\frac{\lambda_c}{\lambda_\alpha})^{\gamma+1}}, \quad (2.33)$$

where $\sigma_{s,\max}$ denotes the biggest possible smoothing scale and λ_c is the central wavelength of the region under consideration. Having stipulated equation (2.30) we measure q (at λ_c) from the simulations by performing a single parameter χ^2 fit of the function

$$\gamma_Y(u) = \begin{cases} \sigma_n^2(e^{-\tau_{\text{eff}}(\lambda_c)}) + \frac{\sigma_{e^{-\tau}}^2(\lambda_c)}{\sqrt{2\frac{\sigma_{\text{LSF}}^2}{q^2} + 1}} & u = 0 \\ \frac{\sigma_{e^{-\tau}}^2(\lambda_c)}{\sqrt{2\frac{\sigma_{\text{LSF}}^2}{q^2} + 1}} \exp\left[\frac{-u^2}{2(2\sigma_{\text{LSF}}^2 + q^2)}\right] & u > 0 \end{cases} \quad (2.34)$$

to the mean auto-covariance function of the 1000 simulated spectra. Since equation (2.30) (and hence equation 2.34) is an approximation we do not *a priori* expect a statistically acceptable fit. Nevertheless, in practice this procedure provides a reliable estimate of q because both the shape (width) *and* normalisation of γ_Y are sensitive to q . Fig. 2.3 shows the measured mean auto-covariance function of S1 and its fit. The same is also plotted for two other sets of spectra (cf. Table 2.1), S7 (same model as S1 but the spectra are of higher resolution) and S5 (larger mode of the Doppler parameter distribution). It is evident that a Gaussian does not adequately represent the auto-covariance functions; a Gaussian has too much power on small scales and too little power on larger scales. Indeed, each fit produces an unacceptably large χ^2 , although we point out that in any case a somewhat larger than usual χ^2 must be anticipated because of the non-Gaussian and correlated nature of the measurement errors of γ_Y . However, we recall that we are mostly interested in the typical width and strength of the correlation rather than its exact shape. Since both sets of spectra S1 and S7 should yield the same value for q , the purpose of set S7 was to check whether the above method of determining q is robust and to provide an estimate of the true error in q as opposed to the formal error as calculated from the χ^2 fit. As expected, q is of the order of the mode Doppler parameter, μ_b , for a range of sensible values for μ_b , as seen from S5. In fact, q is seen to vary almost linearly with μ_b , which justifies $q(\lambda) = q(\lambda_c)\lambda/\lambda_c$. We have also

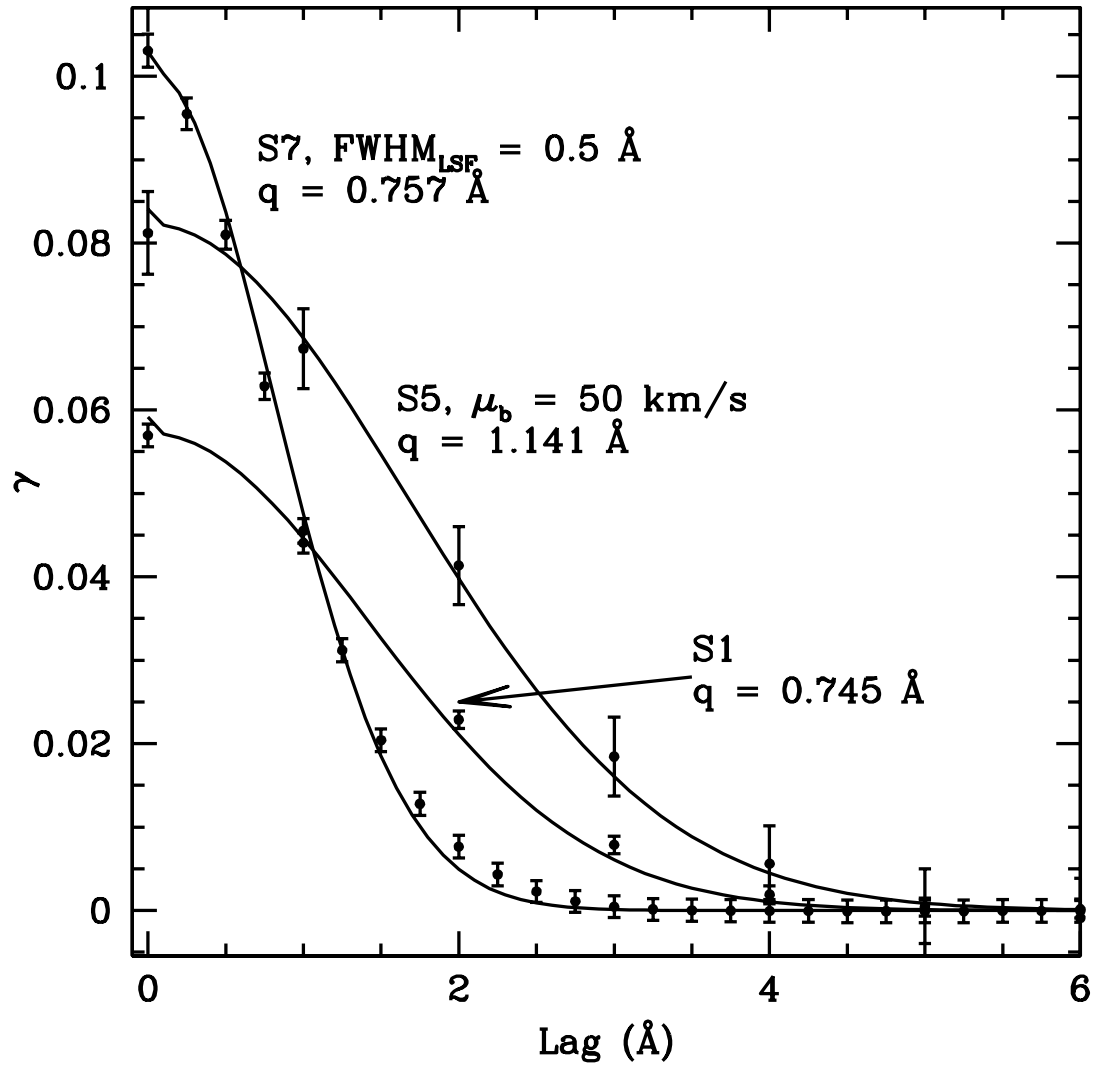


Figure 2.3: Auto-covariance functions of different models as indicated and best fits (solid lines). For clarity, all errorbars have been exaggerated by a factor of 10.

investigated the behaviour of q as a function of the other model parameters and have found, as expected, that q is only sensitive to the parameters of the Doppler parameter distribution, μ_b and σ_b , and of the column density distribution, β . It is insensitive to the redshift evolution, overall normalisation and the quality of spectra since the q values measured from models S3, S4, S7 and S8 are all comparable. We conclude that the error in estimating q is dominated by the errors in μ_b , σ_b and β .

2.3.2 Comparison of analytical to numerical results

With the values of B and q thus determined we can now directly compare the results from the simulations with equations (2.28) and (2.31). Figs. 2.4 and 2.5(a) show cross-sections of the mean and rms transmission triangles of S1 as functions of wavelength at smoothing scale $\text{FWHM}_s = 3.2 \text{ \AA}$. Fig. 2.5(b) shows a cross-section through the rms transmission triangle as a function of smoothing scale at $z = 2.87$. The dashed lines show the calculations. Using the covariance matrix implied by equation (2.34), a χ^2 test performed on the base of the mean transmission triangle yields $P(> \chi^2) = 0.12$ and thus the model agrees very well with the simulations. For the rms the agreement is not quite as good. We find that for very large smoothing scales ($\text{FWHM}_s > 100 \text{ \AA}$) the model underestimates the rms by ~ 4 per cent. For smaller (and more relevant) scales the model fares progressively better.

We have repeated this exercise for all sets of simulations listed in Table 2.1 and have always found the same good agreement. In addition, we have repeated the calculations in Section 2.2.4 and the analysis of the simulated data for the case of a top hat smoothing function and these also agree very well. Thus we conclude that the errors in determining any fluctuations of the Ly α absorption around its expected mean and in estimating their significance will be dominated by the uncertainties in the assumed values of the parameters β , μ_b , σ_b and to lesser extent γ and the overall normalisation. Any errors made in any of the approximations of the previous sections are small compared to these uncertainties.

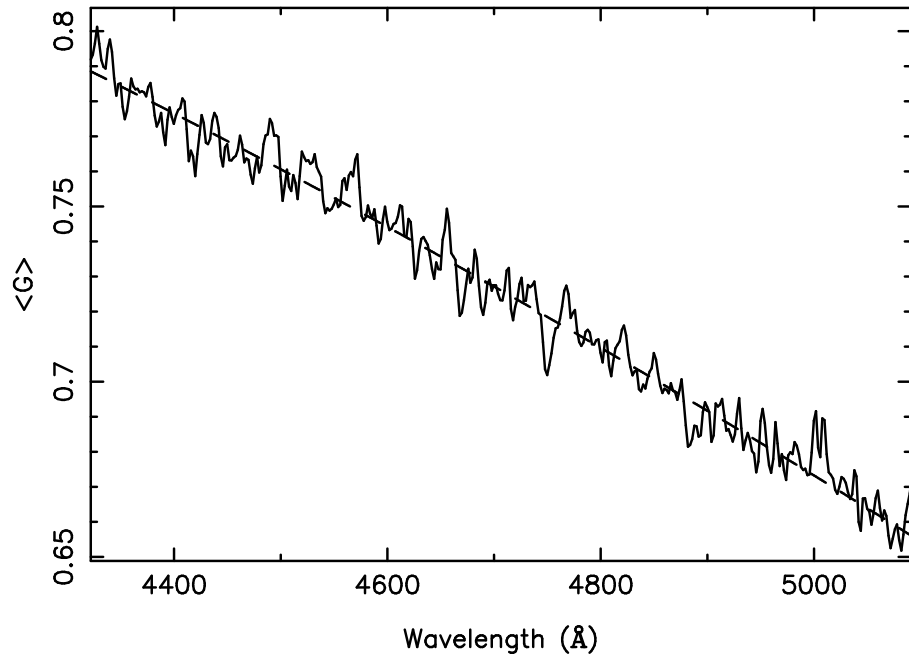


Figure 2.4: Cross-section of the mean transmission triangle (cf. Fig. 2.1) at $\text{FWHM}_s = 3.2 \text{ \AA}$. The dashed line shows the prediction of equation (2.28).

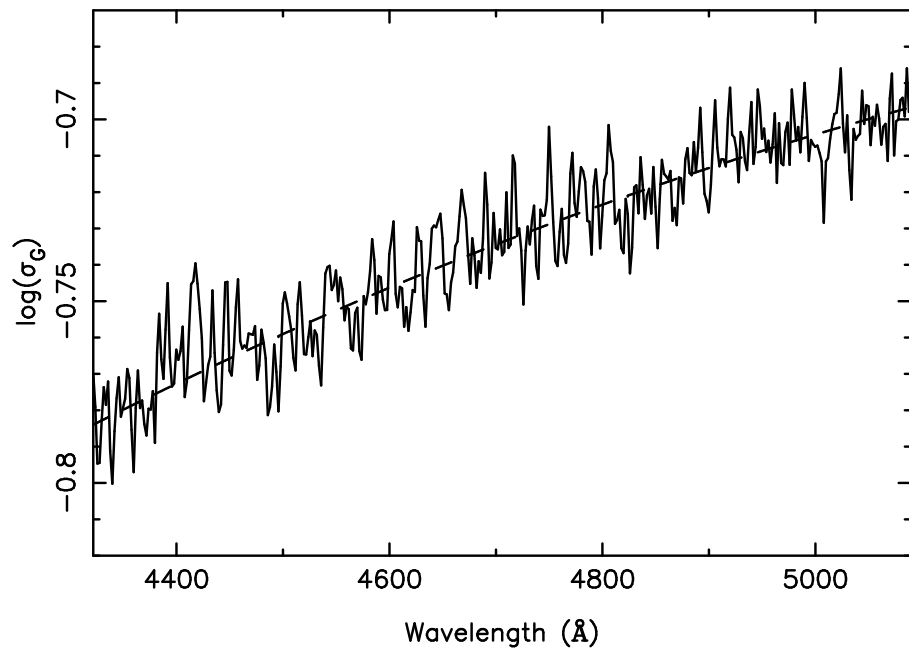


Figure 2.5: (a) Cross-section of the rms transmission triangle (cf. Fig. 2.2) at $\text{FWHM}_s = 3.2 \text{ \AA}$. The dashed line shows the prediction of equation (2.31).

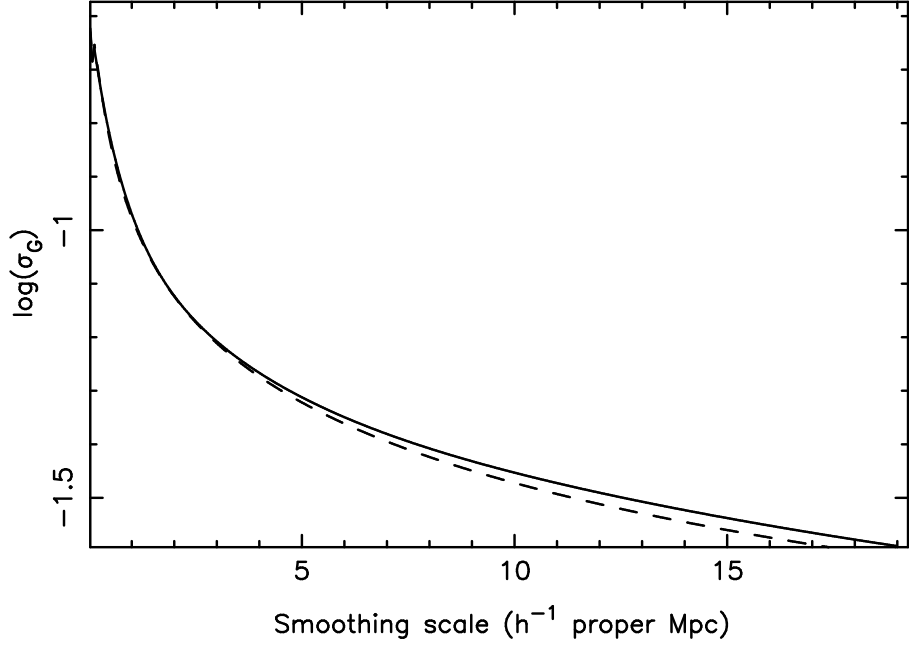


Figure 2.5: (b) Cross-section of the rms transmission triangle (cf. Fig. 2.2) at $z = 2.87$. The dashed line shows the prediction of equation (2.31).

2.3.3 Sensitivity

With all the calculations and parameter values in place we can now answer the questions: ‘How statistically significant is an enhancement of the local absorption line number density over the mean line number density at redshift z by a factor of δn on the scale of $x h^{-1}$ Mpc?’ and ‘At what redshift is an overdensity of δn on the scale of $x h^{-1}$ Mpc most significant?’ To address these questions we plot the quantity

$$\frac{e^{-\delta n \tau_{\text{eff}}} - e^{-\tau_{\text{eff}}}}{\sigma_G}$$

in Figs. 2.6(a) and (b) as a function of δn and z respectively for a scale of $5 h^{-1}$ proper Mpc (FWHM of smoothing Gaussian), assuming the parameters of S1. From Fig 2.6(a) we see that for a given redshift we can expect a maximum signal which cannot be exceeded. This is due to saturation as the number density of absorption lines increases rapidly towards higher redshift. Fig. 2.6(b) tells us that for a given level of overdensity there is an optimum redshift at which this level of

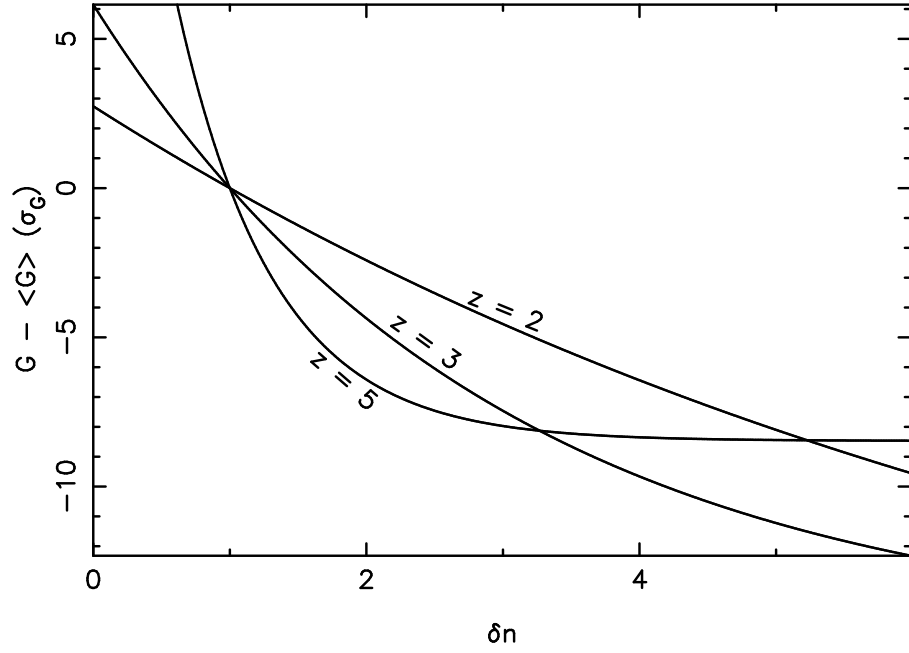


Figure 2.6: (a) Expected signal in units of σ_G of an overdensity of absorption lines of scale $5 h^{-1}$ proper Mpc (FWHM of smoothing Gaussian) at redshifts 2, 3 and 5.

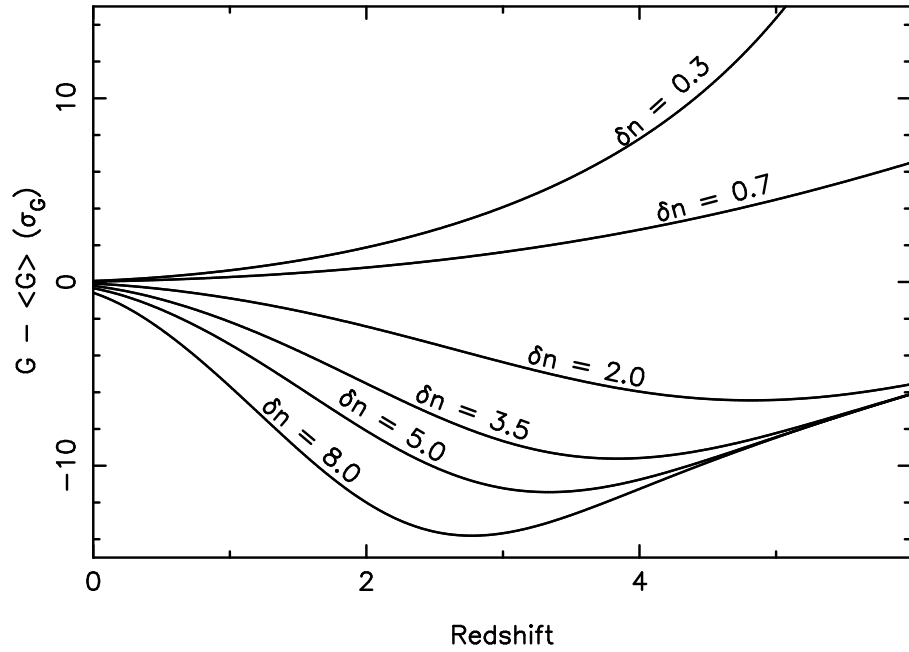


Figure 2.6: (b) Same as (a) as a function of redshift for the indicated overdensities.

overdensity will produce a maximum signal.

At this point it is necessary to comment on the exact significance of, e.g., a ‘ 3σ event’. For small smoothing scales the pdf of G is inherently non-Gaussian such that we expect the probability of G lying within 3σ of the mean to be smaller than 0.9973. In fact the pdf is skewed such that the probability of a $+3\sigma$ event (a void) is lower than the probability of a -3σ event (a cluster). At larger smoothing scales the Central Limit Theorem guarantees Gaussianity. Thus a 3σ event at large smoothing scales is statistically more significant than a similar event at small smoothing scales. This additional complication must be kept in mind.

2.3.4 Comparison to TPCF

Groups of QSOs that are closely spaced in the plane of the sky can be used to map out the large-scale 3-dimensional structure of the intervening absorbing gas by identifying absorption features that are approximately coincident in redshift space in two or more spectra. One of the advantages of the analysis presented here is that it can easily be applied to the spectra of such groups: the transmission triangles of the different spectra are simply averaged where they overlap. For sight-line separations of several arcminutes, different lines of sight will not intersect the same absorber, so that according to our null-hypothesis of an unclustered Ly α forest different lines of sight are uncorrelated. Therefore the variance of a mean transmission triangle (averaged over multiple lines of sight) at (λ, σ_s) is simply given by $\sigma_G^2(\lambda, \sigma_s)$ divided by the number of triangles overlapping at (λ, σ_s) . Thus the signal of any structure extending across several lines of sight will be enhanced.

In order to compare our analysis directly to a ‘traditional’ two-point correlation function analysis we have simulated spectra of a close group of QSOs where the absorbers are clustered. In view of the modern, large hydrodynamic simulations of structure formation which reproduce many of the observed properties of the Ly α forest, the simulations presented here must be understood in the sense of a toy model. The advantage of our simulation is the flexibility to model different cluster-

ing characteristics, thus enabling us to test our method comprehensively. It is not important for these particular clustering models to describe reality accurately since our aim is to compare the relative sensitivity of a two-point correlation function analysis and the technique we have developed here. The validity of this test is unlikely to depend strongly on the type of clustering. We have explored two clustering scenarios:

1. Absorbers are clustered according to the gravitational quasi-equilibrium distribution (GQED) function (Saslaw & Hamilton 1984). We implement this scenario by following an approach first developed by Neyman & Scott (1952) and described by Sheth & Saslaw (1994): we distribute clusters of absorbers randomly in a cosmological volume and draw the number of absorbers of a given cluster from the distribution (Saslaw 1989)

$$h(N) = \begin{cases} b & N = 0 \\ \frac{N^{N-1}}{N!} (1-b)b^{N-1} e^{-Nb} & N > 0. \end{cases} \quad (2.35)$$

b is the only parameter of the model and is defined as the ratio of potential and kinetic energies of the cluster ($0 \leq b \leq 1$). It is related to the two-point correlation function by (Saslaw & Hamilton 1984)

$$b \equiv -\frac{W}{2K} = \frac{2\pi G m^2 n}{3kT} \int_0^\infty \xi(r) dr, \quad (2.36)$$

where T and m are the temperature and mass of the cluster, n is the average number density and k and G have their usual meanings. We choose $b = 0.3$ (Sheth & Saslaw (1994) estimate for galaxies $b_0 \approx 0.75$) and members of a cluster have a velocity dispersion of 500 km s^{-1} . We assume clusters to be spherical and distribute absorbers within a cluster according to a King profile (King 1966).

2. Absorbers form ‘walls’. Considering the connection of the Ly α forest with galaxies at low redshift and the repeated findings of independent groups that galaxies form sheet- and wall-like structures (Broadhurst et al. 1990; Ettori, Guzzo, & Tarenghi 1997; Einasto et al. 1997; Connolly et al. 1996; Di Nella et al. 1996) it is conceivable that such structures may also be found in the Ly α forest. In addition,

at high redshift several hydrodynamic simulations have shown that the absorbing gas forms filaments, sheets and wall-like structures (Cen et al. 1994; Miralda-Escudé et al. 1996; Cen & Simcoe 1997; Hernquist et al. 1996; Zhang, Anninos, & Norman 1995; Petitjean, Mückel, & Kates 1995; Mückel et al. 1996; Riediger, Petitjean, & Mückel 1998; Wadsley & Bond 1997; Bond & Wadsley 1998), although these structures are of a smaller scale than we are interested in. In any case, we have included this model where walls of absorber overdensities extend across several lines of sight in order to demonstrate the better sensitivity of our analysis compared to a conventional *cross*-correlation analysis of fitted absorption lines.

For both scenarios we have computed 100 sets of simulated spectra of a close group of four QSOs using the parameters of S1.

Fig. 2.7 shows the result of our new analysis for the case of GQED clustering. For all spectra we have computed their transmission triangles, subtracted the mean given by equation (2.28) and divided by the rms given by the square-root of equation (2.31). We shall refer to the result as ‘reduced’ transmission triangles. In the reduced triangles all residual fluctuations are given in terms of their statistical significance rather than their absolute magnitude. In panel (a) of Fig. 2.7 we plot the histogram of the minimum values (maximally significant overdense absorption) measured in these reduced transmission triangles of the individual spectra. The distribution peaks at -3.6σ but in a significant fraction of cases (~ 40 per cent) we have a greater than 4σ detection. Panels (b) and (c) show that these detections are not spurious but actually arise from the clusters. In panel (b) we plot the distribution of scales (FWHM of smoothing Gaussian) at which the minima of panel (a) are detected. Clearly we recover the correct velocity dispersion of the clusters. We loosely define the ‘strongest’ cluster in a spectrum as the cluster with the highest total column density and plot in panel (c) the histogram of differences in velocity space between the strongest clusters and the detected minima, Δ . Although there is clearly a peak at 0 km s^{-1} of the correct width, there are a large number of cases where the detected minima do not coincide with the strongest clusters. However,

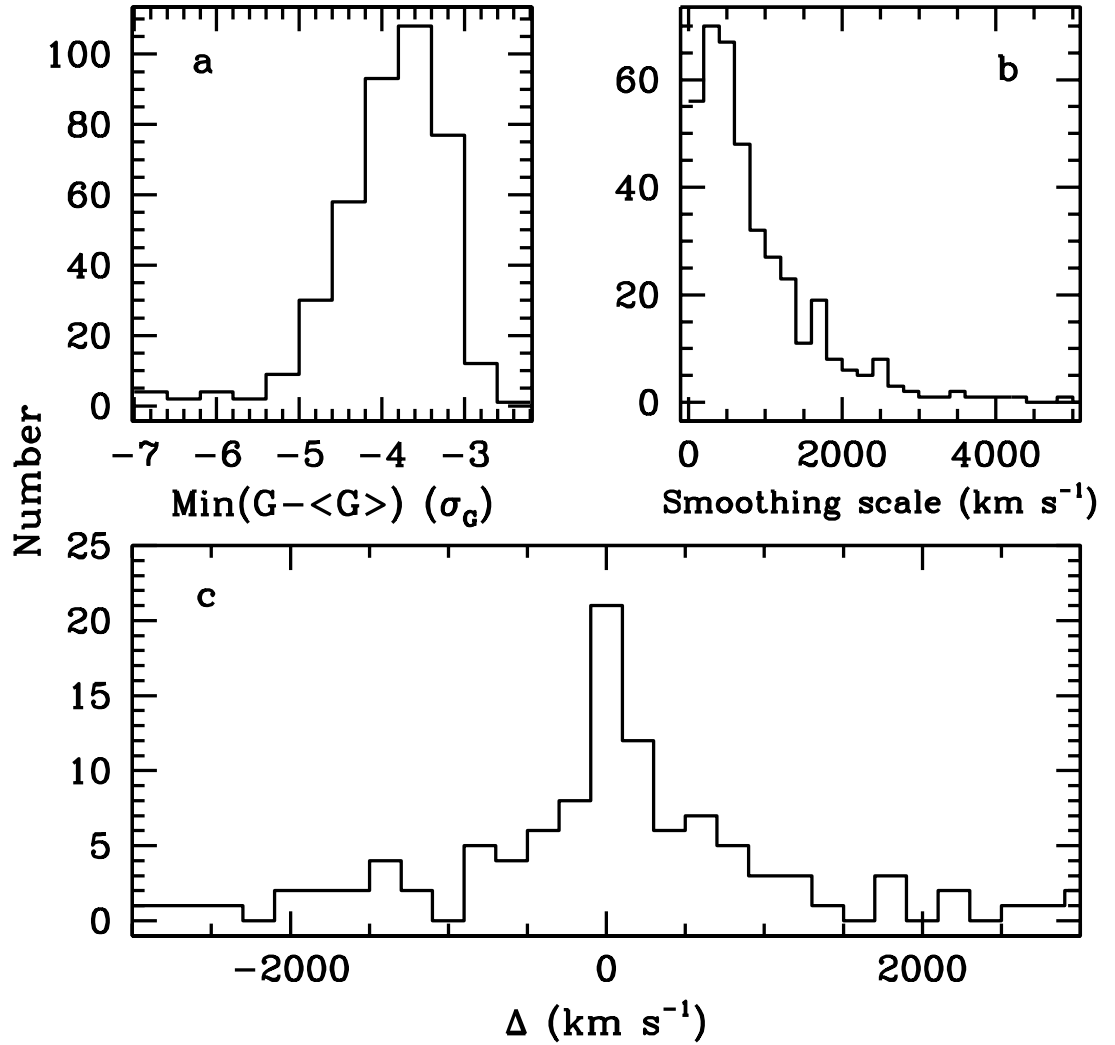


Figure 2.7: Distributions of (a) values and (b) scales of minima detected in reduced transmission triangles of spectra with GQED clustering. (c) Distribution of differences between the positions of the ‘strongest’ clusters (see text) and the minima of (a).

these mismatches do *not all* indicate spurious detections. Rather, they are mostly due to our definition of the strongest cluster, since it does not guarantee that the strongest cluster will produce the maximum absorption.

We now compare the results above with a two-point correlation function (tpcf) analysis. We compute both ‘real’ and ‘observed’ tpcfs from two separate lists of absorption lines. A ‘real’ list is derived from the input line list used to create the spectrum by simply applying an equivalent width detection threshold. To mimic blending due to instrumental resolution we generate an ‘observed’ line list from the input line list by blending all lines that lie within one FWHM_{LSF} of each other into a single line and imposing an equivalent width detection limit. The position of the blended line is taken as the equivalent width weighted average of its components. We estimate the 3σ equivalent width detection limit in our simulated data to be 0.26 \AA . The two-point correlation function is calculated as

$$\xi(\Delta v) = \frac{N_{\text{obs}}(\Delta v)}{N_{\text{exp}}(\Delta v)} - 1, \quad (2.37)$$

where N_{obs} and N_{exp} are the observed and expected number of pairs at separation Δv . We account for the evolution of the mean line number density in the calculation of N_{exp} . The individual line correlation functions of a set of four spectra are averaged to increase the signal to noise ratio.

In panel (a) of Fig. 2.8 we show the distribution of the maximally significant values detected in the averaged ‘observed’ (solid line) and ‘real’ (dotted line) two-point correlation functions. For an underlying clustered set of absorption lines, these distributions will be slightly sensitive to the bin size chosen in computing the tpcfs. To some extent this reflects one of the difficulties with the tpcf; one must chose *a priori* a bin size, without prior knowledge as to what an ‘optimal’ size might be. In practice, observers often chose the smallest convenient size which is larger than the instrumental resolution. We have done similarly in this experiment and have chosen 120 km s^{-1} .

The solid histogram in panel (a) peaks narrowly at 1.8σ . Only 3 per cent of the detections are $> 3\sigma$. Panel (b) shows the correlation scales at which the maxima

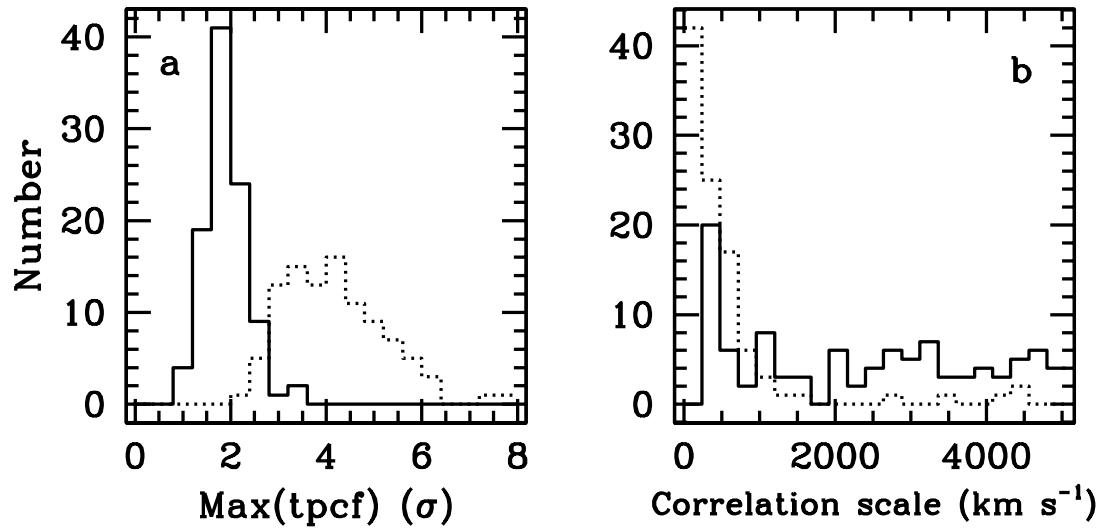


Figure 2.8: Distributions of (a) values and (b) correlation scales of averaged two-point correlation function maxima using ‘observed’ line lists (solid lines) and ‘real’ line lists (dashed lines).

are detected and we see that at least 50 per cent of the detections are spurious. The dotted histograms show the results for the ‘real’ tpcfs: significant detections (a) at the right scale (b). However, a comparison with panel (a) of Fig. 2.7 shows that a tpcf analysis, even with *infinite* resolution (but finite S/N) and a *perfect* line fitting algorithm, does only marginally better in uncovering the presence of clustering than our new analysis using intermediate resolution.

Fig. 2.9 shows the results for the case of a ‘wall’ of absorbers which is simulated by multiplying the redshift distribution of absorbers with a top hat function. The simulated wall is located at $z = 2.78$, it is $5 h^{-1}$ Mpc thick and is overdense by a factor of $\delta n = 2$. As described above we have averaged the individual transmission triangles of each set of four spectra. The distributions of the values, positions and scales of the minima detected in the reduced averaged triangles are plotted in panels (a), (b) and (c) respectively. *All* detections are above the 3σ level and from panel (b) we see that all detections are due to the wall. Taking the top hat shape of the wall into account, its thickness has correctly been recovered in panel (c). Using the peaks of the three distributions we calculate an overdensity of 2.6 (see also Fig. 2.6). As in Fig. 2.8 we plot in panel (d) the distribution of the maximum values detected in the averaged two-point correlation functions using the ‘observed’ (solid line) and the ‘real’ (dotted line) line lists. In addition, we performed a *cross*-correlation analysis and show the result as the dashed histogram. Both auto- and cross-correlations fail to deliver a significant result. In fact, even with *infinite* resolution and a *perfect* line fitting algorithm, the auto-tpcf analysis does a worse job of uncovering the ‘wall’ than our analysis using intermediate resolution.

For both cases discussed above we have demonstrated that our new analysis is substantially more sensitive to the presence of non-random structure in the Ly α forest than a traditional two-point correlation function analysis when applied to intermediate resolution data. To further illustrate this point we show in Fig. 2.10 the same distributions as in Figs. 2.7, 2.8 and 2.9 for the case where absorbers are randomly distributed. We note that the distributions of transmission minima

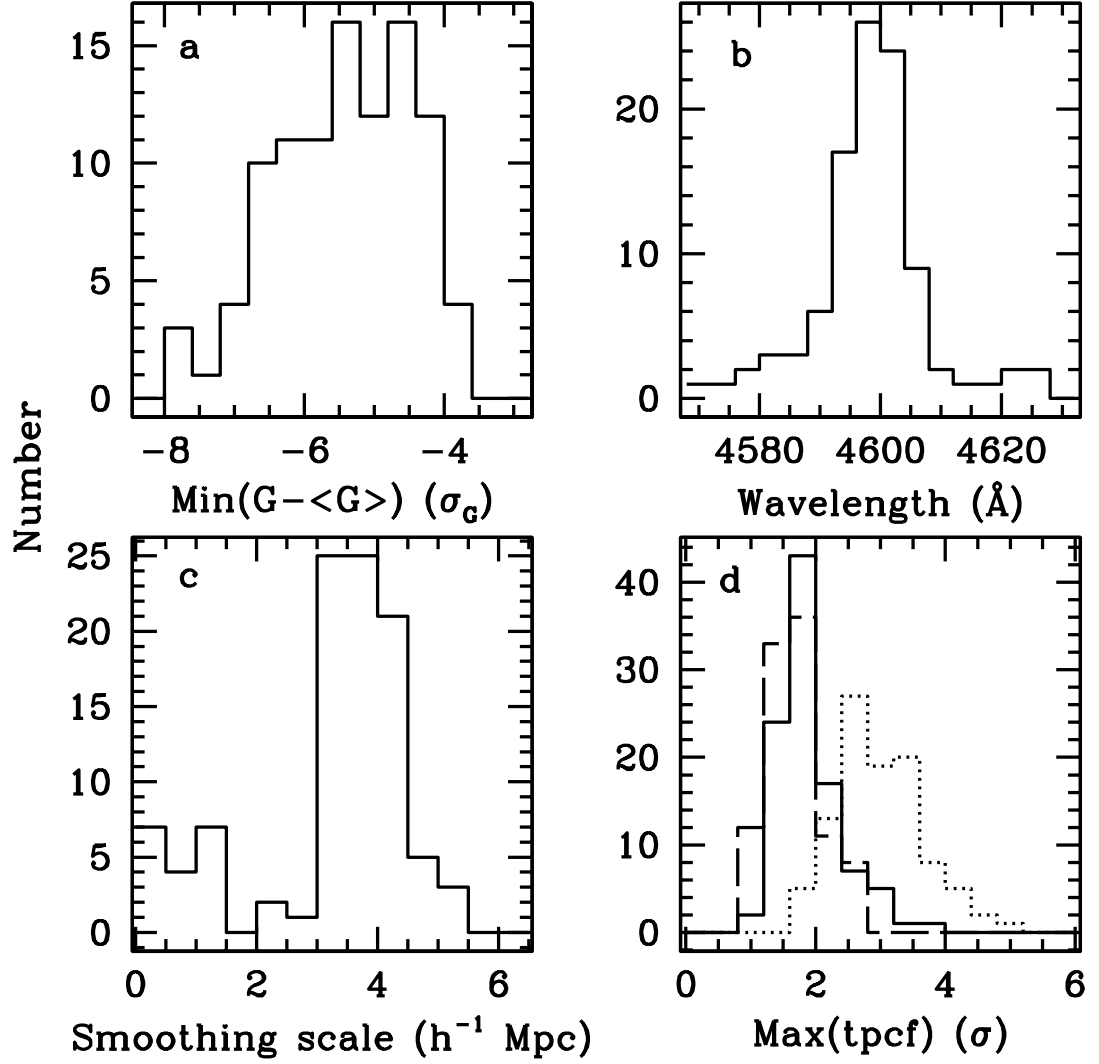


Figure 2.9: Distributions of (a) values, (b) positions and (c) scales of minima detected in reduced averaged transmission triangles, where absorbers form a ‘wall’ at 4600 \AA . (d) Distribution of maxima of averaged auto- (solid line) and cross-correlation (dashed line) functions using ‘observed’ and ‘real’ (auto only, dotted line) line lists.

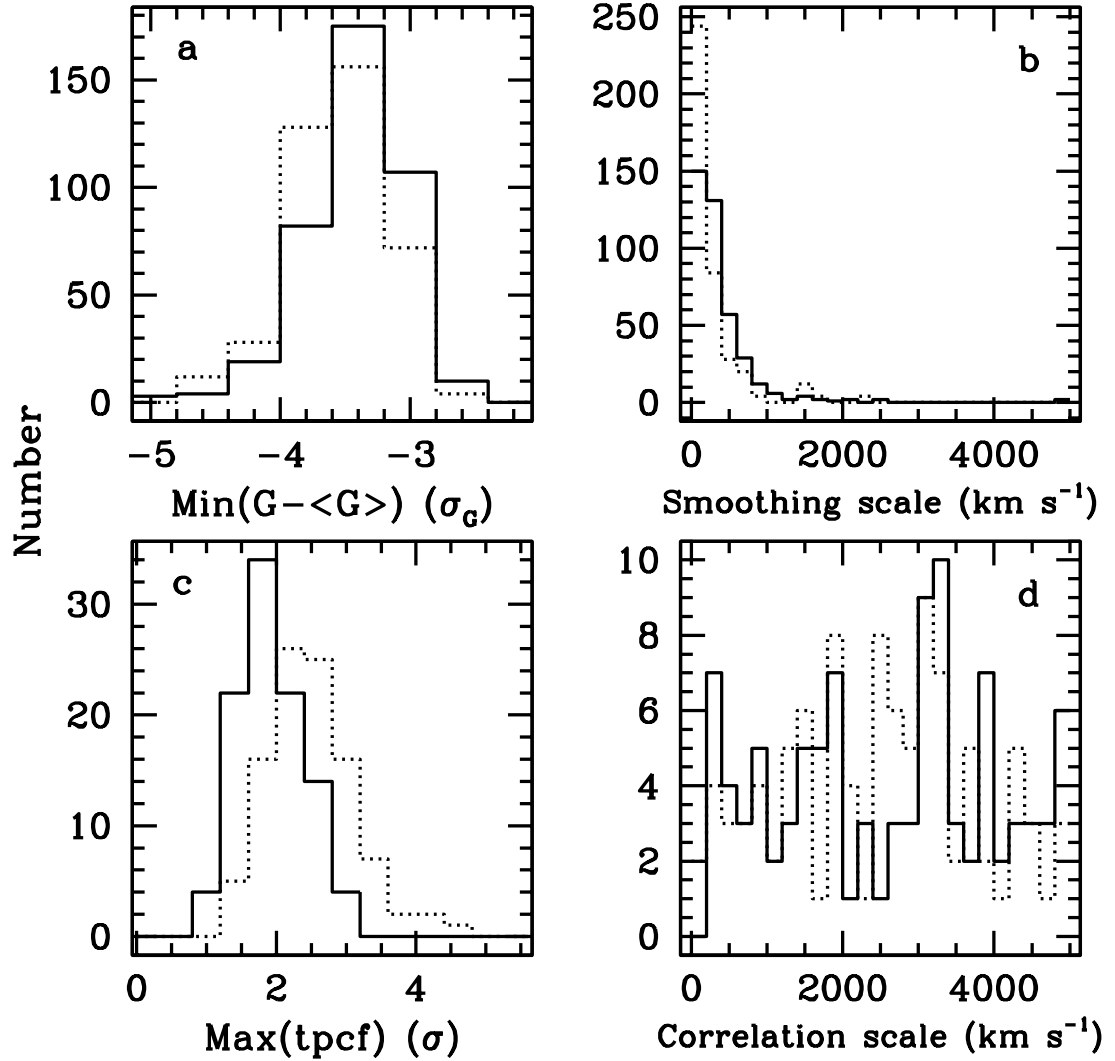


Figure 2.10: Distributions of (a) values and (b) scales of minima detected in reduced individual (solid lines) and averaged (dotted lines) transmission triangles, where absorbers are distributed randomly. The dotted histograms were renormalised. Distributions of (c) values and (d) correlation scales of maxima of averaged two-point correlation functions using ‘observed’ (solid lines) and true (dotted lines) line lists.

in Figs. 2.7 and 2.9 differ substantially from the one in Fig. 2.10, whereas the distributions of tpcf maxima are very similar. In panel (b) of Fig. 2.10 we see the effect of the non-Gaussian statistics at small smoothing scales as discussed above: the minimum value in a transmission triangle is more likely to occur at small smoothing scales than at large ones which is why the minima are not evenly distributed over all scales as are the maxima of the tpcf.

2.4 Conclusions

In this chapter we have developed a new technique to test for non-random structure in the Ly α forest. This new technique does not require line fitting but is rather based on the statistics of the transmitted flux. We have tested the relevant analytic calculations and approximations against simulated data and have found excellent agreement. We have argued that the accuracy of our method is limited by the precision of the continuum fit and by the errors in the line distribution parameters rather than by errors introduced by analytic approximations. We have shown our new analysis to be substantially more sensitive to non-randomness in intermediate resolution data than a traditional two-point correlation function analysis. Finally, we have presented evidence that, in the case of a coherent structure of absorbers extending across several lines of sight, our analysis using *intermediate* resolution data is at least comparable, if not superior, in sensitivity to a tpcf analysis using *high* resolution data.

Chapter 3

Analysis of the LSS toward a group of ten QSOs

3.1 Introduction

In this chapter we apply the technique developed in the previous chapter and investigate the large-scale structure of the Ly α forest both in velocity and real space by considering a close group of ten QSOs. The QSOs are contained within a ~ 1 deg² field so that the Ly α forest is probed on Mpc scales.

There have been many studies of the clustering properties of the Ly α forest. Webb (1987a) was the first to report a weak signal in the two-point correlation function of fitted absorption lines on scales of $\lesssim 100$ km s⁻¹. This result was later confirmed (Ostriker, Bajtlik, & Duncan 1988; Chernomordik 1995; Cristiani et al. 1995; Kulkarni et al. 1996; Cristiani et al. 1997; Khare et al. 1997) and some investigators found considerably stronger signals (Ulmer 1996; Fernández-Soto et al. 1996). There have also been detections on larger scales. Meiksin & Bouchet (1996) used a nearest neighbour statistic to derive correlations on scales of 0.5–3 h^{-1} Mpc. Pando & Fang (1996) employed the discrete wavelet transform to demonstrate the existence of clusters on scales of 10–20 h^{-1} Mpc in the Ly α forest at a significance level of 2–4 σ and that the number density of these clusters decreases with increasing

redshift. More recently, they observed non-Gaussian behaviour of Ly α forest lines on scales of 5–10 h^{-1} Mpc at a confidence level larger than 95 per cent (Pando & Fang 1998). Mo et al. (1992) even reported 60 and 130 h^{-1} Mpc as characteristic scales of the Ly α forest. All of these studies however are based on analyses of individual lines of sight.

By comparing the absorption characteristics in two (or more) distinct, but spatially close lines of sight, it is possible to investigate directly the real space properties of Ly α systems on various scales. The multiple images of gravitationally lensed QSOs have been used to establish firm lower limits on the sizes of Ly α clouds. Smette et al. (1995) found that the Ly α forests of the two images of HE 1104–1805 (separation 3.0 arcsec) are virtually identical and inferred a 2σ lower limit of 50 h^{-1} kpc on the diameter of Ly α clouds, assumed to be spherical, at $z = 2.3$. More information on the sizes of Ly α absorbers has been gained from the studies of close QSO pairs with separations of several arcsec to ~ 7 arcmin. All of the most recent analyses have concluded that Ly α absorbers have diameters of a few hundred kpc (Fang et al. 1996; Dinshaw et al. 1997; Dinshaw et al. 1998; Petitjean et al. 1998; D’Odorico et al. 1998) and Crotts & Fang (1998) found that correlations among neighbouring lines of sight persist for separations up to 0.5–0.8 h^{-1} Mpc for lines with $W > 0.4 \text{ \AA}$. A tentative detection of increasing cloud size with decreasing redshift (as would be expected for absorbers expanding with the Hubble flow) was reported by Fang et al. (1996) and Dinshaw et al. (1998). The possibility remains however, that the coincidences of absorption lines are due to spatial clustering of absorbers and that the inferred ‘sizes’ in fact are an indication of their correlation length (Dinshaw et al. 1998; Cen & Simcoe 1997) as may be evidenced by the correlation of the estimated ‘size’ with line of sight separation found by Fang et al. (1996).

Analyses to determine the shape of absorbers, as proposed e.g. by Charlton, Churchill, & Linder (1995), have so far been inconclusive. Several authors agree that the current data are incompatible with uniform-sized spherical clouds but are

unable to decisively distinguish between spherical clouds with a distribution of sizes, flattened disks, or filaments and sheets (Fang et al. 1996; Dinshaw et al. 1997; D’Odorico et al. 1998). However, from the analysis of a QSO triplet Crotts & Fang (1998) found evidence that lines with $W > 0.4 \text{ \AA}$ arise in sheets.

For still larger line of sight separations most work has concentrated on metal absorption. Williger et al. (1996), e.g., used a group of 25 QSOs contained within a $\sim 1 \text{ deg}^2$ region to identify structure in C IV absorption on the scale of $15\text{--}35 h^{-1} \text{ Mpc}$. Within this group, a subset of ten QSOs is suitable for studying the large-scale structure of the Ly α forest. A cross-correlation analysis of these data, performed by Williger et al. (2000), revealed a 3.7σ excess of line-pairs at velocity splittings $50 < \Delta v < 100 \text{ km s}^{-1}$. Thus Williger et al. concluded that the Ly α forest seems to exhibit structure on the scale of $\sim 10 h^{-1} \text{ Mpc}$ in the plane of the sky. However there was no excess at smaller velocity splittings and no dependence of the signal on angular separation was found.

Finally, the largest line of sight separations were investigated by Elowitz, Green, & Impey (1995), who studied a group of four QSOs, projected within $2^\circ 8'$ on the sky. Probing scales of $\sim 30 h^{-1} \text{ Mpc}$ in the plane of the sky, no significant cross-correlation signal was found out to a velocity separation of 10^4 km s^{-1} .

From the results outlined above it appears that the Ly α forest shows significant correlations across lines of sight at all but the largest scales probed. In this chapter we identify more precisely the upper limit of these correlations. To this end we re-analyse the group of ten QSOs of Williger et al. in the South Galactic Pole region. We employ the new technique developed in Chapter 2 which is based on the statistics of the transmitted flux rather than the statistics of fitted absorption lines. The South Galactic Cap region has one of the highest known QSO densities in the sky and the dataset is the most useful for large-scale structure studies of the Ly α forest published so far. We find evidence for a transition from strong correlations for proper line of sight separations¹ $< 3 h^{-1} \text{ Mpc}$ to a vanishing correlation for line

¹We use $q_0 = 0.5$, $\Lambda = 0$ and $H_0 = 100 h \text{ km s}^{-1} \text{ Mpc}^{-1}$ throughout this chapter.

Table 3.1: QSOs analysed.

Object	α_{1950}			δ_{1950}			z_{em}
	<i>h</i>	<i>m</i>	<i>s</i>	°	'	"	
Q0041–2638	00	41	15.19	–26	38	35.9	3.053
Q0041–2707	00	41	24.38	–27	07	54.3	2.786
Q0041–2607	00	41	31.11	–26	07	41.7	2.505
Q0041–2658	00	41	38.38	–26	58	30.0	2.457
Q0042–2627	00	42	06.42	–26	27	45.3	3.289
Q0042–2639	00	42	08.20	–26	39	25.0	2.98
Q0042–2656	00	42	24.89	–26	56	34.4	3.33
Q0042–2714	00	42	44.12	–27	14	56.6	2.36
Q0042–2657	00	42	52.29	–26	57	15.3	2.898
Q0043–2633	00	43	03.10	–26	33	33.6	3.44

of sight separations $> 6 h^{-1}$ Mpc.

The rest of this chapter is organised as follows: in Section 3.2 we briefly describe the data. Section 3.3 briefly recapitulates the method and our results are presented in Section 3.4. We consider a number of uncertainties in Section 3.5 and conclude this chapter with a discussion of our results in Section 3.6.

3.2 The data

The data for the present analysis were kindly provided by G. M. Williger and his collaborators. The spectra were gathered as part of a larger survey designed to reveal the large-scale clustering properties of CIV systems (Williger et al. 1996). The observations were made on the CTIO 4-m telescope using the Argus multifibre spectrograph. The instrumental resolution was $\sim 2 \text{ \AA}$ and the signal-to-noise ratio per pixel reached up to 40 per 1 \AA pixel. We stress that all observations and data reduction were performed by Williger et al. (1996).

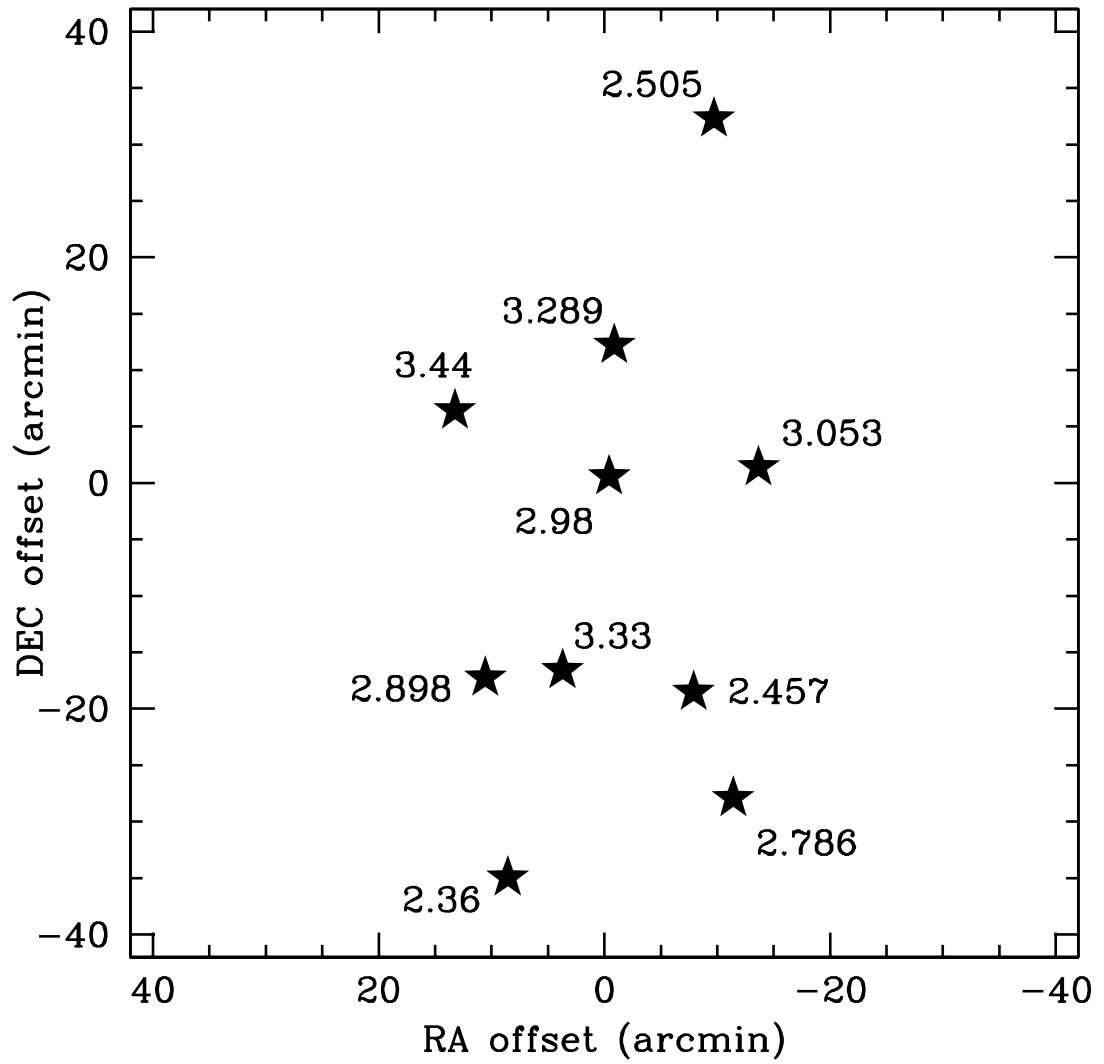


Figure 3.1: Distribution of QSOs in the sky. The field is centered on $\alpha = 00^{\text{h}}42^{\text{m}}10^{\text{s}}$ and $\delta = -26^{\circ}40'$ (B1950). Stars mark the positions of the QSOs listed in Table 3.1 and emission redshifts are indicated.

Of the original sample of 25 QSO spectra only 14 cover any part of the region between the Ly α and Ly β emission lines. In order to avoid the proximity effect (see Chapter 5) we exclude from the analysis those parts of the spectra which lie within 3000 km s $^{-1}$ of the Ly α emission line. This leaves us with 11 spectra. We have excluded an additional spectrum from the analysis (Q0043–2606) because of its low S/N and small wavelength coverage. We are thus left with the same sample as used by Williger et al. (2000). We list these QSOs, their positions and redshifts in Table 3.1 and show their distribution in the sky in Fig. 3.1. The data cover $2.17 < z < 3.40$. The angular separations range from 6.1 to 69.2 arcmin or 1.4 to 16.3 h^{-1} proper Mpc and the emission redshifts range from 2.36 to 3.44.

3.3 Analysis

We employ the method developed in Chapter 2 to identify local over- or underdensities of Ly α absorption using the statistics of the transmitted flux. The significance of a possible cluster of absorbers is enhanced by first filtering out the high frequency ‘noise’ of individual absorption lines. We use a Gaussian as the smoothing function and denote the smoothed spectrum by $G(\lambda, \sigma_s)$. We then proceed to compare the observed transmission with the mean transmission expected on the basis of the simple null-hypothesis that any Ly α forest spectrum can be described by a collection of individual absorption lines whose parameters are uncorrelated and distributed according to

$$\eta(z, N, b) \propto (1+z)^\gamma N^{-\beta} \exp \left[\frac{-(b - \mu_b)^2}{2\sigma_b^2} \right]. \quad (3.1)$$

Thus, in particular, the null-hypothesis presumes an unclustered Ly α forest. To assess the statistical significance of any differences between the observed and expected transmissions the comparison is done in terms of the rms of the transmission, although we will also use simulations to account for the non-Gaussian distribution of the transmitted flux.

Equations (2.28), (2.31) and (2.16) describe the expected mean and variance of

the transmitted flux. Before we can evaluate these expressions we need the values of all the parameters involved: γ was determined by Williger et al. (1998) for the present data to be 2.5. Subsequent to the present study this value was revised to 2.0 (Williger et al. 2000), but as discussed in Section 3.4.2 this change does not significantly affect our results. We take β from recent high resolution studies as 1.5 (Hu et al. 1995; Lu et al. 1996; Kim et al. 1997; Kirkman & Tytler 1997). As in Chapter 2 we determined the width of the auto-covariance function of a ‘perfect’ spectrum (i.e. before it passes through the instrument), q , from simulations. We simulated each spectrum of the dataset 100 times in accordance with the null-hypothesis, using the γ and β values as above and $\mu_b = 30 \text{ km s}^{-1}$, $\sigma_b = 8 \text{ km s}^{-1}$ and $b_{\text{cut}} = 18 \text{ km s}^{-1}$ (Hu et al. 1995; Lu et al. 1996; Kim et al. 1997; Kirkman & Tytler 1997). The simulated data have the same resolution as the real data but a constant (conservative) S/N of 20. The simulations are normalised to give the same mean effective optical depth as the real data.

The exact values of the parameters above are of course a source of uncertainty in the present analysis and we will discuss the pertaining effects in Sections 3.4.2 and 3.4.3.

Although a high signal-to-noise ratio in the QSO spectra is not of great importance for the analysis itself (as the noise is quickly smoothed over, see equation 2.31), it is nevertheless important for reliable continuum fitting. Uncertainties in the placement of the continuum are a potential source of error in the method used here. A small error in the zeroth or first order of the fit introduces an arbitrary offset from the expected mean transmission. However, this is easily dealt with by determining the normalisation of the mean optical depth, B (cf. equation 2.8), for each spectrum individually:

$$B = - \left(\frac{\lambda_\alpha}{\lambda_c} \right)^{\gamma+1} \ln[G(\lambda_c, \sigma_{s,\text{max}})], \quad (3.2)$$

where $\sigma_{s,\text{max}}$ denotes the largest possible smoothing scale and λ_c is the central wavelength of the spectrum. Thus we fix the normalisation for each spectrum at the tip of its transmission triangle.

With the values of all the parameters in place, we can transform a given transmission triangle into a ‘reduced’ transmission triangle by

$$RG(\lambda, \sigma_s) = \frac{G - \langle G \rangle}{\sigma_G}. \quad (3.3)$$

The reduced transmission triangle shows the residual fluctuations of the Ly α transmission around its mean in terms of their statistical significance.

3.4 Results

3.4.1 Single lines of sight

In Fig. 3.2 we show the result of the analysis described above for all the QSOs listed in Table 3.1. The vertical lines show the Ly α positions of known metal systems which were primarily taken from Williger et al. (1996) (their Table 3). A search using NED² uncovered only three additional systems, all towards Q0042–2627 (York et al. 1991). Not surprisingly we see overdense Ly α absorption at the positions of *all* metal systems. We take this as an indication that our method correctly identifies overdensities.

Fig. 3.2 clearly demonstrates the presence of structures on scales as large as many hundred km s⁻¹. In all there are seven features which are significant at the more than $-4\sigma_G$ level. We now briefly describe these quite significant detections:

Q0041–2707: This spectrum shows three very significant overdensities in Ly α . The first, $-6.2\sigma_G$ at $(\lambda, \text{FWHM}_s) = (3983 \text{ \AA}, 4179 \text{ km s}^{-1})$, is caused by an unsaturated cluster of lines which has no associated metal system. The second very significant ($-6.0\sigma_G$) overdensity in this spectrum lies at $(4062 \text{ \AA}, 498 \text{ km s}^{-1})$ and is caused by a saturated blend. It seems to be associated with either or both of two metal systems detected in C IV and Si IV, Si II and C IV respectively. The third

²The NASA/IPAC Extragalactic Database (NED) is operated by the Jet Propulsion Laboratory, California Institute of Technology, under contract with the National Aeronautics and Space Administration.

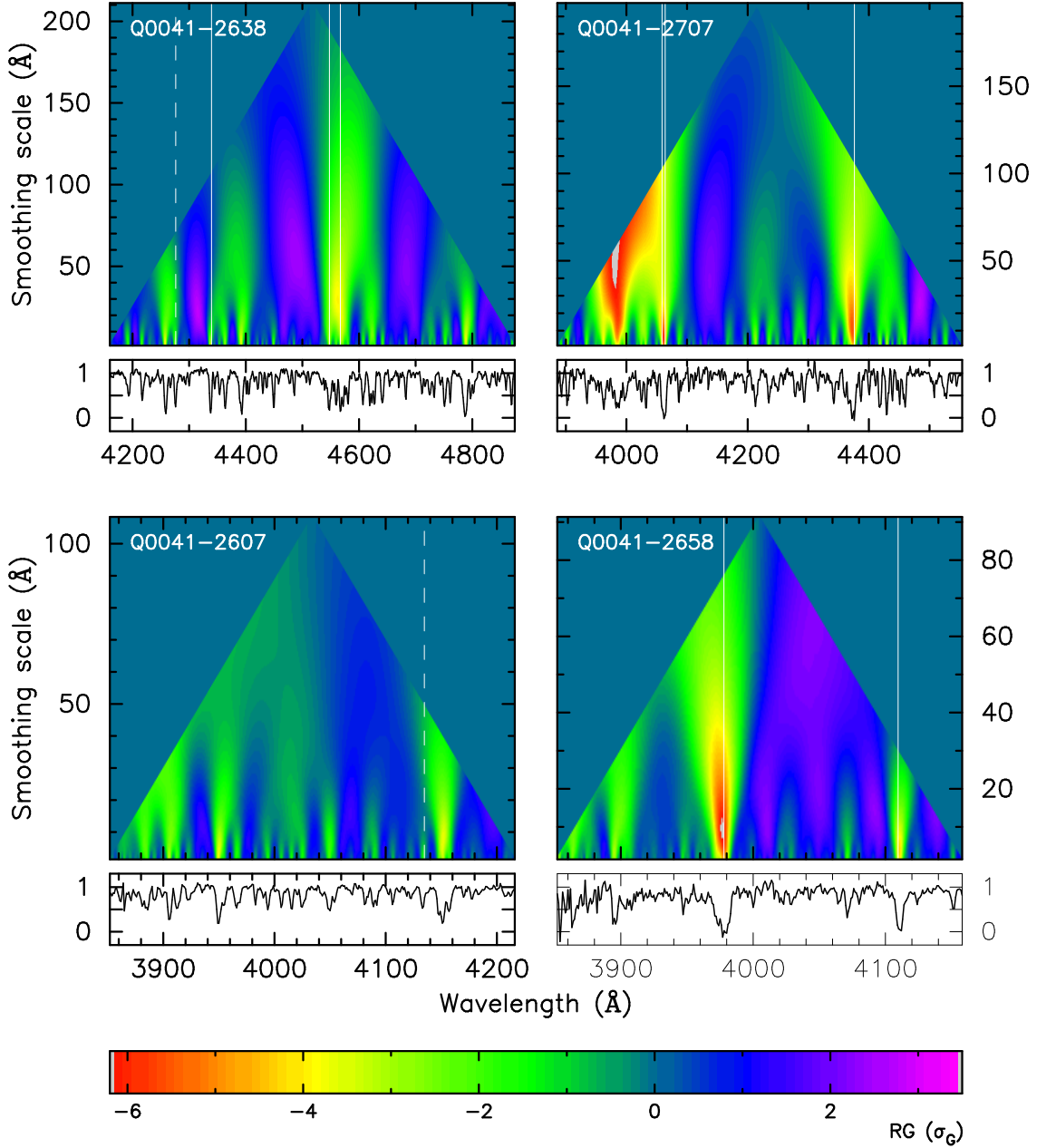
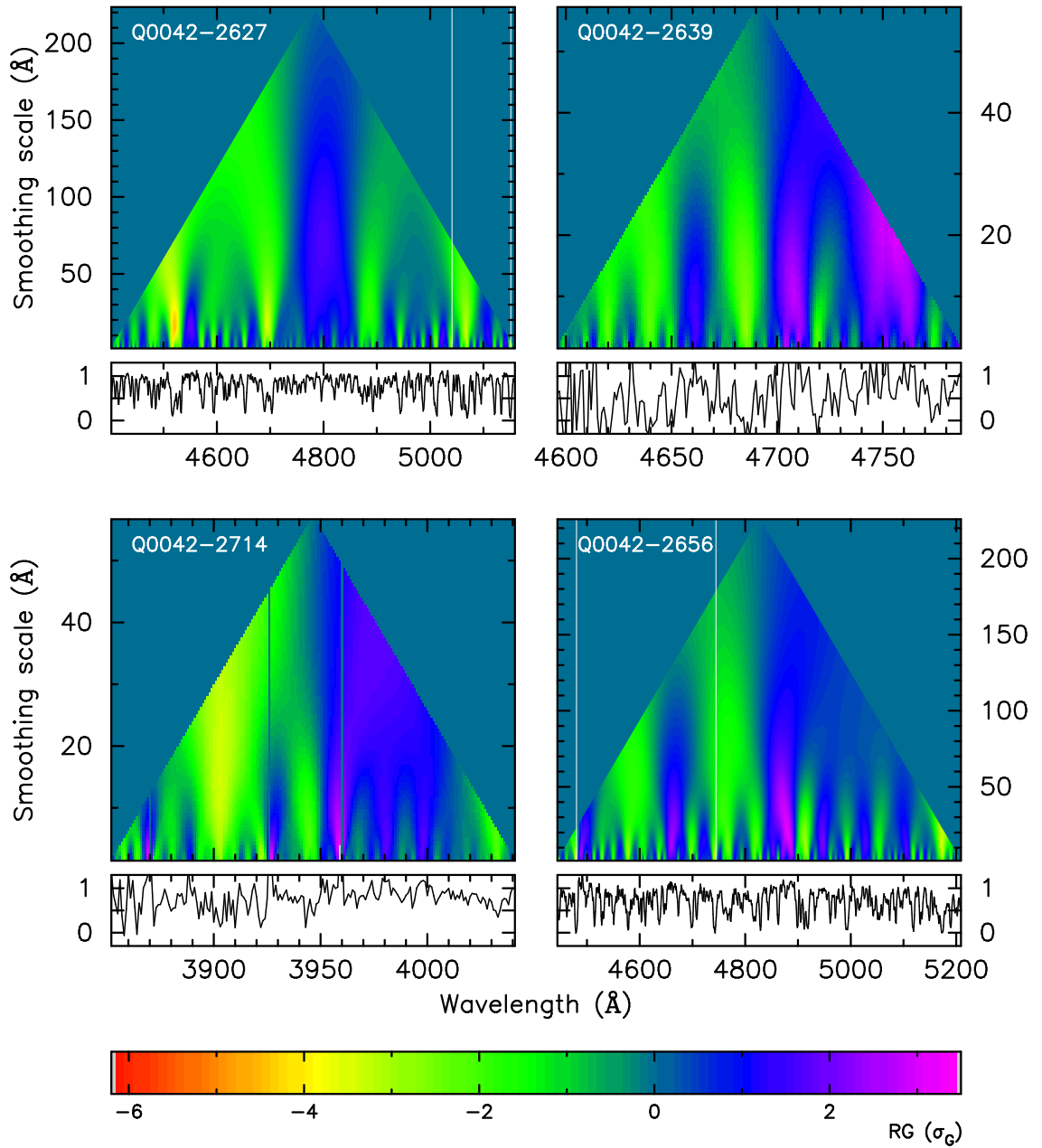
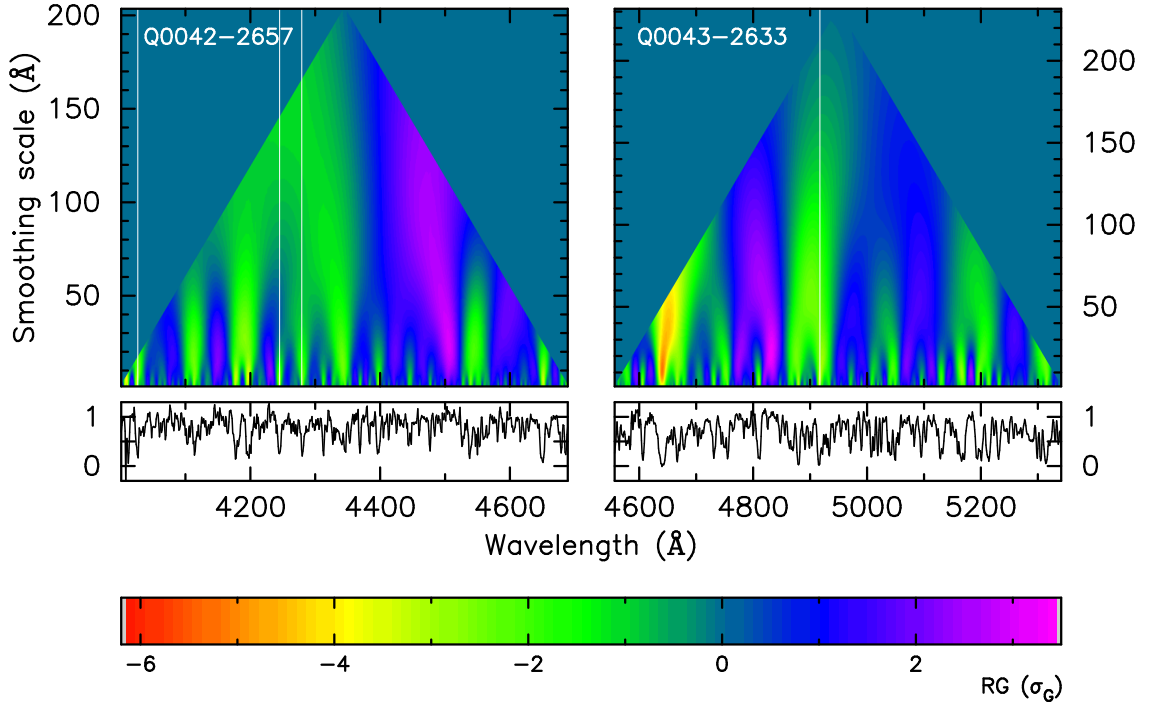


Figure 3.2: Reduced transmission triangles and normalised spectra of the QSOs listed in Table 3.1. The smoothing scale on the vertical axis is the FWHM of the smoothing Gaussian. Regions of overdense absorption appear yellow and red, underdense regions appear blue and purple. The vertical lines indicate the observed Ly α wavelengths of known metal absorption systems. Dashed lines mark the positions of metal systems that do *not* have an associated Ly α local minimum (see text).

Figure 3.2 – *continued*

Figure 3.2 – *continued*

significant system is again associated with metals, is significant at the $-5.6\sigma_G$ level and lies at $(4373 \text{ \AA}, 745 \text{ km s}^{-1})$.

Q0041-2658: The most significant overdensity in the entire sample is a $-6.3\sigma_G$ overdensity at $(3977 \text{ \AA}, 686 \text{ km s}^{-1})$, caused by a broad, clearly blended and saturated feature which is associated with C II, Si IV, C IV and Al II absorption. There is also a $-4.3\sigma_G$ overdensity at $(4111 \text{ \AA}, 278 \text{ km s}^{-1})$, again associated with metals (S II and C IV).

Q0042-2627: A $-4.5\sigma_G$ overdensity at $(4522 \text{ \AA}, 1071 \text{ km s}^{-1})$, with no associated metals, caused by a broad cluster of lines.

Q0043-2633: A $-5.2\sigma_G$ overdensity at $(4641 \text{ \AA}, 778 \text{ km s}^{-1})$, with no associated metals, caused by a broad, saturated feature.

3.4.2 Local minima

The probability density function (pdf) of G is inherently non-Gaussian, such that e.g. the probability of G lying within $3\sigma_G$ of the mean is smaller than 0.9973. In fact, the pdf of G is a function of smoothing scale with the Central Limit Theorem guaranteeing a Normal distribution at very large smoothing scales. (We have attempted to continually remind the reader of this point by the persistent use of the notation ‘ σ_G ’.) In light of this difficulty it is necessary to estimate reliable significance levels by using simulated data.

To further demonstrate and quantify the significance of the overdensities presented in the previous section we investigate the statistics of local minima in the reduced transmission triangles by comparing them with the statistics of local minima derived from simulated data. We simply define a ‘local minimum’ (LM) as any pixel in a reduced transmission triangle with

$$RG(\lambda, \sigma_s) < -2.0\sigma_G \quad (3.4)$$

and where all surrounding pixels have larger values. If there is more than one LM in the same wavelength bin (but at different smoothing scales) then we delete the less significant one, since we do not want to count the same structure more than once. Given the resolution of the data it is evident that unclustered absorption lines will produce LM on the smallest smoothing scale ($= 1.5 \text{ \AA}$). We may anticipate that the total number and distribution of these LM depend sensitively on the parameters of the underlying line distribution (3.1). Thus we exclude all LM on the smallest smoothing scale from all further analyses in order to reduce the model-dependence of our results.

Note that with this definition, almost all metal lines have a Ly α LM within 300 km s^{-1} (vertical lines in Fig. 3.2).

As mentioned in Section 3.3, we have simulated 100 datasets ($= 1000$ spectra), essentially by putting down Voigt profiles with parameters drawn from distribution (3.1) (see Chapter 2 for the exact technique). We then applied the same procedures

as outlined above: first we constructed the reduced transmission triangles for all simulated spectra and then we determined the LM.

In the real data we found 103 LM whereas the simulated data yielded on average 51 LM with an rms dispersion of 7.6. The maximum number of LM found in the 100 simulated datasets was 70. Thus there is an excess of the total number of LM over the expected number at the > 99 per cent confidence level. In Fig. 3.3 we plot

$$\zeta(x) = \frac{N_{\text{obs}}(x)}{N_{\text{exp}}(x)} - 1, \quad (3.5)$$

where N_{obs} (N_{exp}) is the observed (expected, as derived from the simulations) number of LM and $x = RG$ (significance level of LM in units of σ_G) or $x = \text{FWHM}_s$ (FWHM of smoothing Gaussian).

From panel (a) we can see that there is a tendency for the excess to be more significant for the stronger LM. For the leftmost bin we found two LM in the data but *none* in the 100 simulated datasets. Extrapolating from lower significance levels we find $N_{\text{exp}} = 0.013$ for this bin, which is the value used in panel (a). A Kolmogorov–Smirnov test indicates that the distributions $N_{\text{obs}}(RG)$ and $N_{\text{exp}}(RG)$ disagree at the 95.6 per cent confidence level. The excess is strengthened further and the confidence level is increased to > 99 per cent by excluding all LM with smoothing scales $< 250 \text{ km s}^{-1}$ thus showing that the excess is dominated by the larger scale LM. In smoothing scale-space we also observe an excess which occurs on scales of up to 1200 km s^{-1} (panel b). By excluding LM with $RG > -4\sigma_G$, the excess on scales $< 250 \text{ km s}^{-1}$ disappears but it persists on larger scales thus showing that it is dominated by the more significant LM.

Q0041–2707 and Q0041–2658 exhibit the most significant structures, as can be seen in Fig. 3.2 (and as discussed in Section 3.4.1). If these two objects are removed from the sample the excess of LM is slightly reduced but remains significant at the 6.1σ level. The effect also persists if we exclude non-significant substructure from the analysis by deleting all LM which lie within the subtriangle defined by another more significant LM on larger smoothing scales. The removal of all LM that lie within 300 km s^{-1} of known metal lines again slightly weakens the excess of LM but

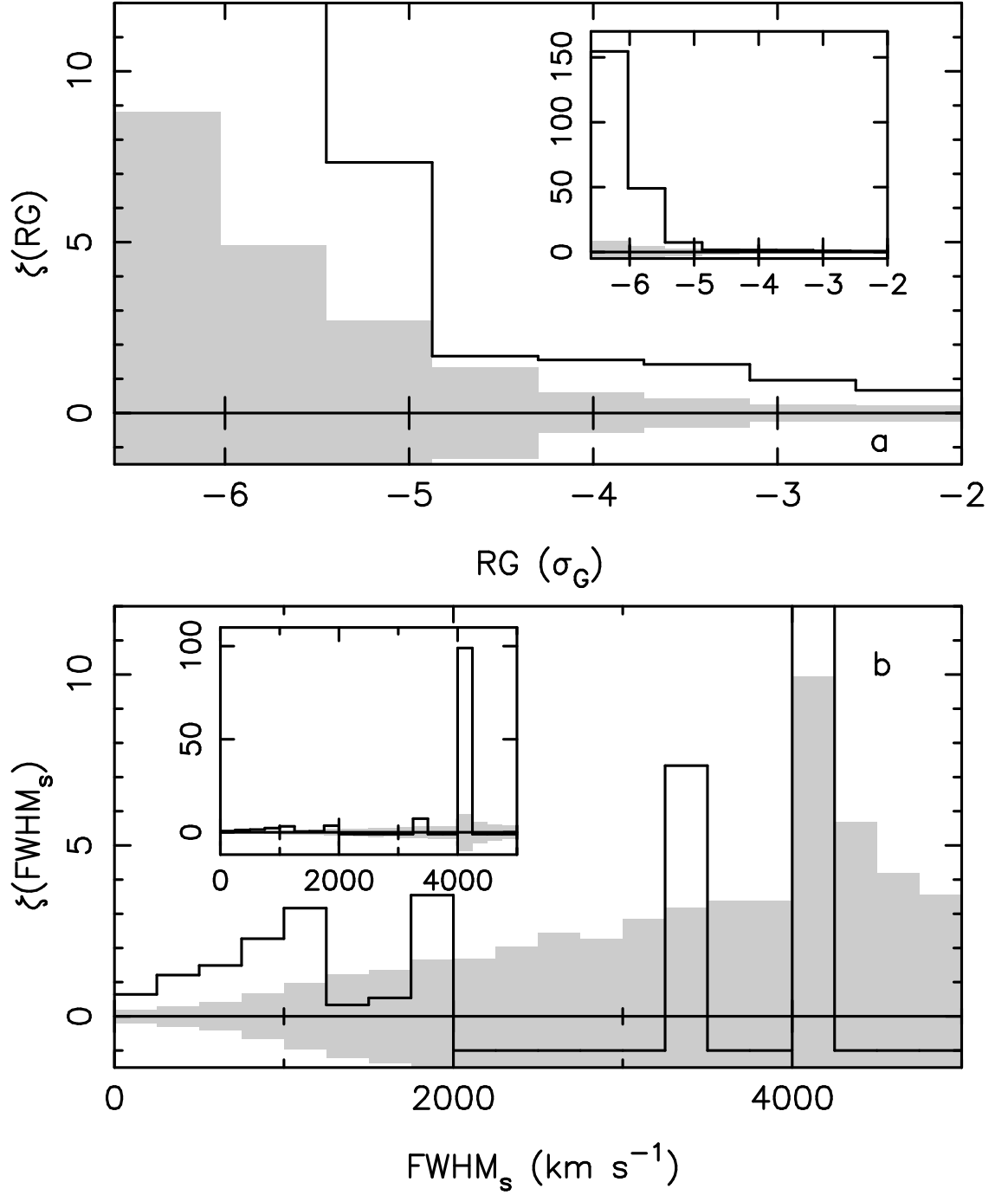


Figure 3.3: (a) Excess of observed number of local minima in reduced transmission triangles over the expected number (= mean of 100 simulations) as a function of the significance level of the local minima (see equation 3.5). ± 1 rms levels as derived from the simulations are indicated by the grey shaded areas. (b) Same as (a) as a function of smoothing scale (FWHM of smoothing Gaussian). The insets show the same plots but with expanded ζ -scales.

does not remove the effect.

If we have used incorrect values for the observational parameters of equation (3.1) then we have over- or underestimated either the absolute value of the transmission fluctuations or their statistical significance or both. This may affect both the normalisation and the shape of the distributions $N_{\text{obs}}(x)$. The exclusion of LM on the smallest smoothing scale from the analysis was designed to minimise the effect of changes of the above parameters on $N_{\text{exp}}(x)$. We have checked the success of this strategy by creating six more sets of simulations, each consisting of 10 datasets (= 100 spectra). For each of these sets we varied one parameter: $\beta = 1.7$, $\beta = 1.3$, B (overall normalisation) decreased and increased by 20 per cent, $\mu_b = 40 \text{ km s}^{-1}$ and $S/N = 10$. We have found no significant variation of the total number of LM in any of these simulations. The shapes of the distributions of LM as functions of RG and FWHM_s also agree well with the distributions for the ‘standard’ case. The only exception was the $\beta = 1.3$ model which produces less significant LM compared to the ‘standard’ case (although this has little effect on $\zeta(RG)$). In assessing the robustness of the result of Fig. 3.3 with respect to our choice of parameter values we thus only need to consider how the individual parameters affect N_{obs} .

Given equation (3.2), σ_G is virtually independent of γ for all reasonable values. Thus the only effect of changing γ is to change the size of the fluctuations, $G - \langle G \rangle$ in equation (3.3). Because we normalise $\langle G \rangle$ at the central wavelength of a spectrum (see equation 3.2) an increase in γ will decrease the magnitude of overdensities at longer wavelengths while increasing the magnitude of overdensities at shorter wavelengths and vice versa. Thus there will only be an appreciable effect if overdensities tend to lie to one side of a spectrum which is not the case. In addition, a wrong γ value cannot explain why the local minima occur almost exclusively on certain velocity scales. Nevertheless, we re-determined the LM for the real data for $\gamma = 2.2$ and $\gamma = 2.8$ and the effect is small.

By determining the normalisation of the effective optical depth for each spectrum individually we avoid over- or underestimation of $G - \langle G \rangle$ caused by small errors in

the zeroth and first order of the continuum fits of the *individual* spectra. However, if the continua are *systematically* low or high then we will under- or overestimate the mean optical depth normalisation, B , and thus under- or overestimate σ_G . However, re-analysing the real data with B increased by 20 per cent we still find 98 LM, significantly above the expected number of 51 ± 7.6 .

The parameters μ_b , σ_b and b_{cut} all affect the parameter q in equation (2.31). Kim et al. (1997) reported a possible evolution of μ_b with redshift over a range covered by the present data. If this were correct and if too small a value for q were indeed the reason for the observed excess of LM then one would expect the excess to be larger at smaller redshifts where μ_b may be higher. Separating the data into a high and a low redshift bin we find $N_{\text{obs}}(N_{\text{exp}}) = 53(25 \pm 5.0)$ and $50(26 \pm 5.2)$ for the low and high redshift bins respectively. In any case, we have re-analysed the data for $\mu_b = 40 \text{ km s}^{-1}$ (which corresponds to an increase of q of ~ 30 per cent, since q is roughly linear in μ_b) and still found 84 LM.

Finally we have considered $\beta = 1.3$ which also has the effect of increasing σ_G . A re-analysis of the data yielded 79 LM which is still too large to be compatible with the simulations.

From the tests described above we conclude that the result presented in Fig. 3.3 is quite robust: there exist structures in the Ly α forest on scales of up to $\sim 1200 \text{ km s}^{-1}$ at the > 99 per cent confidence level. This result constitutes clear evidence for the non-uniformity of the Ly α forest on large scales despite repeated findings that the two-point correlation function of absorption lines shows no signal on scales $\gtrsim 300 \text{ km s}^{-1}$ (e.g. Cristiani et al. 1997).

3.4.3 Double lines of sight

So far we have not taken advantage of the fact that the QSOs of Table 3.1 are a close group in the plane of the sky. We shall now examine possible correlations *across* lines of sight. One of the advantages of the analysis used above is that it is easily applied to multiple lines of sight: transmission triangles are simply averaged

Table 3.2: Pairs of QSOs grouped according to their proper transverse separation.

$d < 3 h^{-1} \text{ Mpc}$	$3 h^{-1} \text{ Mpc} < d < 6 h^{-1} \text{ Mpc}$	$6 h^{-1} \text{ Mpc} < d$
Q0041-2638 Q0042-2639	Q0041-2638 Q0042-2627	Q0041-2638 Q0041-2707
Q0041-2707 Q0041-2658	Q0041-2638 Q0042-2656	Q0041-2638 Q0041-2607
Q0042-2627 Q0042-2639	Q0041-2638 Q0043-2633	Q0041-2638 Q0042-2657
Q0042-2627 Q0043-2633	Q0041-2707 Q0042-2714	Q0041-2707 Q0041-2607
Q0042-2639 Q0043-2633	Q0041-2707 Q0042-2656	Q0041-2707 Q0042-2627
Q0042-2656 Q0042-2657	Q0041-2707 Q0042-2657	Q0041-2607 Q0041-2658
	Q0041-2607 Q0042-2627	Q0041-2607 Q0042-2714
	Q0041-2658 Q0042-2714	Q0041-2607 Q0042-2657
	Q0041-2658 Q0042-2657	Q0042-2627 Q0042-2656
	Q0042-2639 Q0042-2656	Q0042-2627 Q0042-2657
	Q0042-2639 Q0042-2657	
	Q0042-2714 Q0042-2657	
	Q0042-2656 Q0043-2633	
	Q0042-2657 Q0043-2633	
$\bar{d} = 2.45 h^{-1} \text{ Mpc}$	$\bar{d} = 4.59 h^{-1} \text{ Mpc}$	$\bar{d} = 9.67 h^{-1} \text{ Mpc}$

where they overlap. Given the transverse separations of the QSOs in this group and assuming reasonable absorber sizes, two different lines of sight will not probe the same absorbers. According to our null-hypothesis of an unclustered Ly α forest, two different lines of sight are therefore uncorrelated. Thus the variance of a mean transmission triangle (averaged over multiple lines of sight) is given by $\sigma_G^2(\lambda, \sigma_s)/n$, where n is the number of triangles used at (λ, σ_s) . This procedure should enhance structures that extend across multiple lines of sight and suppress those that do not.

Here we present our results for the case $n = 2$. We have sorted all pairs of QSOs into one of three groups according to the proper transverse separation, d , of the pair (calculated at the redshift of the lower redshift QSO): $d < 3 h^{-1}$ Mpc, $3 h^{-1}$ Mpc $< d < 6 h^{-1}$ Mpc and $6 h^{-1}$ Mpc $< d$. Table 3.2 lists those pairs within the groups for which the relevant spectral regions overlap.

As in Section 3.4.2 we proceeded to construct ζ , but this time using only the overlap regions of the reduced mean triangles. Fig. 3.4 shows $\zeta(RG)$ and $\zeta(\text{FWHM}_s)$ for the three cases listed above. The top row shows the results for small transverse separations, the middle row for intermediate and the bottom row for large transverse separations. There is evidence for a trend: with increasing separation we detect fewer and fewer overdensities at large significance levels and large smoothing scales relative to the simulations.

In panel (a) there is an excess of LM which is somewhat weaker than that seen for single lines of sight (Fig. 3.3a). However, we detected one LM at $-7.5\sigma_G$. In contrast, the 100 simulated datasets revealed *no* LM with $RG < -6\sigma_G$. (Extrapolating from lower significance levels gives $N_{\text{exp}} = 0.0033$ for this bin.) This very significant overdensity lies at $z = 2.272$ and is produced by the near-coincidence in redshift space ($\Delta v \approx 450 \text{ km s}^{-1}$) of the two most significant single-line of sight overdensities of the entire sample. These two overdensities are found in the spectra of Q0041–2658 and Q0041–2707. The two lines of sight are separated by $2.31 h^{-1}$ Mpc and are the second closest pair in the sample. This is a very clear example of a coherent structure traced by Ly α absorption extending across two lines of sight.

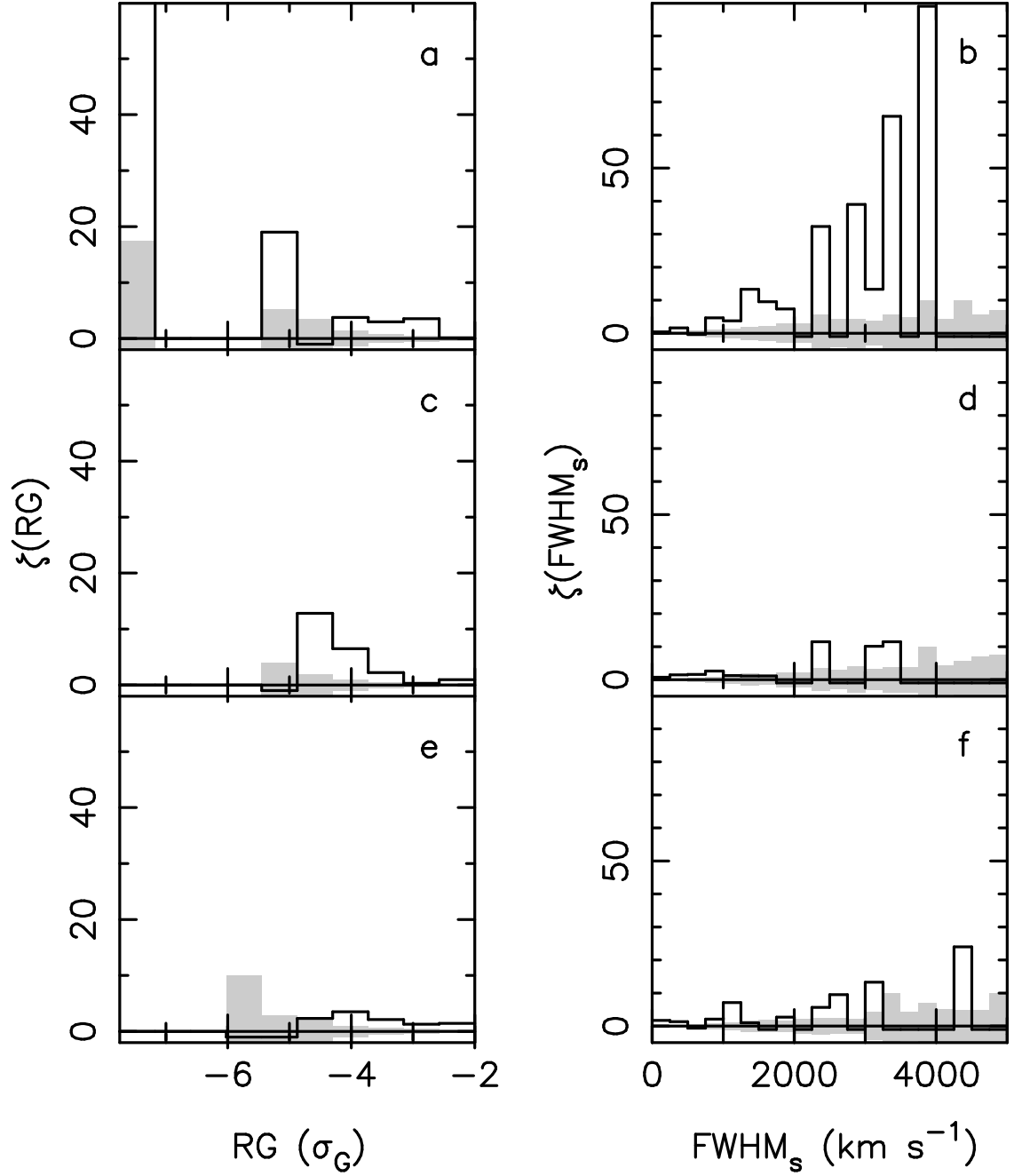


Figure 3.4: Excess of observed number of local minima in reduced mean transmission triangles of QSO pairs over the expected number (= mean of 100 simulations) as a function of the significance level (panels a, c, e) and the smoothing scale (panels b, d, f). The value of the leftmost bin of panel (a) is $303. \pm 1$ rms levels as derived from the simulations are indicated by the grey shaded areas. The top row shows the result for QSO pairs with $d < 3 h^{-1} \text{ Mpc}$, the middle row for $3 h^{-1} \text{ Mpc} < d < 6 h^{-1} \text{ Mpc}$ and the bottom row for $6 h^{-1} \text{ Mpc} < d$.

Table 3.3: Kolmogorov–Smirnov probabilities that the observed and expected distributions of RG values and smoothing scales agree for the three line of sight separation groups.

	$P_{\text{KS}}(RG)$	$P_{\text{KS}}(\text{FWHM}_s)$
$d < 3$:	7×10^{-5}	8×10^{-5}
$3 < d < 6$:	0.011	0.017
$6 < d$:	0.49	0.46

In all we detect $N_{\text{obs}}(N_{\text{exp}}) = 41(14 \pm 4.7)$, $62(28 \pm 6.9)$ and $65(25 \pm 6.4)$ LM for small, intermediate and large separations respectively. Thus the excess of the *total* number of LM does not seem to vary. However, the *shapes* of the distributions change quite significantly with line of sight separation. In Table 3.3 we list KS probabilities that the simulated and observed distributions of RG values and smoothing scales agree for the three groups. At small separations, the simulated distributions disagree strongly with the observations, producing too few LM at large significance levels and at large smoothing scales. However at large separations, the distributions agree very well.

If the observed excess of LM in Figs. 3.3 and 3.4(a) were simply due to an incorrect choice of the values for the parameters of equation (3.1) as discussed in Section 3.4.2, then it is hard to understand why that excess should be so strongly reduced for large line of sight separations. The removal of the pair Q0041–2707 - Q0041–2658 leaves the result qualitatively unchanged as does the removal of substructure as outlined in Section 3.4.2. The removal of all LM that have a metal system within 300 km s^{-1} in either of the spectra of the pair somewhat weakens the excess of panel (a) but does not remove the significance of the effect, since we still obtain $P_{\text{KS}}(RG) = 9 \times 10^{-4}$ and $P_{\text{KS}}(\text{FWHM}_s) = 3 \times 10^{-5}$ at small separations but good agreement at large separations (cf. Table 3.3).

A possible explanation for the trend of the decreasing excess with line of sight

separation could be that the group of close QSO pairs is dominated by those QSOs whose spectra show the most significant overdensities and that these QSOs are absent from the group of large-separation pairs. However, by inspection of Table 3.2 we can see that each of the groups contains at least eight of the ten QSOs at least once. In particular, Q0041–2707 and Q0041–2658 are present in all groups and both appear in the group of close QSOs only once.

To further investigate whether the excess of LM seen in the double lines of sight (DLOS) is simply due to the excess already detected in the single lines of sight (SLOS) we attempt to identify the structures in the SLOS that give rise to the LM detected in the DLOS: for each LM in a DLOS we search for the most significant LM in each of the constituent SLOS within 1000 km s^{-1} (our results do not depend sensitively on this value). If the LM in the DLOS is due to a structure extending across the two lines of sight then one would expect less significant LM in both of the constituent SLOS. However, if the LM in the DLOS is due to a strong overdensity which does not extend across both SLOS then one would expect to find a LM in only one of the SLOS. If LM are found in both SLOS, then they may be quite dissimilar and one should be of greater significance than the LM in the DLOS. For each LM in the DLOS we have computed the following quantity:

$$\frac{RG_i}{RG_D} - 1, \quad i = 1, 2$$

where RG_i denotes the LM in the two SLOS and RG_D that of the DLOS. This quantity measures how the SLOS-LM compare with the DLOS-LM they produce. In Fig. 3.5 we plot as thick solid lines the histograms of this measure for the three groups of QSO pairs (top = small separation, bottom = large separation). We have also computed the same histograms for the 100 simulated datasets and display the mean and mean ± 1 rms histograms as thin solid lines and grey shaded areas respectively. There is a small number of cases where no LM can be found in either of the single sight-lines and these are excluded from this analysis.

All panels of Fig. 3.5 show a large excess of the observed distributions over the simulated ones. This is not overly surprising since we already know that the total

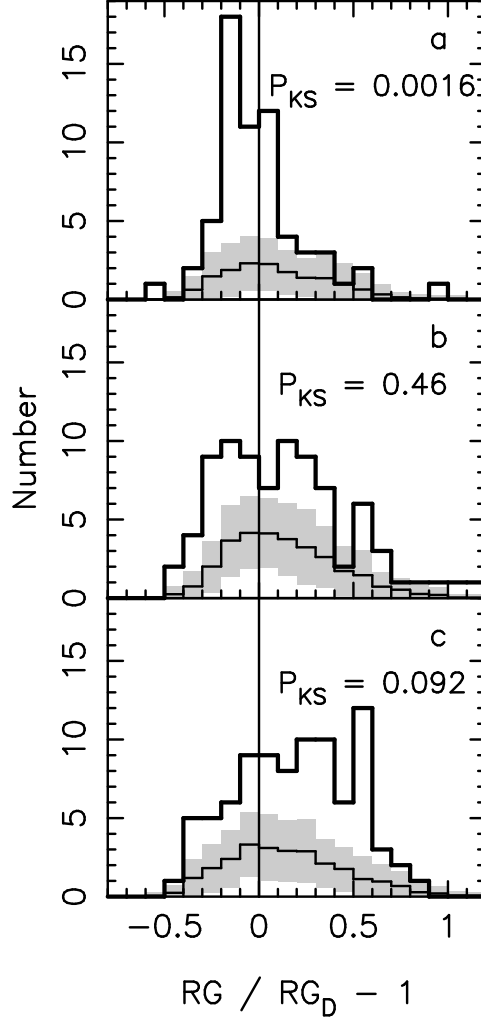


Figure 3.5: Histograms of the indicated quantity for all local minima detected in the reduced mean transmission triangles of QSO pairs (thick lines). The thin lines show the mean histograms computed from 100 simulations. ± 1 rms levels as derived from the simulations are indicated by the grey shaded areas. The top row shows the result for QSO pairs with $d < 3 h^{-1}$ Mpc, the middle row for $3 h^{-1}$ Mpc $< d < 6 h^{-1}$ Mpc and the bottom row for $6 h^{-1}$ Mpc $< d$. We also show KS probabilities that the simulated and observed distributions agree.

number of LM exceeds the expected number at all separations. However, at small separations (panel a) the excess is skewed to values $RG/RG_D - 1 < 0$. A KS test shows that the simulated and observed distributions disagree at the > 99 per cent confidence level. This discrepancy disappears for larger line of sight separations.

In addition, we have also counted the number of DLOS-LM which are produced by only a single SLOS-LM and found that the excess of such cases increases from 2.2σ over 3.4σ to 4.4σ for increasing line of sight separation.

Again, the removal of certain subclasses of LM (those of the Q0041–2707 - Q0041–2658 pair, substructure, those associated with metal lines) does not change the results significantly.

In summary, the results above show that for small line of sight separations two SLOS-LM combine to make a DLOS-LM of greater significance, whereas for large line of sight separations the structures seen in the SLOS are ‘diluted’. We thus take the anti-correlation of the excess of LM seen in the reduced mean transmission triangles of double-lines of sight with sight-line separation as strong evidence for the existence of structures on scales of up to $3 h^{-1}$ proper Mpc in the Ly α forest.

3.4.4 Correlation with metal lines

Not surprisingly, all the metal systems that were found in the present data have associated overdense Ly α absorption. We have repeatedly remarked in the sections above that the removal of LM that are associated with metal lines does not change the results qualitatively. Here, we take the opposite approach: we have repeated the analysis of the previous section only for those DLOS-LM that have a metal system within 1000 km s^{-1} in either of the constituent SLOS. The corresponding figure to Fig. 3.4 shows only a marginal trend with line of sight separation, with $P_{\text{KS}}(RG) = 0.091$ for small separations, which is entirely due to the close pair Q0041–2658 and Q0041–2707. The corresponding figure to Fig. 3.5 and its KS tests also indicate that the DLOS-LM are due to chance alignments or single SLOS-LM at *all* separations, however the numbers are very low and we cannot draw any definite

conclusions.

It must be kept in mind that the subdivision into LM with and without metals is subject to a strong selection effect since the work by Cowie et al. (1995) and Songaila & Cowie (1996) has clearly shown that the census of C IV in the present data must be significantly incomplete. Thus the distinction made here is more one between high column density and low column density structures rather than between metals and Ly α only. Therefore in the real data we have selected LM that are due to high column density structures whereas in the simulations we have basically drawn a random sample of LM since in the simulated data the column density is unrelated to the presence of metals.

Nevertheless, it appears that the high column density structures traced by metal lines do not produce overdense Ly α absorption at the distances probed by this sample, with one notable exception, in contrast to the lower column density Ly α only systems. On the other hand, there is little difference between the distributions of smoothing scales for those LM that are associated with metal lines and those that are not. A KS test gives a probability of 0.3 that the two distributions are the same.

3.4.5 Triple lines of sight

QSO triplets can provide important constraints on the shape of Ly α absorbers. It is possible that the excess of LM seen in the DLOS is mainly due to filamentary structures. If this were the case then one would expect LM of close triple lines of sight (TLOS) to be caused by two, not three SLOS-LM. However, if the absorption is sheet-like in nature then one would expect to find three similar SLOS-LM per TLOS-LM.

We have repeated the analysis of Section 3.4.3 for triple lines of sight. Table 3.4 lists triplets of QSOs grouped according to their pairwise transverse line of sight separations as in Table 3.2. The triplets of the first two groups form more or less equilateral triangles on the sky. However, due to the larger extent of the full group

Table 3.4: Triplets of QSOs grouped according to their proper transverse separation.

$d < 3 h^{-1} \text{ Mpc}$	$3 h^{-1} \text{ Mpc} < d < 6 h^{-1} \text{ Mpc}$	$6 h^{-1} \text{ Mpc} < d$
Q0042-2627 Q0042-2639 Q0043-2633	Q0041-2638 Q0042-2656 Q0043-2633	Q0041-2638 Q0041-2707 Q0041-2607
	Q0041-2707 Q0042-2714 Q0042-2657	Q0041-2638 Q0041-2607 Q0042-2657
	Q0041-2658 Q0042-2714 Q0042-2657	
$\bar{d} = 2.82 h^{-1} \text{ Mpc}$	$\bar{d} = 4.73 h^{-1} \text{ Mpc}$	$\bar{d} = 8.92 h^{-1} \text{ Mpc}$

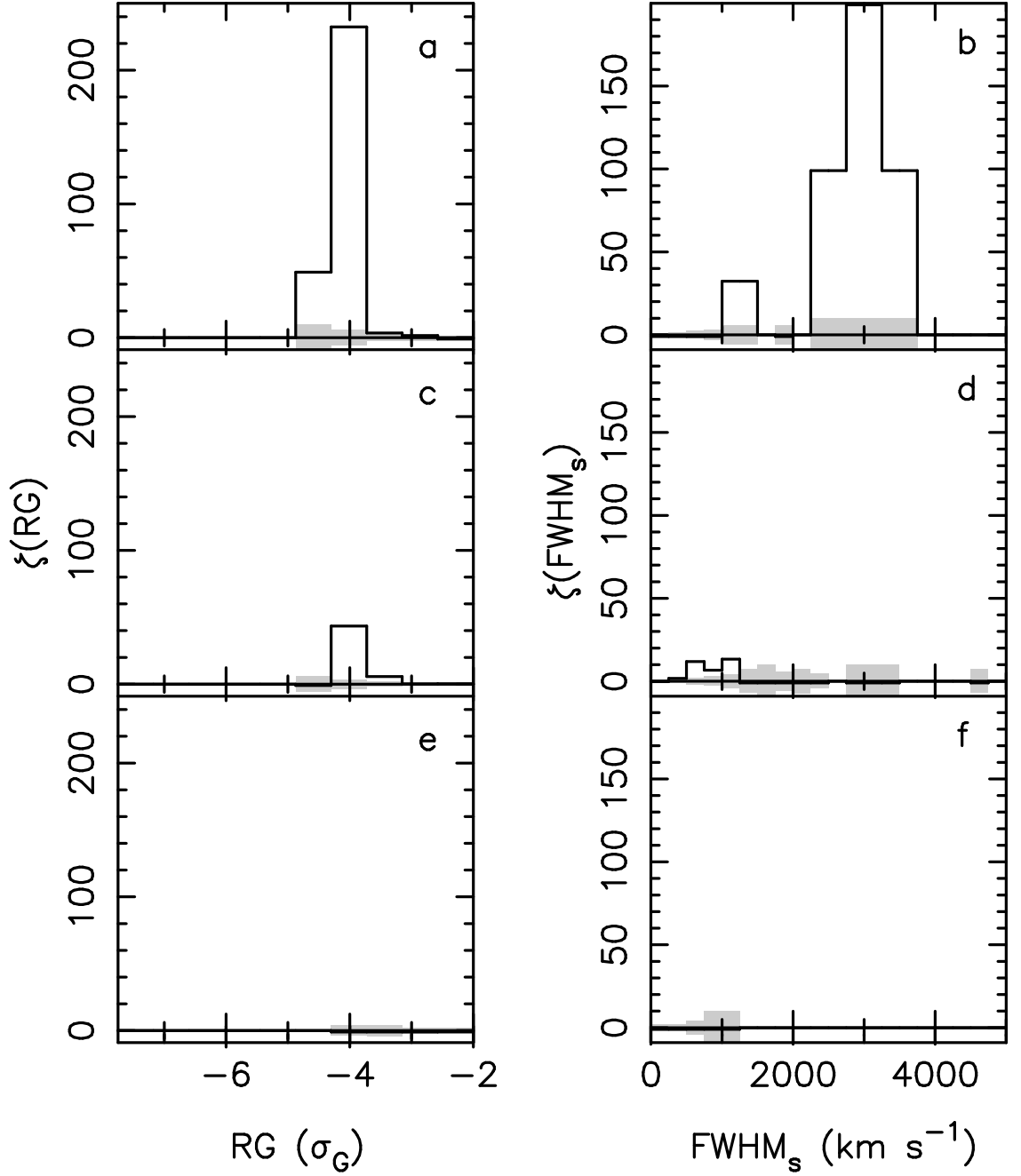


Figure 3.6: Excess of observed number of local minima in reduced mean transmission triangles of QSO triplets over the expected number (= mean of 100 simulations) as a function of the significance level (panels a, c, e) and the smoothing scale (panels b, d, f). ± 1 rms levels as derived from the simulations are indicated by the grey shaded areas. The top row shows the result for QSO triplets with pairwise separations $d < 3 h^{-1} \text{ Mpc}$, the middle row for $3 h^{-1} \text{ Mpc} < d < 6 h^{-1} \text{ Mpc}$ and the bottom row for $6 h^{-1} \text{ Mpc} < d$.

in the DEC direction than in the RA direction, the triplets of the last group form somewhat flatter triangles. Unfortunately, our QSO sample is not dense enough to provide more than one to three triplets per group.

Fig. 3.6 shows the results. Again we see an anti-correlation of the excess of LM with line of sight separation (panels a, c and e). However, for the smallest separations we find that 7 of the 10 identified TLOS-LM are due to only two (and not three) SLOS-LM. The vast majority of SLOS-LM are of smaller significance than their respective TLOS-LM. Therefore it seems that at least in the case of this particular QSO triplet the absorption more often extends across only two lines of sight than across three. However, the numbers are small and thus we cannot draw any definite conclusions from this result.

3.5 Uncertainties

In previous sections we have already addressed the uncertainties introduced by the observational errors on the values of the parameters of equation (3.1) and by random and systematic errors in the lowest orders of the continuum fits.

However, there is another aspect of the continuum fitting process which could potentially bias the number of detected overdensities in the Ly α forest. Large-scale overdensities could be included in the continuum fits and thus removed from the spectra to some extent if the fitting function is too flexible or if the spectral regions over which the continua are fit are too small.

The continua for the present set of spectra were derived by fitting Chebyshev polynomials of order 3–6 to overlapping regions of spectra $\sim 200 \text{ \AA}$ in length. A sigma clipping algorithm was employed during the fitting and regions of heavy absorption were avoided. Thus we believe that it is unlikely that we have underestimated the number of overdensities due to the continuum fits.

Conversely one might ask whether the detected overdensities are indeed due to density fluctuations of the intervening absorption rather than being caused by intrinsic continuum features or artifacts of the data gathering process which were

not removed by the continuum fits. Without prior knowledge of such features it is very difficult to distinguish between such spurious and ‘real’ fluctuations. However, the fact that the absorption overdensities seem to correlate across neighbouring lines of sight seems to suggest that most of the overdensities are indeed due to intervening absorption.

We also point out that the detected fluctuations in the absorption density do not necessarily imply that there exists *gravitationally* induced structure in the absorbing gas. The structure could also be due to large-scale fluctuations in the intensity of the ionizing radiation (cf. Chapter 5).

Finally, we must keep in mind that the results presented here may not be representative. There are at least two selection effects at work.

First, the sort of study we have presented in this chapter requires a sample of QSOs with an unusually high spatial density. It is conceivable that the large-scale environment of such groups is atypical with respect to the density and distribution of QSO absorption line systems.

Secondly, we must consider the effects of gravitational lensing. Although it is widely acknowledged that weak gravitational lensing by large-scale structure has some effect on the QSO luminosity function (e.g. Pei 1995; Hamana, Martel, & Futamase 2000), particularly at its steep bright end, the extent of the effect and a possible association of the lensing matter with QSO absorption systems is less certain. Thus it is currently unclear whether studies of the number density of absorption lines (or clusters thereof) are biased because of gravitational lensing (Vanden Berk, Quashnock, & York 1996 and references therein; Holz & Wald 1998). We must therefore admit the possibility that some of the QSOs of the present study were discovered only because they are gravitationally lensed by large-scale structure and that the same lensing matter is also somehow responsible for the overdensities that we have detected in the Ly α forest.

3.6 Conclusions and discussion

We summarise our main results as follows:

1. We have analysed the Ly α forest spectra of ten QSOs at $\langle z \rangle = 2.81$ contained within a $\sim 1 \text{ deg}^2$ field using a new technique based on the statistics of the transmitted flux. Comparison with two-point correlation function analyses (Section 3.4.2), along with the results of Chapter 2, suggests that this new method is more sensitive to the presence of large-scale structure than the two-point correlation function of individually identified absorption lines.

2. We find structure on scales of up to 1200 km s^{-1} along the line of sight and on scales of up to $17 h^{-1} \text{ Mpc}$ (comoving) in the transverse direction. We confirm the existence of large-scale structure in the Ly α forest at the > 99 per cent confidence level (Pando & Fang 1996; Williger et al. 2000).

3. We find strong correlations across lines of sight with proper separation $< 3 h^{-1} \text{ Mpc}$. For intermediate separations the correlation is weaker and there is only little evidence for correlation at line of sight separations $> 6 h^{-1} \text{ Mpc}$ (Fig. 3.4). We thus present the first evidence for a dependence of the correlation strength on line of sight separation and place an upper limit of $6 h^{-1} \text{ Mpc}$ on the transverse correlation scale at $z = 2.81$.

Assuming that the absorbing structures are expanding with the Hubble flow, we find that the line of sight and transverse correlation scales are roughly comparable ($1200 \text{ km s}^{-1} H^{-1}(z = 2.81) = 1.6 h^{-1} \text{ Mpc}$) with a suggestion that the absorbers might be flattened in the line of sight direction since we still detect somewhat significant correlations on transverse scales of $4.6 h^{-1} \text{ Mpc}$. Furthermore, the analysis of the only close QSO triplet of the sample showed that many coincident absorption features are common to only two spectra, perhaps indicating an elongated shape in the plane of the sky. However, no firm conclusions can be drawn here until more QSO triplets have been analysed.

Using a comparatively small sample with significantly smaller line of sight separations, Crofts (1989) and Crofts & Fang (1998) found a stronger correlation signal

for lines with $W > 0.4 \text{ \AA}$ than for weaker lines. In contrast, Williger et al. (2000) found from their analysis of the present South Galactic Pole data that the inclusion of weak lines ($W > 0.1 \text{ \AA}$) strengthened their correlation signal. Here we can tentatively confirm the Williger et al. (2000) result. This is in agreement with the results of Cen & Simcoe (1997) who predicted from their numerical simulations that high column density lines have smaller correlation lengths than low column density ones. This is already evident from a visual inspection of the three-dimensional distribution of the absorbing gas in the simulations at different overdensities. Large overdensities are confined to relatively small, more or less spherical regions whereas small overdensities form extended filaments and sheets.

It is interesting to compare our results with predictions from hydrodynamical simulations. The typical length of the low column density filaments in the simulations is of the order of $1 h^{-1} \text{ Mpc}$ in proper units (Miralda-Escudé et al. 1996; Zhang et al. 1998). Cen & Simcoe (1997) performed a detailed analysis of double-lines of sight in a Λ CDM simulation. They concluded that for proper line of sight separations $> 500 h^{-1} \text{ kpc}$ any coincident absorption is due to unrelated and spatially uncorrelated clouds. They pointed out however that a significant amount of power is missing from their simulation on the scale of the simulated box size ($10 h^{-1} \text{ Mpc}$). Even after correcting for this effect though, the transverse correlation scale predicted from these simulations remains significantly smaller (by about a factor of 3) than the one derived in this work. To investigate this discrepancy it will be necessary to perform a detailed comparison by subjecting simulated spectra, drawn from a suitable (i.e. large) simulation box, to the same analysis we have presented here.

The clustering of other classes of cosmologically distributed objects, such as galaxies and QSOs, is usually quantified in terms of the two-point correlation function. Measurements of the two-point correlation function are conventionally parameterised as a power law: $\xi(r) = (r_0/r)^\gamma$ (Peebles 1993), where r is measured in comoving coordinates. Loveday et al. (1995) found $r_0 = 5.1 h^{-1} \text{ Mpc}$ for present-day galaxies, although this result depended on both galaxy morphology and luminosity.

Galaxy clusters seem to correlate on scales of $r_0 \approx 15 h^{-1}$ Mpc (e.g. Dalton et al. 1994 and references therein), where r_0 may depend on cluster richness. At higher redshifts Croom & Shanks (1996) found $r_0 = 5.4 h^{-1}$ Mpc for a sample of > 1500 QSOs with $0.3 < z < 2.2$ and little evidence for evolution of clustering in comoving coordinates. Giavalisco et al. (1998) derived $r_0 = 2.1 h^{-1}$ Mpc for a sample of 871 Lyman break galaxies at $z = 3$ and Quashnock & Vanden Berk (1998) found $r_0 = 3.4 h^{-1}$ Mpc for C IV absorption systems at $z = 2.2$.

Since we have used a different clustering statistic and since there is no straightforward way to relate our statistic to the two-point correlation function it is difficult to perform a detailed comparison of our results to the values above. However, r_0 for the Ly α forest is unlikely to be larger than the largest scales where we have detected significant clustering.

Croft et al. (1998) and Nusser & Haehnelt (1999) have outlined schemes for recovering the power spectrum of mass fluctuations from Ly α forest spectra. Recently, Croft et al. (1999) performed the first such measurement on scales of 2–12 h^{-1} Mpc from 19 intermediate resolution QSO spectra at $z = 2.5$. Although we have concentrated in this work only on identifying typical correlation scales, our results confirm the usefulness of intermediate resolution data for large-scale structure studies when analysing the distribution of the transmitted flux directly. Since the Ly α forest is thought to trace the mass distribution more closely than galaxies we are likely to gain the most direct measurement of the bias between galaxy and mass clustering by comparing the power spectrum of the Ly α forest with that of galaxies (Croft et al. 1999).

There is a very good saying that if triangles invented a god, they would make him three-sided.

Baron de Montesquieu

Chapter 4

The cosmological distance and redshift between any two objects

4.1 Introduction

In cosmology and extragalactic astronomy one frequently needs to calculate the distance between two objects given their redshifts and their angular separation on the sky. As larger and larger cosmological volumes are probed by wide field redshift surveys such as 2dF and the Sloan Digital Sky Survey, or by QSO absorption line studies, the effects of non-Euclidean geometry become increasingly important. In the past, authors have frequently relied on approximations when calculating the distance between two cosmological objects, presumably for calculative ease. Such approximations are valid only for small distances and are particularly useful when examining or highlighting the feasibility of geometrical means to measure cosmological parameters as was done e.g. by Alcock & Paczyński (1979), Phillipps (1994) and Popowski et al. (1998). However, many practical applications are not limited by computing time and since an exact solution to the problem exists the approximations seem unnecessary. These applications include the construction of the real-space two-point correlation function of various objects such as galaxies (e.g.

Yoshii, Peterson, & Takahara 1993) and QSO absorption systems (Williger et al. 1996; Dinshaw & Impey 1996), as well as studies of the effect of local sources of ionizing radiation on their surrounding intergalactic medium (e.g Fernández-Soto et al. 1995; Chapter 5). The latter application actually requires knowledge of not only the distance between two objects but also of the redshift experienced by a photon travelling from one object to another.

Despite its fundamental nature we have failed to find a thorough discussion of this problem in the literature. Since the topic of the next chapter will be an investigation of the proximity effect in the sample of QSO spectra introduced in the previous chapter we feel that a detailed, explicit treatment is called for. In this short ‘interlude’ we thus present a new variant of the solution to the distance problem (Sections 4.2 and 3.4), discuss its relation to existing approaches (Section 4.4) and finally investigate the validity of the most frequently used approximation (Section 4.5).

For clarity and brevity we have limited ourselves here to homogeneous Friedmann (zero-pressure) cosmologies with no cosmological constant ($\Lambda = 0$). The inclusion of Λ renders some of the explicit expressions non-analytical and thus (in the context of this exposition) unnecessarily complicates matters.

4.2 The distance between any two objects

We begin by writing the familiar Robertson-Walker line element as:

$$ds^2 = -c^2 dt^2 + a^2(t) \left[d\chi^2 + \Sigma^2(\chi)(d\theta^2 + \sin^2 \theta d\phi^2) \right], \quad (4.1)$$

where

$$\Sigma(\chi) = \begin{cases} \sin \chi & k = +1 \\ \chi & k = 0 \\ \sinh \chi & k = -1. \end{cases} \quad (4.2)$$

Putting the Earth at the origin of the coordinate system one can use this metric and the Friedmann equations to calculate the distance from Earth (at $\chi = 0$) to an

object at redshift z , corresponding to a comoving coordinate χ ,

$$r = a_0 \Sigma[\chi(z)] = \frac{c}{H_0 q_0^2} \frac{1}{1+z} \left[q_0 z + (q_0 - 1) \left(\sqrt{1 + 2q_0 z} - 1 \right) \right] \quad (4.3)$$

(e.g. Misner, Thorne, & Wheeler 1973), where a_0 , H_0 and q_0 are the scale factor, Hubble and deceleration parameters at the present epoch (subscript 0).

Now consider an object 1 (the ‘receiver’) observed on Earth today at z_1 and an object 2 (the ‘emitter’) at z_2 separated by an angle α on the sky (cf. Fig. 4.1). Object 2 emits a photon towards object 1 which is received by object 1 at the same time as object 1 emits the photon we receive from it today (i.e. at the epoch corresponding to z_1). What is the distance, r'_2 , between these two objects at the time of the photon reception and what is the redshift, z'_2 , of the photon as observed by object 1?

An observer at object 1 would write equation (4.3) as

$$r'_2 = a_1 \Sigma(\chi'_2) = \frac{c}{H_1 q_1^2} \frac{1}{1+z'_2} \left[q_1 z'_2 + (q_1 - 1) \left(\sqrt{1 + 2q_1 z'_2} - 1 \right) \right], \quad (4.4)$$

where χ'_2 is the comoving coordinate distance between objects 1 and 2 (cf. Fig. 4.1) and

$$\begin{aligned} a_1 &= \frac{a_0}{1+z_1}, \\ H_1 &= H_0(1+z_1)\sqrt{1+2q_0 z_1}, \\ q_1 &= q_0 \frac{1+z_1}{1+2q_0 z_1} \end{aligned} \quad (4.5)$$

are the scale factor, Hubble and deceleration parameters at the time object 1 emitted the photons we receive today. Thus we see that the problems of calculating r'_2 and z'_2 are equivalent since knowledge of one provides knowledge of the other via equation (4.4). Here we choose to find z'_2 .

Note that r'_2 does *not* describe in general the shortest distance between objects 1 and 2 along a $t = \text{const}$ hypersurface of spacetime. Nevertheless, in many applications r'_2 is the quantity of interest. For example, when considering the radiative effect of a QSO on a nearby object one needs the luminosity distance between the

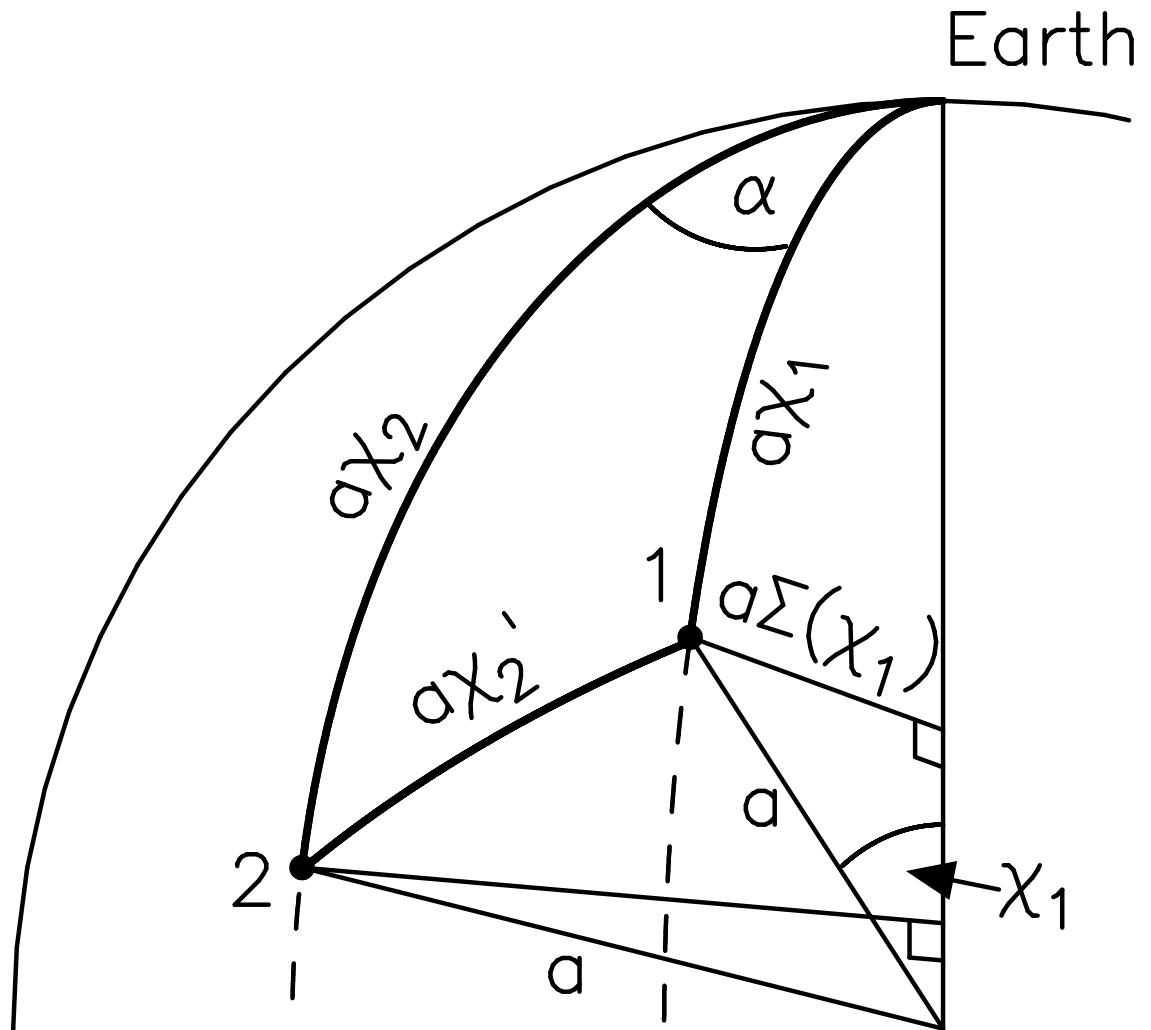


Figure 4.1: In the case $k = +1$ objects 1 and 2 and Earth form a triangle with geodesic sides (thick lines) on the surface of a 2d sphere of radius a . The Earth is at the origin of the coordinate system ('north pole'). From the centre of the sphere the angle between Earth and object 1 is χ_1 . A photon emitted by object 1 towards Earth travels along the geodesic connecting the two (thick line). The length of this path (= distance between object 1 and Earth) is $a\chi_1$. $a\Sigma(\chi_1) = a \sin \chi_1$ is the distance from object 1 to the central axis of the sphere. Essentially this is the angular diameter distance or luminosity distance (modulo factors of $1 + z$) from Earth to object 1. χ_2' is the unknown angle between objects 1 and 2 at the centre of the sphere and $a\chi_2'$ is the unknown length of the connecting geodesic.

two which is given by $r'_{L2} = r'_2(1 + z'_2)$. In any case, it is most practical to solve the problem for z'_2 and then calculate the distance required for a given application from z'_2 .

As we are dealing with three points (Earth and objects 1 and 2) in a 3-dimensional space (described by the spatial part of the metric, equation 4.1) it seems intuitive that it must be possible to reduce the problem to two dimensions as one can always find a 2d hypersurface that contains all three points. Since we are interested in measuring 3d distances the hypersurface should be chosen such that the distance between any two points of the surface (as measured along the surface) is identical to the 3d distance between the same two points. We call such surfaces totally geodesic. It is clear that a totally geodesic hypersurface containing a given set of three points can only be constructed from the geodesics connecting the three points. Since these geodesics are unique there can be only one such surface.

In equation (4.1) we introduced a polar coordinate system (χ, θ, ϕ) . Clearly, the hypersurface described by $\phi = \text{const}$ is totally geodesic. (Note that the surfaces $\chi = \text{const}$ and $\theta = \text{const}$ are not.) Since the curvature of the 3d space under consideration is constant, one can generate *all* totally geodesic hypersurfaces from any given one by mere translations and rotations. Therefore, for a given set of three points there must exist a coordinate system $(\tilde{\chi}, \tilde{\theta}, \tilde{\phi})$ such that $\tilde{\phi} = \text{const}$ describes the unique totally geodesic hypersurface containing these three points. Since this new coordinate system can be constructed from the old one by translation and rotation, the form of the metric in this new system is identical to equation (4.1). Restraining this metric to the $\tilde{\phi} = \text{const}$ hypersurface we have

$$dl^2 = a^2 \left[d\tilde{\chi}^2 + \Sigma^2(\tilde{\chi})d\tilde{\theta}^2 \right]. \quad (4.6)$$

Thus we can see that the triangle Earth–object 1–object 2 lies either on a 2d sphere, a plane or a 2d hyperboloid ($k = +1, 0, -1$) embedded in 3d Euclidean space. This triangle has geodesic sides χ_1 , χ_2 , and χ'_2 (connecting the two objects) and the angle α at Earth. The case $k = +1$ is shown in Fig. 4.1.

The objective is now to express the unknown side χ'_2 in terms of the known sides

χ_1 , χ_2 and the angle α . We first note that all formulae of Euclidean trigonometry have corresponding formulae in spherical and hyperbolic trigonometry. These can be expressed simultaneously for all three curvatures using Σ . In particular, we can generalize the half-angle formulae in this way and use them to show that

$$\Sigma^2 \left(\frac{\chi'_2}{2} \right) = \Sigma^2 \left(\frac{\chi_2 + \chi_1}{2} \right) \sin^2 \frac{\alpha}{2} + \Sigma^2 \left(\frac{\chi_2 - \chi_1}{2} \right) \cos^2 \frac{\alpha}{2}. \quad (4.7)$$

This is a more compact and symmetrical version of the generalized cosine rule (see Section 4.4).

Using the same methods that were employed in the derivation of equation (4.3) we can relate the right-hand side of equation (4.7) to z_1 and z_2 :

$$a_0 \Sigma \left(\frac{\chi_2 \pm \chi_1}{2} \right) = \frac{c}{H_0 q_0} \frac{1}{\sqrt{(1+z_1)(1+z_2)}} \frac{P_{\pm}}{2}, \quad (4.8)$$

where

$$P_+ = \frac{1}{q_0} \left[(q_0 - 1) \left(\sqrt{1 + 2q_0 z_1} + \sqrt{1 + 2q_0 z_2} - 1 \right) + \sqrt{(1 + 2q_0 z_1)(1 + 2q_0 z_2)} - q_0 \right] \quad (4.9)$$

and

$$P_- = \left(\sqrt{1 + 2q_0 z_2} - \sqrt{1 + 2q_0 z_1} \right). \quad (4.10)$$

Furthermore, setting $\chi_1 = z_1 = 0$ it follows from equation (4.8) that

$$a_0 \Sigma \left(\frac{\chi_2}{2} \right) = \frac{c}{H_0 q_0} \frac{1}{\sqrt{1+z_2}} \frac{1}{2} \left(\sqrt{1 + 2q_0 z_2} - 1 \right) \quad (4.11)$$

and for an observer at object 1

$$a_1 \Sigma \left(\frac{\chi'_2}{2} \right) = \frac{c}{H_1 q_1} \frac{1}{\sqrt{1+z'_2}} \frac{1}{2} \left(\sqrt{1 + 2q_1 z'_2} - 1 \right), \quad (4.12)$$

thus relating the left-hand side of equation (4.7) to z'_2 . Solving

$$P = \frac{1}{2} \frac{1}{\sqrt{1+z'_2}} \left(\sqrt{1 + 2q_1 z'_2} - 1 \right) \quad (4.13)$$

for z'_2 yields (positive solution)

$$z'_2 = \frac{2P^2}{(q_1 - 2P^2)^2} \left(1 + q_1 - 2P^2 + \sqrt{\frac{q_1^2}{P^2} + 1 - 2q_1} \right), \quad (4.14)$$

where

$$\begin{aligned} P^2 &= \left(\frac{a_1 H_1 q_1}{c} \right)^2 \Sigma^2 \left(\frac{\chi'_2}{2} \right) \\ &= \frac{1}{4} \frac{1+z_1}{1+z_2} \frac{1}{1+2q_0 z_1} \left(P_+^2 \sin^2 \frac{\alpha}{2} + P_-^2 \cos^2 \frac{\alpha}{2} \right). \end{aligned} \quad (4.15)$$

Note that z'_2 does not depend on H_0 .

4.2.1 $\Lambda \neq 0$

For completeness we now briefly consider the case $\Lambda \neq 0$. Equation (4.7) is of course still valid. However, in relating this equation to the observables z_1 , z_2 and z'_2 we have made use of the fundamental relationship between an object's comoving radial coordinate and its redshift,

$$\chi(z) = \frac{c}{a_0 H_0} \int_1^{1+z} \left[\Omega_0 x^3 + (1 - \Omega_0) x^2 \right]^{-\frac{1}{2}} dx, \quad (4.16)$$

which in turn is derived from the Friedmann equations. For $\Lambda \neq 0$ these take on a different structure and instead of the above relationship we have

$$\chi(z) = \frac{c}{a_0 H_0} \int_1^{1+z} \left[\Omega_0 x^3 + (1 - \Omega_0 - \lambda_0) x^2 + \lambda_0 \right]^{-\frac{1}{2}} dx, \quad (4.17)$$

where $\lambda_0 = \Lambda c^2 / 3H_0^2$. Unfortunately this integral is non-analytical but Kayser, Helbig, & Schramm (1997) developed an efficient method (which also accommodates inhomogeneity) to compute $\Sigma(\chi)$ numerically.

Note that other density contributions with unusual equations of state can be dealt with in the same way. All that needs to be done is to establish $\chi(z)$ or, equivalently, $\Sigma[\chi(z)]$. In principle, one could then proceed to use equation (4.7) to find z'_2 and r'_2 . However, when $\chi(z)$ is not available analytically it is probably more practical to use the generalized cosine rule (see Section 4.4, equation 4.23) instead of equation (4.7). In any case, one is still left with the problem of inverting $\Sigma[\chi(z)]$ in order to find z'_2 . However, since we can compute

$$\frac{d\Sigma}{dz} = \sqrt{1 - k\Sigma^2(z)} \frac{d\chi}{dz} \quad (4.18)$$

it should be possible to employ an efficient root finding algorithm for this task.

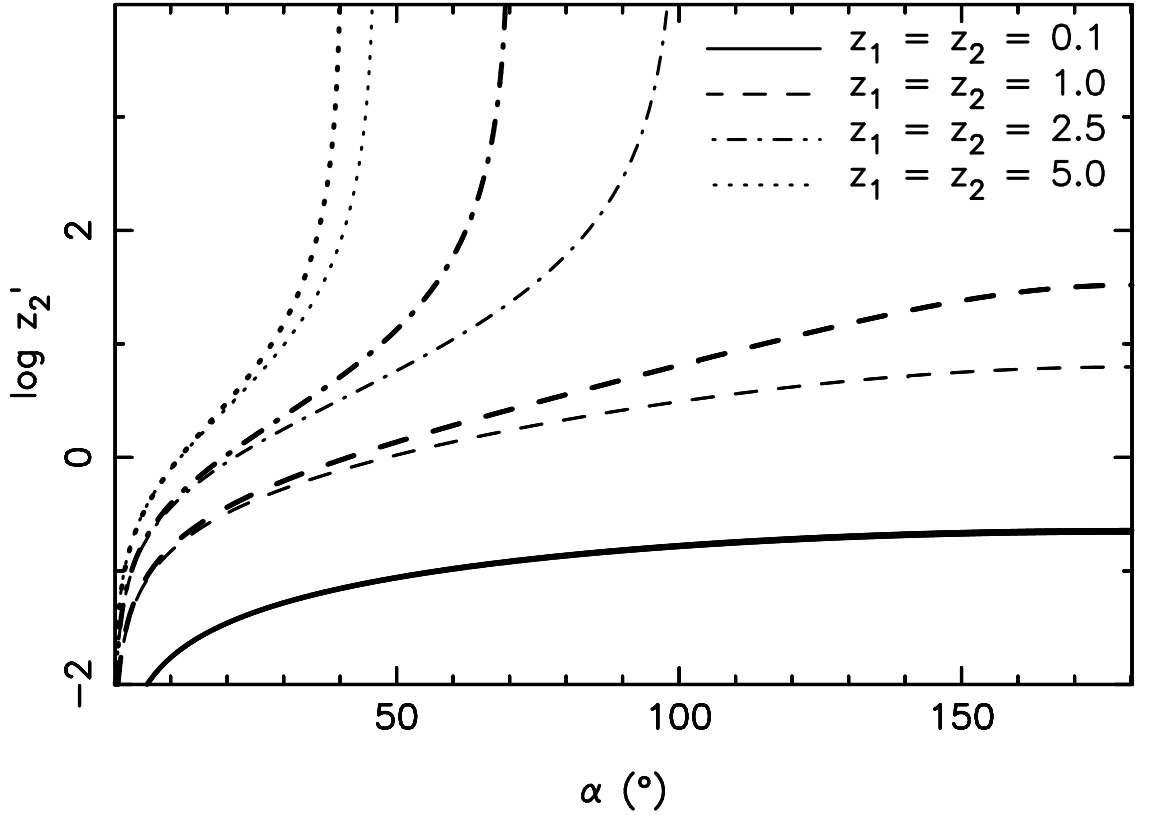


Figure 4.2: z'_2 as a function of α (angle on the sky between receiver and emitter), $z_1 = z_2$. Thick lines are for $q_0 = 0.5$, thin lines for $q_0 = 0.15$.

4.3 Results

As cosmologists are often used to thinking in terms of redshift rather than distance, we show the result of the above calculations in Figs. 4.2–4.6 in terms of z'_2 , the redshift of object 2 as seen by object 1.

Figs. 4.2 and 4.3 explore the special case $z_1 = z_2$. In Fig. 4.2 we show $z'_2(\alpha)$ with $z_1 = z_2$ fixed at various values. The thick lines show the case of a flat universe ($\Omega_0 = 2q_0 = 1$) and the thin lines show the case of an open universe with $\Omega_0 = 0.3$. Note that for large values of $z_1 = z_2$ there is some α_∞ such that $z'_2 \rightarrow \infty$ for $\alpha \rightarrow \alpha_\infty$. This is the particle horizon of object 1 at the epoch corresponding to z_1 . At that time, light emitted from objects separated from object 1 by angles $> \alpha_\infty$ has not had time to reach object 1 since the Big Bang (ignoring inflation). In Fig. 4.3 we

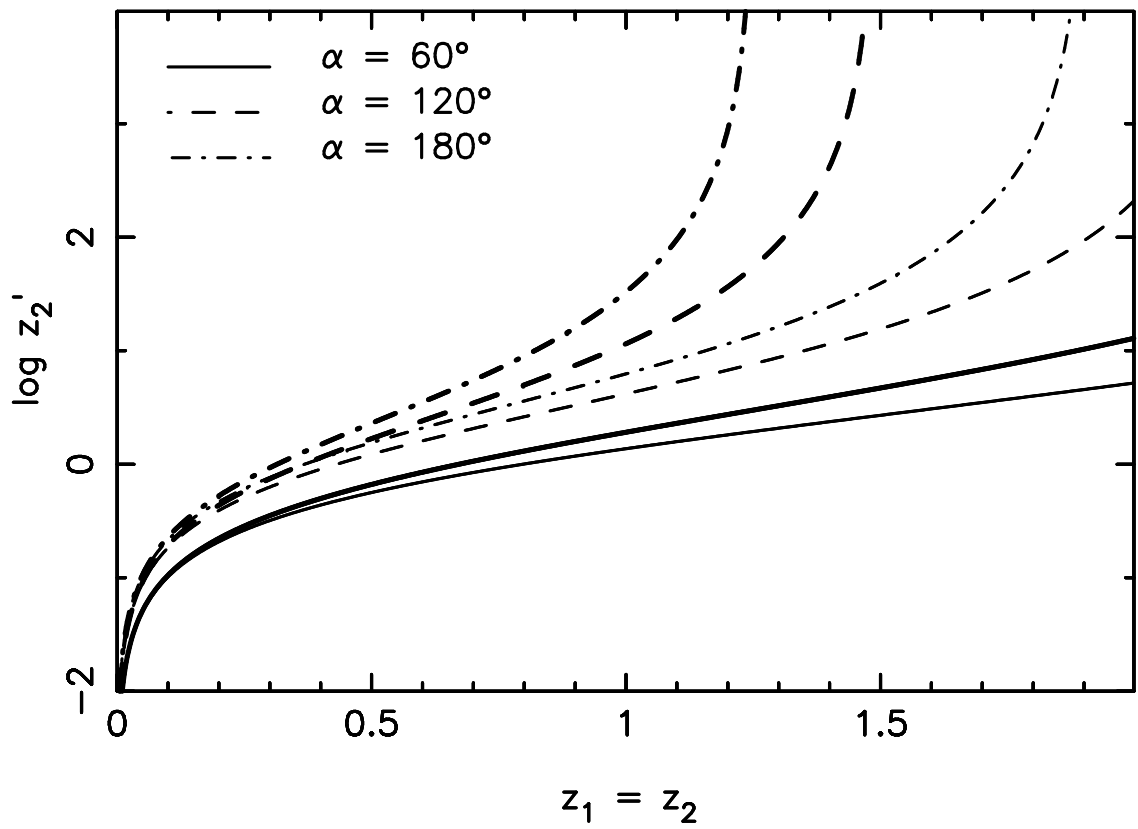


Figure 4.3: z_2' as a function of $z_1 = z_2$. Thick lines are for $q_0 = 0.5$, thin lines for $q_0 = 0.15$.

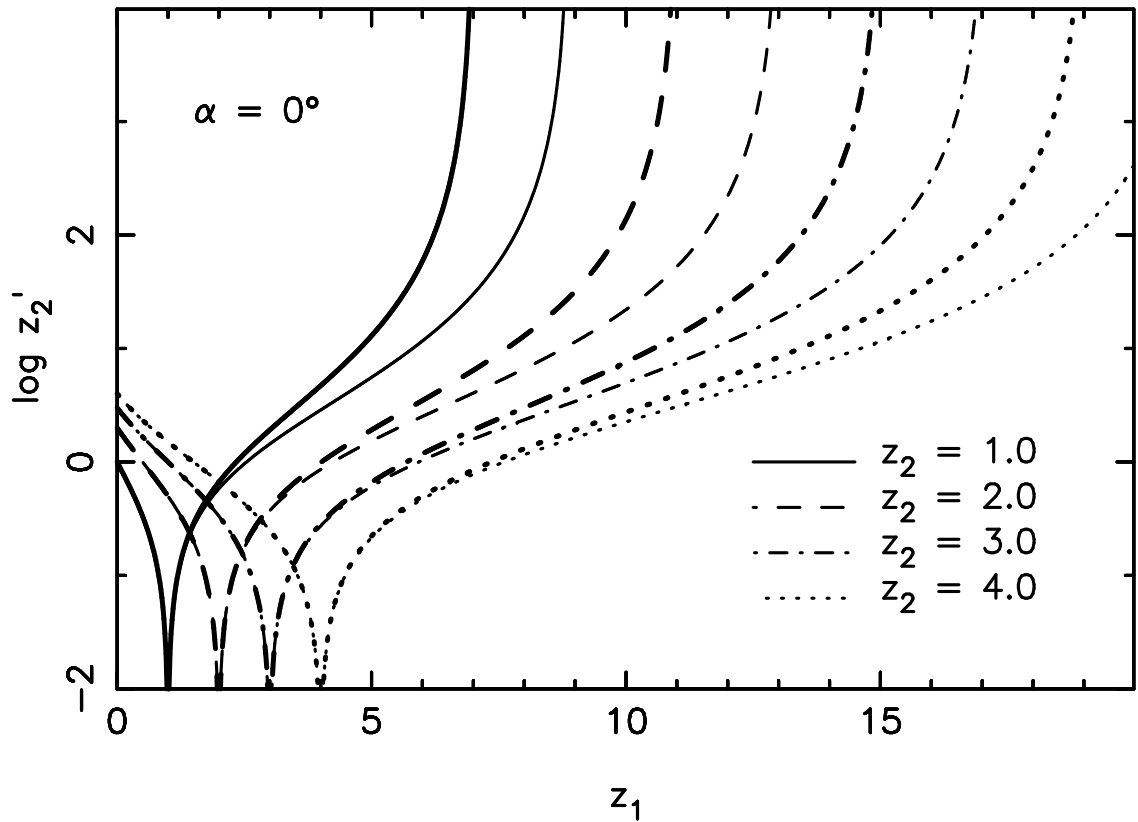


Figure 4.4: z'_2 as a function of z_1 (redshift of receiver), $\alpha = 0$. Thick lines are for $q_0 = 0.5$, thin lines for $q_0 = 0.15$. Since $\alpha = 0$, z'_2 is independent of cosmology for $z_1 < z_2$.

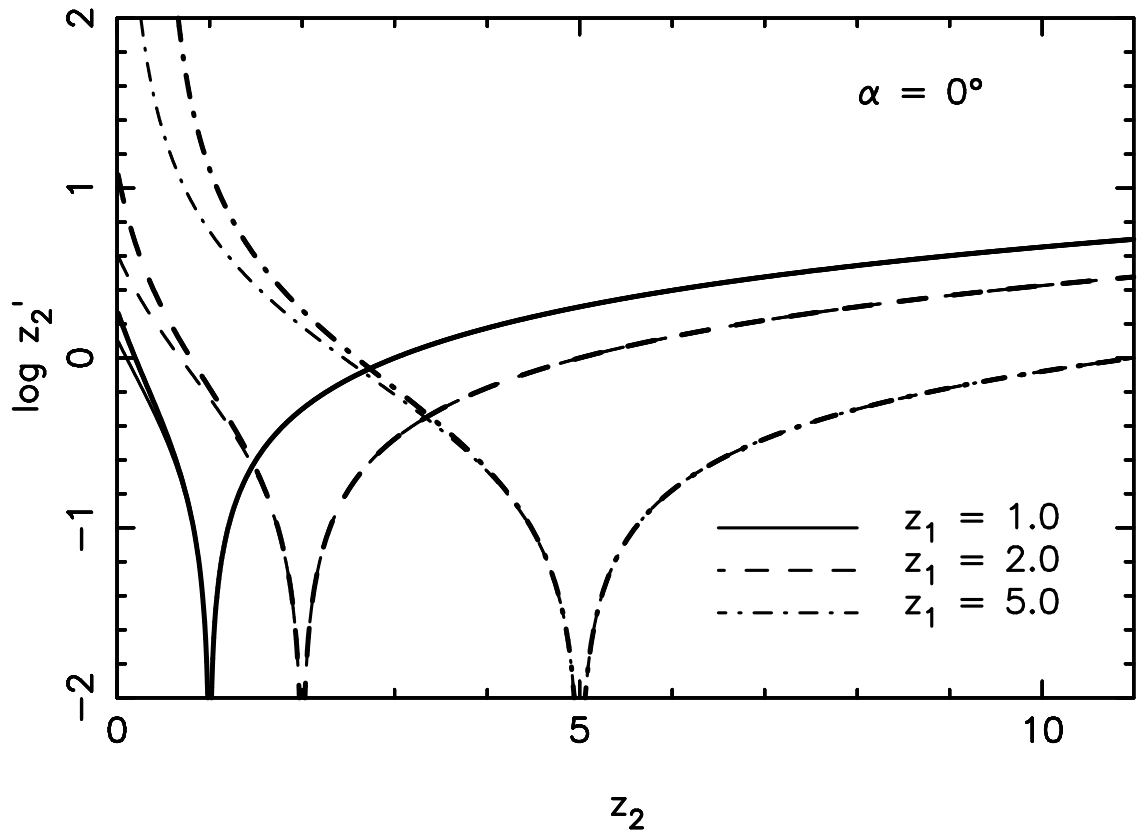


Figure 4.5: z'_2 as a function of z_2 (redshift of emitter), $\alpha = 0$. Thick lines are for $q_0 = 0.5$, thin lines for $q_0 = 0.15$. Since $\alpha = 0$, z'_2 is independent of cosmology for $z_1 < z_2$.

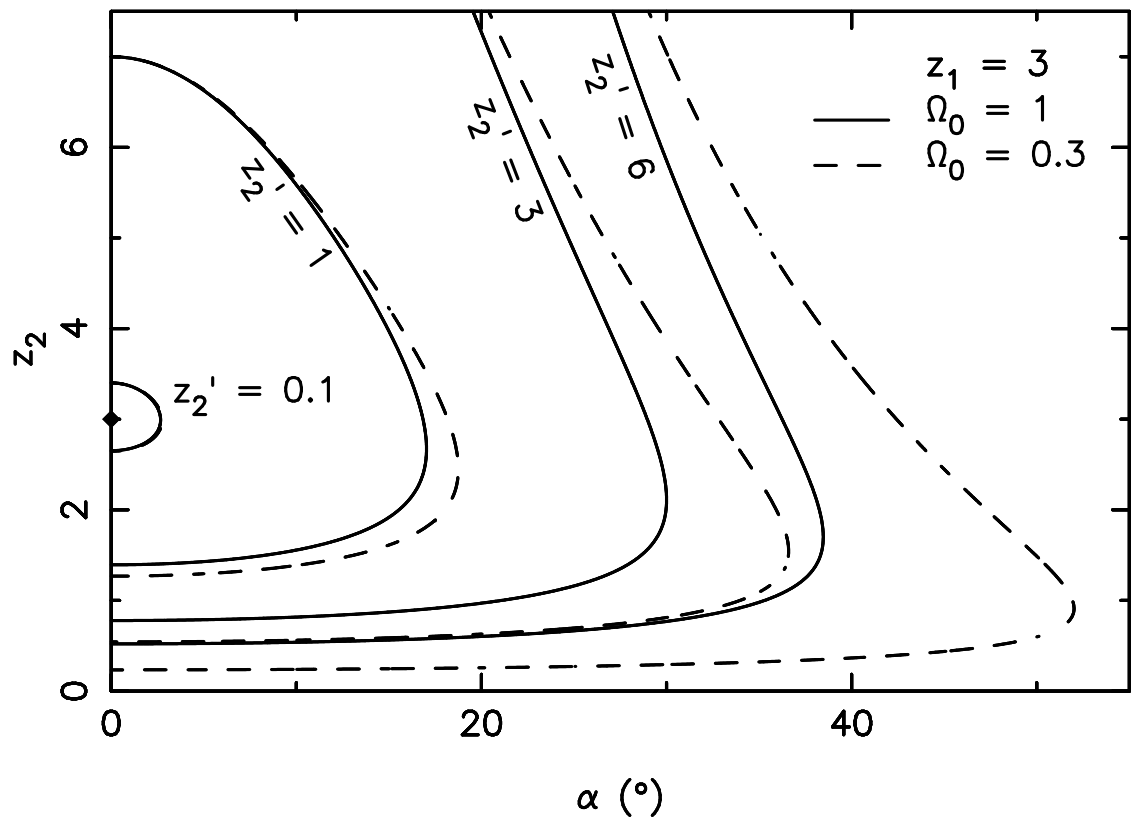


Figure 4.6: z'_2 as a function of z_2 and α (emitter position). The receiver is at $z_1 = 3$ and $\alpha = 0$ (marked by a diamond). The contours are lines of constant z'_2 . Solid lines are for $q_0 = 0.5$, dashed lines for $q_0 = 0.15$.

fix α at various angles and show z'_2 as a function of $z_1 = z_2$. The case $\alpha = 180^\circ$ is often incorrectly used in undergraduate physics textbooks (e.g. Halliday, Resnick, & Walker 1993, p. 1128–1129) as an example of how to add velocities in Special Relativity, a method which will give a wrong result for z'_2 .

In Figs. 4.4 and 4.5 we consider the special case $\alpha = 0$ and plot z'_2 as a function of z_1 and z_2 respectively. Thick lines again represent a flat universe, thin lines an open universe. Whenever $z_1 < z_2$ (and $\alpha = 0$), z'_2 is of course given by

$$1 + z'_2 = \frac{1 + z_2}{1 + z_1} \quad (4.19)$$

which is the only case where z'_2 is independent of the cosmological model, since in this case the time of emission of the photon received by object 1 is the same as the time corresponding to z_2 . Note that although $\chi'_2(z_1, z_2, \alpha) = \chi'_2(z_2, z_1, \alpha)$ (cf. equation 4.23), the same does *not* hold for z'_2 (cf. equations 4.14 and 4.15). Fig. 4.5 also provides the solution to an interesting thought experiment. What is the redshift, z_{refl} , of a photon emitted by ourselves ($z_2 = 0$) which was reflected back to us by a comoving mirror at z_1 ? The answer is

$$1 + z_{\text{refl}} = (1 + z_1)[1 + z'_2(z_1, z_2 = 0)]. \quad (4.20)$$

Finally we plot in Fig. 4.6 lines of constant z'_2 as a function of z_2 and α for a receiver at $z_1 = 3$. In this plot the flat and open cosmologies are represented by the solid and dashed lines respectively.

4.4 Relation to other solutions

We are aware of two original solutions to the problem in the literature, Peacock (1999), p. 71, and Osmer (1981). Neither of them consider z'_2 .

Instead of equation (4.7), Peacock considers the generalized cosine rule which directly gives $\Sigma(\chi'_2)$. Introducing the cosine equivalent of $\Sigma(\chi)$,

$$\Xi(\chi) = \sqrt{1 - k\Sigma^2(\chi)}, \quad (4.21)$$

we have

$$\Xi(\chi'_2) = \Xi(\chi_1) \Xi(\chi_2) + k \Sigma(\chi_1) \Sigma(\chi_2) \cos \alpha \quad (4.22)$$

which can be written as

$$\begin{aligned} \Sigma^2(\chi'_2) &= \Sigma^2(\chi_1) \Xi^2(\chi_2) + \Sigma^2(\chi_2) \Xi^2(\chi_1) + k \Sigma^2(\chi_1) \Sigma^2(\chi_2) \sin^2 \alpha \\ &\quad - 2 \Sigma(\chi_1) \Sigma(\chi_2) \Xi(\chi_1) \Xi(\chi_2) \cos \alpha. \end{aligned} \quad (4.23)$$

When only r'_2 is needed the use of this equation seems more practical than our solution presented in Section 4.2. However, when using the generalized cosine rule the analogues of equations (4.14) and (4.15) are more complicated so that in cases where z'_2 is (also) of interest, e.g. when calculating the luminosity distance $r'_{L2} = r'_2(1 + z'_2)$, the new solution is to be preferred.

Osmer's solution may be considered the most rigorous as it is based on a general result of differential geometry in maximally symmetric spaces. Weinberg (1972), p. 413, showed how to transform to a coordinate system which has been 'quasitranslated'. Osmer uses this equation to transform from a coordinate system in which objects 1 and 2 have particularly simple coordinates (see discussion in Section 4.2) to one where the origin has been translated from Earth to object 1. The result is then given by

$$\Sigma^2(\chi'_2) = \Sigma^2(\chi_2) \sin^2 \alpha + [\Sigma(\chi_2) \Xi(\chi_1) \cos \alpha - \Sigma(\chi_1) \Xi(\chi_2)]^2. \quad (4.24)$$

This equation of course reduces to equation (4.23) and thus the comments made there apply equally to Osmer's solution.

4.5 Validity of approximation

Probably the most common approximation for the comoving distance is (e.g. Yoshii, Peterson, & Takahara 1993; Phillipps 1994)

$$a_0^2 \chi_2'^2 \approx a_0^2 \chi_{A2}'^2 = a_0^2 \Sigma^2[\chi(\bar{z})] \alpha^2 + \left[a_0 \frac{d\chi}{dz}(\bar{z}) \right]^2 \Delta z^2, \quad (4.25)$$

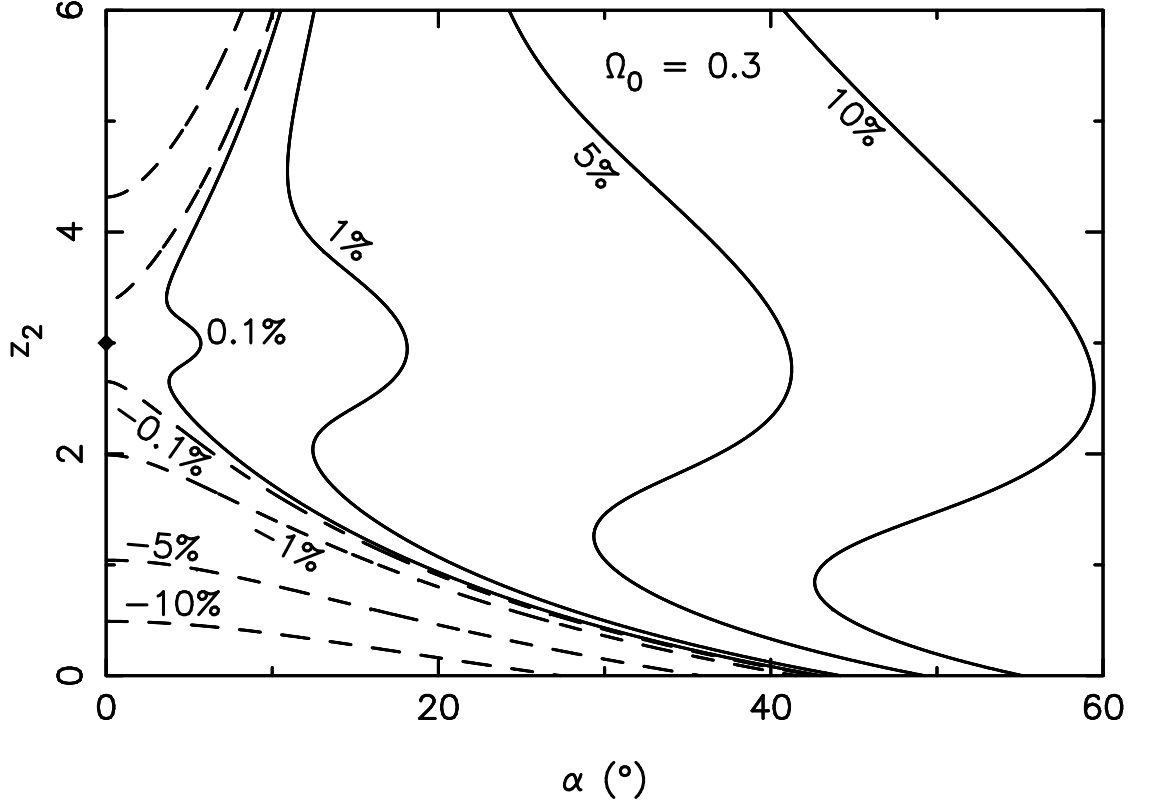


Figure 4.7: The contours are lines of constant $\frac{a_0 \Delta \chi'_2}{a_0 \chi'_2}$, the fractional error made when using equation (4.25) for $z_1 = 3$ (marked by a diamond) and $q_0 = 0.15$. The contour levels are indicated.

where $\Delta z = z_1 - z_2$ and $\bar{z} = (z_1 + z_2)/2$ and

$$a_0 \frac{d\chi}{dz}(z) = \frac{c}{H(z)}. \quad (4.26)$$

In Fig. 4.7 we plot the fractional error made when using equation (4.25),

$$\frac{a_0 \Delta \chi'_2}{a_0 \chi'_2} = \frac{a_0 \chi'_{A2} - a_0 \chi'_2}{a_0 \chi'_2}, \quad (4.27)$$

against z_2 and α for object 1 at $z_1 = 3$ and for $q_0 = 0.15$. We see that the approximation gives both too large and too small distances (solid and dashed contours) depending on the position in the z_2 - α plane. Note the ‘ridges’ along which the approximation incidentally gives the correct distance.

The special case $\Delta z = 0$ deserves some further attention as it corresponds to the well-known angular diameter problem: what is the length, L , of a rod at z which

subtends an angle α as seen from Earth? Commonly, the answer is given as

$$L_A = \alpha r_A = \frac{\alpha a_0 \Sigma(\chi)}{1+z} \quad (4.28)$$

where r_A is the angular diameter distance. However, strictly speaking L_A is the length of the line $\chi = \text{const}$ connecting the two ends of the rod at the epoch z , which is *not* the shortest distance between the ends. The length of the geodesic connecting the two ends is given by $a\chi'_2$ which we can derive from equation (4.7). Setting $\chi_1 = \chi_2 = \chi$ and $z_1 = z_2 = z$ we arrive at

$$L = a\chi'_2 = \frac{a_0}{1+z} 2 \Sigma^{-1} \left[\Sigma(\chi) \sin \frac{\alpha}{2} \right]. \quad (4.29)$$

The fractional error made when using equation (4.28), $\frac{\Delta L}{L} = \frac{L_A - L}{L}$, is of course the same as in (4.25) for $\Delta z = 0$ since the extra factor $(1+z)$ cancels out. However, comparing equations (4.28) and (4.29) it is particularly easy to see that approximations such as (4.25) actually contain two approximations: (a) small angle and (b) neglect of curvature (for $k = \pm 1$). For example, $\frac{\Delta L}{L}$ is independent of z in the flat case but is larger and varies with z for the open case.

Chapter 5

The (foreground) proximity effect

5.1 Introduction

The study of many physical processes at high redshift requires knowledge of the intensity of the UV background radiation, J . For example, it is thought that the Ly α forest in QSO absorption spectra is caused by highly photo-ionized gas and thus an estimate of the total mass content of the intergalactic medium (IGM) depends on J (Rauch et al. 1997; Weinberg et al. 1997). It is also one of the parameters that define the environment in which galaxies form (e.g. Susa & Umemura 2000), and its value and evolution provide important constraints on the objects believed to be the origin of the background (e.g. Bechtold et al. 1987; Haardt & Madau 1996). At high redshift, the background is often measured from the proximity effect, i.e. the observed underdensity of Ly α forest absorption lines in the vicinity of background QSOs.

Nearly 20 years ago Carswell et al. (1982) first noted that the mean density of Ly α absorption lines seemed to increase with redshift when comparing the spectra of several different QSOs and yet decrease along individual lines of sight. Murdoch et al. (1986) confirmed this ‘inverse effect’, established that it was confined to the vicinity of the QSO (hence ‘proximity effect’) and offered two possible explanations: i) the absorbers near a QSO may be too small to fully cover the continuum emitting

region or ii) absorbers in the vicinity of a QSO may be more highly ionized than elsewhere due to the QSO's UV radiation.

Carswell et al. (1987) first used the second explanation to derive rough estimates of the intensity of the UV background at the Lyman limit, J . In a seminal paper Bajtlik, Duncan, & Ostriker (1988) (hereafter BDO) explored this possibility in detail. They developed a quantitative ionization model and, for the first time, measured J from the observed underdense absorption near 19 QSOs and their observed luminosities. Using a substantially larger sample Lu, Wolfe, & Turnshek (1991) confirmed this measurement and found no evidence to support alternative explanations for the proximity effect. Espey (1993) subsequently used the same data to quantify the effect of underestimating QSO redshifts on measurements of J from the proximity effect.

Bechtold (1994) investigated possible correlations of the proximity effect with redshift, optical/UV luminosity and radio power and found only a marginal correlation with luminosity. Nevertheless, these results qualitatively further supported the hypothesis that the proximity effect was due to the extra UV flux in the vicinity of a QSO rather than some other property of a QSO or its environment. In the most comprehensive intermediate resolution study to date Scott et al. (2000) analysed a sample of 74 spectra. Like Bechtold (1994), they divided their sample into low and high luminosity subsamples and found that the relative deficit of absorption lines within $1.5 h_{75}^{-1}$ Mpc of the background QSOs was more significant in the latter.

Following up on earlier work (Giallongo et al. 1993; Cristiani et al. 1995), Giallongo et al. (1996) studied the proximity effect at high spectral resolution. They assembled a sample of 10 high resolution spectra and, estimating the intensity of the background and the parameters of the Ly α absorption line distribution simultaneously, they found a somewhat lower value of J than most previous studies (cf. Fig. 5.1). On the other hand, Srianand & Khare (1994) found no evidence of the proximity effect at all. In their thorough analysis of 11 high resolution spectra Cooke, Espey, & Carswell (1997) gave a detailed account of the various statisti-

cal and systematic errors and biases involved in the measurement of J from the proximity effect. Like previous authors they found no evidence to suggest that the background intensity evolved with redshift.

We summarize these and other measurements of J in Fig. 5.1. It is worth noting that not all the points in this plot are independent of one another. There are large overlaps in the data used. For example, Q0014+813 is included in eight of these studies. In addition, all except one of these measurements are based on ‘line counting’, i.e. the statistics of individual absorption lines. Only Lu et al. (1996) considered the integrated absorption in 100 Å bins and Zuo (1992) obtained a rough estimate of J from W^{-1} correlations (where W is the rest equivalent width) and Møller & Kjærgaard (1992) used a basic flux statistics approach to investigate the foreground proximity effect. Thus no alternative methods seem to have been explored in any detail.

Most authors have found good agreement between their data and the ionization model of BDO and alternative explanations for the proximity effect have not received much observational support. The sizes of Ly α absorbers inferred from observations of close QSO pairs (e.g. Dinshaw et al. 1998 and references therein) seem to rule out the possibility that the absorbers are too small to completely cover the background QSO. In addition, Lu, Wolfe, & Turnshek (1991) found no difference between the W distribution of lines near QSOs and that of lines far from QSOs. They also eliminated a broken power law for the redshift distribution of lines as a possible cause for the proximity effect.

Thus increased ionization due to the extra UV flux from the QSO seems to remain as the only credible explanation for the proximity effect. However, it implies two observable effects:

1. The proximity effect should correlate with QSO luminosity. More luminous QSOs should deplete larger regions more thoroughly than less luminous ones. BDO claimed that this effect was present in their data and that it was consistent with the expectations from their ionization model. Bechtold (1994) and Scott et al. (2000)

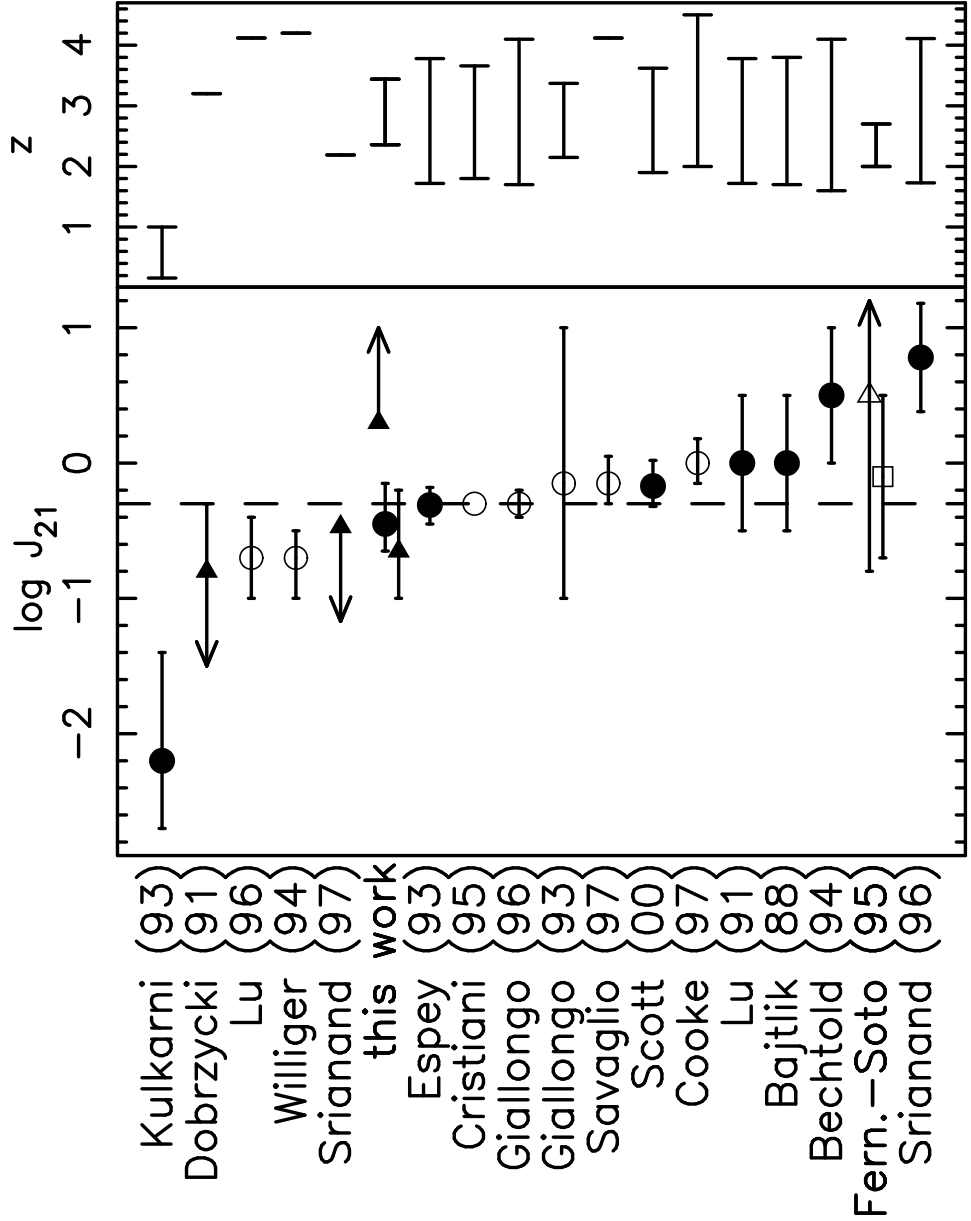


Figure 5.1: Summary of previous proximity effect measurements of the mean background Lyman limit intensity, J , in units of 10^{-21} ergs s^{-1} cm^{-2} Hz^{-1} sr^{-1} . Solid and open symbols represent measurements from intermediate and high resolution data respectively. Estimates from the background (foreground) proximity effect are shown as circles (triangles), those that include both are shown as squares. Error bars are 1σ . The dashed line marks the value of J at $z = 2.5-3$ computed by Haardt & Madau (1996) for a background dominated by the observed QSO population and for a $q_0 = 0.1$ cosmology. The top panel shows the redshift intervals covered by the various studies.

also found a weak correlation. Lu, Wolfe, & Turnshek (1991) on the other hand found no evidence for a correlation at all but nevertheless concluded on the basis of simulations that this was consistent with the ionization model. Srianand & Khare (1996) could not identify a correlation either.

2. In addition to the ‘classical’ background proximity effect there should be a foreground proximity effect where the absorbing gas along the line of sight to a background QSO is depleted by the UV radiation of a close-by foreground QSO. Studying a triplet of QSOs separated by 2 to 3 arcmin Crofts (1989) found no evidence for the existence of the foreground proximity effect. Møller & Kjærgaard (1992) added another spectrum to this triplet and confirmed the negative result. Dobrzycki & Bechtold (1991) observed a ~ 10 Mpc void in the spectrum of Q0302–003 with a foreground QSO separated from its line of sight by 17 arcmin. However, the foreground QSO was displaced from the void by $\sim 3600 \text{ km s}^{-1}$, implying either that the QSO radiates anisotropically or that it turned on on a time-scale comparable to the light travel time from the QSO to the void. Fernández-Soto et al. (1995) studied three QSO pairs separated by 3.8 to 12.6 arcmin but they were unable to reject the non-existence of the effect by more than $\sim 1\sigma$. Finally, Srianand (1997) reported a ~ 7 Mpc void in the spectrum of Tol 1038–2712 with a foreground QSO at the redshift of the void and separated by 17.9 arcmin. Like Dobrzycki & Bechtold he showed that it was unlikely that the void was a chance occurrence. Thus there currently exists only a single example where an underdensity of absorption lines in the spectrum of a background QSO can be explained by the presence of a foreground QSO without making extra assumptions.

The main goals of this chapter are to introduce a new method to analyse QSO spectra for the proximity effect and to address the two problems described above. The data used in this investigation were already introduced in Section 3.2. They consist of the spectra of a close group of 10 QSOs which have not been included in any previous studies. Thus the analysis presented here is independent from others in the sense that it uses both a different method as well as different data. In

Section 5.4 we measure J from the classical proximity effect and demonstrate its correlation with QSO luminosity. In Section 5.5 we turn to the foreground proximity effect. Finally, we consider a range of uncertainties in Section 5.6 and discuss our results in Section 5.7.

Unless explicitly stated otherwise we use $q_0 = 0.5$, $\Lambda = 0$ and $H_0 = 100 h \text{ km s}^{-1} \text{ Mpc}^{-1}$ throughout this chapter.

5.2 The data

The spectra used in this chapter are identical to those of Chapter 3 (see Section 3.2). Again, we would like to point out that all observations and data reduction were performed by Williger et al. (1996).

A search of the literature revealed seven additional QSOs in the field of the original set of ten QSOs and in the appropriate redshift range. These will be considered as potential foreground ionizing sources. The angular separations range from 6.1 to 95.8 arcmin and the emission redshifts range from 2.18 to 3.44. The distribution of all of these QSOs in the sky is shown in Fig. 5.2.

Since absolute spectrophotometry was not available for any of these QSOs we had to estimate continuum flux densities from observed B -band magnitudes. Assuming a power law continuum $f_\nu \propto \nu^\alpha$ the observed flux density f_ν at observed wavelength λ is given by

$$f_\nu(\lambda) = \left[\frac{\lambda_X}{\lambda(1+z_Q)^{-1}} \right]^\alpha (1+z_Q) 10^{-0.4(m_X - k_X)} f_{\nu X}(0) \quad (5.1)$$

where λ_X , m_X , k_X and $f_{\nu X}(0)$ are the central wavelength, observed magnitude, K -correction and 0-magnitude flux (Allen 1991) of the X -band respectively. For $X = V$ and $\alpha = -0.6$ this equation gives a flux 1.6 times higher than Tytler's (1987) empirical formula. However, note that Tytler used the K -corrections of Evans & Hart (1977) whereas we use the K -corrections given by Cristiani & Vio (1990) because they extend beyond $z = 2.5$. For some QSOs continuum slopes were

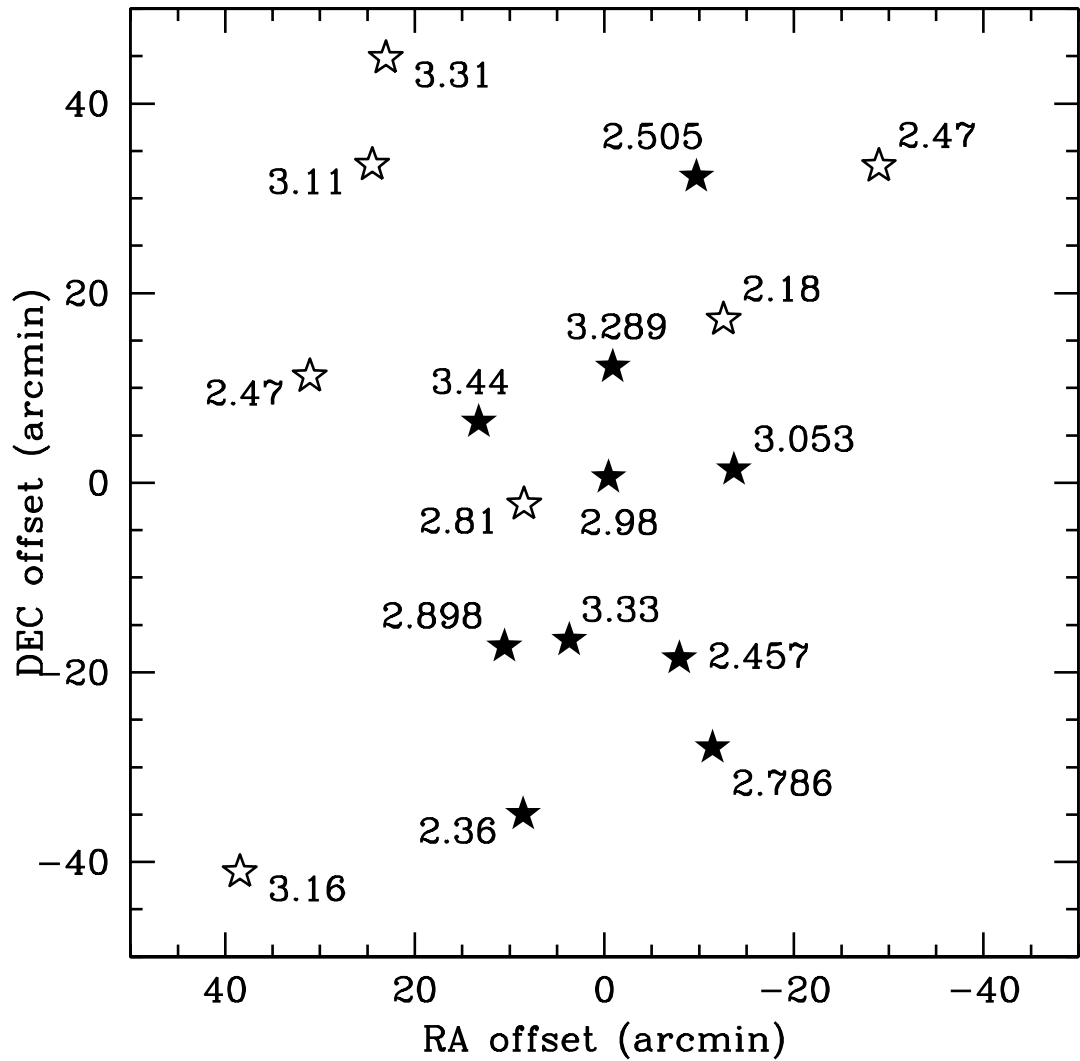


Figure 5.2: Distribution of QSOs in the sky. The field is centered on $\alpha = 00^{\text{h}}42^{\text{m}}10^{\text{s}}$ and $\delta = -26^{\circ}40'$ (B1950). Solid stars mark the positions of the QSOs whose spectra are analysed in this chapter. Empty stars mark the positions of additional foreground QSOs in the field. Emission redshifts are indicated.

not available. In these cases we used $\alpha = -0.6$ which is similar to the value of -0.5 given by Francis (1993).

We correct the above flux value for Galactic extinction by applying a correction factor $10^{0.4A(\lambda)}$ where

$$A(\lambda) = R_V E(B - V) \frac{A(\lambda)}{A(V)}. \quad (5.2)$$

We use $R_V = A(V)/E(B - V) = 3.1$ which is the average value for the diffuse interstellar medium (Clayton & Cardelli 1988). The variation of the extinction with wavelength relative to that at V , $A(\lambda)/A(V)$, is given by O'Donnell (1994) (optical) and Cardelli, Clayton, & Mathis (1989) (UV). $E(B - V)$ is taken from the dust map of Schlegel, Finkbeiner, & Davis (1998). This procedure is equivalent to first correcting m_B for Galactic extinction and then applying a correction to α due to the wavelength dependence of the extinction.

Gaskell (1982) first pointed out that QSO redshifts measured from high ionization emission lines like Ly α or C IV are systematically lower than redshifts measured from lower ionization lines like Mg II or the Balmer series which are thought to indicate the systemic redshifts. When estimating J from the classical proximity effect using QSO redshifts derived from high ionization lines, the result will be too high because the lower QSO redshift implies a higher QSO flux at a given cloud and therefore (for the same observed effect) a higher background. Espey (1993) showed that a velocity shift of $\sim 1500 \text{ km s}^{-1}$ lowered the value of J from $\log J = -20.75$ to -21.30 in Lu, Wolfe, & Turnshek's (1991) data.

The redshifts of the QSOs considered in this chapter were all determined from high ionization lines. However, since there is considerable disagreement in the literature over the values of the line shifts and possible correlations with QSO luminosity and/or emission line properties (e.g. Tytler & Fan 1992 and references therein), it is difficult to reliably correct for this effect. We shall therefore resort to determining J as a function of line shift in Section 5.4.2.

In Table 5.1 we list the redshifts, B -band magnitudes, continuum slopes and Lyman limit luminosities (equations 5.1 and 5.6) of all the QSOs considered.

Table 5.1: QSOs used in the analysis.

Object	z_Q	m_B^a	α	$L_\nu(912)^b$	Refs.
Q0041–2607	2.505	17.23	−0.60	15.01	1, 2
Q0041–2638	3.053	18.35	−0.53	12.17	1, 2
Q0041–2658	2.457	18.70	−0.88	2.34	1, 2
Q0041–2707	2.786	18.03		10.14	1, 2
Q0042–2627	3.289	18.55		13.29	1, 2
Q0042–2639	2.98	20.05	−0.09	4.59	3
Q0042–2656	3.33	19.55	−0.80	4.11	3
Q0042–2657	2.898	18.78		5.88	1, 2
Q0042–2714	2.36	19.88		1.09	4, 2, 5
Q0043–2633	3.44	19.61	−0.77	5.01	3
Additional foreground QSOs:					
Q0040–2606	2.47	19.48		1.80	4, 2
Q0041–2622	2.18	19.28		1.69	4, 2, 5
Q0042–2642	2.81	20.60	−1.40	0.28	3
Q0043–2555	3.31	20.53	−0.89	1.43	3
Q0043–2606	3.11	20.37	−0.96	1.07	3
Q0044–2628	2.47	19.28		2.18	4, 2, 5
Q0044–2721	3.16	20.17	−0.45	3.05	3

^aThe typical error on m_B is 0.15.

^bIn units of $10^{30} h^{-2} \text{ ergs s}^{-1} \text{ Hz}^{-1}$.

References: (1) Redshifts and B_J magnitudes from Hewitt, Foltz, & Chaffee (1995). Where given, continuum slopes were measured from low resolution spectra kindly provided by Paul Francis.

(2) We converted from B_J to Johnson B using the colour equation of Blair & Gilmore (1982) and assuming $(B - V) = 0.3$.

(3) Warren, Hewitt, & Osmer (1991). Conversion to B magnitudes using the colour equation of Warren et al. (1991).

(4) Drinkwater (1987).

(5) Redshifts from Williger et al. (1996).

5.3 Analysis

5.3.1 Method

Essentially, we use the method of Chapter 2 to look for regions of underdense absorption (i.e. ‘voids’) in Ly α forest spectra near the positions of suspected sources of ionizing radiation. These sources may be the background QSOs themselves or foreground sources near the line of sight to the background QSOs. The technique does not rely on investigating variations of the number density of individual absorption lines but rather uses the statistics of the transmitted flux directly. Thus it elegantly sidesteps all problems related to the incompleteness of lines due to limited spectral resolution and signal-to-noise, W -limited versus N -limited samples (Chernomordik & Ozeroy 1993; Srianand & Khare 1996) and Malmquist bias (Cooke, Espey, & Carswell 1997).

As described in Section 2.2 we identify large-scale regions of underdense absorption by convolving a spectrum with a smoothing function in order to filter out the high frequency ‘noise’ of individual absorption lines. In this chapter we will use both Gaussian and top-hat smoothing functions and we denote the resulting transmission triangles by $G(\lambda, \sigma_s)$ and $T(\lambda, \sigma_s)$ respectively.

5.3.2 Incorporating local ionizing sources

In Section 2.2 we calculated the mean (equation 2.28) and the variance (equations 2.31 and 2.16) of the transmitted flux under the assumption that any Ly α forest spectrum can be represented by a collection of individual absorption lines whose parameters are distributed according to (3.1). In this chapter we will use the same values for the parameters of the distribution (3.1) as in Section 3.3, except that we now use $\gamma = 2.0$ (Williger et al. 2000).

In order to measure J it is necessary to extend our model of the transmitted flux to incorporate local fluctuations of the ionizing radiation caused by discrete sources. We adopt the simple ionization model of BDO which basically consists of

the assumption that the absorbing gas is highly photo-ionized so that an absorber's column density is inversely proportional to the incident ionizing flux. Thus in regions of enhanced ionizing radiation we must modify equation (3.1):

$$\frac{d^2\mathcal{N}}{dz dN} \propto (1+z)^\gamma N^{-\beta} [1 + \omega(z)]^{1-\beta}, \quad (5.3)$$

where

$$\omega = \frac{F_\nu(\lambda_{\text{LL}})}{4\pi J(z)}. \quad (5.4)$$

$F_\nu(\lambda_{\text{LL}})$ is the flux from the ionizing source (IS) received by the absorber at wavelength $\lambda_{\text{LL}} = 912 \text{ \AA}$ in the restframe of the absorber. The IS may be the background QSO itself or it may be a different, foreground QSO. The validity of equation (5.3) is subject to the limitation that the spectral shape of the background J below the Lyman limit is similar to that of the IS. This will be the case if the QSOs are the dominant contributors to the background, if the IGM is optically thin (see Espey 1993 for a discussion of the optically thick case) and if the emission from the IGM does not drastically alter the shape of the background (Haardt & Madau 1996).

F_ν may be calculated from

$$F_\nu(\lambda_{\text{LL}}) = \frac{L_\nu \left(\frac{\lambda_{\text{LL}}}{1+z'_{\text{IS}}} \right)}{4\pi r_{\text{L}}^2(z_a, z'_{\text{IS}})} (1 + z'_{\text{IS}}). \quad (5.5)$$

$r_{\text{L}}(z_a, z'_{\text{IS}})$ denotes the luminosity distance between the absorber and the IS which, in general, is a function of the absorber redshift, z_a , and the redshift of the IS as seen by the absorber, z'_{IS} . Since we will consider the foreground proximity effect, where the absorber does not lie along the line of sight to the IS, z'_{IS} is in turn a function of z_a, z_{IS} , and the angle α by which the absorber and the IS are separated on the sky. See Chapter 4 on how to calculate z'_{IS} and $r_{\text{L}}(z_a, z_{\text{IS}}, \alpha)$. Note the bandwidth correction factor $(1 + z'_{\text{IS}})$ which is usually ignored at this point. The intrinsic luminosity of the IS, L_ν , is related to the observed flux at the observed wavelength λ by

$$L_\nu \left(\frac{\lambda}{1+z_{\text{IS}}} \right) = f_\nu(\lambda) \frac{4\pi r_{\text{L}}^2(z_{\text{IS}})}{1+z_{\text{IS}}}, \quad (5.6)$$

where $r_L(z_{\text{IS}})$ is the luminosity distance from Earth to the IS. Thus we have

$$\omega(z_a, z_{\text{IS}}, \alpha) = \frac{f_\nu \left(\lambda_{\text{LL}} \frac{1+z_{\text{IS}}}{1+z'_a} \right)}{4\pi J(z_a)} \frac{1+z'_{\text{IS}}}{1+z_{\text{IS}}} \left[\frac{r_L(z_{\text{IS}})}{r_L(z_a, z_{\text{IS}}, \alpha)} \right]^2. \quad (5.7)$$

The above ionization model is easily incorporated into our transmission model. Because of equation (2.8) the modification (5.3) implies

$$B \rightarrow B(z_a) = B [1 + \omega(z_a, z_{\text{IS}}, \alpha)]^{1-\beta}. \quad (5.8)$$

It is unlikely that we will be able to constrain the redshift evolution of the background with the present sample as previous studies of similar size but larger redshift coverage have been unable to do so (Cooke, Espey, & Carswell 1997; Giallongo et al. 1996). However, the background is expected to peak smoothly in the redshift range covered here (Haardt & Madau 1996) and the near constancy of J at $z > 2$ has been supported by the consistency of simulations with the redshift evolution of the Ly α forest (Davé et al. 1999). For these reasons we assume $J(z) = \text{const.}$

5.3.3 Further improvements

The inclusion of the proximity effect in our model renders one of the approximations of Chapter 2 in the derivation of equations (2.28) and (2.31) invalid. There we used the fact that the mean (and the variance) of the transmitted flux, $\langle e^{-\tau} \rangle = \exp[-B(\lambda/\lambda_\alpha)^{\gamma+1}]$, is approximately linear in λ over the scales of interest, so that, e.g.,

$$\langle G \rangle(\lambda, \sigma_s) = \frac{1}{\sqrt{2\pi} \sigma_s} \int \langle e^{-\tau} \rangle(\lambda') \exp \left[-\frac{(\lambda - \lambda')^2}{2\sigma_s^2} \right] d\lambda' \simeq \exp \left[-B \left(\frac{\lambda}{\lambda_\alpha} \right)^{\gamma+1} \right]. \quad (5.9)$$

Because of the introduction of ω , approximations like the one above are no longer valid and we must now carry out all convolutions explicitly:

$$\begin{aligned} \langle G \rangle_J(\lambda, \sigma_s) &= \frac{1}{2\pi \sigma_{\text{LSF}} \sigma_s} \iint \exp \left[-B(z) \left(\frac{\lambda''}{\lambda_\alpha} \right)^{\gamma+1} \right] \\ &\times \exp \left[-\frac{(\lambda' - \lambda'')^2}{2\sigma_{\text{LSF}}^2} \right] \exp \left[-\frac{(\lambda - \lambda')^2}{2\sigma_s^2} \right] d\lambda'' d\lambda' \end{aligned} \quad (5.10)$$

and

$$\sigma_{GJ}^2(\lambda, \sigma_s) = \frac{1}{\sqrt{2\pi} \hat{\sigma}_s} \int \left[\frac{\sigma_n^2(\lambda')}{2\sqrt{\pi} \sigma_s/p_s} + \frac{\sigma_{e^{-\tau}}^2(\lambda')}{\sqrt{2\frac{\sigma_{\text{LSF}}^2 + \sigma_{\text{LSF}}^2}{q^2(\lambda')} + 1}} \right] \times \exp \left[-\frac{(\lambda - \lambda')^2}{2\hat{\sigma}_s^2} \right] d\lambda', \quad (5.11)$$

where $\hat{\sigma}_s = \sigma_s/\sqrt{2}$.

When investigating the classical proximity effect it will be helpful to use a top-hat smoothing function rather than a Gaussian because we are working at the ‘edge’ of the data. The equivalent of equations (5.10) and (5.11) are given by

$$\begin{aligned} \langle T \rangle_J(\lambda, \sigma_s) &= \frac{1}{\sqrt{2\pi} \sigma_{\text{LSF}} 2\sigma_s} \int_{\lambda-\sigma_s}^{\lambda+\sigma_s} \int \exp \left[-B(z) \left(\frac{\lambda''}{\lambda_\alpha} \right)^{\gamma+1} \right] \\ &\times \exp \left[-\frac{(\lambda' - \lambda'')^2}{2\sigma_{\text{LSF}}^2} \right] d\lambda'' d\lambda' \end{aligned} \quad (5.12)$$

and

$$\begin{aligned} \sigma_{TJ}^2(\lambda, \sigma_s) &= \frac{1}{2\sigma_s} \int_{\lambda-\sigma_s}^{\lambda+\sigma_s} \left[\frac{\sigma_n^2(\lambda')}{2\sigma_s/p_s} + \frac{\sigma_{e^{-\tau}}^2(\lambda')}{\sqrt{2\frac{\sigma_{\text{LSF}}^2 + \sigma_{\text{LSF}}^2}{q^2(\lambda')} + 1}} \right. \\ &\times \left. \frac{2}{2\sigma_s} \int_0^{2\sigma_s-2|\lambda-\lambda'|} \exp \left(-\frac{\lambda''^2}{2[2\sigma_{\text{LSF}}^2 + q^2(\lambda')]} \right) d\lambda'' \right] d\lambda'. \end{aligned} \quad (5.13)$$

As one approaches the background QSO in the classical proximity effect the flux from the QSO increases and $B(z)$ decreases. Thus very close to the QSO the model predicts a mean transmission of almost 1 and a variance of almost 0. This is clearly unphysical as absorption lines with $z_a \approx z_Q$ and even with $z_a \gtrsim z_Q$ are frequently observed. One of the reasons for this observation may be that absorbers have peculiar velocities (Srianand & Khare 1996; Loeb & Eisenstein 1995). We accommodate peculiar velocities by convolving $B(z_a)$ with a Gaussian of width 300 km s^{-1} .

We determined the normalisation constant B directly from the data. First, we excluded all spectral regions with $\omega \geq 0.1$ from background QSOs, assuming a fiducial value of $\log J = -21.0$. For the present sample, the average size of the excluded regions translates to 5000 km s^{-1} . For the remainder of each spectrum we

then computed $T(\sigma_{s,\max})$ where $\sigma_{s,\max}$ is the largest possible smoothing scale. To these we then fitted our absorption model with B as a free parameter.

5.4 Results on classical proximity effect

5.4.1 Significance

With an absorption model and all its parameters in place we can proceed by transforming the transmission triangle of a given spectrum, $T(\lambda, \sigma_s)$, to a ‘reduced transmission triangle’ (RTT) by

$$RT_J(\lambda, \sigma_s) = \frac{T - \langle T \rangle_J}{\sigma_{TJ}}. \quad (5.14)$$

The reduced triangle has the mean redshift evolution of the absorption removed and shows the residual fluctuations of the Ly α transmission around its mean in terms of their statistical significance. When neglecting the proximity effect in the calculation of $\langle T \rangle$ (i.e. $J = \infty$), its presence in the data should be revealed by a region of $RT_\infty > 0$ near the red edge of the triangle.

We can consider the entire dataset at once in a compact manner by constructing a combined RTT: we first shift the spectra into the restframes of the QSOs, construct their transmission triangles and then average them where they overlap. Since different lines of sight are uncorrelated the variance of this composite is essentially just σ_T^2/n , where n is the number of spectra used. Thus at rest wavelength λ_r and at restframe smoothing scale σ_{sr} we have

$$\begin{aligned} RT_\infty(\lambda_r, \sigma_{sr}) &= \frac{1}{n} \sum_{i=1}^n \{T_i[(1 + z_{Q_i})\lambda_r, (1 + z_{Q_i})\sigma_{sr}] \\ &\quad - \langle T \rangle_{J=\infty}[(1 + z_{Q_i})\lambda_r, (1 + z_{Q_i})\sigma_{sr}]\} \\ &\quad \times \left[\frac{1}{n^2} \sum_{i=1}^n \sigma_{TJ=\infty}^2[(1 + z_{Q_i})\lambda_r, (1 + z_{Q_i})\sigma_{sr}] \right]^{-\frac{1}{2}}, \quad (5.15) \end{aligned}$$

where T_i and z_{Q_i} are the measured transmission and redshift of the i th QSO and we use $J = \infty$ in the calculation of $\langle T \rangle$ and σ_T .

The most significant ‘void’ in this combined RTT lies at $(\lambda_r, \sigma_{sr}) = (1208.6 \text{ \AA}, 3175 \text{ km s}^{-1})$, two pixels away from the red edge of the triangle where one would expect a signature from the proximity effect. It is significant at a level of $5.2\sigma_T$. Excluding each of the individual spectra from the composite in turn results in the significance of the feature varying from $4.2\sigma_T$ to $6.2\sigma_T$, so that the effect is not dominated by any single spectrum although there seems to be some variation in the strength of the effect among the individual spectra. This will be investigated in more detail in Section 5.4.3.

In this context it is helpful to ask what sort of signal one would expect from the data if the ionization model of Section 5.3.2 were correct. In the next section we will answer this question in detail with the help of simulations but one can already gain a useful estimate by simply maximising the expectation value of equation (5.15),

$$\langle RT_\infty \rangle(J) = \frac{\frac{1}{n} \sum_{i=1}^n [\langle T \rangle_J - \langle T \rangle_{J=\infty}]}{\left[\frac{1}{n^2} \sum_{i=1}^n \sigma_{TJ=\infty}^2 \right]^{\frac{1}{2}}}, \quad (5.16)$$

with respect to (λ_r, σ_{sr}) . For example, for $J_{21} = 1$ (where $J_{21} = J \times 10^{21} \text{ ergs s}^{-1} \text{ cm}^{-2} \text{ Hz}^{-1} \text{ sr}^{-1}$) we find a maximum of $5.0\sigma_T$. Note that the expected significance of the signal is not so much a function of the data quality but rather of the number of spectra included in the analysis, since the variance of the transmission is dominated by the ‘noise’ of individual absorption lines.

An alternative explanation for the observed ‘void’ would be a systematic overestimation of the QSO redshifts. In this case we would expect to see an effect similar to the one observed because we would be including parts of the spectra in our analysis which correspond to regions physically behind the QSOs and thus would show much less absorption than expected. Note, however, that the redshifts of the QSOs were determined from high ionization lines and are thus expected to be too low, as discussed in Section 5.2, and not too high.

We conclude that we have detected a proximity effect at a significance level of > 99 per cent.

5.4.2 Measurement of J

The seemingly most straightforward way to derive an estimate of J would be to directly fit our absorption model to the observed composite transmission triangle with J as a free parameter. Fitting the transmission triangle rather than just the spectra has the advantage of ensuring that the model fits *on all scales*. In the previous section we saw that the data deviate most significantly from a no proximity effect model at a scale of $\sim 3000 \text{ km s}^{-1}$. On the smallest smoothing scale the strongest deviation is only $3\sigma_T$. Thus we can anticipate that by considering all scales we may derive tighter constraints on J . However, the pixels of a transmission triangle are strongly correlated with one another and thus one would need to specify the entire covariance matrix in order to judge the quality of a fit. Instead we will use a much simpler yet effective approach which consists of considering only the most significant positive and negative deviations of the model from the data as a function of J .

We implement this approach by searching for the most significant local extrema of an RTT in the region most likely to be affected by the proximity effect. A local maximum (minimum), LMAX (LMIN), is defined as any pixel in the RTT with $RT_J > 0$ ($RT_J < 0$) and where all adjacent pixels have smaller (larger) values. If there is more than one LMAX (LMIN) in a given wavelength bin (but at different smoothing scales) only the most significant one is considered.

We then define the search region as all those pixels in the RTT for which $\langle RT_\infty \rangle(J)$ is larger than some threshold value η . We begin by setting $\eta = 1.0 \sigma_T$ and search for the most significant LMAX and LMIN in this region. If none are found we increase the size of the search region by decreasing η until the first LMAX (LMIN) has been found. Note that in order to calculate $\langle RT_\infty \rangle(J)$ we need to assume some value for J , which is precisely what we are trying to measure. However, starting with $J_{21} = 1$ the procedure converges after only two iterations. Even without iterating the above procedure ensures that the result does not depend sensitively on the exact value of J (within sensible limits) chosen to define the search region.

In Fig. 5.3 (main panel) we plot both the most significant positive and negative deviations of the model from the data detected in this way as a function of the value of J that was used in the construction of the RTT. The void discussed in the previous section is represented by the dot at $J = \infty$ (model with no proximity effect). For models with $\log J_{21} > 0.0$ the RTT of the data shows significant underdense absorption (i.e. maxima at $> 2\sigma_T$). On the other hand, for small values of J the model predicts too little absorption on smaller scales and the RTT of the data shows significant overdense absorption (i.e. significant minima) for models with $\log J_{21} < 0.1$. Thus there seems to be no value of J for which the model is entirely consistent with the data.

However, recall that we are considering the *maximally* deviant points. For the correct model, the expectation value of the difference between a randomly chosen data point and the model is 0. However, given the additional information of the data point's rank, this is no longer true. For example, the probability distribution function of the maximum of a set of n uncorrelated, normally distributed numbers is given by $P(x) = nG(x) [\int_{-\infty}^x G(x')dx']^{n-1}$, where G is the unit Gaussian. For $n > 1$ both the mode and mean of $P(x)$ are > 0 .

For an RTT the situation is more complicated, primarily because the numbers from which the extrema are chosen are correlated. In order to calculate an expectation value for the significance level of the extrema one would thus have to specify the covariance matrix which is exactly what we wanted to avoid. However, the expectation values of the extrema and their correlation are easily obtained from simulations.

We thus performed 1000 simulations of the dataset ($= 10^4$ spectra, hereafter S1) by randomly placing absorption lines according to the distribution (3.1) and using a constant S/N of 20. No proximity effect was included in the simulations. For each dataset we then constructed its RTT (using $J = \infty$) and found the most significant deviations of the model from the data. The mean significance levels of these 1000 maxima and minima are shown as the dashed lines in Fig. 5.3 and the $\pm 1\sigma$ regions

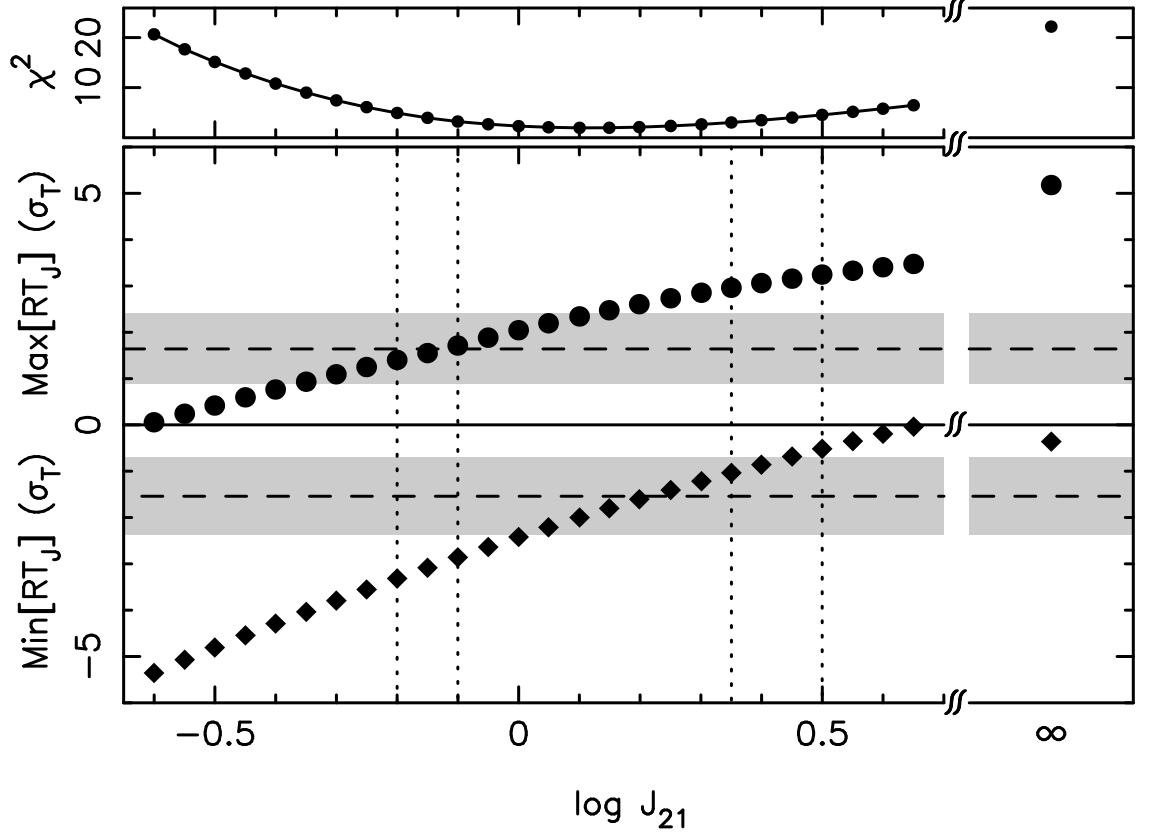


Figure 5.3: Main panel: most significant positive (dots) and negative (diamonds) deviations (in units of σ_T) of the absorption model from the data in the region most likely affected by the proximity of the QSOs as a function of the mean Lyman limit background intensity J . The dashed lines and the grey regions mark the expected and $\pm 1\sigma$ significance levels of these deviations in the case where they are due to random fluctuations (i.e. for the correct model), which were determined from 1000 simulated datasets. The absence of a proximity effect corresponds to $J = \infty$ and is strongly rejected. Top panel: χ^2 of the corresponding points in the main panel. The best fit is achieved for $\log J_{21} = 0.1$ with $\chi^2_{\min} = 1.98$. The inner and outer dotted lines in the main panel mark the formal 68 and 90 per cent confidence intervals respectively.

are shown in grey.

We determine the best fit value of J by calculating χ^2 in the top panel of Fig. 5.3 for each of the data points in the main panel. The best fit is achieved for $\log J_{21} = 0.1^{+0.4}_{-0.3}$, where the errors are the formal 90 per cent confidence limits (outer dotted lines in Fig. 5.3). With $\chi^2_{\min} = 1.98$ the fit is acceptable ($P(\geq \chi^2_{\min}) = 0.16$, where P is the χ^2 -distribution with one degree of freedom).

In order to check the error bars, the quality of the fit and the validity of the procedure as a whole, we performed a second set of 1000 simulations (S2). This time we included the proximity effect according to the ionization model of Section 5.3.2 with $\log J_{21} = 0.1$. Each of these datasets was analysed in the same manner as the real data, i.e. for each we constructed Fig. 5.3 and measured $\log J$. On average, the presence of the proximity effect is detected at the $5.2\sigma_T$ level. The mean of the 1000 $\log J$ measurements is 0.10, 65 per cent of the values lie within the range $-0.15 < \log J_{21} < 0.35$ and 86 per cent of the values lie within the range $-0.3 < \log J_{21} < 0.5$. Finally, the fraction of measurements with $\chi^2_{\min} \geq 1.98$ is 0.10. We thus conclude that our method works well and that the error and quality of fit estimates above are reliable.

Dependence on model parameters

Does the above result depend sensitively on any of the model parameters? Because of the transition (5.8) we must expect the result to depend on β . At a given J , a larger value of β increases the model transmission and thus decreases both the maxima and minima of Fig. 5.3, which will result in a larger measured value for J . For $\beta = 1.7$ and 1.3 we find $\log J_{21} = 0.6^{+0.3}_{-0.25}$ and $-0.45^{+0.45}_{-0.4}$ respectively. However, increasing β also has the effect of decreasing the model variance so that the maxima and minima of Fig. 5.3 move further apart, which decreases the goodness of fit. For $\beta = 1.7$ we find $\chi^2 = 10.1$ and thus the fit is no longer acceptable.

Since the redshift coverage of the present sample is not very large and because we determine the optical depth normalisation, B , directly from the data, our results

cannot depend sensitively on γ . To confirm this we repeated the above analysis for $\gamma = 2.5$ and found $\log J_{21} = 0.15_{-0.3}^{+0.35}$.

Cosmological parameters enter the analysis via the last factor in equation (5.7). h cancels out but the denominator is relatively less sensitive to q_0 than the numerator. For an open Universe this factor is larger than in the flat case and so a larger J will be measured. For $q_0 = 0.15$ we find $\log J_{21} = 0.15_{-0.3}^{+0.4}$ and thus our result does not depend sensitively on the cosmological model.

Emission line shifts

In Section 5.2 we already noted that the redshifts of the QSOs have probably been underestimated since they were determined from high ionization lines. Assuming that all the emission line redshifts are offset from their true systemic values by a velocity Δv to the blue we have repeated the above analysis as a function of Δv . In Fig. 5.4 we show our estimate of J for various values of Δv (dots, solid line). The reduction of J is very similar to that found by Espey (1993) (diamonds, dashed line). From similarly luminous QSOs Espey (1993) estimated the mean velocity shift for the Lu, Wolfe, & Turnshek (1991) QSOs to lie in the range $1300 \text{ km s}^{-1} < \Delta v < 1600 \text{ km s}^{-1}$ and estimated the true background intensity to be $\log J_{21} = -0.3_{-0.22}^{+0.2}$. For our sample of QSOs the Δv -luminosity relationship given by Cooke, Espey, & Carswell (1997) predicts $\Delta v \approx 800 \text{ km s}^{-1}$ which yields $\log J_{21} = -0.45_{-0.3}^{+0.4}$. These results are in good agreement with each other as well as with $\log J_{21} \approx -0.3$ at $z = 2.5\text{--}3$ computed by Haardt & Madau (1996) for a background dominated by the QSO population observed in optical surveys and a $q_0 = 0.1$ cosmology.

5.4.3 Variation with luminosity and redshift

Significance

In Section 5.4.1 we noted that the significance of the proximity effect varied somewhat when excluding individual spectra from the combined RTT. We now examine the proximity effect in individual spectra in order to test whether it is correlated

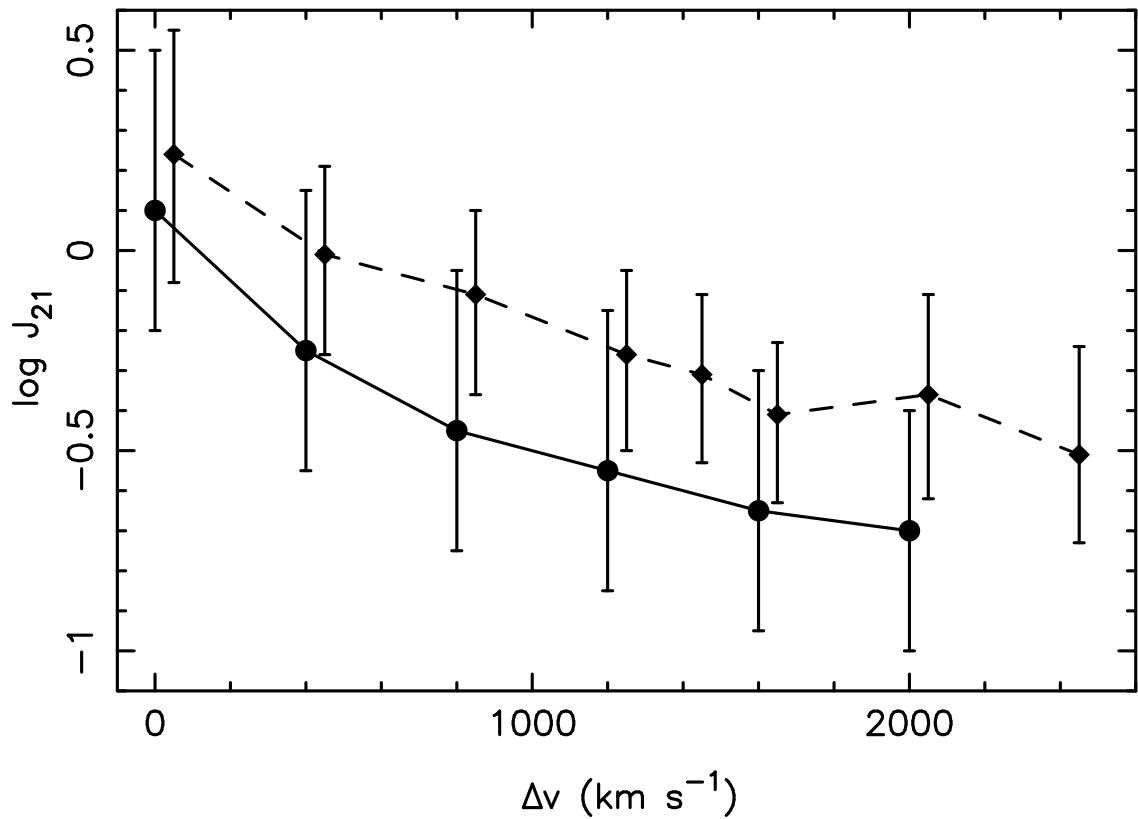


Figure 5.4: Estimated value of the mean Lyman limit background intensity, J , assuming that the measured high ionization emission line redshift of every QSO is smaller than the true systemic value by an amount Δv . Dots, solid line: this work. Diamonds, dashed line (offset by 50 km s^{-1} for clarity): Espey's (1993) analysis of Lu et al.'s (1991) data for comparison. Error bars are 90 per cent confidence limits.

with QSO Lyman limit luminosity or redshift. The former correlation would be expected if the proximity effect were due to the increased ionizing flux in the vicinity of QSOs and the latter if in addition J varied with redshift and/or the luminosities and redshifts of the QSOs were correlated.

We thus constructed the RTTs of the individual spectra (using $J = \infty$) and searched for the most significant positive deviations of the model from the data in the same way as described in Section 5.4.2. In other words, for each QSO we determined the significance of the proximity effect. In Fig. 5.5(a) we plot these maxima as solid dots against QSO Lyman limit luminosity (calculated from equation (5.6) and listed in Table 5.1). For comparison, we analysed two simulated datasets, S1 and S3, in exactly the same way. S1 was already introduced in Section 5.4.2 (no proximity effect model). S3 incorporates the proximity effect according to the ionization model of Section 5.3.2 with $\log J_{21} = -0.45$ and assumes that all QSO redshifts have been underestimated by $\Delta v = 800 \text{ km s}^{-1}$. Writing $M \equiv \text{Max}[RT_\infty]$, we plot as open circles the mean of M found in the 1000 simulated datasets that include the proximity effect (S3). The open squares are the same for the no proximity effect simulations (S1).

Previous authors have presented similar plots (e.g. BDO's Fig. 1) where they plotted the relative deficiency of absorption lines within some constant radius of the QSOs. One of the advantages of our method is that this radius is no longer constant but is rather allowed to vary in order to maximise the significance of the missing absorption.

Let us first examine correlations in the simulated data. For S1 there is clearly no correlation with luminosity which is as it should be. For S3 there seems to be a trend of increasing significance with increasing luminosity. However, the correlation does *not* seem to be as tight as one might expect and there seems to be no well defined relation between the two. Considering that these points are the mean of 1000 simulations this can hardly be due to random error. The only other parameter that varies from QSO to QSO in the simulations is the redshift. In Fig. 5.5(b) we

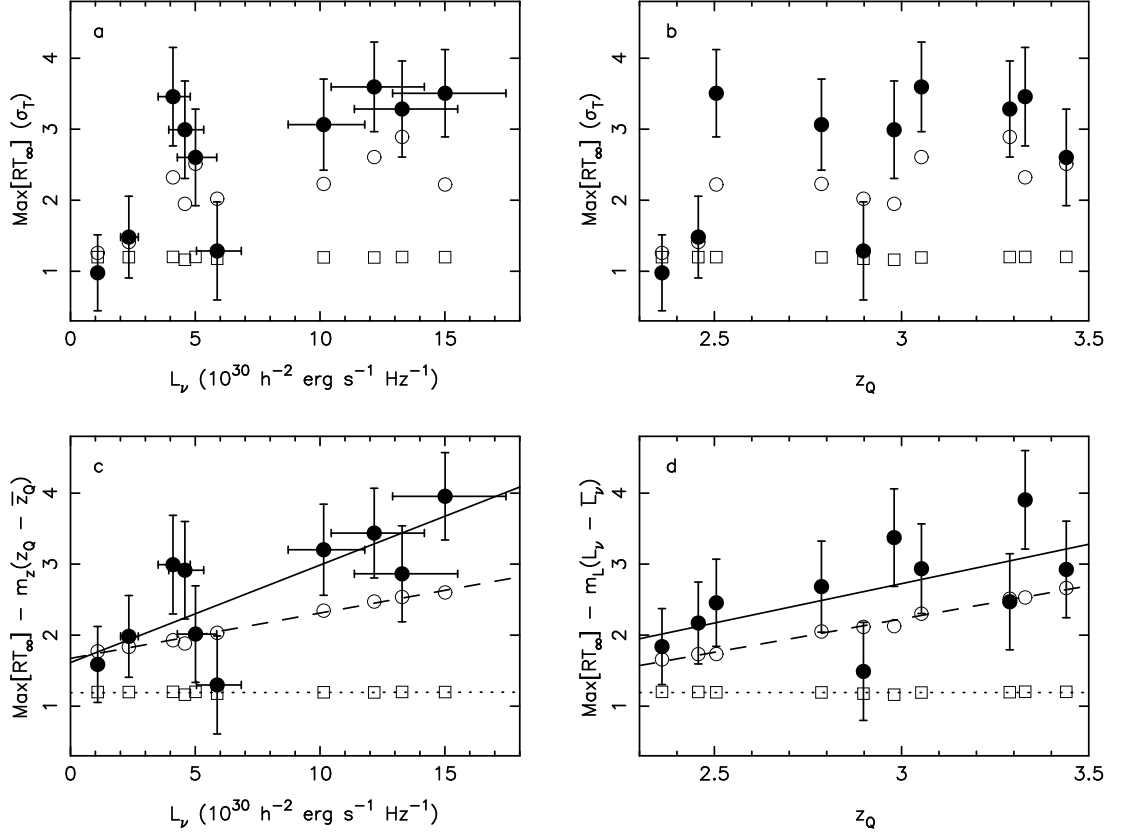


Figure 5.5: (a) Significance of proximity effect in individual QSOs versus QSO Lyman limit luminosity. Solid dots are the data. Open circles are the mean significance levels found in 1000 simulated datasets, where the simulations include a proximity effect according to the ionization model with $\log J_{21} = -0.45$ (S3). The vertical error bars on the data are the $\pm 1\sigma$ ranges found in these simulations. Open squares: same as open circles but with $J = \infty$ (no proximity effect, S1). (b) Same as (a) but now plotted against QSO redshift. (c) Same as (a) but all significance levels have been scaled to the mean redshift of the sample using equation (5.17) in order to isolate the effect of luminosity on the proximity effect. The solid, dashed and dotted lines show the best fit $f(L_\nu, \bar{z}_Q)$ for the data and the two sets of simulations respectively. (d) Same as (b) but all significance levels have been scaled to the mean luminosity of the sample using equation (5.17) in order to isolate the effect of redshift on the proximity effect. The solid, dashed and dotted lines show the best fit $f(\bar{L}_\nu, z_Q)$ for the data and the two sets of simulations respectively.

plot the significance levels against QSO redshift. Again, for S1 there is no trend. S3 exhibits the same sort of loose correlation as in Fig. 5.5(a). The luminosities and redshifts of the QSOs are not significantly correlated. Recall also that J does not vary with redshift in our simulations. Why then should there be a trend with redshift at all? The reason is that a given underdensity of absorption is more significantly detected when the ‘background’ absorption line density is higher than when it is lower (cf. Fig. 2.6). Thus a given QSO will have a more noticeable proximity effect at high redshift (where the line density is higher) than at low redshift, all else being equal.

We thus surmise that the lack of a well defined relation between the significance of the proximity effect, M , and luminosity for S3 in Fig. 5.5(a) is due to the variation in redshift of the QSOs and that M is a function of both luminosity *and* redshift even though the QSO luminosities and redshifts are not significantly correlated and J does not vary with redshift.

To demonstrate this behaviour we first fit M with the function

$$f(L_\nu, z_Q) = c + m_L L_\nu + m_z z_Q \quad (5.17)$$

and then scale the significance levels to the mean redshift, \bar{z} , and mean luminosity, \bar{L}_ν . The results are plotted in Figs. 5.5(c) and (d) respectively. In Fig. 5.6 we plot M against $m_L L_\nu + m_z z_Q$. We can now see that S3 exhibits almost perfect correlation with both luminosity and redshift and that the linear model (5.17) gives a reasonably good description of the simulations.

The discussion above implies that in order to properly disentangle possible correlations of the proximity effect with luminosity and redshift they should be determined jointly, not separately. We now investigate this effect in more detail.

First, we need to choose a correlation statistic. Previous authors have often used Spearman’s rank correlation coefficient. However, in our case it is reasonable to assume that M is approximately Gaussian distributed and this is indeed observed in the simulations. Therefore it is not necessary to restrict ourselves to a non-parametric test. In addition we have already shown that the linear model (5.17) gives

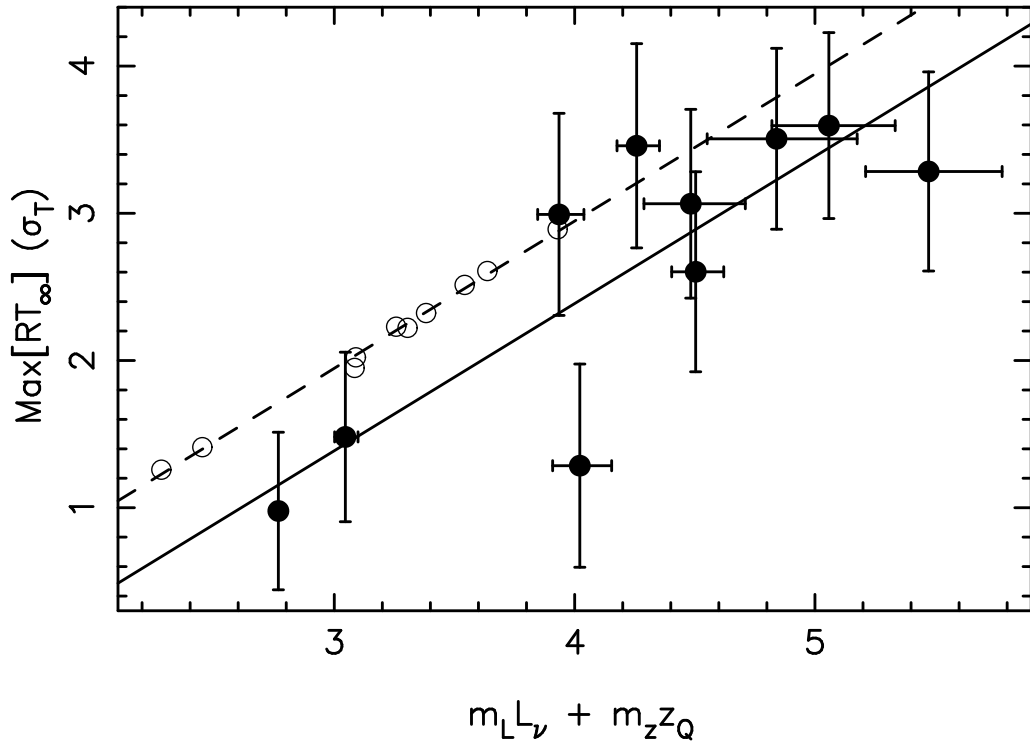


Figure 5.6: Significance of proximity effect in individual QSOs versus a linear combination of QSO Lyman limit luminosity and redshift. Symbols have the same meaning as in Fig. 5.5. The solid and dashed lines show the best fit $f(L_\nu, z_Q)$ for the data and S3 respectively. S1 is not shown because for these points the best fit slopes are $m_L \approx m_z \approx 0$.

a good description of the simulations and from Fig. 5.6 we can judge that it is also an acceptable model for the real data (see also Fig. 5.8c). It is therefore reasonable to use the slopes of a linear χ^2 fit as correlation measures. This also has the advantage that the arguments of the following paragraphs can be understood analytically. In any case, we found that these arguments are qualitatively reproduced when using Spearman's rank correlation coefficient.

The simplest thing we can now do is to determine the slopes for the M - L_ν and M - z_Q relations independently by fitting the functions

$$\begin{aligned} f_L(L_\nu) &= c_L + m'_L L_\nu \\ f_z(z_Q) &= c_z + m'_z z_Q \end{aligned} \quad (5.18)$$

to M . We have done this for the 1000 simulated datasets of both S1 and S3 as well as for the real data. The results are shown in Fig. 5.7(a). The shaded regions in the main panel are the 68 and 95 per cent confidence regions for S1, the contours are the same for S3 and the cross marks the result for the real data.

The first thing we notice is that the values of (m'_z, m'_L) measured in the real data are consistent with the ionization model, but they are inconsistent with the no proximity effect model at $> 3\sigma$. However, note that in the simulations m'_L and m'_z are not independent. Calculating Pearson's correlation coefficient we find

$$\rho(m'_L, m'_z) = \hat{\rho}(L_\nu, z_Q) = 0.14, \quad (5.19)$$

where $\hat{\rho}(L_\nu, z_Q)$ is the correlation coefficient between L_ν and z_Q for the 10 QSOs used here, not that of the parent population ($= \rho(L_\nu, z_Q)$) from which they were drawn, which may well be zero. Thus any measurement in the top right-hand part of the plot deviates from the no proximity effect hypothesis less significantly than what would have been inferred if the correlation between L_ν and z_Q had been neglected. Note that it is the actual numerical value of $\hat{\rho}$ that matters here and not whether or not it is consistent with $\rho(L_\nu, z_Q) = 0$.

What would we expect if the proximity effect were caused by some property, x , of the QSO or its environment unrelated to the QSO's UV flux (' x -model')? As for

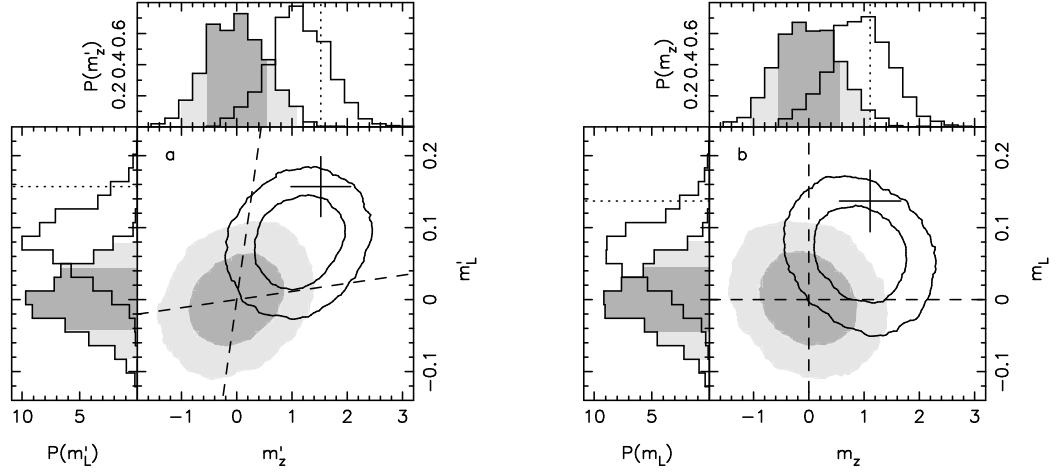


Figure 5.7: (a) The dark and light grey shaded regions show the 68 and 95 per cent confidence regions of (m'_z, m'_L) derived by independently fitting the significance of the proximity effect in the 1000 simulated datasets of S1 (no proximity effect) with (5.18). The contour lines are the same for S3 (ionization model). The cross marks the measured values and formal 1σ errorbars of (m'_z, m'_L) for the real data. The dashed lines correspond to the lines $m_z = 0$ and $m_L = 0$ in panel (b). The upper and left panels show the one-dimensional probability distributions of m'_z and m'_L respectively. The dark and light shaded regions in these panels are the one-dimensional 68 and 95 per cent confidence regions respectively. (b) Same as (a) for (m_z, m_L) , derived by fitting the significance of the proximity effect with (5.17).

the ionization model we would expect a correlation of M with z_Q because this is simply the effect of increasing absorption line density with increasing redshift. Since $\hat{\rho}(L_\nu, z_Q) \neq 0$ we therefore expect the centre of the shaded ellipses in Fig. 5.7(a) to move along the line

$$m'_L = m_L^z m'_z = \hat{\rho}(L_\nu, z_Q) \sqrt{\frac{V(z_Q)}{V(L_\nu)}} m'_z \quad (5.20)$$

(marked by a dashed lined), where V denotes the sample variance. Thus a measurement in the top right-hand part of the plot deviates less significantly from the x -model than what would have been inferred if the correlation between L_ν and z_Q had been neglected.

This complication can be avoided if we use (m_z, m_L) of equation (5.17) instead of (m'_z, m'_L) . Fig. 5.7(b) shows the result of fitting (5.17) to the simulations and the data. The relationship between Figs. 5.7(a) and (b) can be most easily understood by writing down the linear coordinate transformation which relates (m'_z, m'_L) and (m_z, m_L) as

$$\begin{pmatrix} m_z \\ m_L \end{pmatrix} = \frac{1}{1 - \hat{\rho}^2} \begin{pmatrix} 1 & -m_z^L \\ -m_L^z & 1 \end{pmatrix} \begin{pmatrix} m'_z \\ m'_L \end{pmatrix}. \quad (5.21)$$

We can now see that they are related by a Lorentz transformation followed by a stretch of $(1 - \hat{\rho}^2)^{-\frac{1}{2}}$ and that the line $m'_L = m_L^z m'_z$ is transformed to the line $m_L = 0$. Thus in this frame of reference we do not have to worry about $\hat{\rho}$ when asking whether the data is compatible with the x -model, except for the fact that we now have $\rho(m_L, m_z) = -\hat{\rho}(L_\nu, z_Q)$.

In Figs. 5.8(a), (b) and (c) we plot the distribution of minimum χ^2 values obtained from fitting (5.18) and (5.17) respectively. The shaded histogram (S1) follows the χ^2 -distribution quite well in all cases. However, both the real data (dotted line) and the ionization model (S3, solid histogram) are not well modelled by the independent fits (5.18).

Thus we conclude that the observed significance of the proximity effect is a linear function of both redshift and luminosity and is well described by a function of the form (5.17). This observed correlation with luminosity *and* redshift is inconsistent

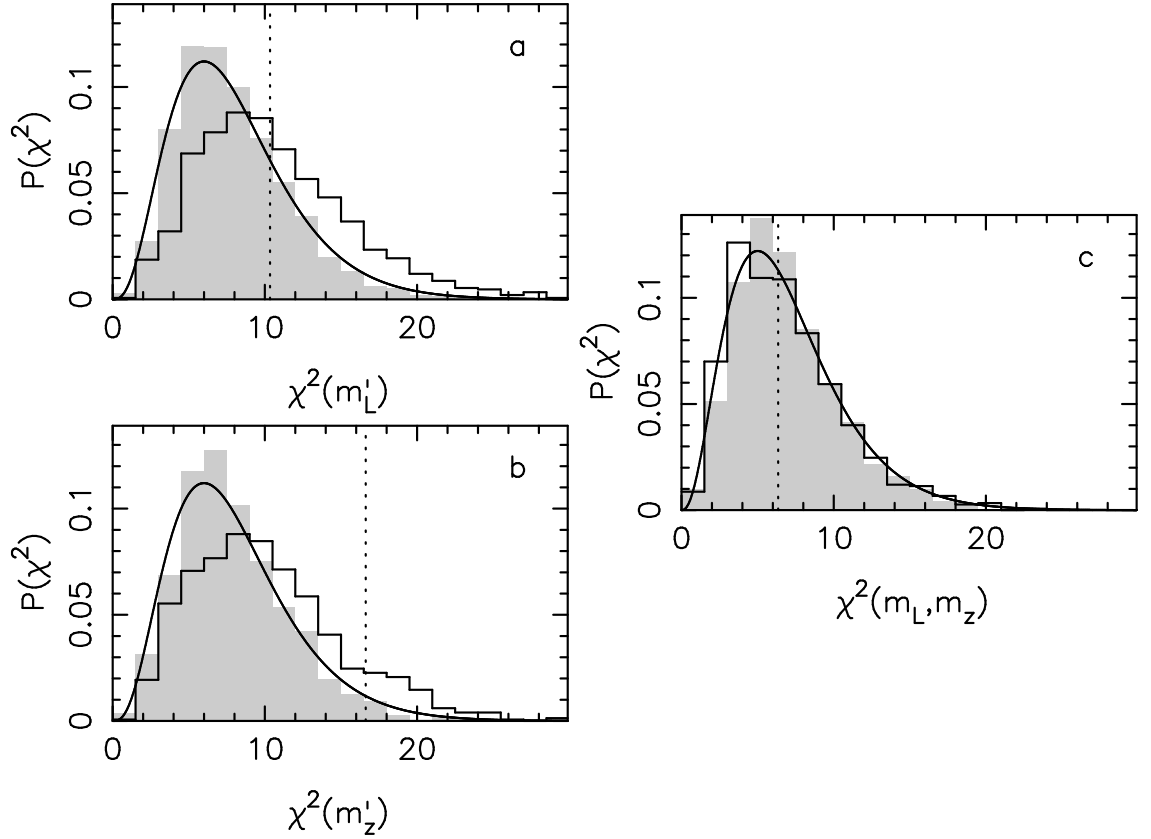


Figure 5.8: (a) The grey shaded histogram is the distribution of minimum χ^2 values obtained from fitting $f_L(L_\nu)$ (equation 5.18) to the 1000 simulated datasets of S1 (no proximity effect). The solid histogram is the same for S3 (ionization model). The dashed line marks the value of χ^2 for the real data. The smooth solid line shows the χ^2 -distribution for eight degrees of freedom. (b) Same as (a) for $f_z(z_Q)$. (c) Same as (a) and (b) for $f(L_\nu, z_Q)$ (equation 5.17). The solid line shows the χ^2 -distribution for seven degrees of freedom.

with the no proximity effect model at the 3.5σ level. A model that exhibits correlation with redshift but not luminosity is excluded at the 2.6σ level. These values take into account the correlation between L_ν and z_Q of the present dataset. If we had ignored this correlation we would have inferred 4.1σ and 3.2σ respectively.

The discussion above enables us to go one step further. Consider again the x -model. If x is indeed uncorrelated with L_ν for the general QSO population, i.e. $\rho(x, L_\nu) = 0$, then for our sample we would most likely find $\hat{\rho}(x, L_\nu) = 0$, which we have implicitly assumed in the previous discussion. However, $\hat{\rho}(x, L_\nu)$ may well be $\neq 0$, either because of random fluctuations or because $\rho(x, L_\nu) \neq 0$. This would induce a spurious correlation between M and L_ν . What value of $\hat{\rho}(x, L_\nu)$ is required so that the x -model is consistent with the data? Assuming $\hat{\rho}(x, z_Q) = 0$ we find that $\hat{\rho}(x, L_\nu)$ has to lie in the range

$$0.37 < \hat{\rho}(x, L_\nu) < 0.80 \quad (5.22)$$

in order to be consistent with the data at the 1σ level. Thus in the present dataset, the hypothetical property x would have to be noticeably correlated with luminosity.

Since we do not know the distribution from which x is drawn it is not possible to reliably estimate whether this result excludes the hypothesis that x and L_ν are not correlated in the parent population. However, assuming Gaussianity in both x and L_ν , we find that the most likely value of $\hat{\rho}(x, L_\nu) = 0.59$ excludes the hypothesis $\rho(x, L_\nu) = 0$ at the ~ 96 per cent confidence level (using Student's t -distribution).

By comparing the data with S3 in Fig. 5.7(b) it is apparent that the observed dependence of the proximity effect on redshift is entirely accounted for by the evolution of the number density of absorption lines and there is no evidence to suggest that J varies over the redshift range considered here. It is also apparent that this conclusion is not overly sensitive to our choice of γ , the evolutionary index of the absorption line density. On the other hand, the data do not exclude some (positive or negative) evolution either. In any case, if J is due to the known QSO population then it is expected to peak smoothly in the redshift range covered here (Haardt & Madau 1996) and thus one would not expect strong evolution.

Size

If the ionization model is correct one would in principle also expect the size of the region affected by the QSO's UV flux to be correlated with luminosity. We can test for this effect by noting the size of the smoothing function at which the maxima M of Fig. 5.5 were detected. However, in the simulations we find that the distribution of sizes is very broad and almost one-tailed and thus difficult to characterise. In addition the distributions for S1 and S3 overlap almost completely with only the peak moving to slightly larger values for S3. There is also some evidence that for the ionization model the distribution of sizes moves to larger values for larger luminosities but again the effect is small compared to the extent of the distribution. Thus we are forced to conclude that this is not a powerful test and simply note that the detected sizes in the real data range from ~ 500 to ~ 7000 km s $^{-1}$ and lie well within the 90 per cent confidence ranges of both S1 and S3 in all cases.

5.5 Results on foreground proximity effect

5.5.1 Existence of the effect

We now exploit the fact that the QSOs of Table 5.1 are a close group in the plane of the sky. Essentially, we repeat here the analysis of Section 5.4.1: for each pair of background QSO (BQSO) and foreground ionizing source (IS), we shift the spectrum of the BQSO into the restframe of the IS and construct its transmission triangle using $J = \infty$. We now use a Gaussian smoothing function because we are no longer working at the 'edge' of the data. We then average all the transmission triangles where they overlap, creating a composite RTT. Thus in equation (5.15) T_i still refers to the measured transmission of the BQSO (but is replaced by G_i because we now use a Gaussian smoothing function) and we replace z_{Q_i} with z_{IS_i} , where i now labels a BQSO-IS pair. If the foreground proximity effect exists, it should be more significant in this composite RTT than in any individual RTTs and is expected to appear as a region of $RG_\infty > 0$ near $\lambda_r = \lambda_\alpha$. From now on we exclude all

spectral regions within 5000 km s^{-1} of the BQSOs from the analysis in order not to contaminate our results with the background proximity effect.

Before we proceed we need to consider the following complication. For each BQSO-IS pair we can calculate $\omega_p = \omega(z = z_{\text{IS}}, z_{\text{IS}}, \alpha)$ (assuming $\log J_{21} = -0.45$, cf. equation 5.7). ω_p is the maximum value a given IS can achieve along the line of sight to a BQSO, separated on the sky by an angle α . Pairs with large ω_p should show a strong proximity effect. However, below some value of ω_p the proximity effect will be essentially non-existent. Adding pairs with ω_p below this value to the composite may in fact decrease the overall significance of the effect.

We thus construct several composite RTTs, each with a different lower limit on ω_p , which we denote by ω_c . Thus $RG_J(\omega_c)$ refers to a composite reduced transmission triangle in which all BQSO-IS pairs with $\omega_p > \omega_c$ are included.

Each of these RTTs was searched for the most significant positive deviation of the model from the data in the interval $[-1000 \text{ km s}^{-1}, +2000 \text{ km s}^{-1}]$ around λ_α . The interval is asymmetric to allow for underestimated QSO redshifts. In Fig. 5.9 we plot these maxima versus ω_c . For comparison we have performed the same analysis on the 1000 simulated datasets of S1 (no proximity effect). We plot the mean and $\pm 1\sigma$ significance levels as the dashed line and hashed region respectively. Clearly, our data are consistent with the absence of any foreground proximity effect.

Given the luminosities and inter-sightline spacings of the present set of QSOs, do we expect to be able to detect a signal? To answer this question we have created a fourth set of 1000 simulations (S4). These include the effects of all foreground IS with $\omega_p > 0.5$ and $\log J_{21} = -0.45$. Subjecting S4 to the same analysis as above yields the dotted line and grey shaded region in Fig. 5.9. Evidently, if J has indeed the value that was measured from the background proximity effect and if QSOs radiate isotropically, then we should be able to detect the foreground proximity effect at the $2\text{--}4\sigma$ level in our data.

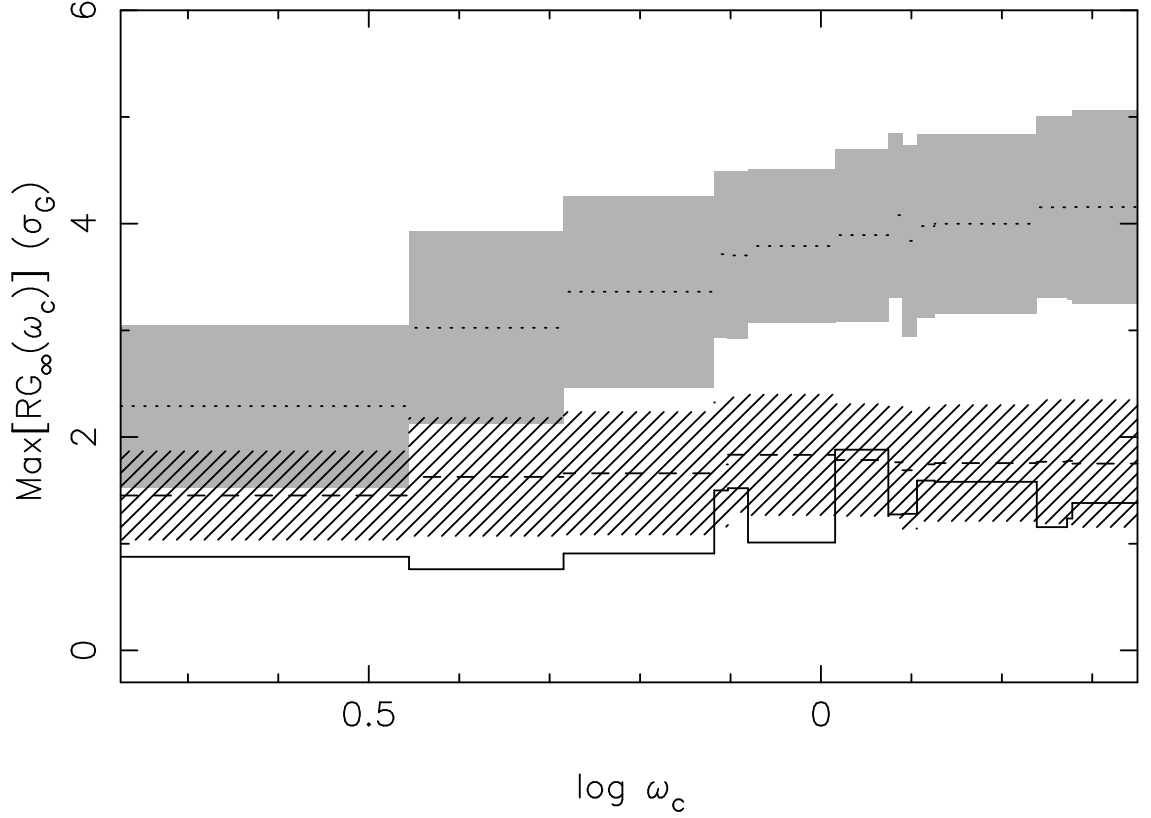


Figure 5.9: Significance of the foreground proximity effect as derived from composite RTTs which include all BQSO-IS pairs with $\omega_p > \omega_c$. The solid line is the data. The dotted line and grey shaded regions are the mean and $\pm 1\sigma$ significance levels found in 1000 simulated datasets that include the foreground proximity effect according to the ionization model with $\log J_{21} = -0.45$ (S4). The dashed line and hashed region are the same for $J = \infty$ (no proximity effect, S1). The number of BQSO-IS pairs included in the RTT increases from 1 at the left end of the plot to 14 at the right end.

5.5.2 Lower limit on J

The above result implies that we can at least derive a lower limit to J under the assumption that QSOs radiate isotropically. Setting $\omega_c = 0.5$ we have repeated the analysis of Section 5.4.2 using a foreground RTT that includes 14 BQSO-IS pairs. The result is shown in Fig. 5.10. We can see that the data are consistent with a large range of values of J , including $J = \infty$. However, for small values of J the model predicts too little absorption to be compatible with the data. From this constraint we derive a lower limit of $\log J_{21} > 0.3$ (90 per cent confidence).

From Fig. 5.4 we can see that this lower limit is larger than the upper limit derived from the background proximity effect for all $\Delta v \gtrsim 200 \text{ km s}^{-1}$. If we did not underestimate J in Section 5.4.2 then the simplest explanation for this discrepancy is that QSOs radiate anisotropically. If we require that the lower limit derived from the lack of a foreground proximity effect coincides with the upper limit of the background measurement then the QSOs of our sample must emit less ionizing radiation in the plane of the sky than along the line of sight to Earth by at least a factor of 1.4 for $\Delta v > 400 \text{ km s}^{-1}$. This number increases to 2.2 for $\Delta v > 800 \text{ km s}^{-1}$.

5.5.3 The Q0042–2639 quadrangle

Having established that the dataset as a whole does not exhibit any evidence for the existence of the foreground proximity effect, we now present a possible exception to this rule. From Fig. 5.2 we can see that Q0042–2639 is surrounded by four nearby background QSOs. Interestingly, all four show underdense absorption near the position of the foreground QSO. In Table 5.2 we list the BQSO name, the angular separation from the foreground QSO, the significance of the underdensity, M (in units of σ_G), the velocity offset of the underdensity from the foreground QSO redshift and finally the size of the underdensity (FWHM of the smoothing Gaussian). In the last line we list the same quantities for the composite RTT of the four BQSOs. Note that the offsets from the foreground QSO's redshift are of

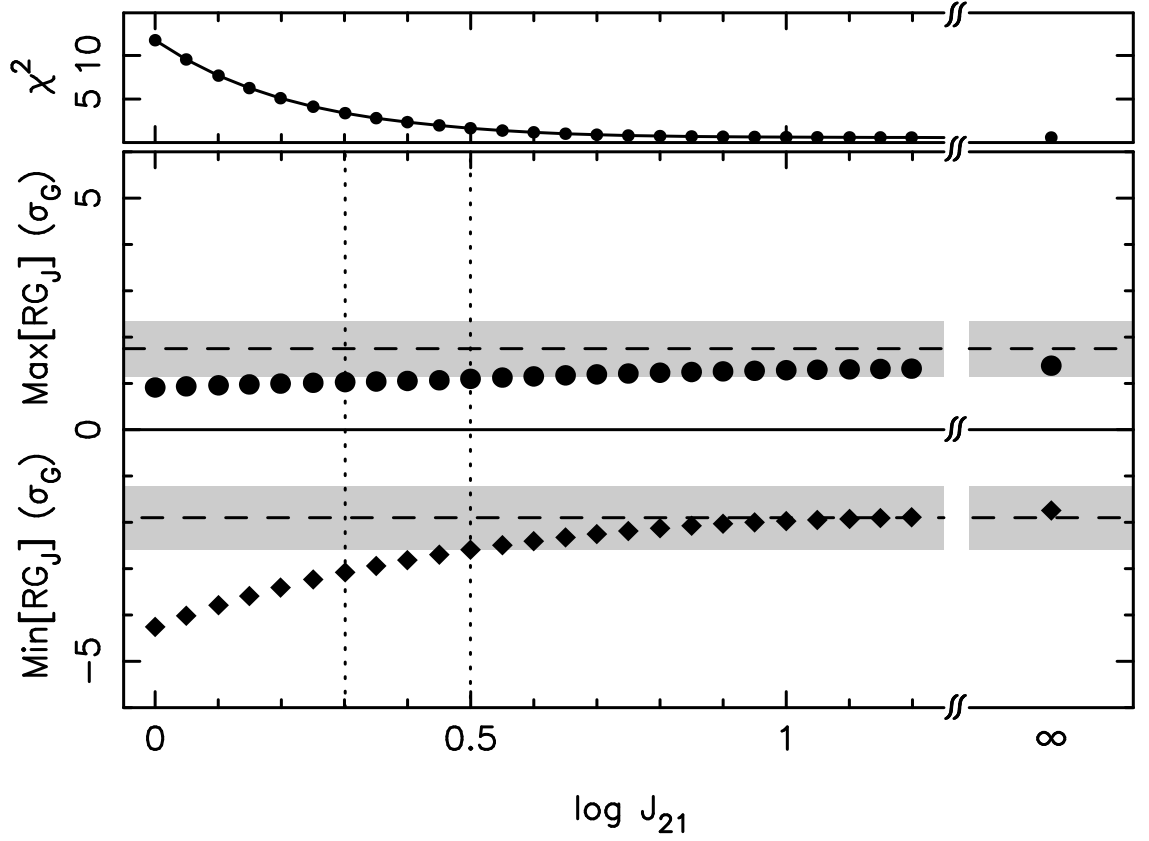


Figure 5.10: This plot is the equivalent of Fig. 5.3 for the foreground proximity effect. In the main panel we show the most significant positive (dots) and negative (diamonds) deviations (in units of σ_G) of the absorption model from the data in the regions near the positions of close-by foreground QSOs as a function of the mean Lyman limit background intensity J . The dashed lines and the grey regions mark the expected and $\pm 1\sigma$ significance levels of these deviations in the case where they are due to random fluctuations. The data are consistent with the absence of a foreground proximity effect ($J = \infty$). Thus we cannot derive an upper limit on J . The two dotted lines mark the 68 and 90 per cent confidence lower limits on J .

Table 5.2: The Q0042–2639 quadrangle.

BQSO	α arcmin	M σ_G	Δ km s ⁻¹	FWHM _s km s ⁻¹
Q0043–2633	13.6	2.97	−460	1260
Q0042–2627	11.7	3.11	−2390	5530
Q0041–2638	11.9	2.71	+230	3120
Q0042–2656	17.6	3.03	+2630	1210
Composite		3.52	+160	1880

the same magnitude but of opposite sign for the two pairs of opposing BQSOs (cf. Fig. 5.2). However, this is no longer true if we add $\gtrsim 400$ km s⁻¹ to the foreground QSO’s redshift.

At first glance, it may seem exceedingly unlikely to find an underdensity in four different lines of sight at a similar position (which happens to coincide with a foreground QSO) by chance. However, the spread of the underdensities in redshift is actually fairly large. Thus when we combine the four lines of sight to a composite RTT the significance level of the ‘void’ rises only marginally from $\sim 3\sigma_G$ in individual lines of sight to $3.5\sigma_G$ in the composite. Nevertheless, in the 1000 simulated datasets of S1 we find that the largest random fluctuations in the composite RTT have a mean significance level of $(1.69 \pm 0.53)\sigma_G$ and thus it seems that the void is in fact genuine. Indeed, a measurement of J from the composite RTT yields $\log J_{21} = -0.65^{+0.6}_{-0.5}$ which is lower than, but consistent with our measurements from the background proximity effect. From Fig. 5.5 (and Table 5.1) we can see that Q0042–2639 also shows a slightly (but not significantly) more prominent background proximity effect than ‘predicted’ by the other QSOs for its luminosity and redshift. Together these observations may be an indication that the luminosity of Q0042–2639 has been underestimated.

5.6 Uncertainties

In Section 5.4.2 we have already quantified the effect of uncertainties in model parameters, QSO redshifts and cosmology. We now discuss a number of other uncertainties associated with the present study.

It is clear that our method is sensitive to errors in the continuum placement, probably more so than the generic ‘line counting’ method. In Chapter 3 we attempted to account for random errors in the lowest orders of the continuum fit by determining the normalisation of the mean optical depth, B , for each spectrum separately. Here we used a single value of B derived from the entire dataset. This has the advantage of making our estimate of J fairly insensitive to the adopted value of γ (the evolutionary power law index). The disadvantage is that errors in the continuum placement should, in principle, increase the scatter when comparing the significance of the proximity effect in individual lines of sight (cf. Fig. 5.5). However, this comparison is based on measurements near the Ly α emission lines of the QSOs where the S/N is in general quite high and thus the continuum more secure. A *systematic* over- or underestimation of continua can only affect our results if such a bias is different for different parts of the spectra. This difference could be caused by the higher S/N and greater curvature of the continuum in the wing of the Ly α emission line.

As our method deals only with the transmitted flux it circumvents all problems that arise from defining a sample of individual absorption lines. These problems include line blending, curve of growth effects (e.g. Scott et al. 2000) and Malmquist bias (Cooke, Espey, & Carswell 1997).

The environment of QSOs may well differ from the intergalactic environment in other aspects than just the intensity of ionizing radiation. Most importantly, there may be additional absorption in the vicinity of QSOs above and beyond the absorption already accounted for in our model. If QSOs are hosted by groups or clusters of galaxies then the gravitational pull of the host will cause infall of the surrounding material and may thus increase the absorption line density near a QSO

(Loeb & Eisenstein 1995). If this effect is not taken into account, the proximity effect will appear weaker than it should and a larger value of J will be inferred. Loeb & Eisenstein (1995) suggested that the magnitude of this effect may be as large as a factor of ~ 3 . If QSO luminosity is correlated with host mass, then more luminous QSOs are affected more strongly by clustering and the value of J derived from the brightest QSOs should be higher than that derived from the faintest. On the other hand, if all QSOs were affected by clustering in the same way, then one might expect the observed slope of the significance-luminosity relation in Fig. 5.5 to be larger than the one expected on the basis of the measured (and overestimated) J . This is actually the case, although not significantly so. However, all of the QSOs in the present sample are radio-quiet. The hypothesis that such QSOs reside in rich galaxy cluster environments has been repeatedly rejected at low redshifts and there seems to be little evolution in the environment of radio-quiet QSOs up to $z < 1.5$ (Croom & Shanks 1999; Smith, Boyle, & Maddox 2000). In any case, it is most likely very difficult to disentangle clustering from the proximity effect and we believe that this issue deserves further study. For now, it remains an uncertainty.

In Section 5.3.2 we assumed that the column density of an absorber is proportional to the inverse of the incident ionizing flux. This is only true for absorbers composed purely of hydrogen. However, Scott et al. (2000) found that the inclusion of metals into the model has an insignificant effect on the derived value of J .

We have also ignored the fact that as radiation travels from a QSO to a given absorber it will be attenuated by all the intervening absorbers. In particular, an intervening strong Lyman limit system will essentially ‘black out’ the QSO entirely. In principle, disregarding this effect causes overestimation of J but Cooke, Espey, & Carswell (1997) concluded that the effect is negligible for $\log N < 17$. Higher column densities produce a conspicuous continuum break at the Lyman limit. Unfortunately, only three of our spectra cover any part of the Lyman limit region. One of these, Q0042–2656, shows a Lyman break but the system lies $\sim 5200 \text{ km s}^{-1}$ away from the QSO. In any case, since high column density absorbers are comparatively

rare we would expect that only a fraction of our QSOs are afflicted by this problem. However, from Fig. 5.5 it is apparent that none of our QSOs shows a proximity effect which is unusually small for its luminosity and redshift. We thus find it unlikely that we have significantly overestimated J due to this effect.

Obscuration by dust in intervening damped Ly α absorption systems may cause a QSO's luminosity and consequently J to be underestimated (Srianand & Khare 1996). Since there are no known damped Ly α absorption systems or candidates in our sample we believe that our value of J is not affected by dust obscuration.

However, there are a number of other factors that create uncertainty in the estimated luminosities of the QSOs. Errors in K -corrections and the QSO continuum slope could be avoided by direct spectrophotometric observations, but there are at least two other more fundamental and probably larger uncertainties:

1. QSO variability. The equilibration time-scale of Ly α absorbers, t_{eq} , is of the order 10^4 years. Thus the observed ionization state of an absorber in the vicinity of a QSO will approximately reflect the ionizing flux received from that QSO averaged over the 10^4 years prior to the epoch of observation, \bar{L} . Let us assume that the intrinsic luminosity of QSOs varies on a single time-scale, t_V . For $t_V \lesssim t_{\text{eq}}$ the QSO's observed luminosity may be different from \bar{L} and thus the strength of the observed proximity effect may be different from that expected on the basis of the ionization model. The same may be true for the foreground proximity effect even when $t_V > t_{\text{eq}}$ if t_V is smaller than the light travel time from the IS to the observed absorption ($\approx 10^6$ years). Obviously, we have no information on QSO variability on such large time-scales. However, Giveon et al. (1999) found that on time-scales of 100 to 1000 days the distribution of brightness deviations about the mean light curves of 42 QSOs has a width of 0.14 mag in the B -band. Thus variability on short time-scales contributes substantially to the uncertainty in the QSOs' luminosities.

2. Gravitational lensing. None of the QSOs in our sample are known to be lensed and at least four of them have been included in searches for multiply imaged QSOs with negative results (Surdej et al. 1993), implying that they are at least not

strongly lensed. However, some or all of them may be weakly lensed by the non-homogeneous distribution of foreground matter on large scales. Ray-tracing experiments performed on simulations of cosmological structure formation have yielded the probability distribution function of the magnification caused by galaxy clusters and large-scale structure (Hamana, Martel, & Futamase 2000; Wambsganss, Cen, & Ostriker 1998). At $z = 3$ the dispersion of this distribution can be as high as 0.4 (with a mean of 1) and the distribution has a power law tail towards large magnification. For the standard model the probability of encountering a magnification of 2 or greater is a few per cent but for a Λ model it is less than 10^{-3} . A magnification by a factor of 1.2 (or a demagnification by a factor 1.2^{-1}) introduces an additional uncertainty of $\pm 2.5 \log 1.2 = \pm 0.2$ mag which is actually larger than the quoted measurement errors on the observed B -band magnitudes.

What are the effects of luminosity uncertainties on our results if we treat them as *random* errors? Any statistical errors should increase the error on J . We can estimate the magnitude of this effect by the following argument. If we measured J from a single QSO then the additional error on J should be on the order of $\Delta(\log J) \approx 0.4\Delta m$, where Δm is the error on the QSO's magnitude. For ten QSOs this error should be smaller by a factor of $\sqrt{10}$. Thus for $\Delta m = 0.5$ mag we find $\Delta(\log J) = 0.063$ which is much smaller than the quoted error of 0.4.

This also shows that the *known* QSO variability, gravitational lensing and measurement errors on the QSO magnitudes cannot increase the errorbars on our foreground and background estimates of J by an amount large enough to make these two values compatible.

However, statistical errors in L_ν will weaken our results on the correlation between the significance of the proximity effect and L_ν . Clearly, for errors as large as $\Delta m = 0.5$ mag (which corresponds to a factor of 1.6 in luminosity) fitting a straight line to the data points in Fig. 5.5 will be almost meaningless. In Section 5.4.3 we estimated that the significance of the proximity effect is correlated with luminosity at the 2.6σ level. For $\Delta m = 0.3$ mag this significance drops to 2.1σ . Thus measurement errors

and the known variability of QSOs alone cannot entirely invalidate the evidence for a correlation of the background proximity effect with QSO Lyman limit luminosity.

In any case it is probably more appropriate to treat both QSO variability and gravitational lensing as *systematic* errors. Because of the steepness of the bright end of the QSO luminosity function a magnitude limited sample of QSOs is more likely to contain magnified QSOs than demagnified ones (e.g. Pei 1995; Hamana, Martel, & Futamase 2000). The same is true for QSOs that are near a peak in their lightcurves (e.g. Francis 1996). Thus either of these effects could cause a systematic overestimation of J . Together they imply that on average the QSO magnitudes may have been overestimated by ~ 0.35 mag which corresponds to an overestimation of J by $\Delta(\log J) = 0.14$.

Note that gravitational lensing and QSO variability on short time-scales ($< 10^4$ years) affect our J estimates from the classical and foreground proximity effects in the same way. However, if QSO luminosities vary on time-scales of $\sim 10^6$ years then this will affect only the latter estimate as explained above. In this case we would expect the QSOs to have been systematically fainter over a period of $\sim 10^6$ years prior to the time they emitted the photons which we receive today, causing us to overestimate J when measuring it from the foreground proximity effect. To reconcile the foreground and background values of J we require a variability of $\Delta m = 2.5 \log 2.2 = 0.86$ mag (assuming $\Delta v = 800 \text{ km s}^{-1}$) on time-scales of $\sim 10^6$ years.

Past authors (Cooke, Espey, & Carswell 1997; Scott et al. 2000) have attempted to test for the presence of gravitational lensing in their data: since high luminosity QSOs are more likely to be lensed than low luminosity ones, an estimate of J from the former group should be higher than from the latter. From Fig. 5.5 we can see that the higher luminosity QSOs of our sample actually show a slightly more prominent proximity effect than expected for $\log J_{21} = -0.45$. Thus a J measurement from these four QSOs will yield a lower value, contrary to the expectation if they were lensed.

5.7 Conclusions

We have analysed the Ly α forest spectra of a close group of 10 QSOs in search of the (foreground) proximity effect using a novel method based on the statistics of the transmitted flux. We list our various measurements of J in Table 5.3 and we summarise our main results as follows:

1. We confirm the existence of the classical background proximity effect at the > 99 per cent confidence level.

2. From the observed underdensity of absorption near the background QSOs we derive $\log J_{21} = 0.1_{-0.3}^{+0.4}$ (90 per cent confidence limits).

3. Correcting all QSO redshifts by $\Delta v = +800 \text{ km s}^{-1}$ we find $\log J_{21} = -0.45_{-0.3}^{+0.4}$. The reduction of J with Δv is consistent with previous results.

4. The significance of the background proximity effect in individual lines of sight is correlated with QSO Lyman limit luminosity at the 2.6σ level, thus lending further support to the hypothesis that the proximity effect is caused by the additional UV flux from background QSOs. We account for the fact that the significance is also correlated with redshift which is due to the evolution of the absorption line density. The magnitude of the correlation is consistent with the expectations from the ionization model. We considered an alternative model for the proximity effect where the underdense absorption is caused by some hypothetical property x of the QSO or its environment. We find that the property x would have to be noticeably correlated with luminosity in our sample and probably in the QSO population in general.

5. The full sample shows no evidence for the existence of the foreground proximity effect.

6. This absence implies a lower limit of $\log J_{21} > 0.3$. If we interpret the discrepancy of this lower limit with previous measurements as evidence that QSOs radiate anisotropically, then they must emit at least a factor of 1.4 less ionizing radiation in the plane of the sky than along the line of sight to Earth.

7. Our sample includes the fortunate constellation of a foreground QSO sur-

Table 5.3: Summary of J measurements and limits.

	$\log J_{21}$	Errors ^a
standard	0.10	+0.40, -0.30
$\beta = 1.3$	-0.45	+0.45, -0.40
$\beta = 1.7$	0.60	+0.30, -0.25
$\gamma = 2.5$	0.15	+0.35, -0.30
$q_0 = 0.15$	0.15	+0.40, -0.30
$\Delta v = 400 \text{ km s}^{-1}$	-0.25	+0.40, -0.30
$\Delta v = 800 \text{ km s}^{-1}$	-0.45	+0.40, -0.30
foreground	> 0.30	
Q0042–2639 quadrangle	-0.65	+0.60, -0.50

^aErrors are 90 per cent confidence limits.

rounded on all sides by four background QSOs with approximately equal separations from the foreground QSO. Contrary to the rest of the sample, this particular QSO induces a foreground proximity effect in the surrounding lines of sight at the 3.5σ level. For this subsample we measure $\log J_{21} = -0.65^{+0.6}_{-0.5}$.

8. Finally, we have discussed possible sources of systematic and additional statistical errors. We conclude that, apart from the uncertainty in the redshifts of the QSOs, clustering of absorption systems around QSOs is the most likely source of systematic error. We also find that the known variability of QSOs reduces the significance of the proximity effect-luminosity correlation to 2.1σ .

From Fig. 5.1 we can see that our measurement of J from the background proximity effect is consistent with most previous measurements. Bechtold (1994) found a somewhat larger value $\log J_{21} = 0.5$ but she did not correct the QSO redshifts, remarking only that a correction of $\Delta v = 1000 \text{ km s}^{-1}$ would lower her value of J by a factor of 3. Srianand & Khare (1996) also found a considerably higher value which is partly due to the fact that they used $\beta = 1.7$. Kulkarni & Fall's (1993)

low value of $\log J_{21} = -2.2$ at $z \approx 0.5$ is usually taken as evidence for an evolving background.

Bechtold (1994) and Scott et al. (2000) noted that the relative deficit of absorption lines near background QSOs was larger for the high luminosity halves of their samples than for the low luminosity ones. However, they did not quantify this effect in any detail and did not compare it to the expectations from the ionization model. BDO identified a trend of the line deficit with luminosity at 1σ significance. Lu, Wolfe, & Turnshek (1991) on the other hand found no such trend. In Figs. 5.5, 5.6 and 5.7 we have presented good evidence that the significance of the proximity effect is indeed correlated with QSO luminosity and redshift. This result was possible because we used a technique that is more sensitive to variations of the absorption density on large scales than the generic line counting method. Using simulations we find that these correlations are entirely consistent with the expectations of the ionization model. However, considering the discussion of Section 5.6 we clearly need to apply our method to a larger sample with a wider range in luminosity to establish this result more firmly. Nevertheless, the present analysis provides further evidence that the interpretation of the proximity effect as being due to increased ionization caused by the extra UV flux from the background QSO is essentially correct.

Although their results were poorly constrained, it is interesting to note that the three BQSO-IS pairs of Fernández-Soto et al. (1995) favoured a similarly high value of J as our full sample of 14 pairs. The non-detections of the foreground proximity effect by Crotts (1989) and Møller & Kjærgaard (1992) also imply a high value of J . On the other hand, all possible positive detections of the foreground proximity effect (Dobrzycki & Bechtold 1991; Srianand 1997; the Q0042–2639 quadrangle) yield J values that are in line with the measurements from the background effect.

One possible explanation is that most of the QSOs were substantially fainter over a period of $\sim 10^6$ years prior to the time they emitted the photons which we receive today. This would cause an overestimate of J when measured from the foreground proximity effect but would not affect the results of the background proximity effect.

As we have already pointed out, the other explanation is that QSOs radiate anisotropically. There is a large body of observational evidence which suggests that the observed characteristics of an Active Galactic Nucleus (AGN) depend on the direction from which it is viewed (see e.g. Antonucci 1993 for a review). The basic theme of unified models for AGN is that some or even all of the many different types of AGN are in fact the same type of object but seen from different directions. In these models the directionality is caused by a thick, dusty and opaque torus which surrounds the central engine. The smooth continuum and broad emission lines of a QSO are thought to originate from within the torus and thus they can only be seen indirectly by scattered light when the torus is viewed approximately edge on.

This scenario has two obvious implications: i) all QSOs show a background proximity effect and ii) whether a foreground proximity effect is seen or not depends on whether nearby absorption systems probed by other sightlines can ‘see’ inside the torus of the QSO. If so, they will roughly see the same continuum as we do, resulting in a measurable depletion of absorption and a corresponding J value which is similar to that derived from the background effect. If not, there will be little or no foreground effect, resulting in a high value or lower limit for J .

Assuming a simple picture of this kind, Dobrzycki & Bechtold (1991) used the velocity offset of their void from the foreground QSO to derive a value of $\sim 140^\circ$ for the opening angle of the torus.

However, it is difficult to explain the case of the Q0042–2639 quadrangle with this scenario. If all of the four underdensities are real and caused by the foreground QSO then it has to emit similar amounts of radiation along three nearly perpendicular axes (north-south, east-west and towards Earth), leaving little room for anisotropic emission.

The current situation is thus uncertain and intriguing enough to stimulate further observations. The motivations and potential gain are clear: by investigating the radiative effects of QSOs (or other AGN) on nearby absorption systems along other lines of sight we can ‘view’ them from different directions which may help

to constrain unified models of AGN. The ideal targets for further observations are dense groups of QSOs at similar redshifts. These are rare in current QSO catalogues but, fortunately, currently ongoing redshift surveys like 2QZ will soon remedy this situation.

And God said: “Let there be Hoyle.” And there was Hoyle. And God looked at Hoyle... And told him to make heavy elements in any way he pleased.

George Gamow

Chapter 6

The primordial deuterium abundance

6.1 Introduction

6.1.1 Big Bang Nucleosynthesis

Background

Big Bang Nucleosynthesis (BBN) and its success in explaining the abundances of the light elements is one of the principal foundations supporting the Hot Big Bang paradigm. Any cosmological theory must be able to account for the observation that the very oldest stars have non-zero abundances of the light elements and that the He abundance is almost universal amongst young and old stars (Hoyle & Tayler 1964). This is difficult to explain if one supposes that He is produced by the same mechanism which is responsible for the production of heavy elements (i.e. nucleosynthesis in stars) but it is natural if the He was already present in the primordial material from which the stars formed. The Hot Big Bang picture offers an explanation for the presence of light elements in primordial gas: at present the Universe is observed

to be expanding and filled with very cold radiation. If we trace the evolution of such a Universe back to earlier epochs we find that at $t \sim 1 - 1000$ s the conditions in the Universe amount to those of a nuclear reactor which synthesizes free protons and neutrons into nuclei. As the Universe expands and cools these nuclear reactions are eventually aborted before heavy nuclei can form and we are left with an elemental mix that contains mostly H and He as well as traces of their isotopes and other light nuclei. The exact composition of this mix depends on the total number of baryons as well as the expansion rate of the Universe during the first few minutes. Standard BBN predicts the abundances of D, ^3He , ^4He and ^7Li as a function of a single parameter η , the baryon-to-photon ratio (cf. Fig. 6.1). The broad consistency of these predictions with the observed pattern of abundances which range over nine orders of magnitude is a striking success of the theory and inspires confidence that the Hot Big Bang is a reasonable approximation of reality.

Physical principles of BBN

We will now briefly review the fundamentals of standard BBN. More detailed discussions can be found in many textbooks, including those by Kolb & Turner (1990), Peebles (1993) and Peacock (1999).

The binding energies of atomic and nuclear structures are of the order of a few tens of eV and MeV. Thus when the temperature of the Universe, i.e. the temperature of the thermal background radiation (CMB), is significantly higher than these values these structures cannot exist and the Universe is filled only with radiation and various kinds of elementary particles. In thermal equilibrium we can treat a given particle species A as a perfect Fermi or Bose gas. Thus the distribution function of species A is given by

$$f_A(\mathbf{p}, t) = \frac{g_A}{(2\pi\hbar)^3} \frac{1}{\exp\left(\frac{E - \mu_A}{kT_A(t)}\right) \pm 1} \quad (6.1)$$

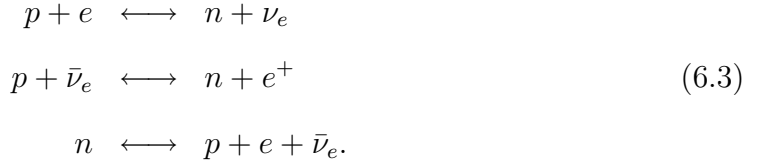
where $E = c(\mathbf{p}^2 + m_A^2 c^2)^{\frac{1}{2}}$, m_A , μ_A , T_A and g_A are the mass, chemical potential, temperature and spin degeneracy factor of species A and k is the Boltzmann constant. The ‘+’ is for fermions, the ‘-’ for bosons. Species A will be in thermal

equilibrium with the background as long as the rate of interaction with the other species is higher than the rate of expansion of the Universe, which is given by the Hubble parameter H .

For $kT \ll m_p c^2 \approx 938$ MeV protons and neutrons will be non-relativistic. The number density of non-relativistic particles is given by

$$\begin{aligned} n &= \int f(\mathbf{p}) d^3\mathbf{p} \approx \frac{g}{2\pi^2\hbar^3} \int_0^\infty p^2 \exp\left(-\frac{mc^2 - \mu}{kT}\right) \exp\left(-\frac{p^2}{2mkT}\right) dp \\ &= \frac{g}{\hbar^3} \left(\frac{mkT}{2\pi}\right)^{\frac{3}{2}} \exp\left(-\frac{mc^2 - \mu}{kT}\right) \end{aligned} \quad (6.2)$$

In thermal equilibrium, the inter-conversion between protons and neutrons proceeds via the reactions



From the conservation of the chemical potential in these reactions we find that $\mu_n + \mu_\nu = \mu_p + \mu_e$ so that $\mu_n - \mu_p = \mu_e - \mu_\nu$. Assuming negligible electron and neutrino chemical potentials (compared to the temperature) we find for the number density ratio of neutrons and protons

$$\frac{n_n}{n_p} = \left(\frac{m_n}{m_p}\right)^{\frac{3}{2}} \exp\left(-\frac{Q}{kT}\right), \quad (6.4)$$

where $Q = (m_n - m_p)c^2 \approx 1.3$ MeV. Therefore the number of protons and neutrons in the Universe is almost identical while $Q \ll kT \ll m_p c^2$.

The inter-conversion between protons and neutrons is only possible as long as the reactions (6.3) proceed faster than the expansion of the Universe. A quantum-field calculation for reaction rates of (6.3) shows that at $kT \gg Q$ all the reaction rates are of the same form:

$$\Gamma \propto T^5. \quad (6.5)$$

The expansion rate, on the other hand, is determined by the energy density of the relativistic particles. The energy density contributed by non-relativistic par-

ticles can be neglected (radiation dominated epoch), as well as the curvature and cosmological constant terms in the Friedmann equation:

$$H^2 = \frac{8\pi G}{3c^2} \rho_{\text{rel}}, \quad (6.6)$$

where G is the gravitational constant. For a relativistic particle species A we can calculate its contribution to ρ_{rel} from (6.1) (remembering that $kT_A \gg m_A c^2$ and $kT_A \gg \mu_A$):

$$\begin{aligned} \rho_A &= \int E f_A(\mathbf{p}) d^3\mathbf{p} \\ &\approx \frac{g_A}{2\pi^2 \hbar^3 c^3} \int_0^\infty \frac{E^3}{\exp\left(\frac{E}{kT_A}\right) \pm 1} dE = \begin{cases} \frac{7}{8} g_A \frac{\pi^2 k^4}{30 \hbar^3 c^3} T_A^4 & \text{fermions} \\ g_A \frac{\pi^2 k^4}{30 \hbar^3 c^3} T_A^4 & \text{bosons} \end{cases} \end{aligned} \quad (6.7)$$

In thermal equilibrium all species will have the same temperature, $T_A = T$. Summing over all species we have

$$\rho_{\text{rel}} = g_{\text{tot}} \frac{\pi^2 k^4}{30 \hbar^3 c^3} T^4, \quad (6.8)$$

where

$$g_{\text{tot}} = \sum_{\text{boson}} g_B + \frac{7}{8} \sum_{\text{fermion}} g_F. \quad (6.9)$$

At energies of a few tens of MeV the only relativistic particles in the background are photons ($g_\gamma = 2$), electrons and positrons ($g_e = g_{\bar{e}} = 2$) and neutrinos ($g_\nu = g_{\bar{\nu}} = 1$) (assumed to have small masses). Therefore

$$g_{\text{tot}} = 5.5 + \frac{7}{4} N_\nu, \quad (6.10)$$

where N_ν denotes the number of light neutrino families. For $N_\nu = 3$ we thus have

$$H = 5.44 \sqrt{\frac{Gk^4}{\hbar^3 c^5}} T^2. \quad (6.11)$$

From the condition $\Gamma = H$ we can determine the temperature, T_D , at which the reactions (6.3) can no longer proceed. A detailed calculation for the reaction rates shows that $kT_D \approx 0.8$ MeV. When T drops below this value the neutron-to-proton ratio ‘freezes out’ at

$$\frac{n_n}{n_p} \approx \exp\left(-\frac{Q}{kT_D}\right) \approx \frac{1}{5}. \quad (6.12)$$

Since the binding energies for D, ${}^3\text{He}$ and ${}^4\text{He}$ are 2.2, 7.7 and 28.3 MeV respectively, one might expect that these nuclei start forming well before n_n/n_p freezes out. From (6.2) one can find a relationship between the abundance of a nucleus A (of mass A and charge Z) and the baryon-to-photon ration $\eta = n_\gamma/n_b = n_\gamma/(n_n + n_p)$:

$$\frac{n_A}{n_b} \propto \left(\frac{T}{m_p}\right)^{\frac{3(A-1)}{2}} \eta^{A-1} \left(\frac{n_p}{n_b}\right)^Z \left(\frac{n_n}{n_b}\right)^{A-Z} \exp\left(\frac{B_A}{kT}\right), \quad (6.13)$$

where B_A is the binding energy of nucleus A and the constant of proportionality depends only on A . As we will see below $\eta = 2.74 \times 10^{-8} \Omega_b h^2$. Thus in order to get an appreciable abundance of A it is not enough for kT to fall below B_A but it must fall further in order to offset the smallness of η . Essentially, because of the large number of photons compared to baryons, there are still enough photons in the high energy tail of the photon distribution to dissociate A even when $kT < B_A$. A detailed calculation shows that, e.g., $n_D = n_n$ occurs at $kT \approx 0.06$ MeV.

Once the temperature drops below this value, D is rapidly produced via $p+n \rightarrow D$, which ‘kick-starts’ a whole network of nuclear reactions. Note that equation (6.13) seems to suggest that ${}^4\text{He}$ should appear before D or ${}^3\text{He}$ since it has a larger binding energy. However, ${}^4\text{He}$ is most easily produced by $D+p \rightarrow {}^3\text{He}$ followed by ${}^3\text{He}+n \rightarrow {}^4\text{He}$ and therefore the production of ${}^4\text{He}$ must await significant amounts of D. Once D is built up, it is rapidly burnt into ${}^4\text{He}$ to achieve the relatively high ${}^4\text{He}$ equilibrium abundance dictated by equation (6.13). The rates of all of these reactions depend sensitively on η : the higher the baryon density, the faster D and ${}^3\text{He}$ are burnt to ${}^4\text{He}$.

As we have seen, n_n/n_p freezes out at $kT \approx 0.8$ MeV and the neutrons remain free until they are bound into nuclei at $kT \approx 0.06$ MeV. In the meantime they will decay via the last of the reactions (6.3). From equation (6.11) we find $t(kT = 0.8\text{MeV}) \approx 1.2$ s and $t(kT = 0.06\text{MeV}) \approx 210$ s. Since the neutron has an e-folding time of 887 s (Peacock 1999), the neutron-to-proton ratio at the time nucleosynthesis sets in is given by

$$\frac{n_n}{n_p} \approx \exp\left(-\frac{1.3 \text{ MeV}}{0.8 \text{ MeV}}\right) \exp\left(-\frac{210 \text{ s}}{887 \text{ s}}\right) = 0.16. \quad (6.14)$$

Because of the process described in the previous paragraph, essentially all neutrons end up in ${}^4\text{He}$ and we can immediately write down the expected ${}^4\text{He}$ mass fraction:

$$Y_P = \frac{m_{\text{He}} n_{\text{He}}}{n_b} \approx \frac{4 \frac{n_n}{2}}{n_p + n_n} = \frac{2 \frac{n_n}{n_p}}{1 + \frac{n_n}{n_p}} = 0.27. \quad (6.15)$$

The production of heavier elements, even those with higher binding energies than ${}^4\text{He}$, is strongly suppressed by the fact that there are no tightly bound nuclei of atomic masses 5 and 8. At the end of nucleosynthesis we are thus left with mostly H (because there were not enough neutrons to bind all the protons into D), ~ 25 per cent ${}^4\text{He}$ (by mass) and traces of D and ${}^3\text{He}$ which are left over from ${}^4\text{He}$ synthesis. The only other nucleus to have formed an appreciable abundance in BBN is ${}^7\text{Li}$.

An exact calculation of these processes involves numerically keeping track of the entire network of nuclear reactions. These calculations are performed as a function of η which is conserved during the expansion. We can convert η to Ω_b , the present-day mass density of baryons in units of the critical density ρ_c , by noting that the present-day number density of photons is given by

$$\begin{aligned} n_{\gamma 0} &= \int f(\mathbf{p}) \, d^3\mathbf{p} = \frac{g_\gamma}{2\pi^2 \hbar^3 c^3} \int_0^\infty \frac{E^2}{\exp\left(\frac{E}{kT_0}\right) - 1} \, dE \\ &= \frac{g_\gamma}{2\pi^2} \left(\frac{kT_0}{\hbar c}\right)^3 \int_0^\infty \frac{x^2}{\exp(x) - 1} \, dx = \left(\frac{kT_0}{\hbar c}\right)^3 \frac{2 \zeta(3)}{\pi^2}, \end{aligned} \quad (6.16)$$

where $T_0 = 2.725$ K (Mather et al. 1999) is the present-day temperature of the CMB and $\zeta(3) = 1.202$ is Riemann's zeta function of order 3. We thus have

$$\begin{aligned} \eta &= \frac{n_b}{n_\gamma} = \frac{n_{b0}}{n_{\gamma 0}} = \left(\frac{\hbar c}{kT_0}\right)^3 \frac{\pi^2}{2 \zeta(3)} \frac{\rho_c \Omega_b}{m_p} = \left(\frac{\hbar c}{kT_0}\right)^3 \frac{3\pi H_0^2 \Omega_b}{16 \zeta(3) G m_p} \\ &= 2.74 \times 10^{-8} \Omega_b h^2. \end{aligned} \quad (6.17)$$

The result of the calculations is shown in Fig. 6.1. As we can see, the abundances of D and ${}^3\text{He}$ are strong functions of $\Omega_b h^2$: the higher the baryon density, the faster D and ${}^3\text{He}$ are burnt to ${}^4\text{He}$ and the fewer D and ${}^3\text{He}$ nuclei remain when the reactions finally freeze out. In contrast, the ${}^4\text{He}$ abundance is not very sensitive to $\Omega_b h^2$, because essentially all of the neutrons end up in ${}^4\text{He}$ anyway. Instead, Y_P depends primarily on the neutron-to-proton ratio at the time the reactions that inter-convert

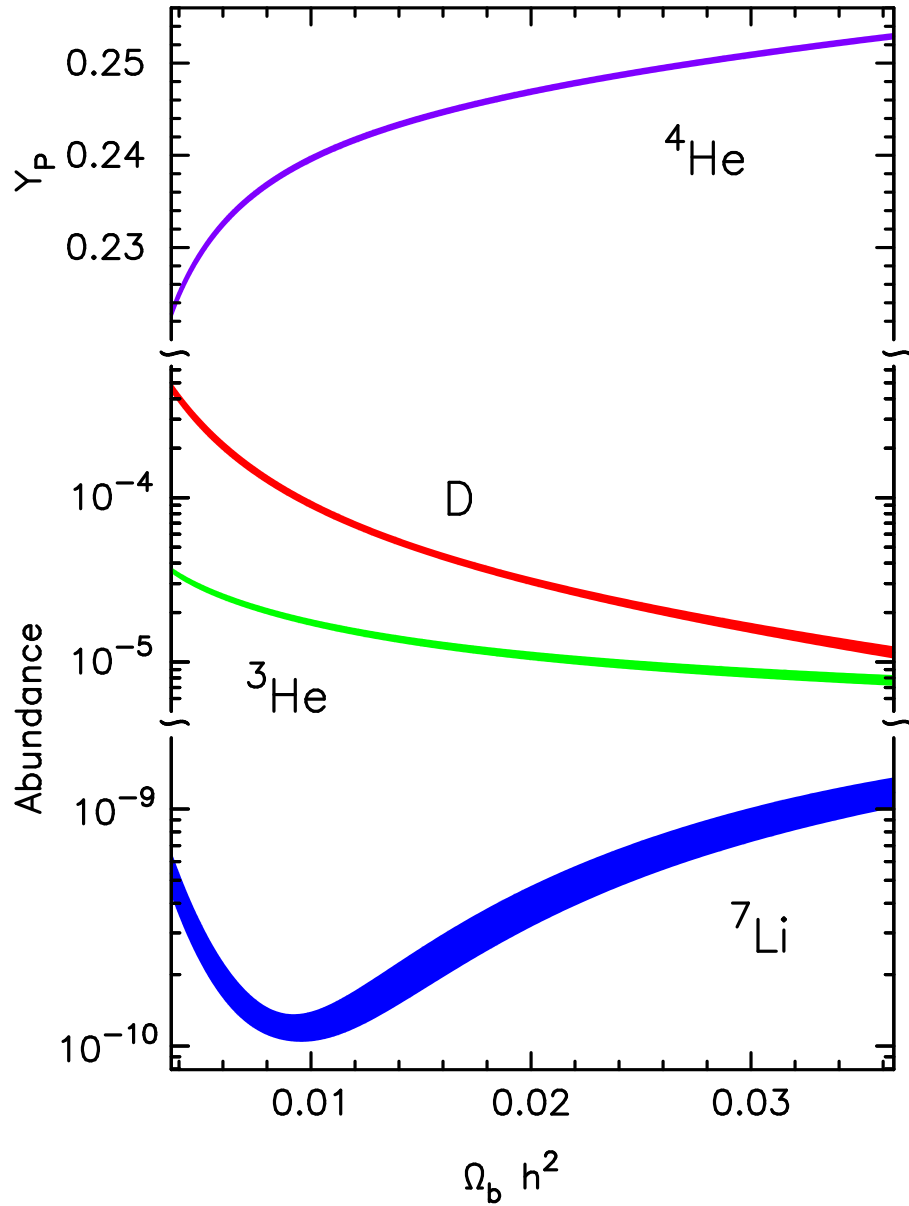


Figure 6.1: 95 per cent confidence limits of the abundances of the light elements relative to H as predicted by homogeneous BBN with $N_\nu = 3$. We plot the abundance by mass for ^4He , by number for the other elements. This plot was created from the analytic fits for the abundances and their error matrix as presented by Burles, Nollett, & Turner (2001). These data are derived from the most up-to-date information on the half-life of the free neutron and nuclear reaction rates as well as their uncertainties.

them freeze out (equation 6.15). This time is determined by the competition between the rates of these reactions and the expansion rate of the Universe. The latter is in turn determined by the relativistic energy density (equation 6.11) and therefore Y_P is a fairly sensitive probe of the number of massless neutrino families, N_ν .

Motivation for further work

Following early work by Alpher, Bethe, & Gamow (1948), Alpher (1948), Gamow (1948a), Gamow (1948b), Hayashi (1950) and Alpher, Follin, & Herman (1953) the basic physics of BBN was essentially in place by the 1950s. The overall picture of a Hot Big Bang subsequently received resounding confirmation by the discovery of the CMB by Penzias & Wilson (1965). This prompted detailed analyses of the processes at work in BBN and the predictions for the abundances of the light elements have not changed dramatically since the work of Peebles (1966) and Wagoner, Fowler, & Hoyle (1967). Over the past decades it has become increasingly clear that there is good agreement between these predictions and observations (e.g. Wagoner 1973; Yang et al. 1984; Walker et al. 1991; Burles, Nollett, & Turner 2001).

As we have seen above, a measurement of a primordial light element abundance translates to a measurement of the baryonic density parameter Ω_b (irrespective of whether the baryons are luminous or not). For at least two decades BBN has provided the most stringent and convincing constraints on Ω_b . The most recent estimate is: $\Omega_b h^2 = 0.019 \pm 0.002$ (Burles, Nollett, & Turner 2001). Together with surveys of luminous and gravitating matter these constraints entail three fundamentally important conclusions (e.g. Walker et al. 1991):

1. Baryons cannot provide enough density to close the Universe.
2. A significant fraction of the baryons may be dark.
3. Most dark matter is non-baryonic.

Despite the fact that these results are quite secure, much work remains focussed on BBN and it remains a central issue in cosmology. There are (at least) two reasons

for this:

1. BBN is our only physical probe of the very early Universe when thermal energies were ~ 1 MeV. As such it constitutes the central link between cosmology and particle physics.

Standard BBN is ‘over-constrained’ since there is only a single free parameter, η , which may be adjusted to account for the observed primordial abundances of D, ^3He , ^4He and ^7Li . As the precision of abundance measurements increases and as we gain a better understanding of systematic errors and of post-BBN chemical evolution, the range of values of η that can accommodate all observations tightens. Eventually, it may no longer be possible to achieve this concordance. This would be unique evidence that some of the assumptions about the early Universe and the Standard Model of particle physics made in standard BBN may not be accurate. In other words, it may point to new physics. Non-standard BBN scenarios were reviewed by e.g. Jedamzik (1998) and include (among others) inhomogeneity, additional flavours of massless neutrinos, other additional sources of relativistic energy density such as gravitational waves or other massless fields, massive neutrinos, large neutrino chemical potentials, matter/antimatter domains, magnetic fields, massive decaying particles, variations of the fundamental constants and alternative theories of gravitation.

2. Comparison between different measurements of the same cosmological parameter, each derived on the basis of entirely different physics, probably provides the strongest test for any cosmological theory that has so far proven successful. A good example of such a test is the comparison of the ‘expansion age’ of the Universe (derived from General Relativity) with the age of the oldest objects in the Universe (derived from nuclear physics) (Lineweaver 1999).

A similar test of standard cosmology will soon be available using Ω_b . The most stringent non-BBN constraint on Ω_b will be provided by measurements of the anisotropy of the CMB. The height of the second peak in the CMB power spectrum is sensitive (among other things) to Ω_b and it is expected that future CMB

missions (PLANCK and MAP) will ‘pin down’ Ω_b to an accuracy of 1 per cent or better (Schramm & Turner 1998). These new data are much anticipated as there currently may be some weak evidence for a discrepancy between Ω_b^{BBN} and Ω_b^{CMB} (e.g. Tegmark & Zaldarriaga 2000).

The physical basis of these measurements is quite different. As we have seen above, at $t \approx 200$ s Ω_b determines how completely D and ^3He are converted to ^4He while at the time of last scattering ($t \approx 300,000$ years) it determines the amplitude of gravity-driven acoustic oscillations in the baryon-photon fluid.

The usefulness of this comparison will be limited by that measurement which has the largest uncertainty. Presently, Ω_b^{BBN} is the most accurate measurement by about an order of magnitude but this will most likely be changed by the PLANCK and MAP missions. It is thus timely to consider ways by which we can improve the precision of Ω_b^{BBN} .

In addition to Ω_b^{BBN} and Ω_b^{CMB} other measures of Ω_b are derived from careful accounting of the baryon budget in the local Universe by more or less direct means (e.g. Fukugita, Hogan, & Peebles 1998) and from the observed opacity of the Ly α forest at $z \approx 3$ (Rauch et al. 1997; Weinberg et al. 1997; Zhang et al. 1998). However, these measurements are unlikely to reach the same level of precision as Ω_b^{BBN} and Ω_b^{CMB} . Nevertheless, they add considerable constraints on the need for dark baryons.

What is the best way to ensure that BBN remains competitive in the so-called ‘new era of precision cosmology’ (Schramm & Turner 1998; Burles, Nollett, & Turner 2001; Kaplinghat & Turner 2001; but see also Disney 2000), in particular with reference to the second point made above, i.e. increased precision and reliability of Ω_b^{BBN} ? To answer this question we now briefly review the difficulties associated with each of the different types of abundance measurements. More detailed reviews are available in the literature and the most recent ones include those by Olive, Steigman, & Walker (2000) and Tytler et al. (2000).

^4He is the second most abundant nuclide in the Universe and its abundance can

be accurately measured in a number of different astrophysical locations. The best estimates of the primordial abundance are obtained by measuring emission line flux ratios in low metallicity extragalactic H II regions. Contamination from ^4He produced in stars is thought to be very low in these sites so that the extrapolation from the lowest metallicity regions to primordial introduces an error no larger than the statistical uncertainties. However, there are a number of systematic uncertainties which are subject of an ongoing debate (e.g. Izotov & Thuan 1998). These include possible underlying stellar absorption of the He emission lines, corrections for collisional excitation and model-dependent corrections for unseen neutral He. In addition, as we have seen above, the amount of ^4He produced in BBN is primarily a function of the number of neutron-to-proton ratio at the time the weak interactions responsible for inter-converting protons and neutrons freeze out. Thus the ^4He abundance is not very sensitive to $\Omega_b h^2$.

Cosmologically interesting ^7Li is observed in very metal-poor halo stars. Probably the greatest difficulty in these measurements is to understand the amount of ^7Li depletion at the surface of these stars due to dilution and/or destruction. The depletion is determined by modelling the surface layers of the stars but these efforts are hampered by imprecise knowledge of the temperature scales and atmospheres of these extremely cool and low mass stars. Additional information on the depletion can be derived from the dispersion of the ^7Li abundance around the ‘Spite-plateau’. Ryan, Norris, & Beers (1999) found virtually no dispersion and concluded that their inferred ^7Li abundance was either primordial or uniformly depleted. They did, however, find a trend of ^7Li abundance with metallicity suggesting that not all ^7Li is primordial but that some is the product of Galactic chemical evolution (nuclear reactions of Galactic cosmic rays with the interstellar medium (ISM)) prior to star formation (Ryan et al. 2000). In addition to these difficulties primordial ^7Li is produced by two distinct processes in BBN. As a consequence the total primordial ^7Li abundance as a function of $\Omega_b h^2$ has a minimum in the range of interest (cf. Fig. 6.1) so that it is not very sensitive to $\Omega_b h^2$ near the minimum and corresponds to two

values of $\Omega_b h^2$ far from the minimum.

At present, observed ${}^3\text{He}$ abundances are not useful for comparison with BBN predictions. Present-day ${}^3\text{He}$ probably has a very complicated history of production, destruction and survival which is only poorly understood (Olive, Steigman, & Walker 2000). Thus the primordial abundance of ${}^3\text{He}$ has never been inferred.

D on the other hand is the ideal baryometer. The D abundance is a strong function of $\Omega_b h^2$ (cf. Fig. 6.1) and Reeves et al. (1973) showed that there are no astrophysical sites (other than BBN) where D can be produced in significant amounts. Thus any measurement of the D abundance provides a firm lower limit to the primordial abundance. There exists a plethora of measurements from the solar system and the (local) ISM (e.g. Lemoine et al. 1999). However, all of these sites have been subject to stellar processing in which D is destroyed. It is therefore difficult to reliably infer anything about the primordial D abundance from these measurements as different Galactic chemical evolution models give rather different answers concerning the amount of D destroyed by astration (Tosi et al. 1998). Furthermore, there may exist unknown processes which affect the D abundance in the ISM as evidenced by the observed scatter in D/H measurements from different locations in the ISM (Vidal-Madjar et al. 1998).

The past decade has seen the emergence of a new type of D/H determination: the possible detection and measurement of D I in high redshift, low metallicity QSO absorption systems. This type of measurement has its own uncertainties and systematics which will become apparent in Section 6.1.2. The most important uncertainty is that an unfortunately placed H I absorption line may mimic absorption from D I and so most D/H measurements from QSO absorption systems include the possibility of D/H= 0, i.e. they are upper limits. Nevertheless, once a suitable absorption system has been identified the measurement of D/H is extremely direct. Furthermore, because of the high redshift and low metallicity of the QSO absorbers it is fairly certain that little ($\lesssim 1$ per cent) D has been destroyed by stellar processing (Jedamzik & Fuller 1997).

For these reasons QSO absorption systems offer an excellent opportunity to derive an accurate and (eventually) reliable estimate of Ω_b^{BBN} . As we will see in Section 6.1.2 the present observational status in this field is not satisfactory. In this chapter we describe a long-term observational programme aimed at securing 10–20 new D/H measurements within the next few years. We stress that this project is very much work in progress.

In the remainder of this section we review the observational status of D/H measurements in QSO absorption systems. In Section 6.2 we describe the strategy of our programme and we present the results of its first phase in Section 6.3. Section 6.4 describes an attempt to derive a D/H constraint from a high resolution spectrum of Q0940–1050.

6.1.2 D/H in QSO absorption line systems

Adams (1976) first pointed out that the absorption spectra of high redshift QSOs may offer an opportunity to measure the abundance of D. He encouraged observers “to examine carefully the profiles of any relatively sharp H $L\alpha$ lines” (Adams 1976). The degree of difficulty of this seemingly simple task is perhaps best testified to by the fact that it took observers 11 years to rise to the challenge.

A measurement of D/H in a QSO absorption system is performed by fitting Voigt profiles to high resolution data. Often, multiple components are required and the fit gives a redshift, z , a column density, N , and a velocity dispersion, b , for each. The fit may be performed simultaneously on several transitions of several different ions in order to better constrain some of the parameters. However, the models constructed in this way are rarely unique and several different models may describe the data equally well. For example, a putative D I feature almost always admits an alternative interpretation as unrelated H I absorption (often called ‘interloper’). This results in considerable ambiguity. Nevertheless, once a model has been established, D/H is simply given by $N(\text{D I})/N(\text{H I})$, because the time-scale for H and D ionization equilibrium is very short (10^5 years) in the low density, photo-ionized intergalactic

medium.

To date only ten absorption systems (observed in nine spectra) have been discussed in relation to D/H in a total of 21 observational papers in refereed journals. We now review each of these in turn.

Q0014+813: Carswell et al. (1994) reported a possible D I feature in the $z = 3.32$ absorption system observed toward Q0014+813. Their data consisted of echelle spectra obtained from the KPNO 4-m telescope at a resolution of 23 and 12.5 km s⁻¹. Covering only the first four lines of the Ly series they supplemented their data with results from earlier observations at lower resolution by Chaffee et al. (1985) who had also established the low metallicity of this absorption system (Chaffee et al. 1986). In agreement with these earlier results Carswell et al. (1994) found two main components in this system. The lower redshift component showed an unambiguous absorption line in its blue wing and they tentatively identified this line as D I, deriving $D/H \approx 24 \times 10^{-5}$ with an error of about 0.3 dex while explicitly admitting the possibility that the line was in fact an H I interloper.

Using 8 km s⁻¹ resolution data from the Keck 10-m telescope, Songaila et al. (1994) derived a value of $D/H \approx (19-25) \times 10^{-5}$, in remarkably good agreement with the previous result considering that their model for the absorption complex was significantly different from that derived by Carswell et al. (1994).

Rugers & Hogan (1996a) re-reduced and re-analysed the data of Songaila et al. (1994). Based on a ‘spike’ in the centre of the putative D I feature they split the blue main component of this complex into two very narrow lines and derived $D/H = (19 \pm 5) \times 10^{-5}$ for both components independently. Curiously, they explained unphysical over-absorption of their model over ~ 30 km s⁻¹ in Ly γ and Ly δ as “artifacts or noise” while at the same time accepting the 3 pixel ‘spike’ in the D I feature as real.

Subsequently, Rugers & Hogan (1996b) presented an analysis of a second, lower redshift system ($z = 2.80$) in the same spectrum. However, due to the $z = 3.32$ system, only Ly α and various metal lines are observable in this system. The latter

were used to fix the position of the lowest redshift component. Determining the H I column density from the far blue damping wing they found an extra component was needed at the expected position of D I to fit the near blue edge of the feature and determined $D/H = 19_{-9}^{+16} \times 10^{-5}$. Strangely though, they rejected the possibility that the putative D I line was in fact an H I interloper on the grounds of its low b -parameter which was in fact as large or larger than the b -parameters of the two main lines of their model for the $z = 3.32$ complex.

Finally, Burles, Kirkman, & Tytler (1999) presented a new Keck spectrum of Q0014+813. Firstly, their data did not show the ‘spike’ identified by Rugers & Hogan (1996a) in the candidate D I feature of the $z = 3.32$ system and they found that it was well fit by a single component. Secondly, its b -parameter was found to be too large to be entirely explained by D I (which, however, is inconsistent with the results of Carswell et al. 1994). Thirdly, they found an asymmetry at the expected H I position in the (unsaturated) higher order lines, concluding that $D/H < 35 \times 10^{-5}$, which is in reasonable agreement with the results of Carswell et al. (1994). Burles, Kirkman, & Tytler (1999) also analysed the $z = 2.80$ system. Not surprisingly, they were able to find a fit using only H I but claimed that they could not put a lower limit on the H I column density of the lowest redshift component.

Q0420–388: Webb (1987b) first analysed an absorption system at $z = 3.08$ using relatively low resolution (26 km s^{-1}) data and derived $D/H \lesssim 10 \times 10^{-4}$. Subsequently, using AAT and CTIO 4-m data, Carswell et al. (1996) re-analysed this system in which the Ly β and Ly ϵ lines placed reasonable constraints on the total D I column density of the two main components of this system. Due to the complexity of the absorption, however, the total H I column density of these two components was only poorly constrained, providing only a lower limit $D/H > 2 \times 10^{-5}$. Assuming a constant O I/H I ratio throughout the complex they derived $D/H = (16\text{--}25) \times 10^{-5}$, while again explicitly admitting the possibility of an H I interloper, i.e. $D/H = 0$.

BR 1202–0725: Wampler et al. (1996) constrained D/H to be $\lesssim 15 \times 10^{-5}$ from their NTT and CTIO 4-m observations of an absorption system at $z = 4.67$.

Additional absorption was clearly required near the expected position of the D I Ly α line of this system. However, in view of an uncertain continuum in the Ly limit region and confusion of the high order series lines with those from a different system, the H I column density is again somewhat uncertain.

PKS 1937–1009: Tytler, Fan, & Burles (1996) presented Keck data of a $z = 3.57$ absorption system with remarkably simple velocity structure. In a straightforward analysis they showed that only two blended components were required to explain the observed absorption in almost the entire Ly series as well as eight different metal transitions. From the additional absorption seen in the blue wing of the Ly α line of the complex they derived $D/H = (2.3 \pm 0.4) \times 10^{-5}$. They rejected the possibility of an H I interloper on the grounds that “this contaminating H would have $b < 18 \text{ km s}^{-1}$, low enough to be unusual”. Remarkably, their final model for this system, which included 64 H I lines unassociated with the main components, contained no less than 10 lines with $b < 18 \text{ km s}^{-1}$ (Burles & Tytler 1998a, Table 2).

Wampler (1996) and Songaila, Wampler, & Cowie (1997) raised doubts about this D/H measurement because it was based on a fairly high column density system, $\log N_{\text{tot}}(\text{H I}) = 17.94$. They argued that in such systems the determination of the velocity structure and in particular of $N_{\text{tot}}(\text{H I})$ is difficult because all the high order series lines are saturated. In such cases $N_{\text{tot}}(\text{H I})$ is constrained by the absorption in the Ly limit which in turn must be inferred from the residual flux below the Ly limit and the continuum in this region. The matter is complicated by the additional absorption from lower redshift systems. Using a new low resolution Keck spectrum to estimate both the residual flux and the continuum Songaila, Wampler, & Cowie (1997) obtained $D/H > 4 \times 10^{-5}$.

Burles & Tytler (1997) attempted to refute these objections and used yet another low resolution Keck spectrum of Q1937–1009 to measure $\log N_{\text{tot}}(\text{H I}) = 17.86 \pm 0.02$, slightly lower than their previous result. However, it is an undeniable fact that the measured optical depth at the Ly limit depends on the assumed additional absorption from lower redshift systems. Burles & Tytler (1997) simply stated that

they used the results of Kirkman & Tytler (1997) to correct for this effect but they did not explore this issue in any detail.

In the most comprehensive D/H analysis to date Burles & Tytler (1998a) relaxed their initial assumptions about this absorption system and explored a variety of models. In particular, they no longer used the metal lines to constrain the positions of the H I components and they included variations of the local continuum in their fits. They also included a model where a single (but not multiple) H I component contaminated the region of D I absorption. All their models were in agreement with $D/H < 3.9 \times 10^{-5}$ but they found “contamination to be unlikely” and concluded $D/H = (3.3 \pm 0.3) \times 10^{-5}$. However, they used their previously measured high value of $N_{\text{tot}}(\text{H I})$ as a constraint and so this result is not overly surprising.

Q1718+4807: Webb et al. (1997) published the first D/H result at low redshift ($z = 0.70$). A high resolution HST spectrum of the Ly α and Si III $\lambda 1206$ lines was supplemented with an IUE spectrum of the Ly limit. All three features were adequately fit by a single component, with Ly α requiring additional absorption at the expected position of D I Ly α and $N(\text{H I})$ well determined by the partial Ly limit. The result: $D/H = (20 \pm 5) \times 10^{-5}$. The number density of Ly α absorption lines at $z = 0.7$ is considerably lower than at $z = 3 - 4$ and therefore the probability of a *random* H I interloper is accordingly smaller. Webb et al. (1997) estimated the probability of a random interloper falling within $\pm 4\sigma$ of the expected D I position at $\lesssim 1$ per cent.

Tytler et al. (1999) added a Keck spectrum of the Mg II $\lambda\lambda 2796, 2803$ doublet to the above data and this showed the same simple velocity structure as the other lines. They relaxed some of the assumptions employed by Webb et al. (1997) and derived $8 \times 10^{-5} < D/H < 57 \times 10^{-5}$ (95 per cent confidence limits). In contrast to their analysis of the Q1937–1009 system, they found that the presence of an H I interloper (i.e. a second component near the position of D I that would allow $D/H = 0$) was “reasonable” in this system, basing their argument essentially on the fact that such simple velocity structures are fairly rare. HST observations of the higher

order Ly lines have been obtained by the Tytler group more than a year ago but so far no result has been published.

Q1009+2956: Burles & Tytler (1998b) repeated the analysis of Burles & Tytler (1998a) and Burles & Tytler (1997) for an absorption system at $z = 2.50$. However, there were two important differences. Firstly, they found that not using the $N_{\text{tot}}(\text{H I})$ constraint as derived from a low resolution spectrum and a model for the additional low redshift absorption did not alter their result for D/H. Secondly, they found evidence for contamination of the D I absorption by H I, as the inclusion of an additional H I line improved their overall fit significantly and allowed the redshifts of the main components to more closely coincide with the redshifts of the metal lines. Accounting for contamination (by a *single* interloper) they quoted a detection, $\text{D/H} = 4.0_{-0.7}^{+0.6} \times 10^{-5}$, rather than an upper limit.

APM 08279+5255: Molaro et al. (1999) reported $\text{D/H} \approx 1.5 \times 10^{-5}$ from a Keck spectrum of an absorption system at $z = 3.51$. Only Ly α , Ly β and several metal transitions are available for this system, with Ly β rendered useless by lower redshift Ly α absorption. Their conclusion is quite remarkable considering that they unambiguously showed that the data clearly permitted D/H as high as 21×10^{-5} . In any case, this system obviously has a complex velocity structure and both C IV and Si IV seem to show substructure on the blue side of the main (and Molaro et al.'s only fitted) component.

Q0130–4021: Using a Keck spectrum, Kirkman et al. (2000) analysed the Ly series lines of a $z = 2.80$ absorption system with apparently very simple velocity structure. Most of the series was fit well by a single component. The high order (Ly-12 and higher) lines were not saturated so that $N(\text{H I})$ was well constrained. Using this single component they found there was only little excess absorption in the blue wing of Ly α and thus concluded $\text{D/H} < 6.7 \times 10^{-5}$. Only an upper limit was possible in this case because a single absorption line could not explain all of the excess absorption. However, the associated weak metal absorption may show some velocity structure and they did not explore the possibility that the data might

accommodate a larger D/H by assuming a slightly more complex structure.

HS 0105+1619: Most recently, O’Meara et al. (2001) presented their analysis of a $z = 2.54$ system, again using Keck data. Of all the systems that have been analysed so far, this one has the highest column density: $\log N_{\text{tot}}(\text{HI}) = 19.42$ as measured from the core and damping wings of Ly α and the Ly limit region. Due to this high value, D I Ly α was lost in the strong H I, but an absorption line was detected near the expected position of D I in Ly β , γ , ϵ , 6 and 7. The absorption was modelled by a single component which was supported by the appearance of the low ionization metal lines. These are thought to trace the H I best since the H is expected to be mostly neutral at these column densities. They measured D/H = $(2.54 \pm 0.23) \times 10^{-5}$. They rejected the possibility of an H I interloper on the grounds that the measured $b(\text{D I}) = 9 \text{ km s}^{-1}$ was too small for an H I line but consistent with the expectations from the b parameters of H I, O I and N I.

For completeness we mention the efforts by Levshakov and collaborators who have also analysed the Q1937–1009, Q1718+4807 and APM 08279+5255 systems using a mesoturbulent absorption model (Levshakov, Kegel, & Takahara 1998a; Levshakov, Kegel, & Takahara 1998b; Levshakov, Kegel, & Takahara 2000). They consistently find D/H $\approx 4 \times 10^{-5}$ in all of these systems.

In summary, Q0014+813 gives at best a high upper limit on D/H. Q1718+4807 provides a strong case for a high value of D/H at low redshift but we currently lack the important observations of the higher order Ly lines. Of the four results published by the Tytler group, one gives an intermediate upper limit, one is contaminated and should thus also be viewed as an upper limit and the remaining two give good evidence of a low value of D/H. However, the dispersion among the quoted D/H values of this group is actually larger than the quoted error bars and thus we suspect that either contamination has not been fully accounted for (contrary to their claims) or that there remain unidentified systematics. We summarise all of the above results on D/H in Fig. 6.2.

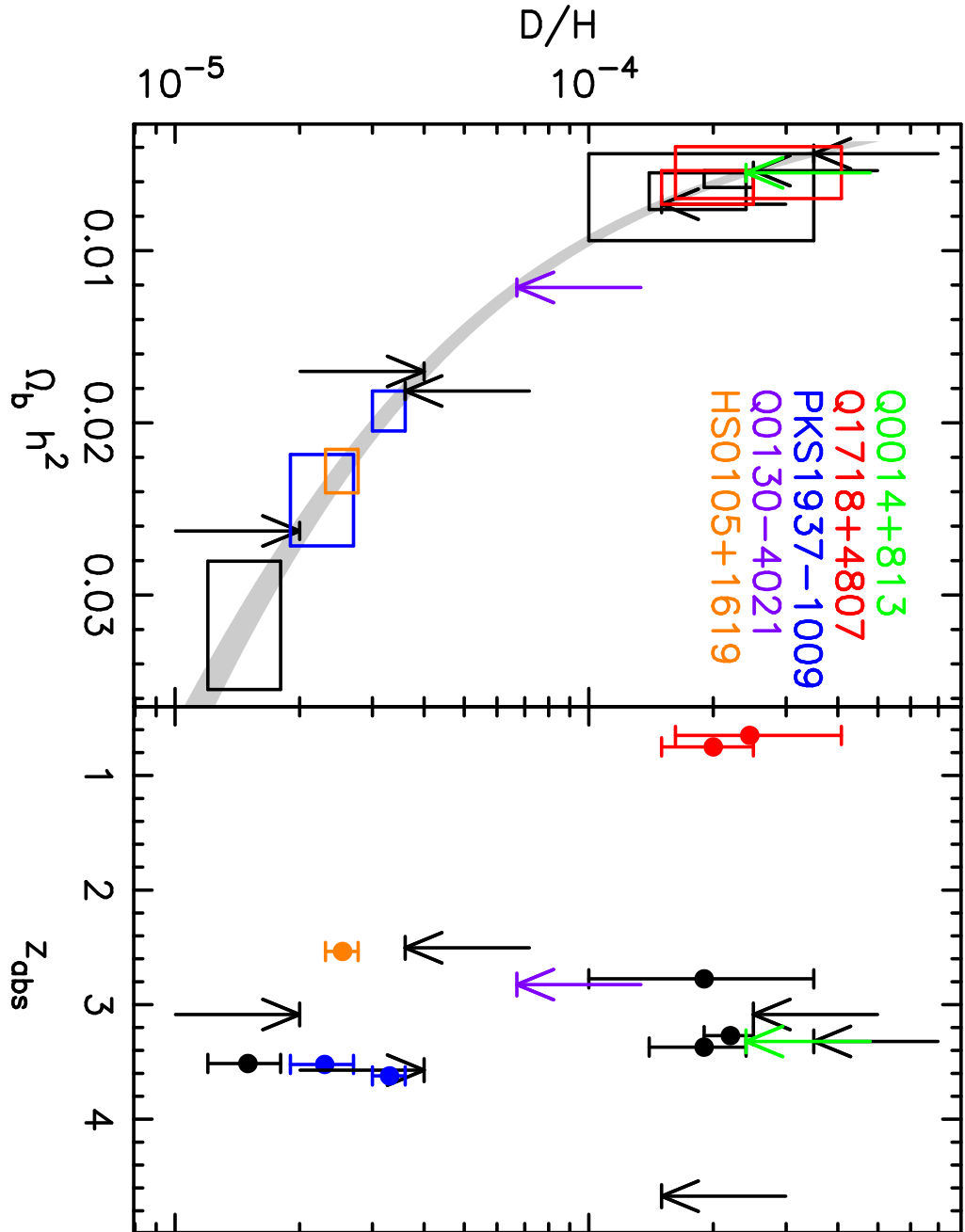


Figure 6.2: Summary of D/H measurements in QSO absorption systems. Some reasonably reliable results are highlighted. We plot upper limits whenever the authors explicitly admitted the possibility of an interloper. We applied redshift offsets to some points for clarity. The grey band is the standard BBN prediction.

6.2 Pre-selection of D/H candidates

In the previous sections we have outlined the motivation for an accurate and reliable measurement of D/H and we have seen that the current observational situation does not meet these criteria. In this section we address the question of how this situation is most efficiently remedied.

6.2.1 The necessity of pre-selection

A reliable D/H estimate requires an accurate measurement of column densities and the ability to resolve possible velocity structure. Hence the final decision whether a given absorption system is suitable for a D/H measurement can only be made from high resolution ($\lesssim 10 \text{ km s}^{-1}$) data. Thus the most reliable way to find new D/H systems is to perform a QSO survey at high resolution. However, since most QSOs are quite faint, high resolution spectroscopy requires the use of an 8-m class telescope. In addition, as we shall see below, suitable D/H systems must meet some rather stringent requirements. They are thus quite rare and we must survey a large number of QSOs to find new ones. Clearly, the amount of large telescope time needed for such a survey is prohibitively high. We are thus faced with the task to select suitable absorption systems from lower resolution spectroscopy.

6.2.2 The ideal D/H absorption system

Webb et al. (1991) and Khersonsky, Briggs, & Turnshek (1995) investigated the characteristics of an absorption system suitable for a determination of D/H. Essentially, only two pieces of information are required to derive these characteristics: i) $D/H \lesssim \text{a few} \times 10^{-4}$ and ii) the Ly series lines of D I are shifted by -81.6 km s^{-1} with respect to the H I lines. The first implies $\log N(\text{H I}) \gtrsim 16.5$ so that D I can be detected with realistic S/N ratios. For column densities near this limit the D I can be seen in Ly α only. For $\log N(\text{H I}) \gtrsim 19$ the D I Ly α line is completely lost in the corresponding H I, but D I is now apparent in the higher order lines. The high H I

column density and ii) imply that the absorber should have a small b -parameter. Otherwise the D I and H I lines will not be well separated and it will be difficult to constrain the parameters of the much weaker D I absorption. In addition to these requirements the absorption system should have as few components as possible. Complex velocity structure may cause either $N(\text{D I})$ or $N(\text{H I})$ to be poorly constrained.

So the ideal absorbers for measuring D/H are those with $\log N(\text{H I}) \gtrsim 16.5$, whose Doppler width is as small as possible, $b \simeq 15 \text{ km s}^{-1}$, and whose velocity structure is as simple as possible, i.e. at least no contaminant at shorter wavelengths than the main H I component, where the D I feature is expected.

6.2.3 Principles of pre-selection

How then can we go about selecting absorbers that are likely to meet the above requirements from low or intermediate resolution spectroscopy? First of all, at $\log N(\text{H I}) \gtrsim 17.0$ an absorber produces a clear Ly break ('Lyman limit system') which can be easily identified even in low resolution spectra. Secondly, by comparing the equivalent widths of several lines in the Ly series we can detect unresolved, low column density sub-components. Thirdly, the position of a spectral feature can usually be determined to an accuracy of 10–20 per cent of the FWHM of the line spread function. Again exploiting curve of growth effects we can place additional constraints on possible sub-dominant absorption by comparing the positions of the various Ly series lines and the Ly limit. Finally, if an absorption system has several narrow, unresolved components which are similarly strong we can treat it as a single line and attempt to deduce the velocity structure from the effective b -parameter.

We illustrate these ideas with a simple example. Consider an absorption system consisting of one main component of $\log N(\text{H I}) = 17.0$, $b = 20 \text{ km s}^{-1}$ at $z = 3$ and an interloper of smaller column density at some distance Δv towards the blue. Let us assume the interloper has $\log N_{\text{I}}(\text{H I}) = 14.0$ and Δv is small enough so that the two components are unresolved in low or intermediate resolution spectra. For

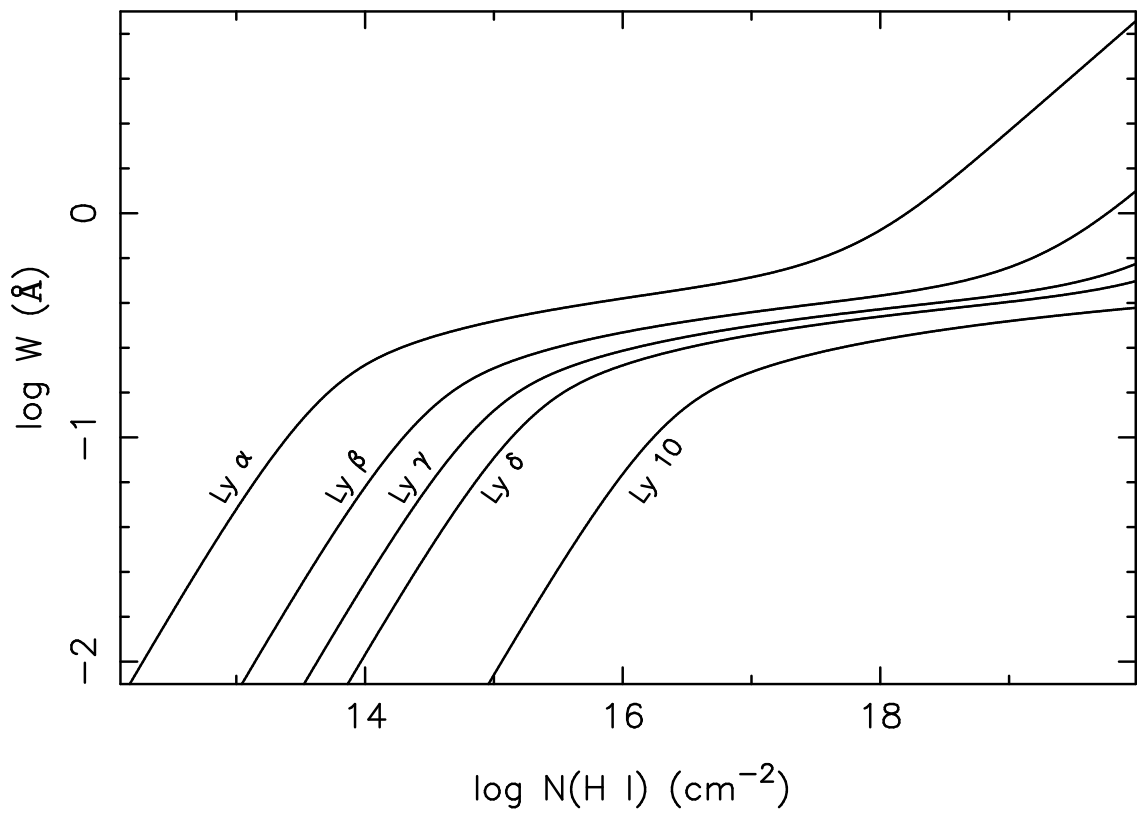


Figure 6.3: Curve of growth for the indicated Ly series transitions. We plot rest equivalent width W versus HI column density for $b = 20 \text{ km s}^{-1}$.

Ly α both components are on the flat part of the curve of growth (cf. Fig. 6.3) so that the interloper actually contributes a substantial fraction of the total equivalent width of the blend. However, in Ly γ , for example, the flat part of the curve of growth is shifted towards higher column densities by ~ 1.5 orders of magnitude (cf. Fig. 6.3). Thus in Ly γ (and all higher series lines) the interloper does *not* contribute significantly to the total equivalent width of the blend. The equivalent widths of the high order lines and the shape of the Ly limit will therefore all be consistent with the $N(\text{H I})$ and b of the main component. The equivalent width of the Ly α line, however, will be too large, indicating the presence of the interloper. We point out that the Ly limit plays a crucial role in this. Even in low resolution data its shape and depth provide very strong constraints on b and $N(\text{H I})$ respectively.

We can construct a parallel argument to the one above for the relative positions of the Ly series lines. As the interloper contributes significantly to the equivalent width of Ly α the position of the blend will be shifted with respect to the position of the main component. The position of Ly γ on the other hand will *not* be significantly different from that of the main component.

In Fig. 6.4 we plot the difference between the positions of the blended Ly α and Ly γ lines, $\delta v_{\alpha\gamma}$, as a function of the interloper column density $N_{\text{I}}(\text{H I})$ for a range of different Δv values. The positions of the blends are approximated as the equivalent width weighted averages of the positions of the individual components. We can see that the maximum shift between Ly α and Ly γ occurs at $\log N_{\text{I}}(\text{H I}) \approx 14.1$. For larger values the interloper approaches the flat part of the growth in Ly γ (cf. Fig. 6.3) where it contributes substantially to the total equivalent width of the blend. Consequently, the difference between Ly α and Ly γ is smaller. For smaller values of $N_{\text{I}}(\text{H I})$ the difference is also smaller because the interloper ‘falls’ down the knee of the curve of growth in Ly α . This behaviour is actually quite desirable because we do not wish to bias against possible systems with high D/H. The position and width of the ‘bump’ in Fig. 6.4 depends on which lines are used for the comparison. If Ly α is used with higher order lines, the bump shifts towards higher column densities

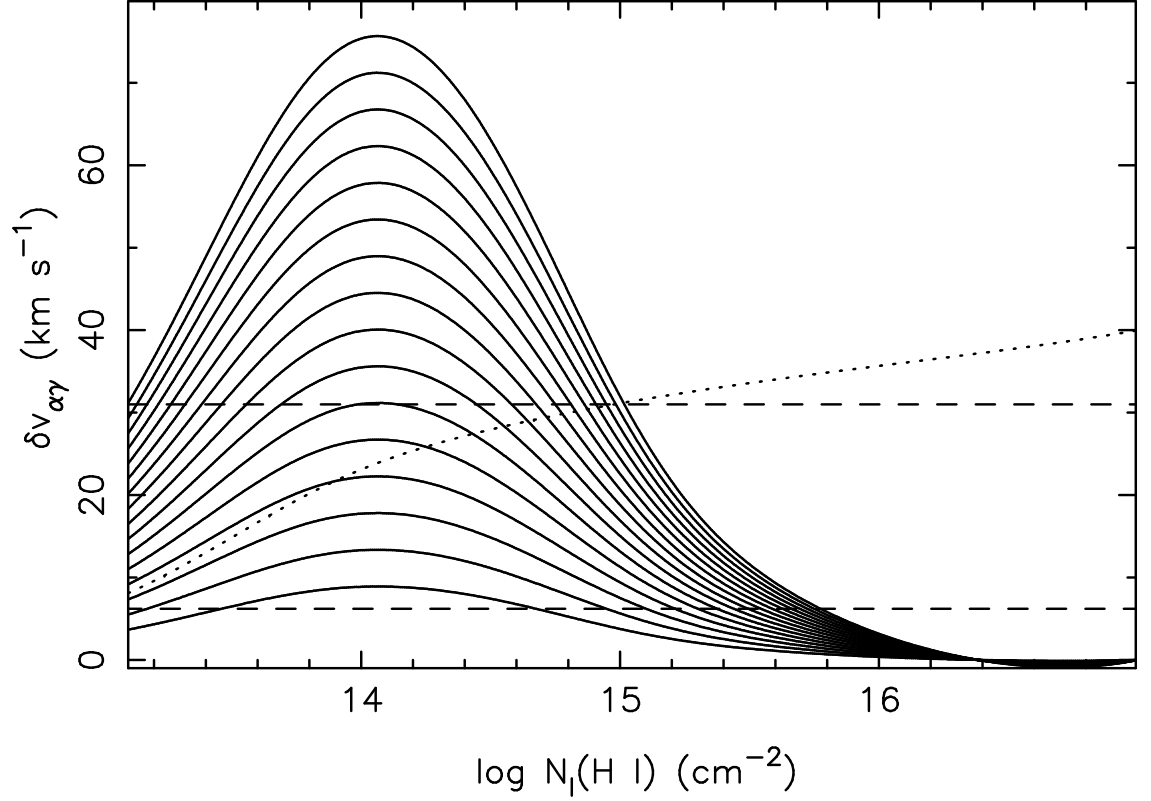


Figure 6.4: A main component with $\log N(\text{H I}) = 17.0$, $b = 20 \text{ km s}^{-1}$ and $z = 3$ is blended with an interloper of $N_{\text{I}}(\text{H I})$, $b = 20 \text{ km s}^{-1}$, which is separated from the main component by Δv . $\delta v_{\alpha\gamma}$ is the difference in the positions of the blended Ly α and Ly γ lines. We plot $\delta v_{\alpha\gamma}$ for several different values of Δv , starting with 40 km s^{-1} (lowest solid line) and then in steps of 20 km s^{-1} to 340 km s^{-1} . The dotted line gives the difference in the positions of the Ly α blend and the main component for $\Delta v = 80 \text{ km s}^{-1}$. The two horizontal dashed lines give the approximate accuracy to which a line position can be determined for a resolution of 5 \AA (upper line) and 1 \AA (lower line).

and becomes more pronounced. Realistically, however, one cannot go very far up the series because of severe blending at low resolution. In any case, Fig.6.4 and the related argument above demonstrate that *at least in principle* we are able to reject systems with sub-dominant components that might interfere with the D/H measurement.

It is apparent that the argument above breaks down if the total column density of the system is divided roughly equally among two or more components. In this case all the components contribute equally to the equivalent widths, their ratios will all be consistent with a single value of $N(\text{HI})$ and b and no line shifts will occur. Essentially, as long as it is unresolved such a system behaves like single line. If the individual components have small b -parameters these systems may in principle be useful for a D/H measurement because the D I line of the bluest components is free of contamination. However, if the components are closely spaced then it is usually difficult to constrain their parameters and therefore we would like to be able to reject these systems.

To investigate this issue we have performed a very simple experiment. We have equally divided a total column density of $N(\text{HI}) = 2 \times 10^{17} \text{ cm}^{-2}$ among three equally spaced components at $z = 3$. Each of the components has $b = 20 \text{ km s}^{-1}$. We have created several spectra for this system, each with a different inter-component spacing. The spectra were convolved with a Gaussian of width 5 \AA . Each of these spectra was then fit with a single Voigt profile using the entire Ly series, including the Ly limit. In Fig. 6.5(a) we plot as solid dots the ‘effective b -parameter’ of the fit versus Δv , the velocity range of the system. We then repeated the experiment with 1 \AA resolution and smaller velocity separations and plot the results as open squares.

For $\Delta v = 0 \text{ km s}^{-1}$ the three component system is identical to a single component with $N(\text{HI})$ equal to the sum of the individual column densities. This is only true because b is the same for all three components ($= 20 \text{ km s}^{-1}$). Thus for $\Delta v = 0 \text{ km s}^{-1}$ we also find $b_{\text{eff}} = 20 \text{ km s}^{-1}$. As Δv is increased b_{eff} also increases in order to fit the larger equivalent widths of the Ly lines. At $\Delta v \approx 190 \text{ km s}^{-1}$

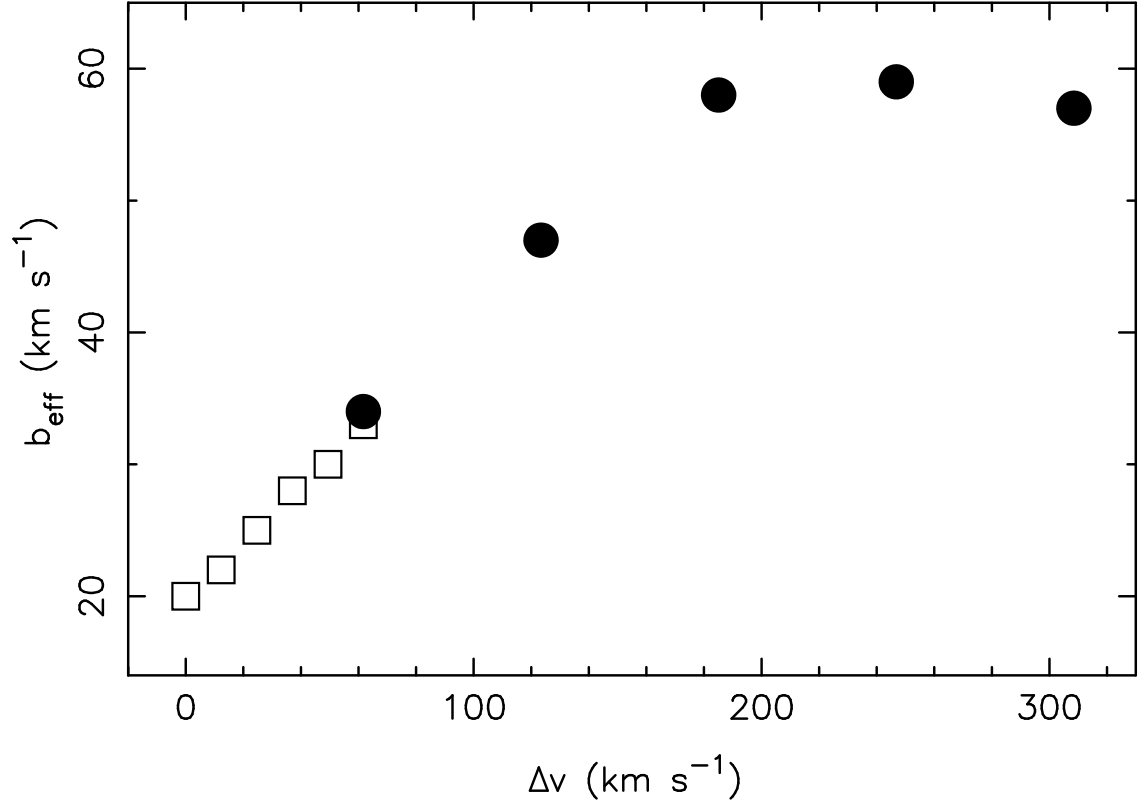


Figure 6.5: (a) Effective b -parameter of a single component fit to a multiple component system versus the total velocity range of the system. The absorption system consists of three identical and equally spaced absorption lines at $z = 3$, each with $b = 20 \text{ km s}^{-1}$ and a total column density of $2 \times 10^{17} \text{ cm}^{-2}$. Solid dots and open squares are for 5 \AA and 1 \AA resolution respectively.

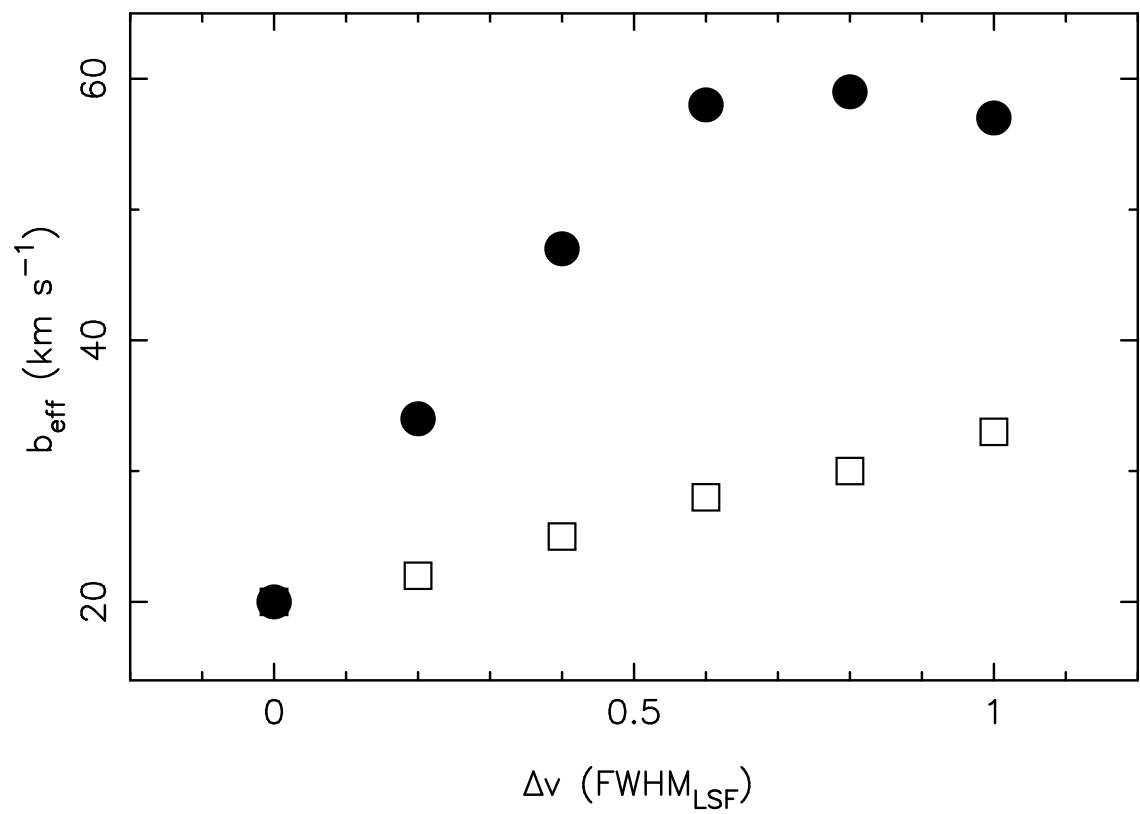


Figure 6.5: (b) Same as (a) but now Δv is given in units of the FWHM of the line spread function.

the three components have more or less completely separated. From then on the equivalent widths are not sensitive to Δv anymore and b_{eff} levels out.

In a sense, the process is actually more efficient at 5 Å resolution than at 1 Å. In Fig. 6.5(b) we again plot b_{eff} versus Δv but now we give Δv in units of the FWHM of the line spread function. Clearly, at 5 Å a Δv corresponding to half a resolution element makes a larger difference to b_{eff} than at 1 Å. The reason for this behaviour is essentially that at 1 Å the contribution to b_{eff} from the b -parameter of the individual lines is relatively larger than at 5 Å. Fig 6.5 demonstrates that we can effectively ‘resolve’ the velocity structure of similarly strong components on scales significantly below the spectral resolution.

In practice most absorption systems will be more complicated than the simple examples we have discussed above. In addition, our efforts to select the simple ones will be hampered by finite S/N and blending of high order lines with lower redshift low order lines. Clearly, a thorough investigation of these issues, involving a large range of detailed simulations, is called for. This is the immediate objective of future work.

6.2.4 Summary

Nevertheless, we believe the discussion above demonstrates that the idea of selecting D/H candidates from lower resolution data is tenable. In any case, given the scarcity of 8-m telescopes some sort of selection process is inevitable. Here, we propose a strategy with two distinct phases. First, we need a low resolution (~ 5 Å) survey of all known bright, high redshift QSOs. The primary purpose of this survey is to find new Ly limit systems and to reject those with obviously very complex velocity structure. In a second phase, the remainder are observed at ~ 1 Å resolution in order to place much tighter constraints on the velocity dispersion of the main components and the column density of possible interlopers near the expected position of D I. The candidates that survive this second round of selection are prime targets for further high resolution observations.

6.3 PD2H: a low resolution spectroscopic QSO survey

The first phase of the observational programme outlined above is well under way. In this section we describe a new, low resolution spectroscopic survey of high redshift, luminous QSOs. The goal of this survey is to identify candidate absorption systems for measurements of the primordial D/H ratio (hence its name “PD2H”).

The target selection for this survey is straightforward. First, observability of the Ly limit from ground-based telescopes requires $z_{\text{em}} \gtrsim 2.9$. Secondly, if a suitable candidate system has been identified, we will eventually have to observe it at high spectral resolution ($\lesssim 10 \text{ km s}^{-1}$) and high S/N. From published Keck data we estimate that this condition implies $m_V \lesssim 18.5$. Applying these selection criteria to the latest QSO catalogue (Véron-Cetty & Véron 2000) gives 209 objects, of which 134 are accessible from the southern hemisphere ($\delta < +15^\circ$) where we conducted most of our observations. As it is essential to accumulate as many spectra as possible, we slightly relaxed these criteria as the survey progressed: we observed fainter and/or lower redshift QSOs whenever no unobserved QSOs were available during an observation run.

In total, we have observed 101 QSOs using the Australian National University 2.3-m Telescope at Siding Spring Observatory and the William-Herschel-Telescope (WHT) at La Palma. Sargent, Steidel, & Boksenberg (1989) (SSB hereafter) and Storrie-Lombardi et al. (1996) (SL hereafter) have conducted similar surveys in the past (using the Hale 5-m Telescope and the WHT respectively) and they have generously made their data available to us. Combining these samples yields a total of 187 spectra of 171 different objects. In Table 5.1 we list the coordinates, redshifts, magnitudes, observation dates and exposure times for the full sample. The coordinates and magnitudes were taken from Véron-Cetty & Véron (2000). The redshifts were taken from the same source except in 13 cases where the redshifts were obviously wrong. In these cases we measured the redshifts from C IV and/or

$\text{Ly}\alpha$ emission lines. In Fig. 6.6 we show the final spectra of the full sample. We include the SSB and SL data in Table 5.1 and Fig. 6.6 to provide a reference for future work. In addition, it is helpful to be able to compare the spectra of those QSOs that were observed by both us and SSB or SL.

Six of our targets turned out not to be high redshift QSOs. These objects are listed in Table 6.2 and their spectra are shown in Fig. 6.7.

In the following sections we describe the observational and data reduction procedures.

Table 6.1: Log of observations.

Object ^a	α_{J2000}			δ_{J2000}			z_{em}	m_V	Telescope	Date	Exposed	Comments ^b
	h	m	s	°	'	"						
Q0001+0842	00	03	42.6	+08	59	40	3.241	19.30	Hale-5m	18/10/87	3000	SSB
									WHT	21/10/99	4500	
Q0004+1711	00	06	47.3	+17	28	14	2.898	18.70	Hale-5m	18/10/87	2000	SSB
Q0004-0137	00	07	09.9	-01	21	04	2.950 ^c	18.50	WHT	20/10/99	1200	
Q0007+0141	00	09	58.7	+01	57	54	2.948	19.30	WHT	20/10/99	1200	
Q0008+0053	00	10	57.6	+01	10	12	3.084	18.50	2.3m	28/10/00	5400	
Q0010+0050	00	13	27.5	+01	06	46	3.076	18.80	WHT	20/10/99	1200	
Q0012+0623	00	15	27.4	+06	40	12	3.170	18.00	2.3m	09/11/99	3600	
Q0019-1522	00	22	08.0	-15	05	39	4.528	19.00	WHT	04/10/92	2700	SL
Q0014+8118	00	17	08.1	+81	35	07	3.387	16.30	Hale-5m	18/10/87	700	SSB
Q0029+0722	00	32	18.3	+07	38	33	3.262	17.44	Hale-5m	18/10/87	2000	SSB
Q0032-3729	00	34	26.8	-37	12	52	3.180	17.90	2.3m	07/10/99	3600	
Q0039-4952	00	41	31.5	-49	36	12	3.240	16.10	2.3m	06/10/99	2700	
Q0041-2638	00	43	42.8	-26	22	11	3.053	17.79	2.3m	06/10/99	3600	
Q0042-2627	00	44	34.1	-26	11	21	3.289	17.67	2.3m	04/10/99	5400	
Q0045-0341	00	47	50.1	-03	25	31	3.130	18.80	Hale-5m	18/10/87	2000	SSB
Q0047-3050	00	50	20.1	-30	34	21	2.973	18.24	2.3m	07/10/99	5400	no autoguiding
Q0049+0121	00	51	59.7	+01	38	04	3.480 ^c	18.97	WHT	21/10/99	3028	close to moon
Q0053-2824	00	56	25.1	-28	08	33	3.616	18.24	Hale-5m	18/10/87	2500	SSB
Q0055-2524	00	58	06.8	-25	08	25	2.940	18.39	2.3m	08/10/99	3600	
Q0055-2659	00	57	58.1	-26	43	14	3.662	17.47	Hale-5m	18/10/87	3200	SSB
									2.3m	28/10/98	3600	
Q0056+0125	00	59	17.6	+01	42	06	3.154	18.60	WHT	20/10/99	1200	
Q0101-3025B	01	03	55.2	-30	09	47	3.150	17.91	Hale-5m	18/10/87	1500	SSB
Q0102-1902	01	05	16.8	-18	46	42	3.037	18.30	Hale-5m	18/10/87	1000	SSB
Q0103+0032	01	06	19.3	+00	48	23	4.437	18.60	WHT	21/08/93	3000	SL
Q0105-2634	01	08	12.4	-26	18	20	3.488	17.73	2.3m	05/10/99	3600	
Q0112+0254	01	14	34.9	+03	09	51	2.819	18.60	Hale-5m	18/10/87	1900	SSB
Q0114-0857	01	17	23.3	-08	41	32	3.163	17.70	Hale-5m	18/10/87	700	SSB

Table 6.1 – *continued*

Object ^a	α_{J2000}			δ_{J2000}			z_{em}	m_V	Telescope	Date	Exposed	Comments ^b
	h	m	s	°	'	"						
Q0130–4021	01	33	01.9	–40	06	28	3.023	17.02	2.3m	05/10/99	3600	
Q0132–1947	01	34	38.6	–19	32	07	3.131	18.00	Hale-5m	18/10/87	1500	SSB
Q0140–3038	01	42	54.7	–30	23	45	3.122	18.00	2.3m	28/10/98	3600	
Q0143–0101	01	46	19.9	–00	46	29	3.159	19.30	WHT	21/10/99	4500	
Q0143–0135	01	45	51.2	–01	20	30	3.141	17.70	Hale-5m	18/10/87	1200	SSB
Q0148–0946	01	51	06.6	–09	32	00	2.850	18.40	Hale-5m	18/10/87	2500	SSB
Q0151–0025	01	53	39.5	–00	11	00	4.194	18.65	WHT	21/08/93	3000	SL
Q0153+0430	01	56	36.0	+04	45	28	2.993	17.90	Hale-5m	18/10/87	800	SSB
Q0201+3634	02	04	55.6	+36	49	18	2.912	17.90	Hale-5m	18/10/87	900	SSB
Q0201+1120	02	03	46.7	+11	34	44	3.640 ^c	19.50	WHT	20/10/99	1200	
Q0201–5026	02	03	45.0	–50	12	26	2.966	18.60	2.3m	08/10/99	3600	
Q0202–4613	02	04	35.5	–45	59	23	3.240	18.40	2.3m	09/11/99	3600	
Q0207–0019	02	09	50.7	–00	05	06	2.853	17.00	Hale-5m	18/10/87	700	SSB
Q0215–3714	02	17	41.8	–37	01	00	2.910	18.00	2.3m	07/10/99	5400	
Q0216+0803	02	18	57.3	+08	17	28	2.990	18.10	Hale-5m	18/10/87	2100	SSB
Q0239–1527	02	41	56.5	–15	14	41	2.786	18.10	Hale-5m	18/10/87	2000	SSB
Q0239–3646	02	41	22.7	–36	33	19	3.100	17.70	2.3m	28/10/00	7200	
Q0241–0146	02	44	01.8	–01	34	02	4.053	18.20	WHT	21/08/93	1800	SL
									2.3m	13/01/99	900	cloudy
									2.3m	18/02/99	3600	
Q0245–0608	02	47	56.5	–05	55	58	4.238	18.60	WHT	21/08/93	3000	SL
Q0246+1750	02	48	54.3	+18	02	50	4.430	18.40	WHT	20/10/99	1200	
Q0249+0118	02	51	51.9	+01	30	57	2.981	18.70	WHT	20/10/99	1200	
Q0249–1826	02	51	47.9	–18	14	29	3.209	18.60	Hale-5m	18/10/87	1500	SSB
Q0249–2212	02	51	40.4	–22	00	27	3.205	17.70	Hale-5m	18/10/87	1500	SSB
Q0256–0000	02	59	05.6	+00	11	22	3.377	17.50	Hale-5m	18/10/87	1500	SSB
Q0301–0035	03	03	41.1	–00	23	22	3.226	18.00	Hale-5m	18/10/87	1500	SSB
Q0302+1705	03	05	04.9	+17	16	53	2.883	18.90	Hale-5m	18/10/87	1800	SSB
Q0302–0019	03	04	49.9	–00	08	13	3.290	17.44	Hale-5m	18/10/87	900	SSB
									2.3m	13/01/99	1800	
Q0308+1902	03	11	42.7	+19	13	40	2.839	18.40	Hale-5m	18/10/87	1200	SSB
Q0308–1921	03	10	28.1	–19	09	44	2.756	17.90	Hale-5m	18/10/87	1200	SSB
Q0316–2023	03	18	25.2	–20	12	19	2.869	18.50	Hale-5m	18/10/87	3600	SSB
Q0324–4047	03	26	17.4	–40	36	50	3.056	17.80	2.3m	05/10/99	3600	
Q0334–2029	03	36	26.9	–20	19	39	3.132	18.20	Hale-5m	18/10/87	1500	SSB
Q0336–0143	03	39	00.9	–01	33	18	3.197	18.80	WHT	20/10/99	1200	
									WHT	21/10/99	5400	
Q0345+0130	03	48	02.2	+01	39	18	3.636	19.94	WHT	20/10/99	1200	
Q0347–3819	03	49	43.7	–38	10	31	3.222	17.80	2.3m	05/10/99	3600	
Q0351–1034	03	53	46.9	–10	25	19	4.351	18.60	WHT	20/09/93	3700	SL
Q0351–3904	03	53	19.2	–38	55	56	3.010	17.00	2.3m	20/02/99	3600	cloudy

Table 6.1 – *continued*

Object ^a	α_{J2000}	δ_{J2000}	z_{em}	m_V	Telescope	Date	Exposed	Comments ^b
	h m s	° ' "						
Q0352–2733	03 54 05.6	–27 24 20	2.823	17.90	Hale-5m	18/10/87	1200	SSB
Q0401–1711	04 03 56.6	–17 03 24	4.236	18.70	WHT	02/02/95	3600	SL
Q0402–3343	04 04 01.9	–33 35 00	3.040	17.60	2.3m	22/02/99	5400	cloudy
Q0405–4418	04 07 18.0	–44 10 14	3.000	17.40	2.3m	28/10/98	3600	
Q0420+0023	04 22 41.8	+00 30 20	2.921	19.00	Hale-5m	18/10/87	1500	SSB
Q0420–3851	04 22 14.8	–38 44 52	3.123	16.92	2.3m	28/10/98	1800	
Q0428–1342	04 30 38.8	–13 35 46	3.249	17.00	2.3m	20/02/99	3600	cloudy
Q0437–5053	04 39 06.9	–50 47 40	2.940	18.60	2.3m	09/11/99	3600	
Q0443–3204	04 45 52.0	–31 58 43	2.710 ^c	18.00	2.3m	21/02/99	3600	
Q0443–4054	04 45 32.6	–40 48 50	3.150 ^c	17.60	2.3m	09/11/99	3600	
					2.3m	28/10/00	5400	
Q0449–1325	04 51 42.6	–13 20 33	3.093	18.20	Hale-5m	18/10/87	1200	SSB
					2.3m	12/01/99	5400	
Q0515–3757	05 17 42.2	–37 54 46	3.020	17.50	2.3m	19/02/99	3600	
					2.3m	21/02/99	1800	
Q0528–2505	05 30 08.0	–25 03 30	2.765	17.34	Hale-5m	18/10/87	900	SSB
Q0558–5040	06 00 08.1	–50 40 36	3.130	17.50	2.3m	13/01/99	3600	
					2.3m	09/11/99	3600	
Q0636+6801	06 42 04.0	+67 58 36	3.177	16.60	Hale-5m	18/10/87	600	SSB
					WHT	21/10/99	1800	
Q0642+4454	06 46 32.0	+44 51 17	3.408	18.49	Hale-5m	18/10/87	1800	SSB
Q0642–5038	06 43 27.0	–50 41 13	3.090	18.10	2.3m	18/02/99	3600	
					2.3m	22/02/99	1800	
Q0731+6519	07 36 21.1	+65 13 11	3.038	18.50	Hale-5m	18/10/87	2000	SSB
Q0748+5624	07 52 45.7	+56 16 43	3.075	19.47	WHT	20/10/99	1200	
Q0749+4239	07 53 03.3	+42 31 30	3.590	18.30	WHT	20/10/99	1200	
Q0805+0441	08 07 57.5	+04 32 34	2.880	18.16	Hale-5m	18/10/87	1500	SSB
Q0830+1133	08 33 14.3	+11 23 37	2.979	18.00	Hale-5m	18/10/87	1200	SSB
					2.3m	19/02/99	3600	
Q0846+1540	08 49 08.1	+15 29 32	2.912	17.80	Hale-5m	18/10/87	1500	SSB
Q0850+2818	08 53 03.6	+28 07 10	2.980 ^c	19.30	WHT	20/10/99	1200	
Q0850+1755	08 53 36.6	+17 43 48	3.210	18.00	WHT	20/10/99	1200	
Q0852+5621	08 56 13.4	+56 10 05	2.999	19.29	WHT	21/10/99	5400	
Q0930+2858	09 33 37.3	+28 45 32	3.428	17.50	WHT	20/10/99	1200	
Q0940–1050	09 42 53.6	–11 04 26	3.054	16.90	2.3m	12/01/99	3600	
Q0941+2608	09 44 42.3	+25 54 44	2.913	18.59	Hale-5m	18/10/87	1525	SSB
Q0945–0411	09 47 49.6	–04 25 14	4.145	18.80	WHT	24/04/92	2700	SL
Q0951–0450	09 53 55.7	–05 04 18	4.369	18.90	WHT	25/04/92	2700	SL
Q0952–0115	09 55 00.1	–01 30 07	4.426	18.70	WHT	24/04/92	1000	SL
Q0956+1217	09 58 52.2	+12 02 45	3.306	17.60	Hale-5m	18/10/87	1000	SSB
					2.3m	13/01/99	3600	

Table 6.1 – *continued*

Object ^a	α_{J2000}			δ_{J2000}			z_{em}	m_V	Telescope	Date	Exposed	Comments ^b
	h	m	s	°	'	"						
Q1013+0035	10	15	49.0	+00	20	19	4.405	18.80	WHT	24/04/92	2700	SL
Q1017+1055	10	20	10.0	+10	40	02	3.158	17.20	Hale-5m	18/10/87	1200	SSB
									2.3m	21/02/99	3600	
Q1031-2458	10	33	59.9	-25	14	27	2.550 ^c	17.50	2.3m	12/01/99	3600	seeing > 3''
									2.3m	21/02/99	1800	
Q1033+1342	10	36	26.9	+13	26	52	3.074	18.00	2.3m	20/02/99	1800	cloudy
									2.3m	21/02/99	1800	
Q1033-0327	10	36	23.7	-03	43	20	4.509	18.50	WHT	17/04/93	2700	SL
									2.3m	18/02/99	3600	
									2.3m	22/02/99	3600	
Q1036-2257	10	39	09.5	-23	13	26	3.130	16.70	2.3m	13/01/99	3600	
Q1050-0000	10	53	20.4	-00	16	50	4.286	18.60	WHT	25/04/92	1800	SL
Q1055-2549	10	58	09.2	-26	05	39	2.880 ^c	17.90	2.3m	19/02/99	3600	
Q1108-0747	11	11	13.6	-08	04	02	3.922	18.10	WHT	25/04/92	1800	SL
									2.3m	20/02/99	3600	
									2.3m	22/02/99	3600	
Q1110+0106	11	12	46.3	+00	49	58	3.918	18.30	WHT	25/04/92	1800	SL
									2.3m	21/02/99	5400	
Q1114-0822	11	17	27.1	-08	38	58	4.495	19.40	WHT	11/04/93	3000	SL
Q1117-1329	11	20	10.3	-13	46	25	3.958	18.00	WHT	24/04/92	1200	SL
									2.3m	19/02/99	3600	
Q1144-0723	11	46	35.6	-07	40	05	4.147	18.60	WHT	25/04/92	1800	SL
Q1159+1223	12	01	47.8	+12	06	30	3.502	17.50	2.3m	18/02/99	3600	seeing 4 – 5''
Q1202-0725	12	05	23.1	-07	42	32	4.694	18.70	WHT	23/04/92	5700	SL
Q1206+1155	12	09	18.0	+11	38	31	3.114	17.60	2.3m	20/02/99	1800	
									2.3m	21/02/99	1800	
Q1208+1011	12	10	57.0	+09	54	27	3.803	17.50	2.3m	18/02/99	5400	seeing 4 – 5''
Q1244+1129	12	46	40.4	+11	13	03	3.147	18.00	2.3m	22/02/99	3600	
Q1302-1404	13	05	25.2	-14	20	41	3.996	18.60	WHT	17/04/93	1500	SL
Q1314-3131	13	17	44.1	-31	47	14	2.960 ^c	17.70	2.3m	20/02/99	3600	cloudy
Q1317-0507	13	20	30.0	-05	23	35	3.700	18.10	2.3m	19/02/99	3600	
Q1328-0433	13	31	30.8	-04	48	51	4.217	19.00	WHT	17/04/93	3000	SL
Q1330+0108	13	32	54.4	+00	52	51	3.510	18.20	2.3m	19/02/99	3600	
Q1335-0417	13	38	03.4	-04	32	35	4.396	19.40	WHT	25/04/92	2700	SL
Q1345-0120	13	48	16.6	-01	35	10	2.945	18.30	2.3m	21/02/99	5400	
Q1346-0322	13	49	16.7	-03	37	15	3.992	18.80	WHT	24/04/92	2700	SL
Q1406+1221	14	08	38.9	+12	07	10	2.970	18.30	2.3m	22/02/99	3600	
Q1410+0936	14	13	21.0	+09	22	05	3.317	17.80	2.3m	22/02/99	3600	
Q1426-0131	14	29	03.0	-01	45	18	3.420	17.80	2.3m	20/02/99	3600	
Q1500+0824	15	02	45.4	+08	13	05	3.943	18.84	WHT	25/04/92	2700	SL
Q1508+5714	15	10	02.8	+57	02	47	4.301	18.90	WHT	17/04/93	3000	SL

Table 6.1 – *continued*

Object ^a	α_{J2000}			δ_{J2000}			z_{em}	m_V	Telescope	Date	Exposed	Comments ^b
	h	m	s	°	'	"						
Q1557+0313	15	59	31.1	+03	04	47	3.891	19.80	WHT	25/04/92	2700	SL
Q1738+3502	17	40	20.3	+35	00	47	3.240	20.80	Hale-5m	18/10/87	3550	SSB
Q1745+6227	17	46	14.0	+62	26	54	3.889	18.80	WHT	21/08/93	3000	SL
Q1759+7539	17	57	46.4	+75	39	16	3.050	16.50	WHT	20/10/99	600	
									WHT	21/10/99	1800	
Q1836+5108	18	37	20.0	+51	11	29	2.827	19.70	Hale-5m	18/10/87	3000	SSB
Q1946+7658	19	44	54.9	+77	05	52	3.051	16.20	WHT	21/10/99	600	
Q2000–3300	20	03	24.0	–32	51	47	3.783	17.30	Hale-5m	18/10/87	2000	SSB
Q2038–0116	20	40	51.4	–01	05	38	2.783	19.10	Hale-5m	18/10/87	2100	SSB
Q2048+3116	20	50	51.1	+31	27	27	3.198	18.00	Hale-5m	18/10/87	3600	SSB
Q2049–3522	20	52	49.4	–35	11	01	3.040	18.45	2.3m	06/10/99	3600	
Q2050–3558	20	53	44.6	–35	46	55	3.490	18.34	2.3m	05/10/99	5400	
Q2054–3533	20	57	57.9	–35	22	00	3.310	18.30	2.3m	06/10/99	5400	no autoguiding
Q2118–4018	21	21	25.0	–40	05	13	2.630 ^c	18.00	2.3m	07/10/99	3600	
Q2126–1551	21	29	12.1	–15	38	42	3.280	17.00	Hale-5m	18/10/87	1500	SSB
Q2128–3532	21	31	36.1	–35	19	03	3.130 ^c	18.50	2.3m	08/10/99	3600	
Q2138–4427	21	41	59.5	–44	13	26	3.170	18.20	2.3m	07/10/99	3600	
Q2139–4434	21	42	25.9	–44	20	18	3.230	17.72	2.3m	08/10/99	3600	
Q2204–4051	22	07	34.3	–40	36	57	3.155	17.57	2.3m	08/10/99	3600	
Q2212–1626	22	15	27.3	–16	11	33	3.990	18.10	WHT	21/08/93	3000	SL
Q2227–3928	22	30	32.9	–39	13	07	3.438	18.60	2.3m	29/10/00	3600	cloudy
									2.3m	31/10/00	3600	
Q2231–0015	22	34	09.0	+00	00	02	3.020	17.39	2.3m	11/06/99	1800	
									2.3m	08/10/99	1800	
Q2233+1310	22	36	19.2	+13	26	20	3.298	18.20	Hale-5m	18/10/87	2000	SSB
Q2233+1341	22	36	27.2	+13	57	13	3.215	20.00	Hale-5m	18/10/87	2100	SSB
Q2235–0301	22	38	22.5	–02	45	53	4.249	18.20	WHT	21/08/93	3000	SL
Q2237–0607	22	39	53.6	–05	52	19	4.558	18.30	WHT	03/10/92	2700	SL
Q2248–1242	22	51	18.1	–12	27	03	4.161	18.50	WHT	21/08/93	3000	SL
Q2249–5037	22	52	44.0	–50	21	37	2.900	17.10	2.3m	07/10/99	1800	
Q2250–3714	22	53	10.8	–36	58	17	3.140 ^c	17.60	2.3m	04/10/99	5400	
Q2311–0341	23	14	07.2	–03	25	28	3.040	18.80	Hale-5m	18/10/87	3600	SSB
Q2313–3356	23	15	56.1	–33	39	46	2.900	18.50	2.3m	07/11/99	5400	
Q2314–3405	23	16	43.3	–33	49	12	2.950 ^c	18.50	2.3m	09/11/99	5400	
Q2318+0119	23	21	14.7	+01	35	54	3.195	18.50	2.3m	07/10/99	3600	
Q2330+0125	23	32	53.1	+01	42	18	3.281	19.88	WHT	20/10/99	1200	
Q2342+3417	23	44	51.3	+34	33	49	3.053	18.40	WHT	20/10/99	1200	
Q2344+0124	23	46	38.6	+01	41	36	3.143	19.22	WHT	20/10/99	1200	
Q2347–4342	23	50	34.3	–43	26	00	2.885	16.90	2.3m	07/11/99	3600	
Q2348–0108	23	50	57.8	–00	52	10	3.014	18.80	Hale-5m	18/10/87	1800	SSB
									WHT	20/10/99	1200	

Table 6.1 – *continued*

Object ^a	α_{J2000}			δ_{J2000}			z_{em}	m_V	Telescope	Date	Exposed	Comments ^b
	h	m	s	°	'	"						
Q2348–4025	23	51	16.1	–40	08	36	3.310	18.10	2.3m	05/10/99	3600	
Q2355+0108	23	58	08.6	+01	25	06	3.400	17.50	2.3m	08/10/99	3600	
Q2355–3858	23	57	45.7	–38	41	30	2.850	18.20	2.3m	31/10/00	5400	
Q2359+0023	00	01	46.8	+00	39	59	2.897	19.00	Hale-5m	18/10/87	3600	SSB
Q2359+0653	00	01	40.6	+07	09	54	3.234	18.40	Hale-5m	18/10/87	2000	SSB
Q2359–0216	00	01	50.0	–01	59	40	2.810	18.60	Hale-5m	18/10/87	1200	SSB

^a Object names were formed uniformly from B1950 coordinates.

^b SSB = Sargent, Steidel, & Bokserberg (1989), SL = Storrie-Lombardi et al. (1996).

^c Redshift was measured from C IV and/or Ly α emission lines.

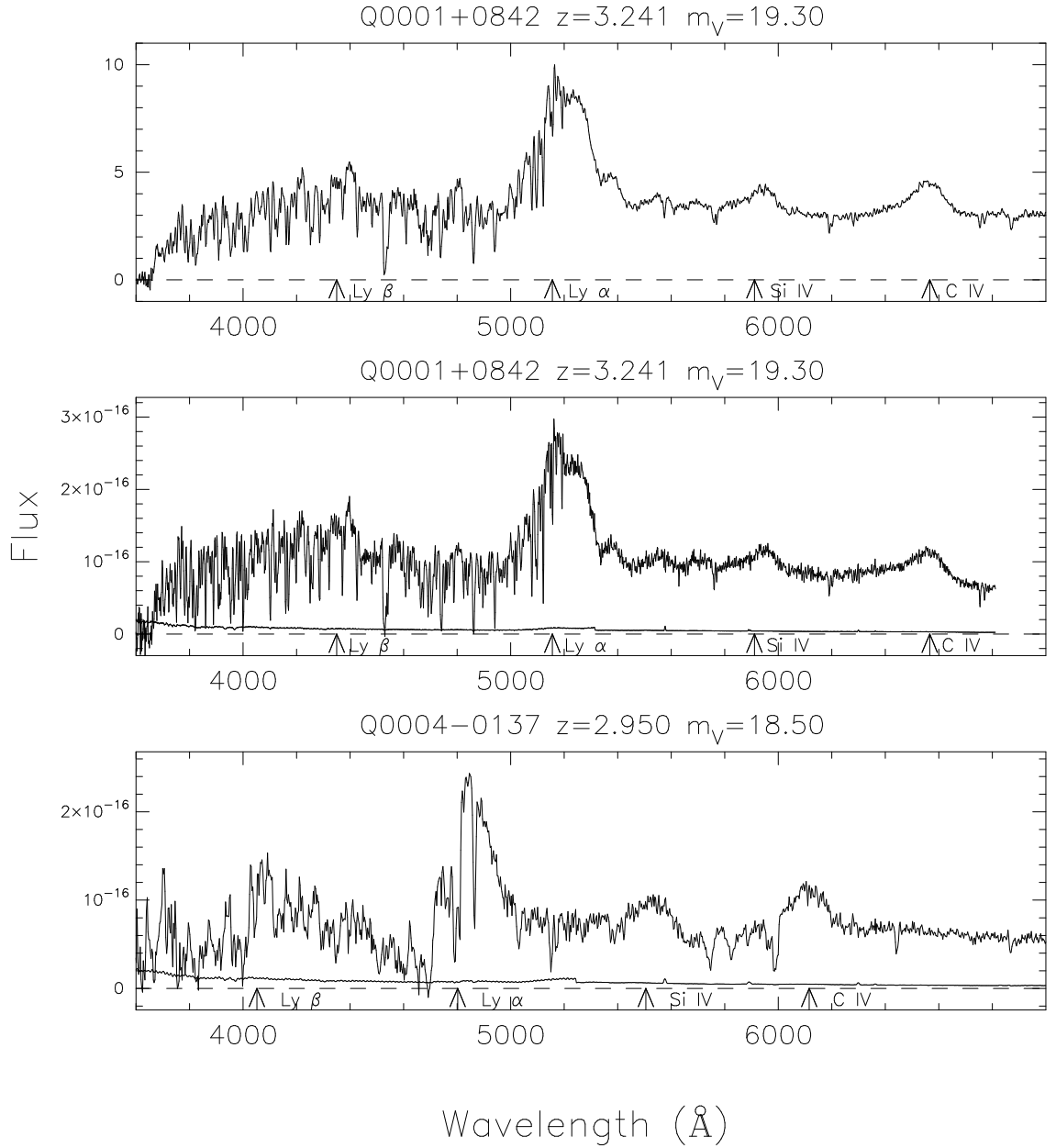
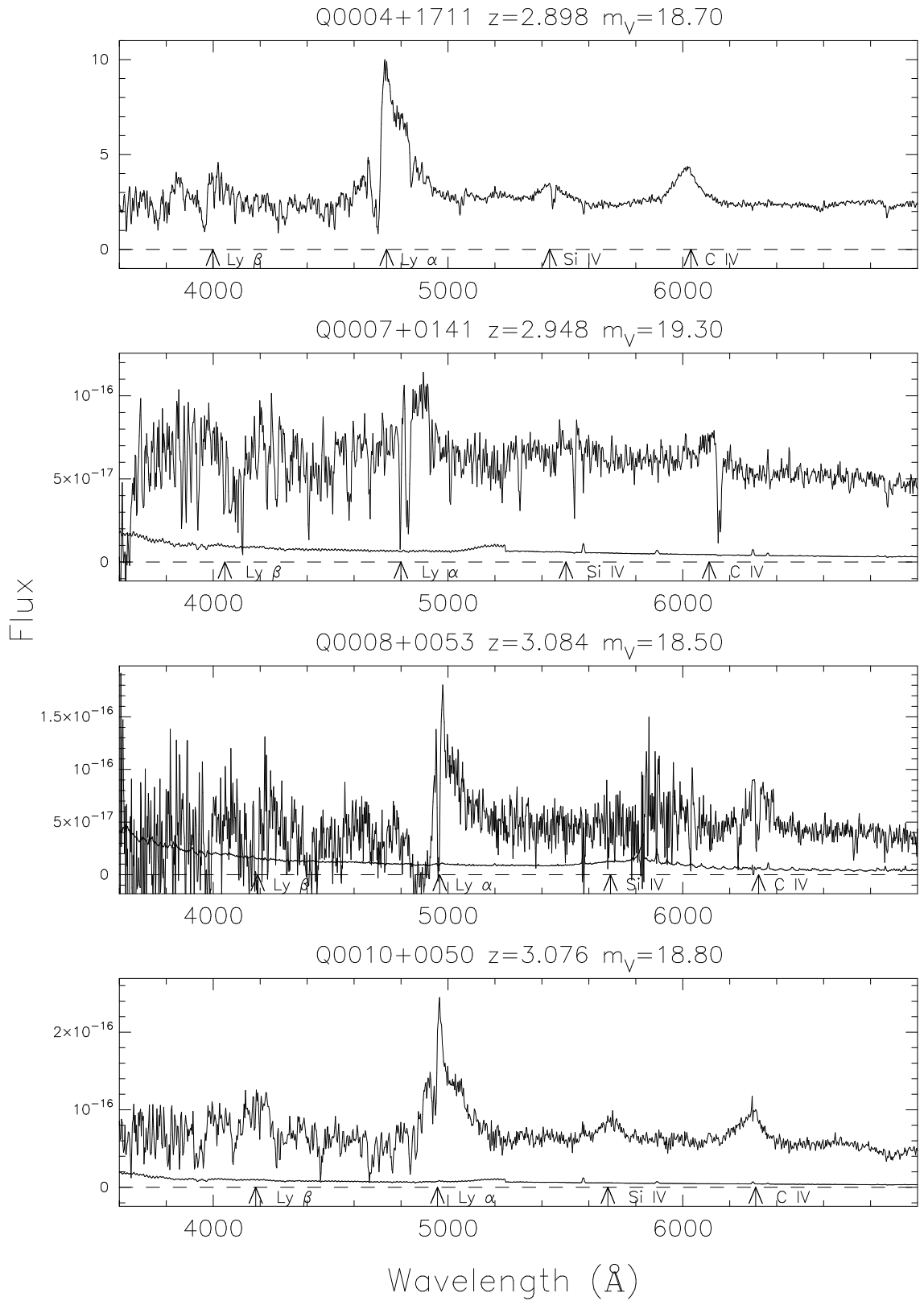
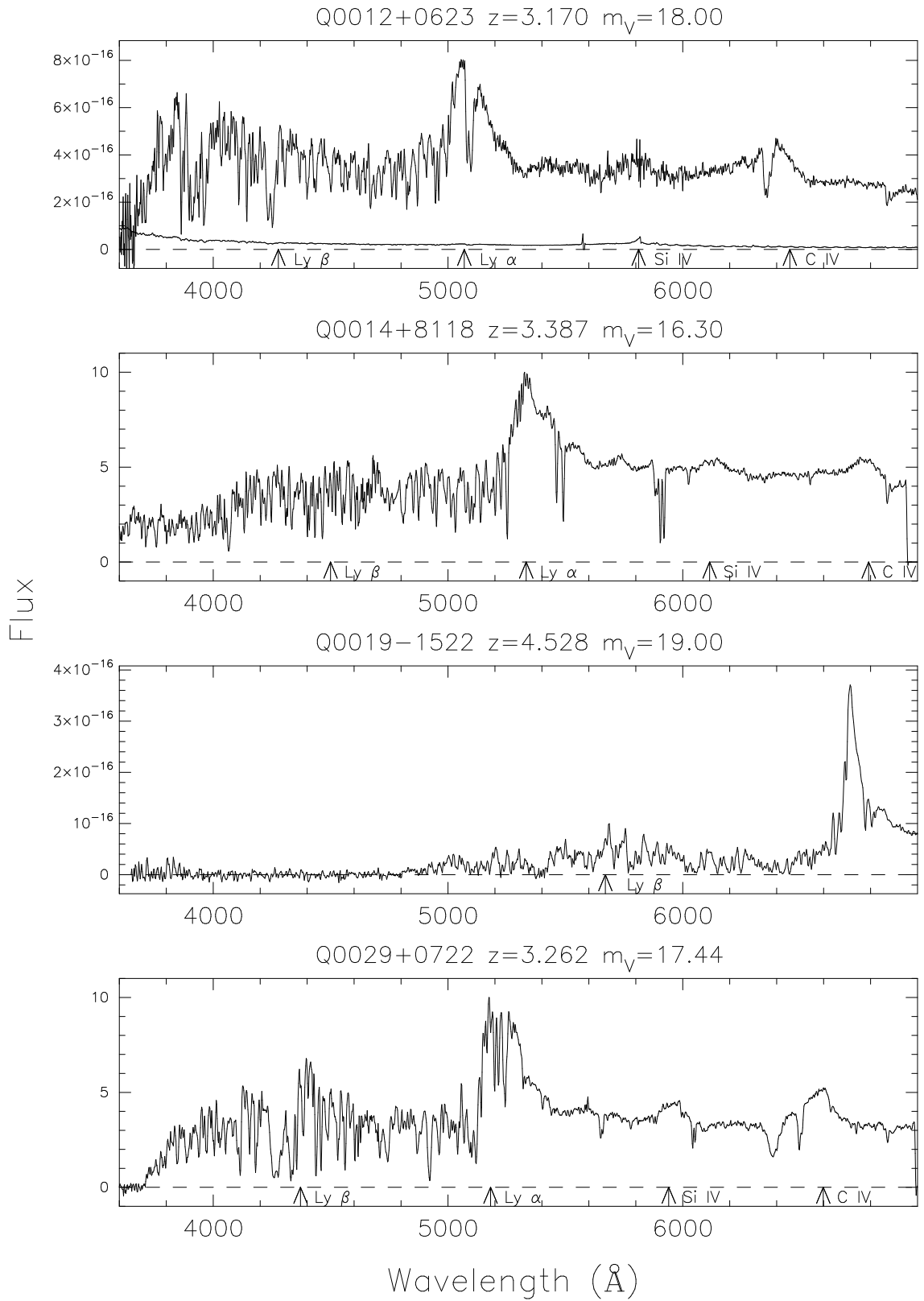
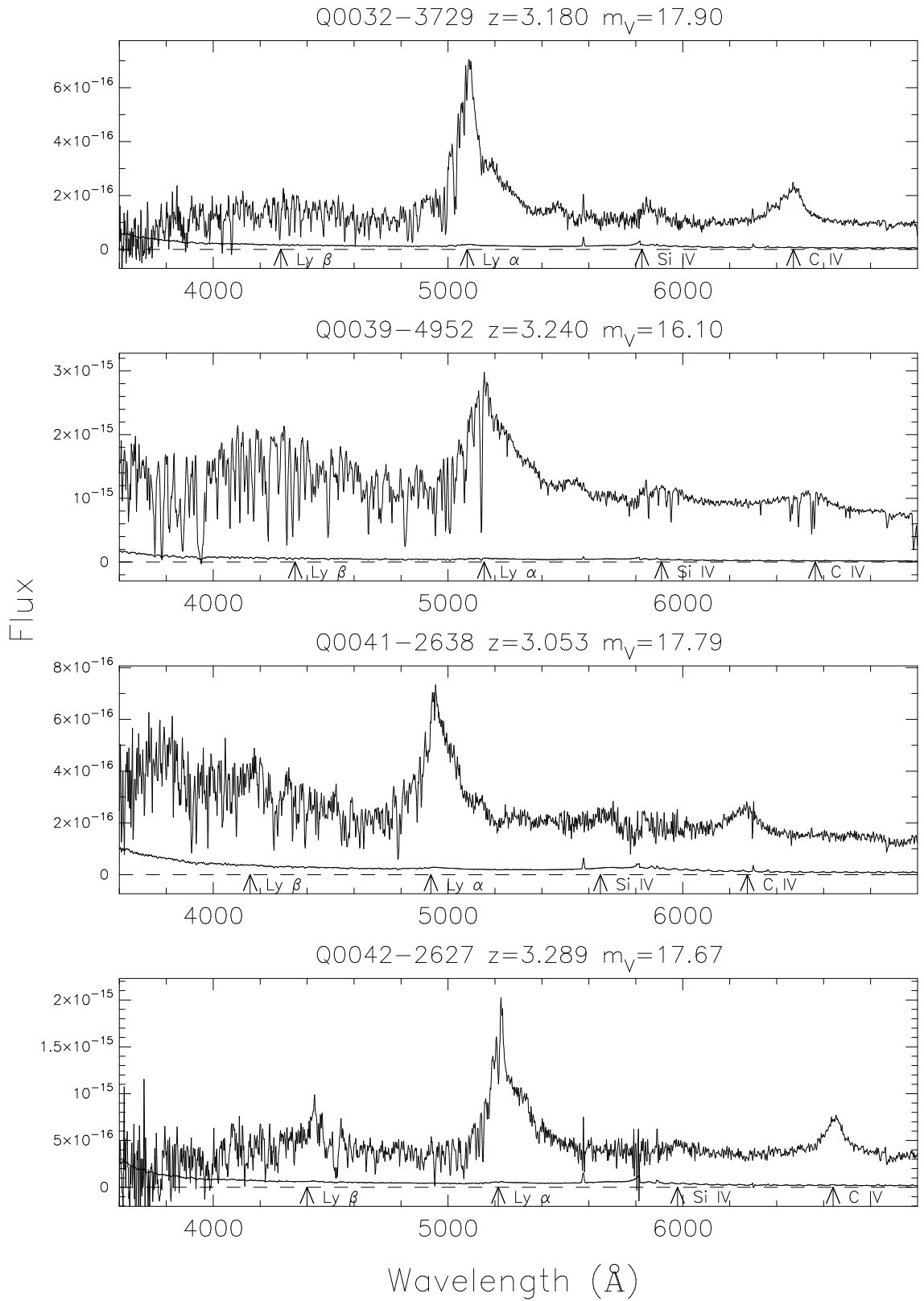
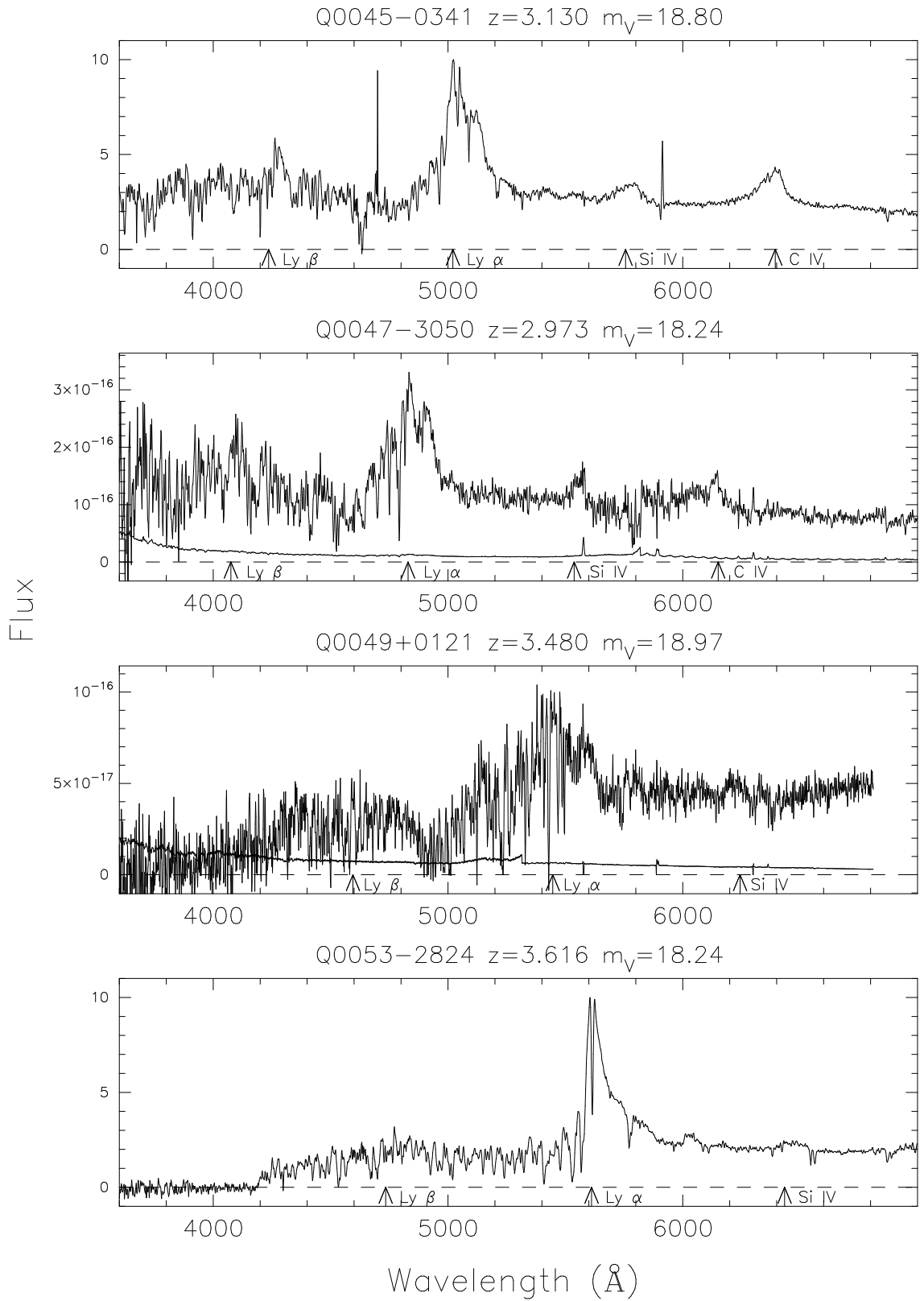


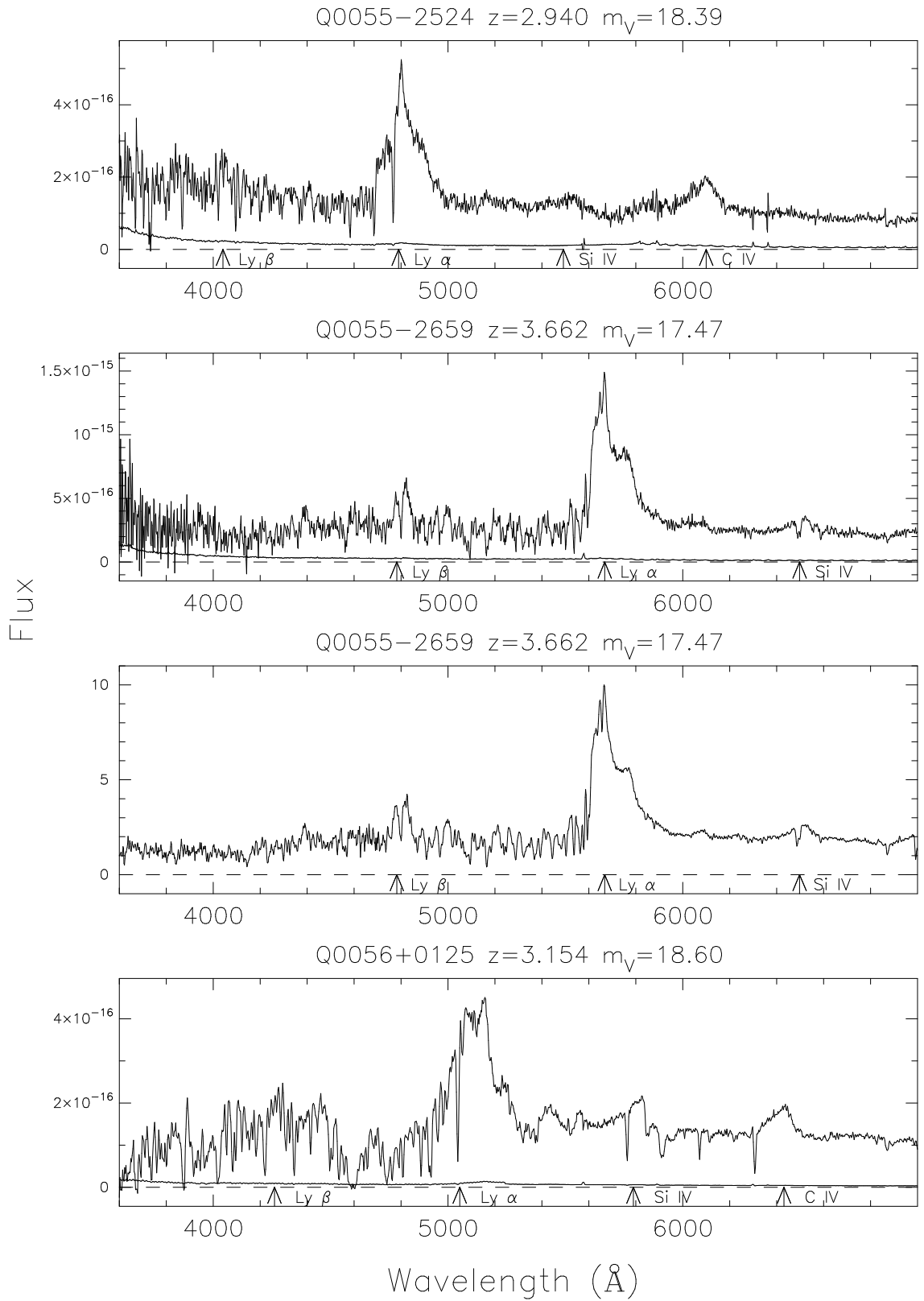
Figure 6.6: Flux calibrated spectra and 1σ error arrays of the full PD2H sample (cf. Table 5.1) versus heliocentric wavelength. The data of SSB and SL have no error arrays and are thus easily distinguishable from our new data. SL's and our data have flux units of $\text{ergs s}^{-1} \text{cm}^{-2} \text{\AA}^{-1}$, SSB's data are shown in arbitrary units. Some emission lines are marked below the zero-flux (dashed) line.

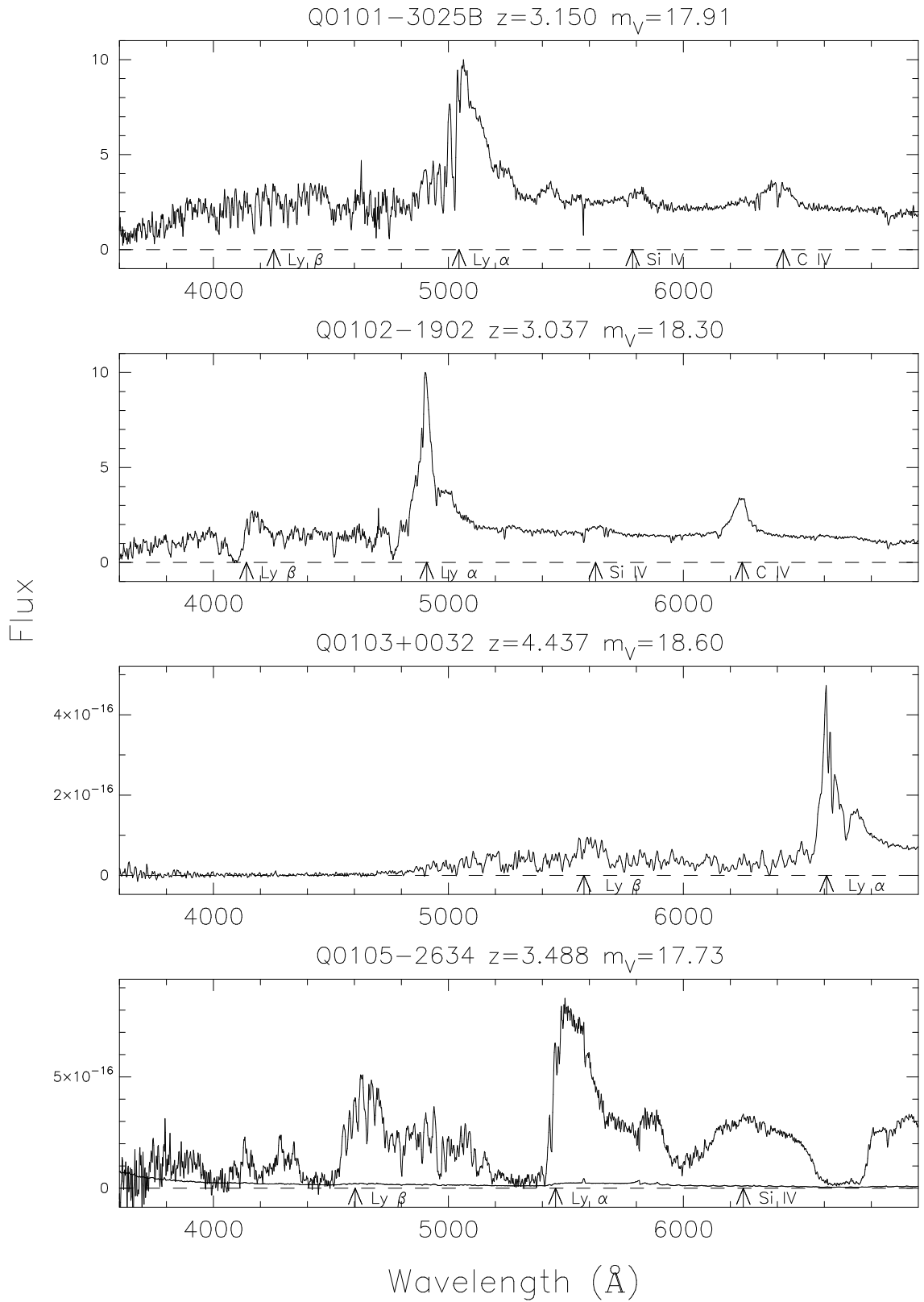
Figure 6.6 – *continued*

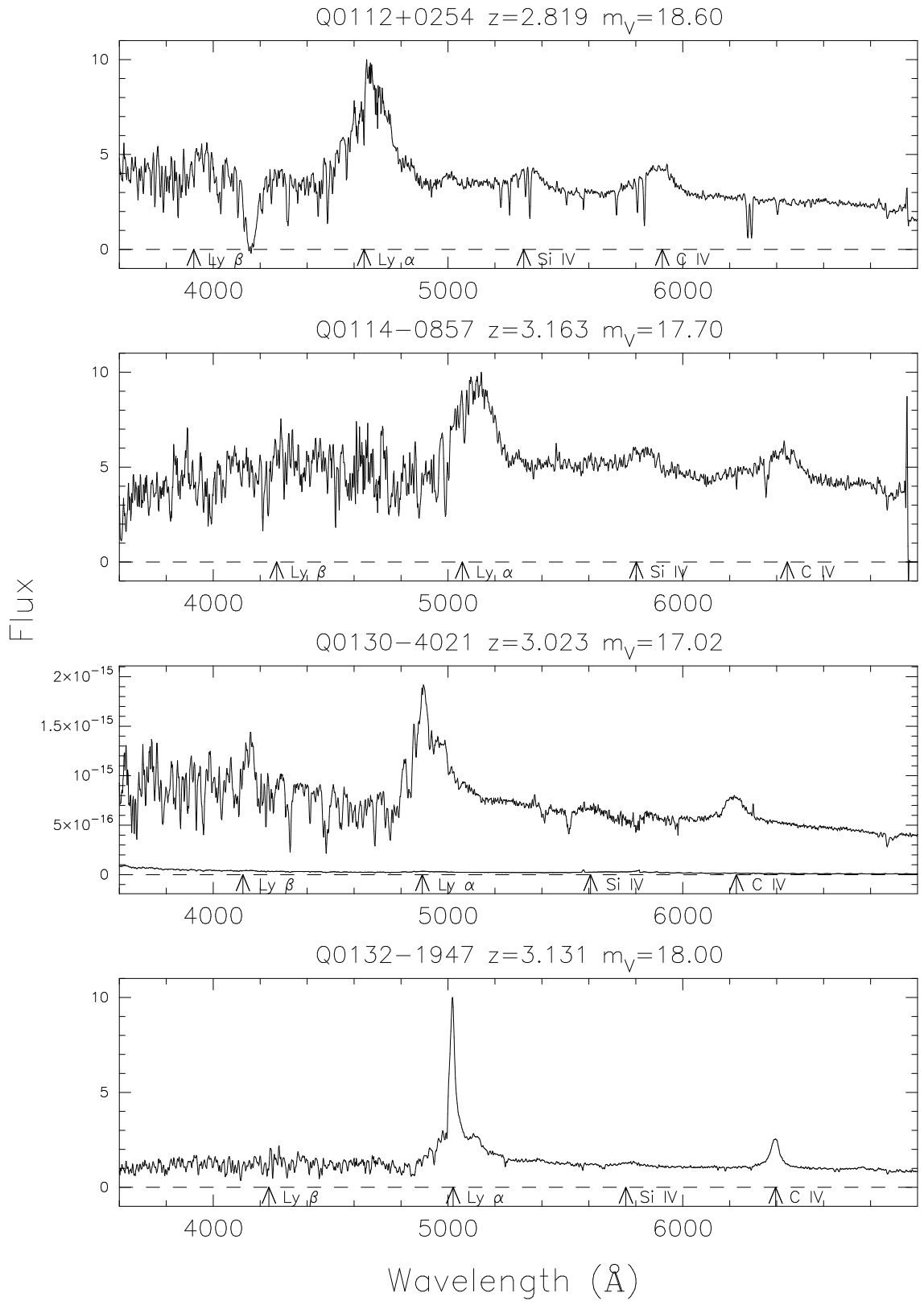
Figure 6.6 – *continued*

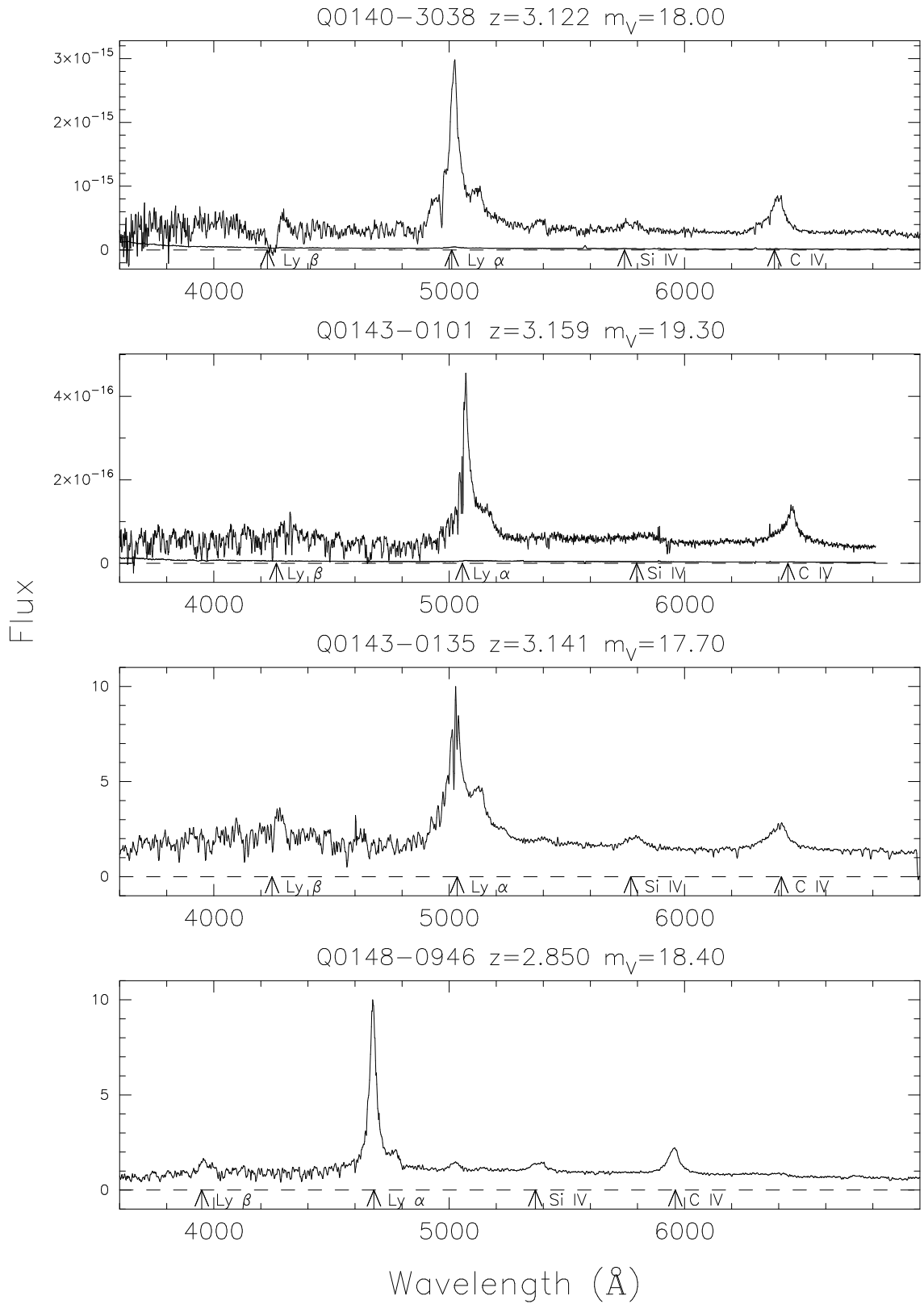
Figure 6.6 – *continued*

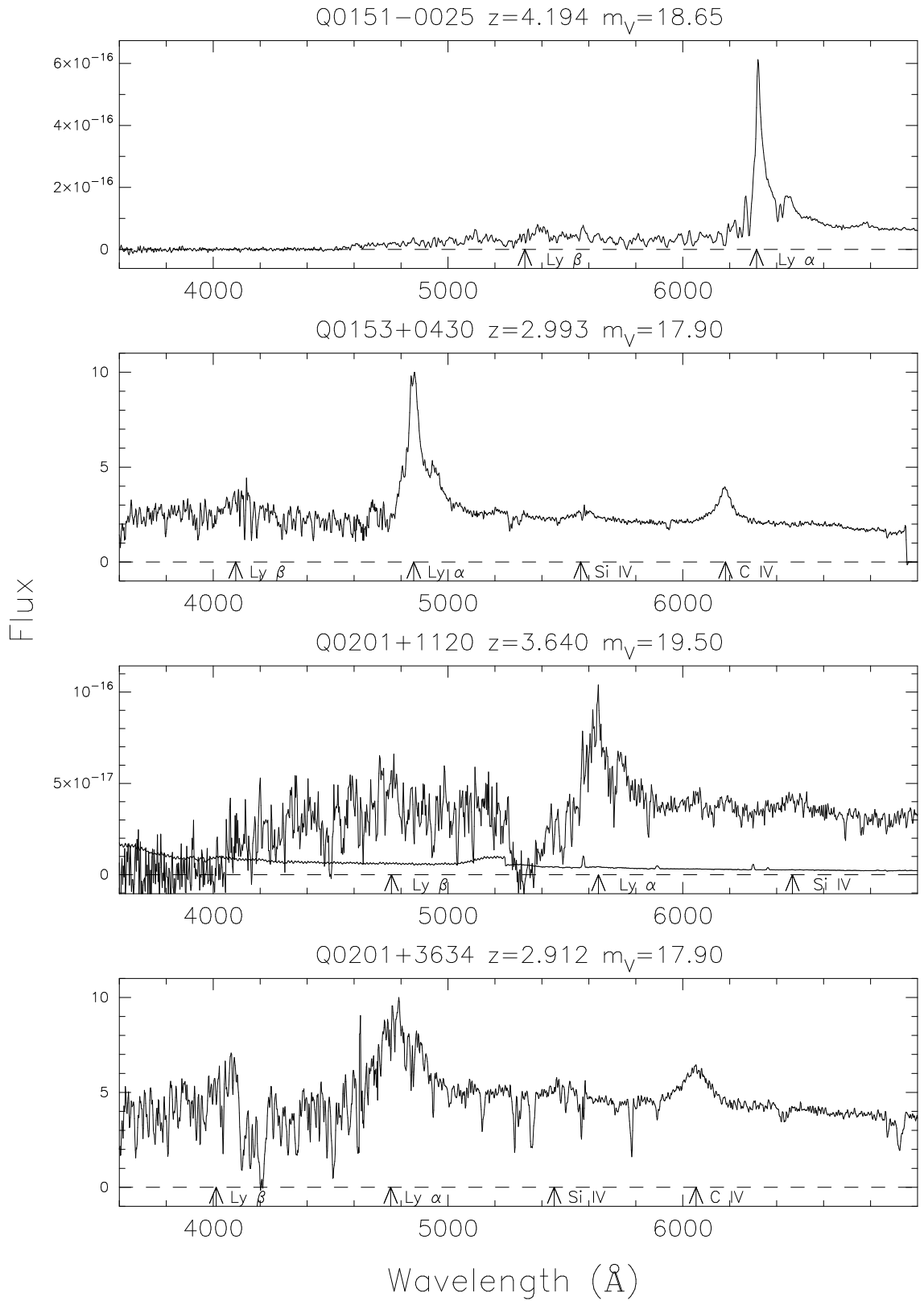
Figure 6.6 – *continued*

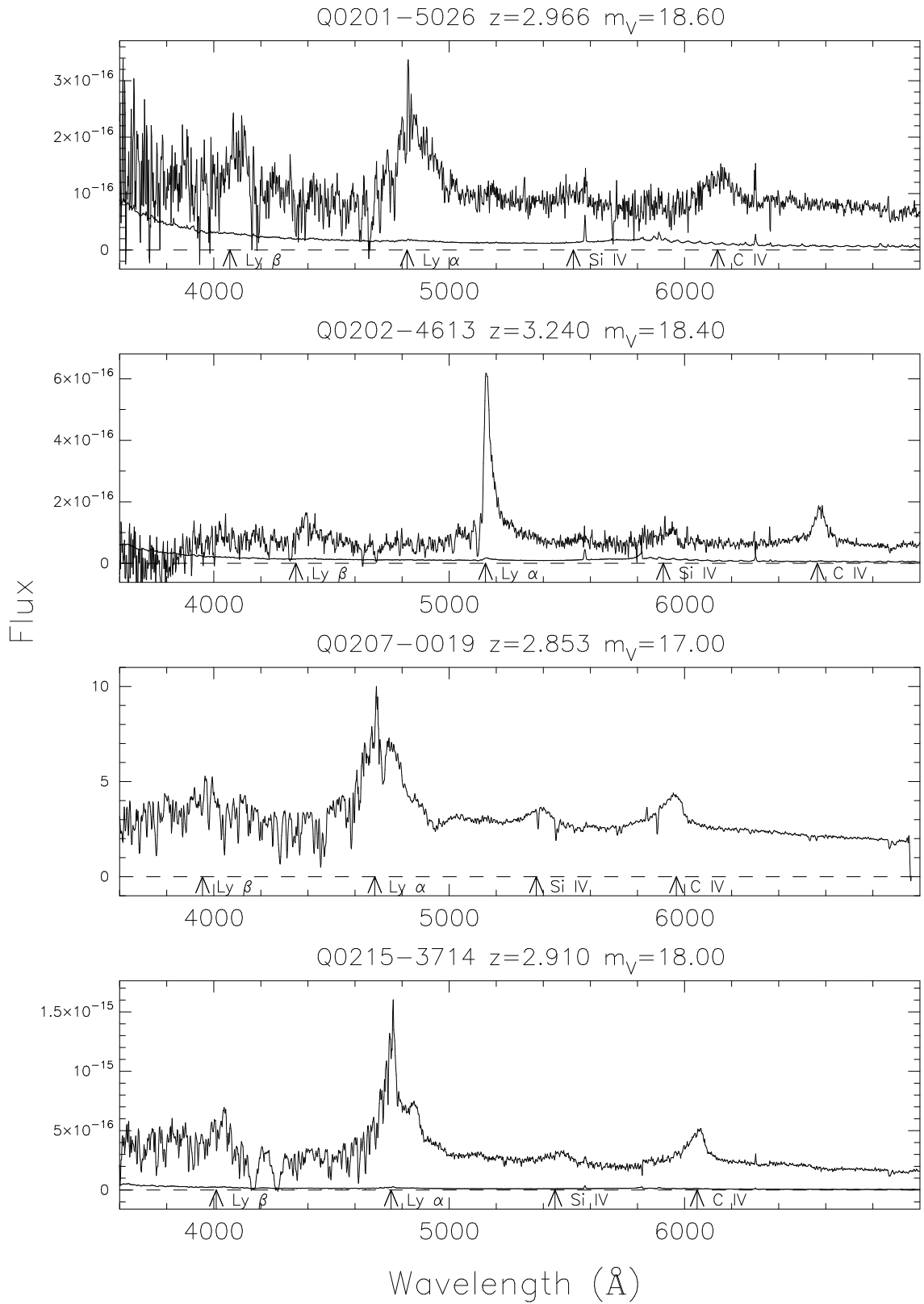
Figure 6.6 – *continued*

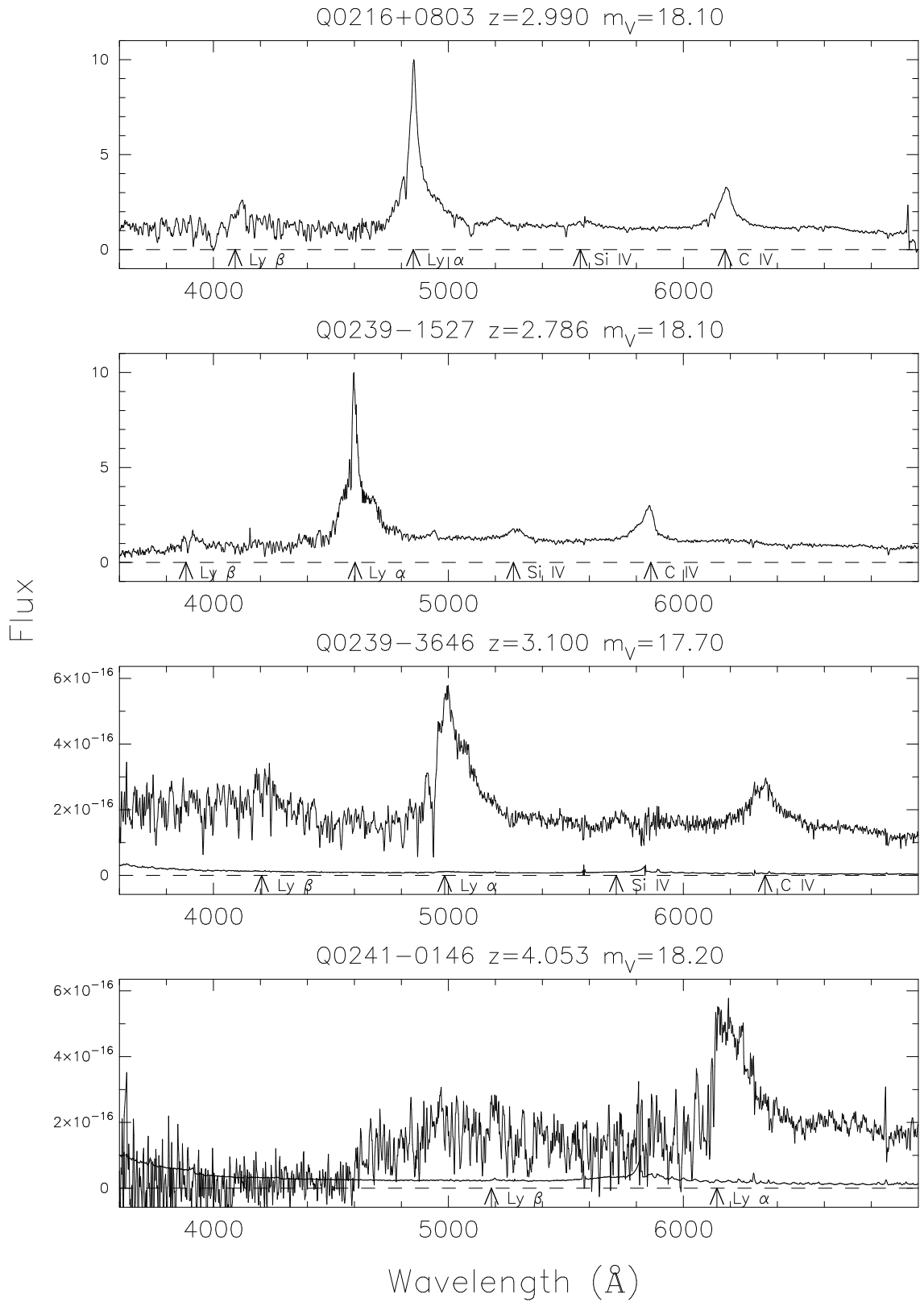
Figure 6.6 – *continued*

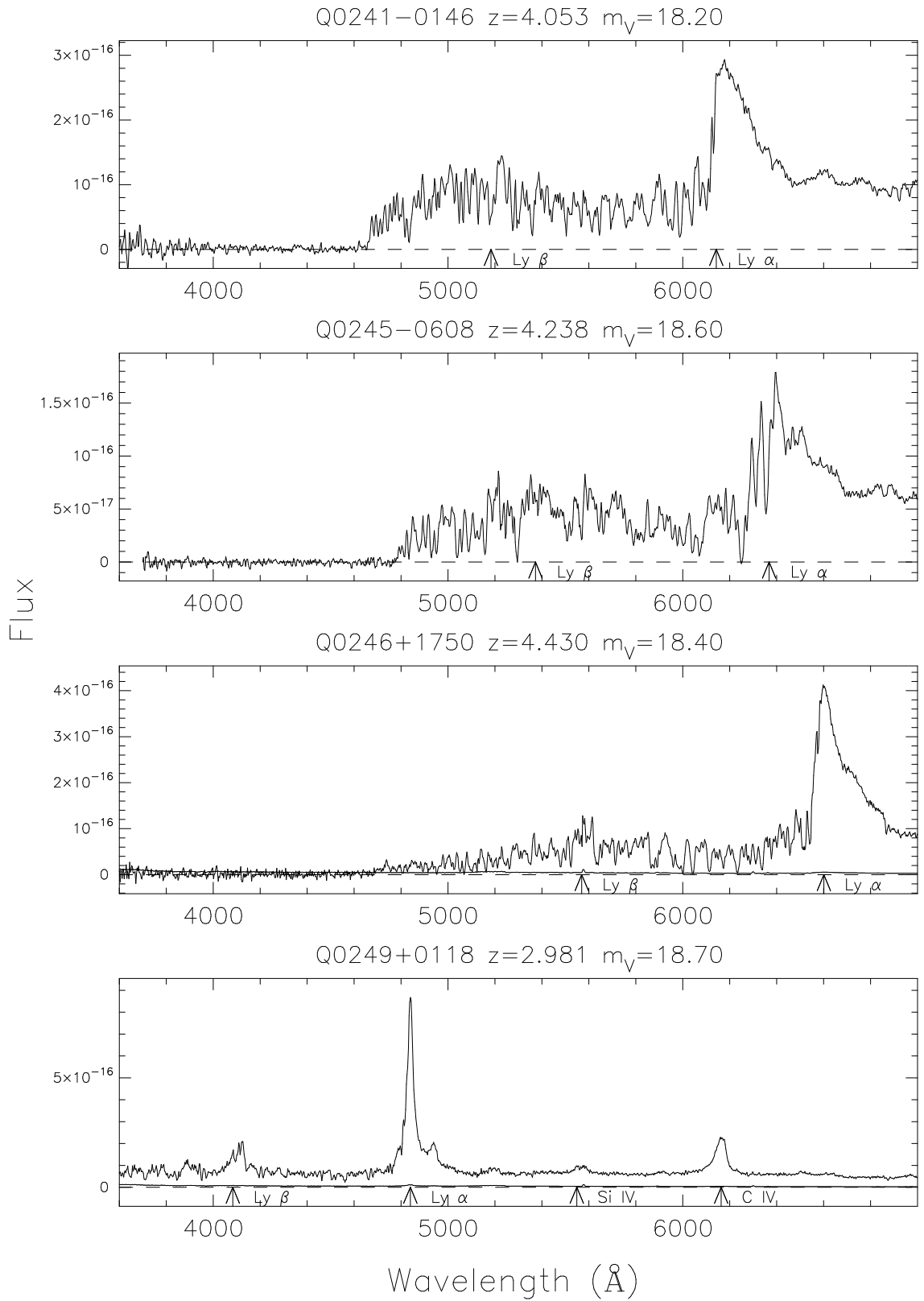
Figure 6.6 – *continued*

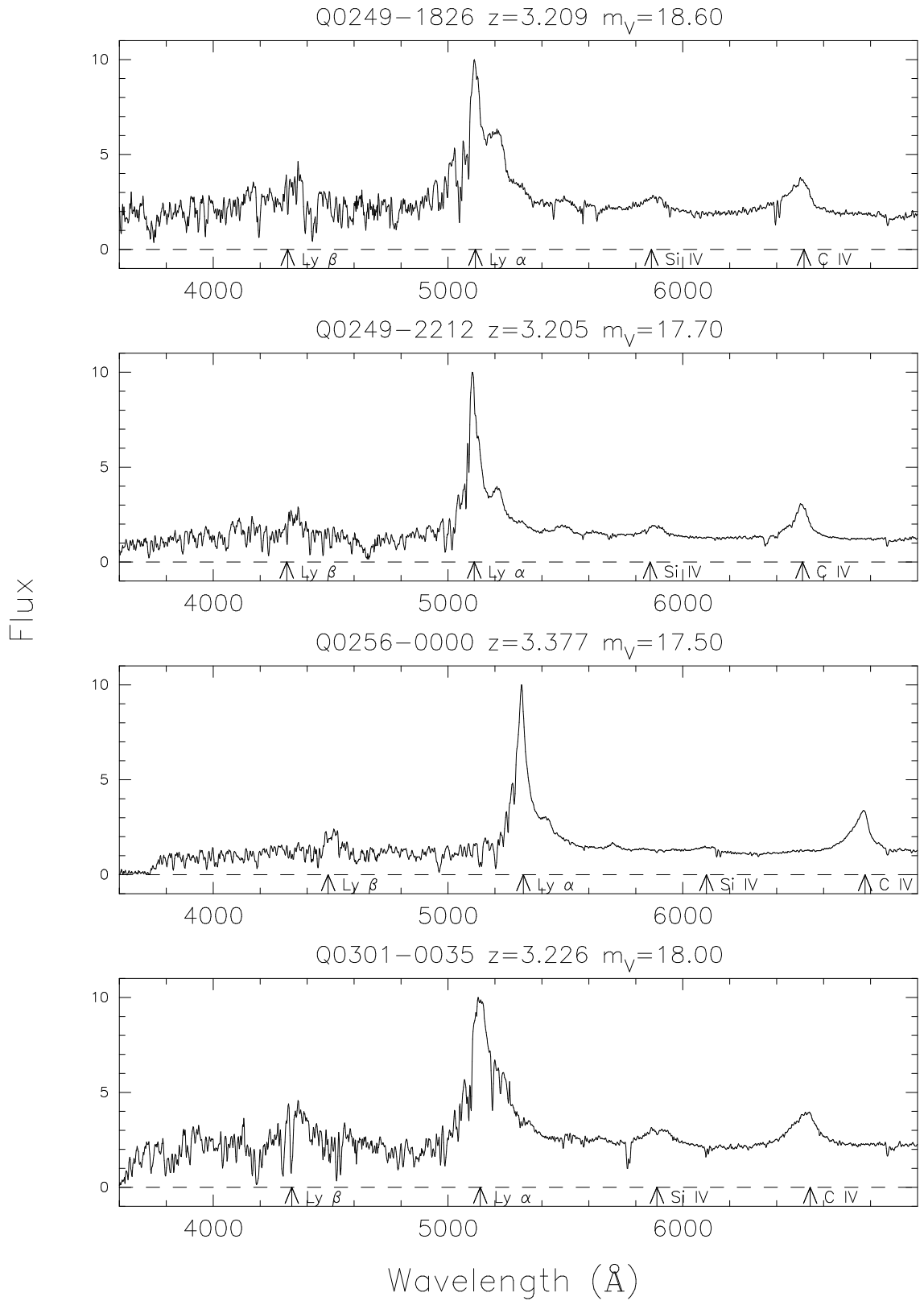
Figure 6.6 – *continued*

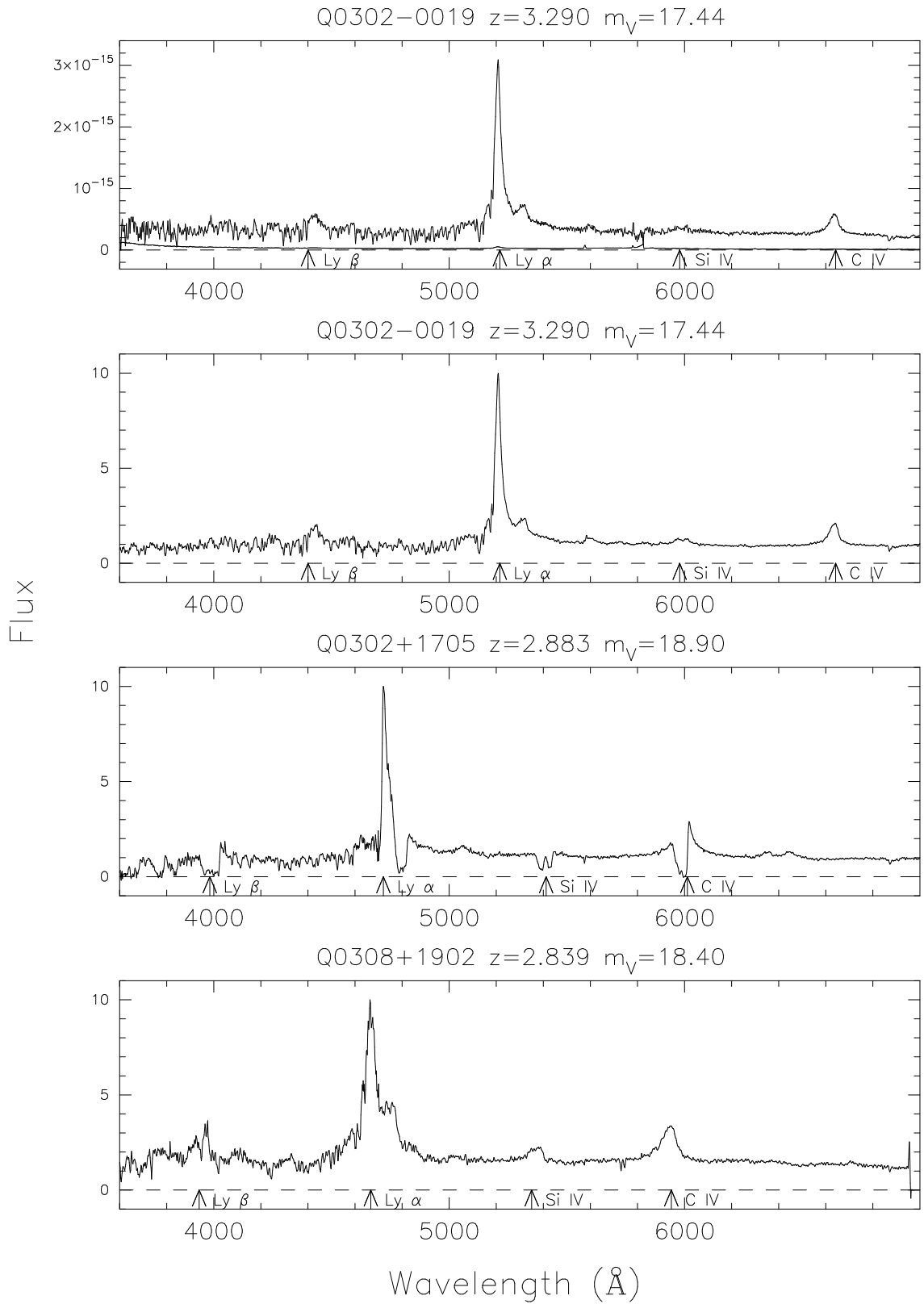
Figure 6.6 – *continued*

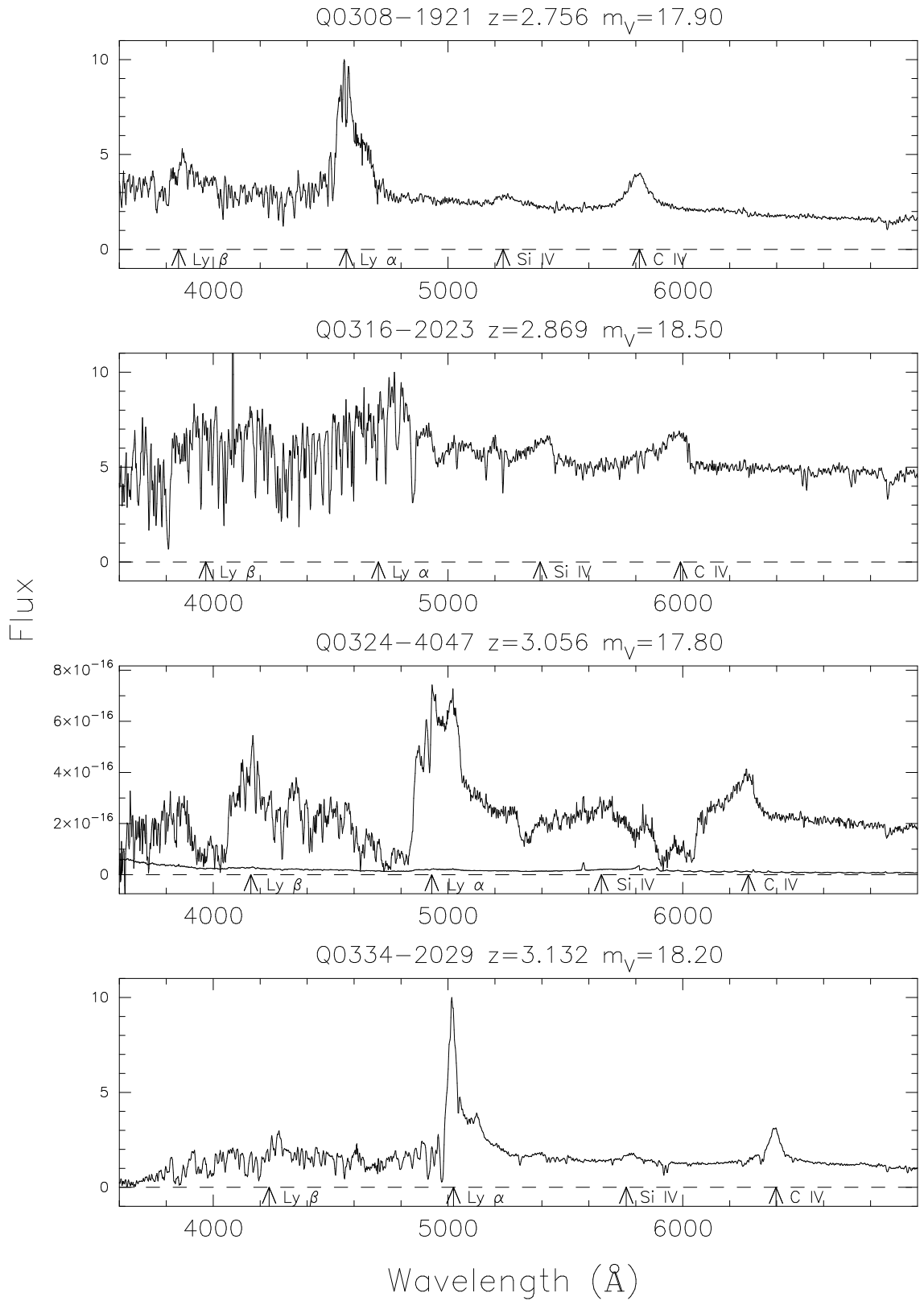
Figure 6.6 – *continued*

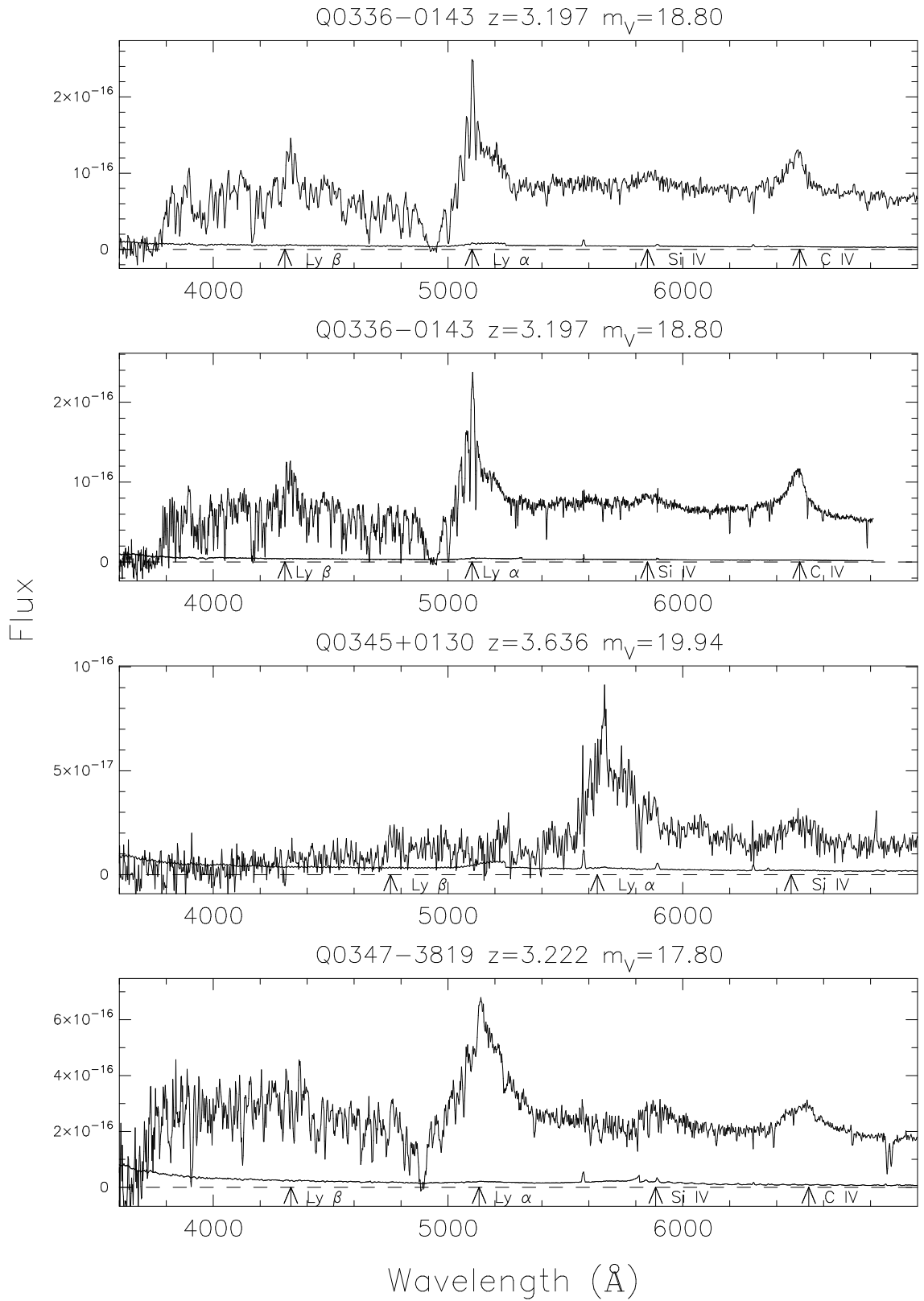
Figure 6.6 – *continued*

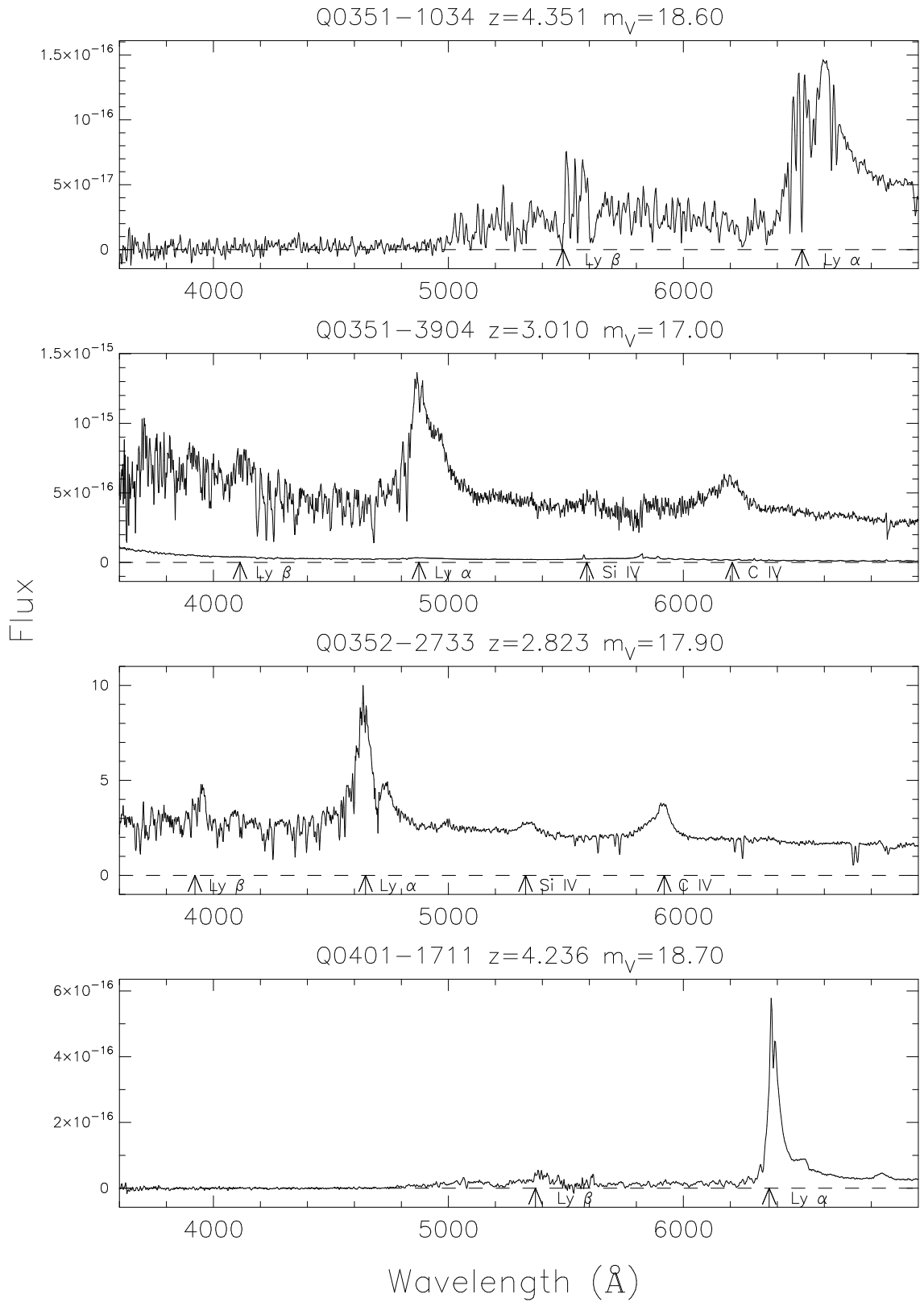
Figure 6.6 – *continued*

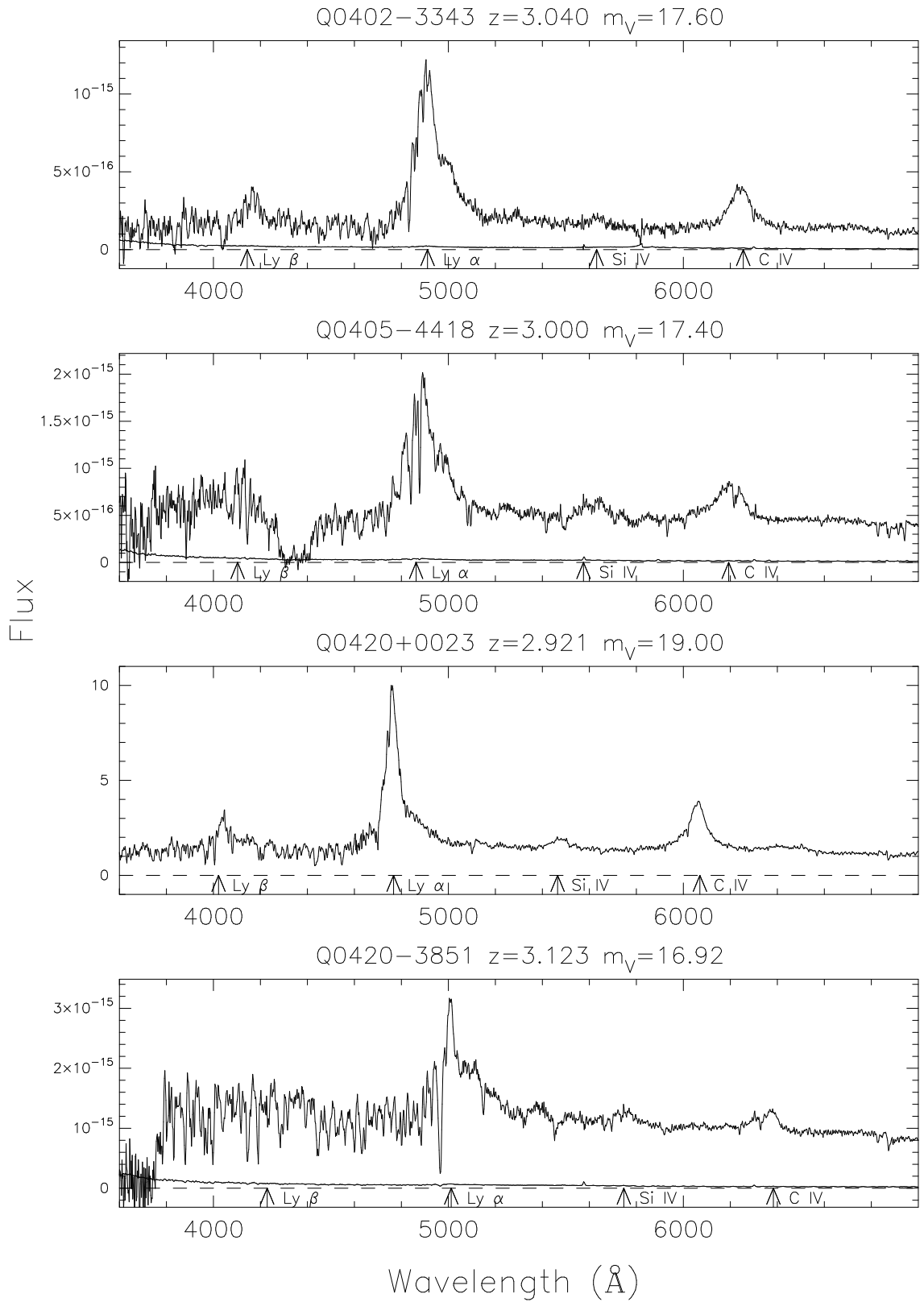
Figure 6.6 – *continued*

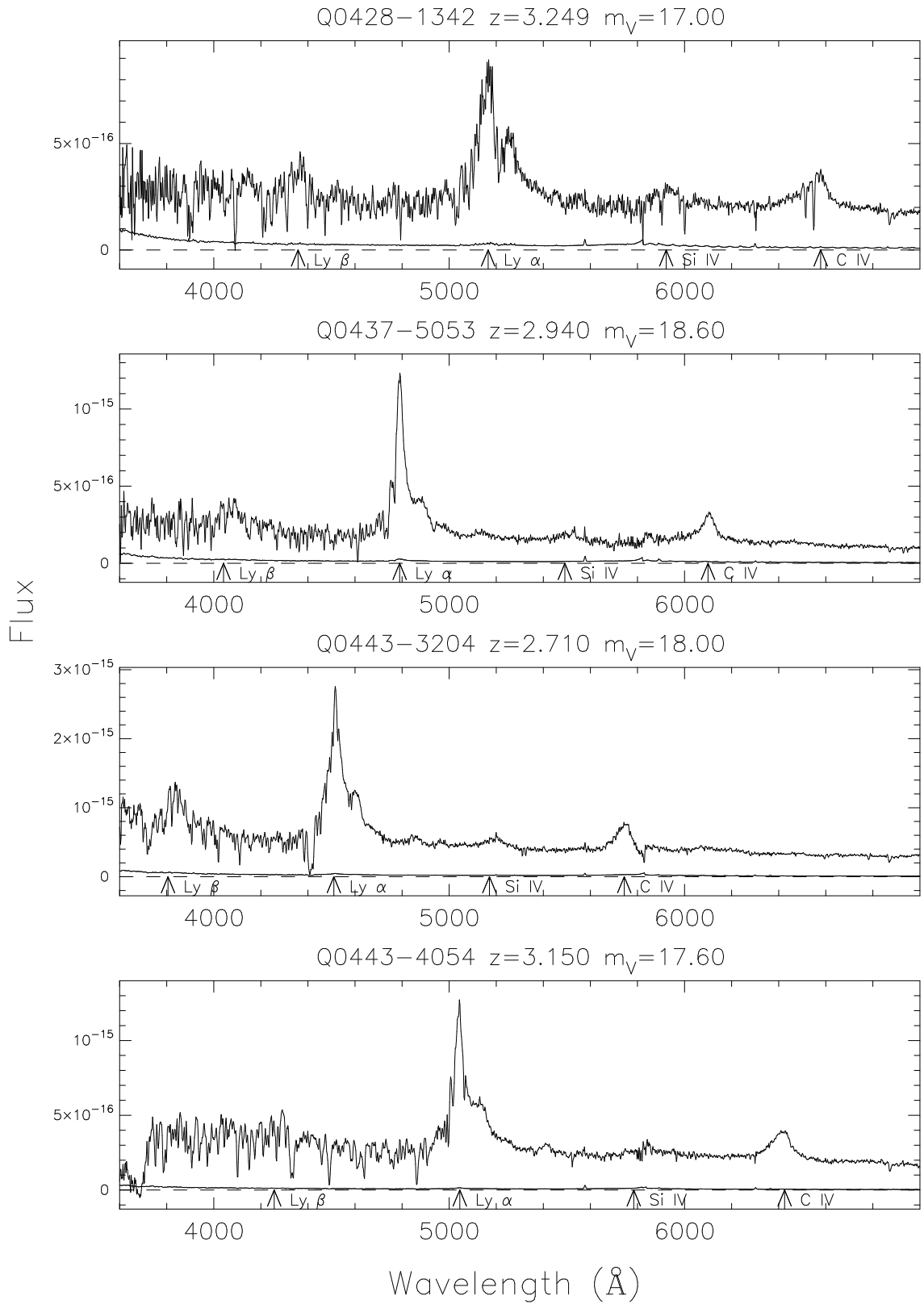
Figure 6.6 – *continued*

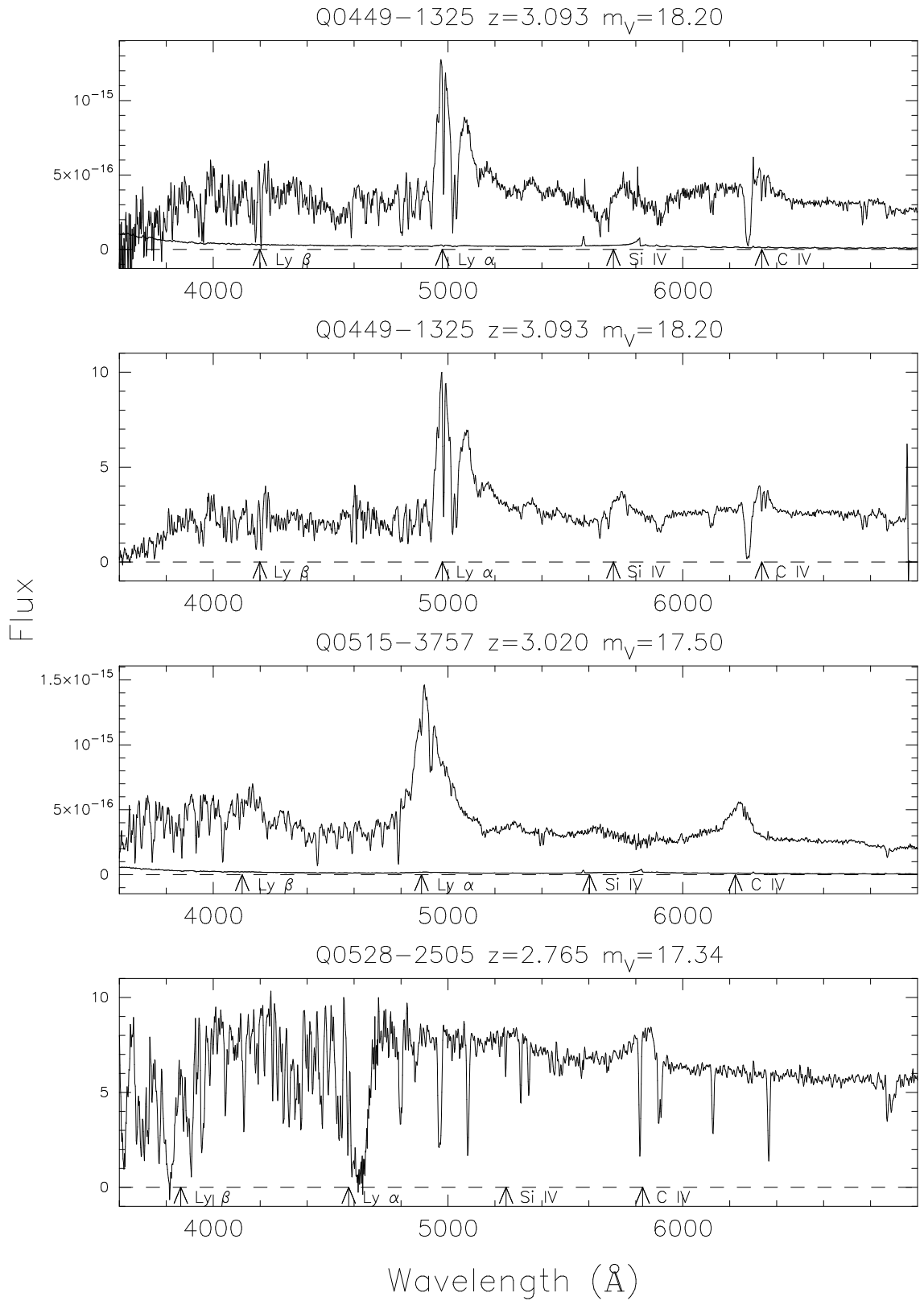
Figure 6.6 – *continued*

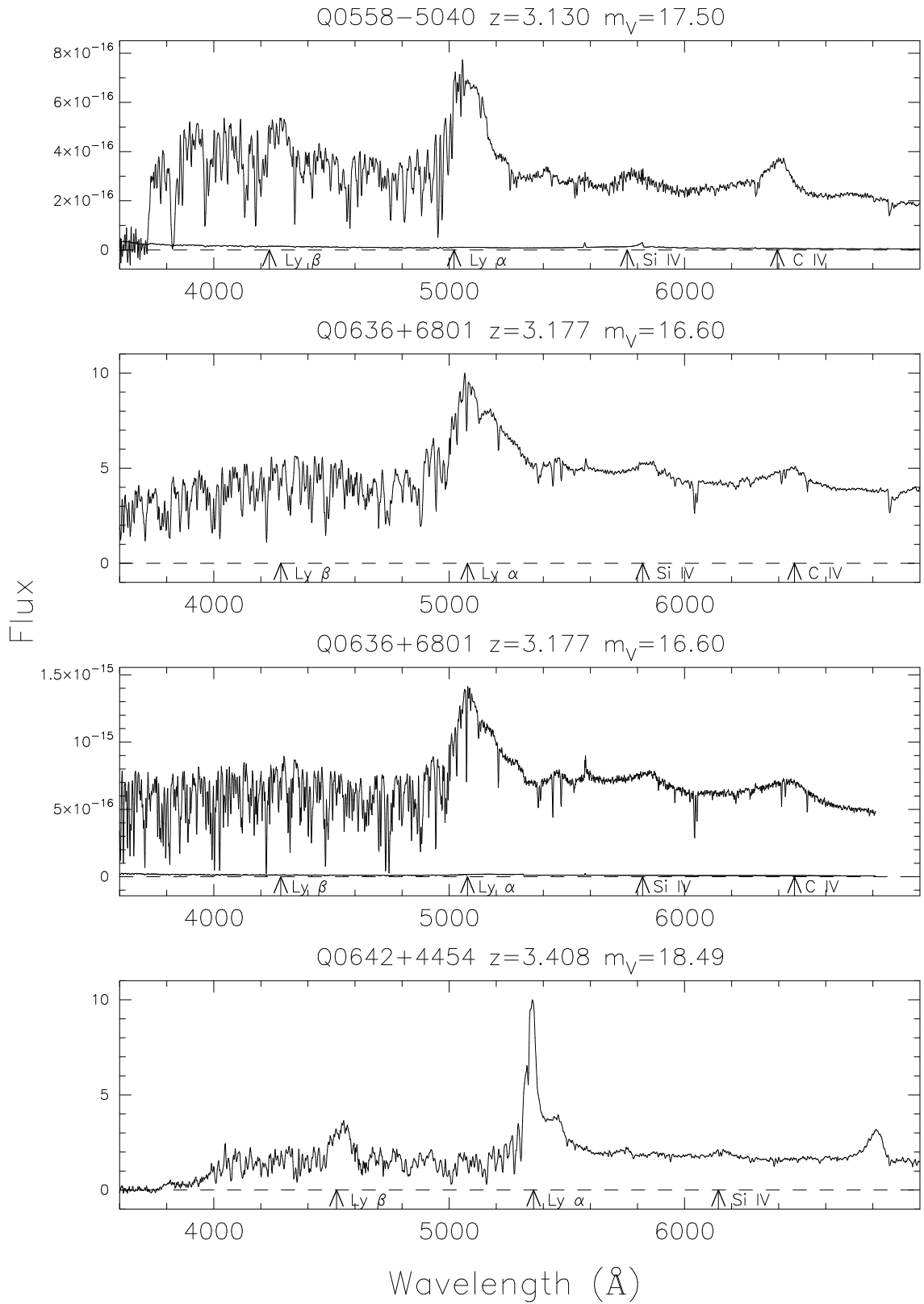
Figure 6.6 – *continued*

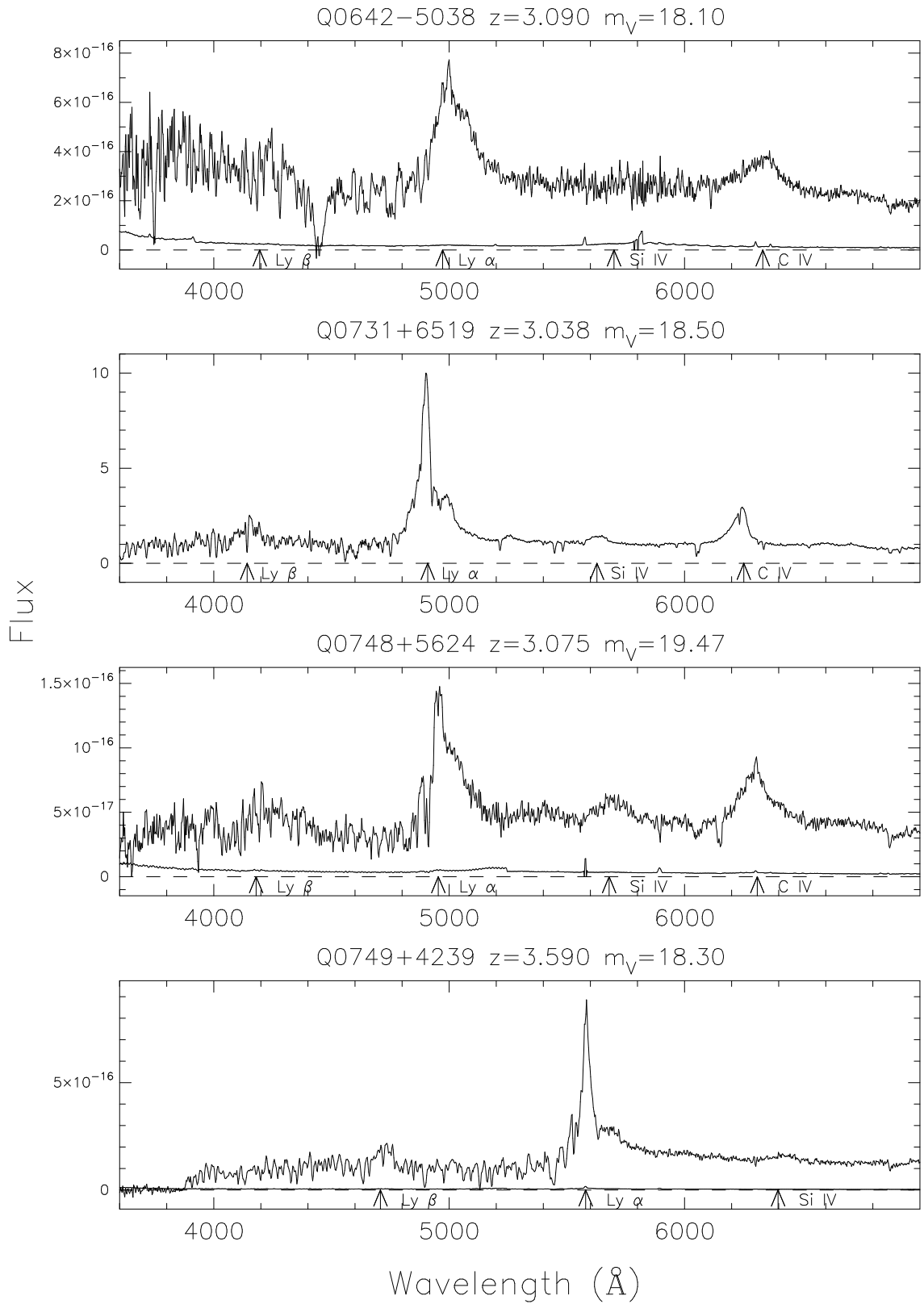
Figure 6.6 – *continued*

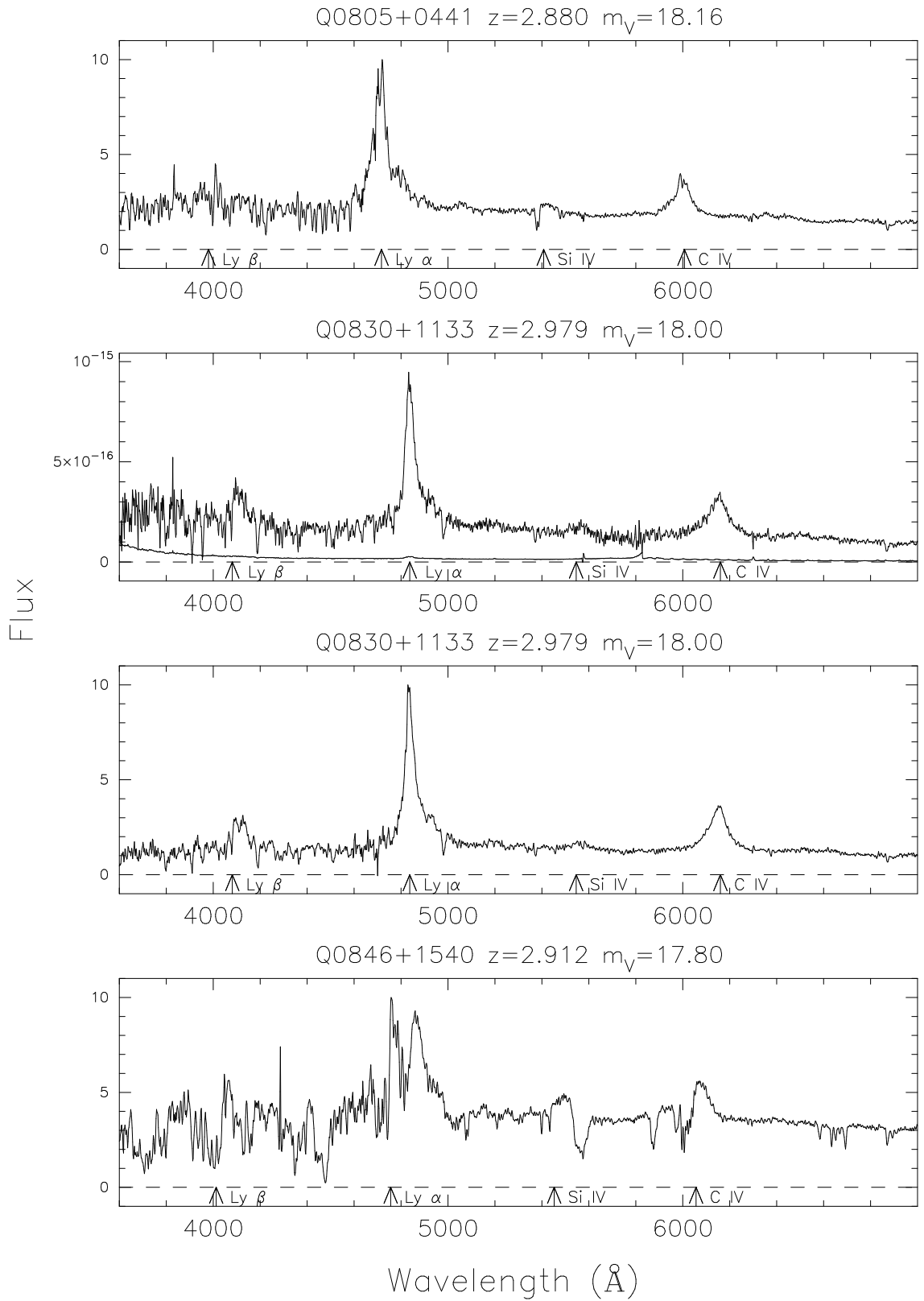
Figure 6.6 – *continued*

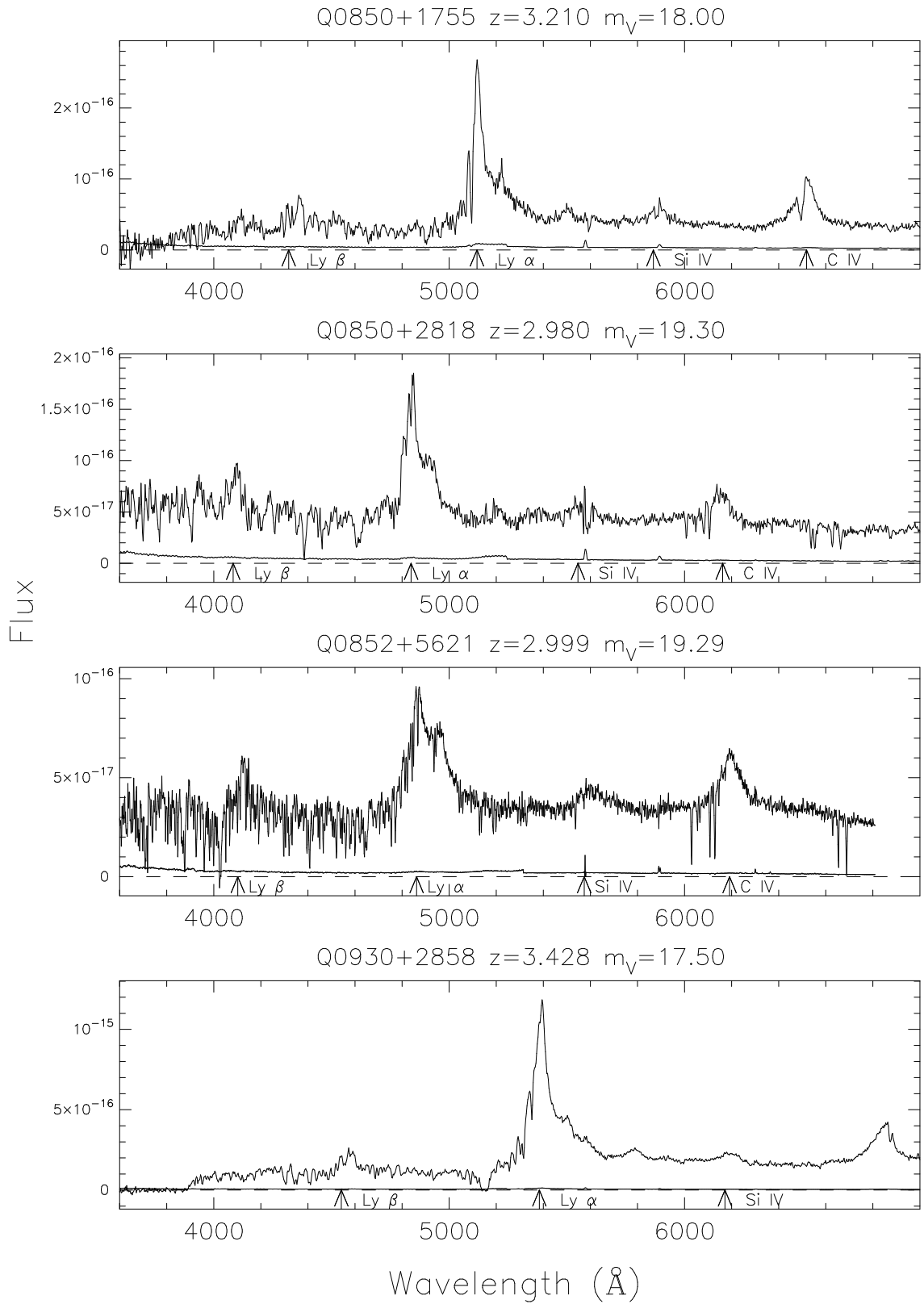
Figure 6.6 – *continued*

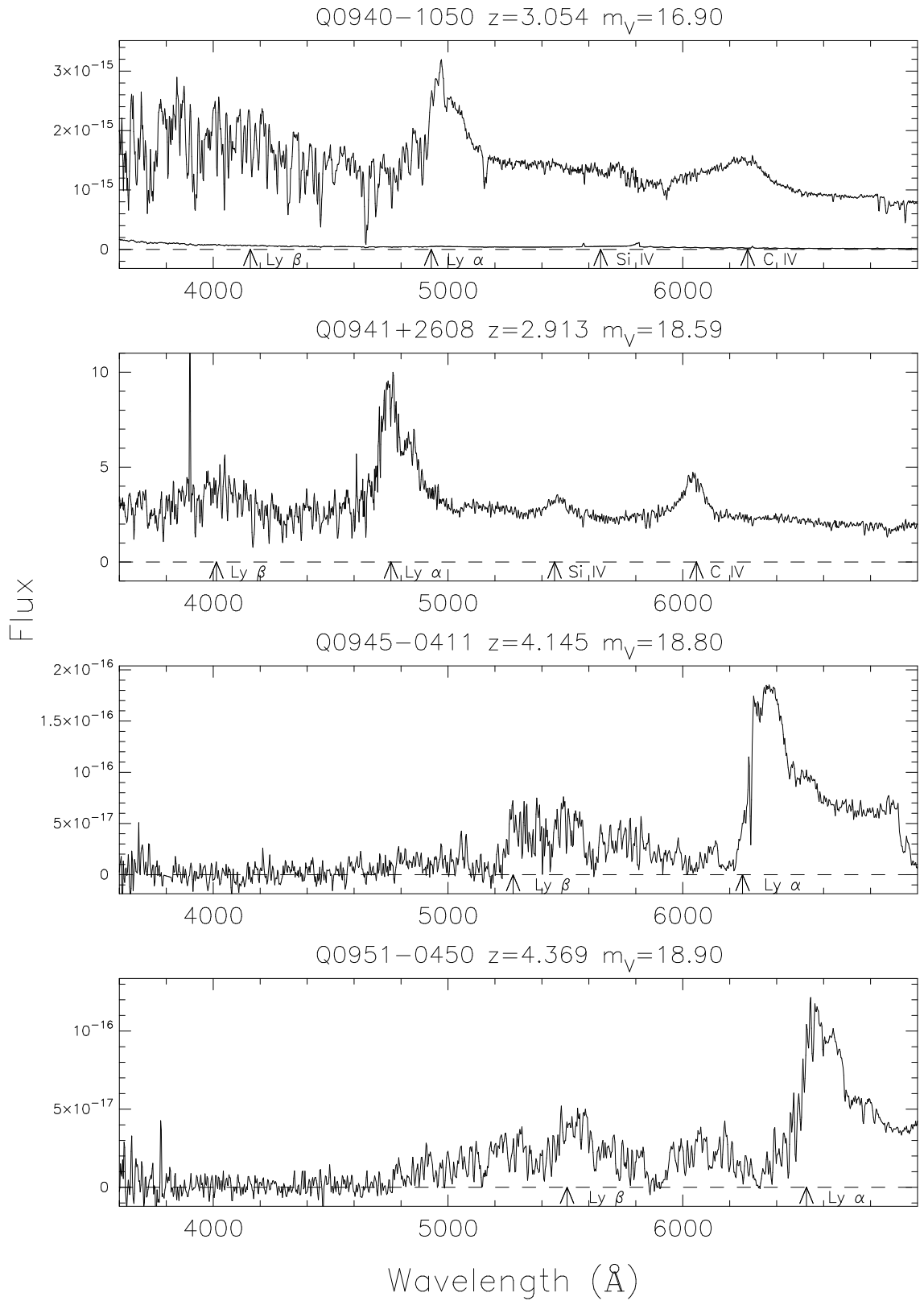
Figure 6.6 – *continued*

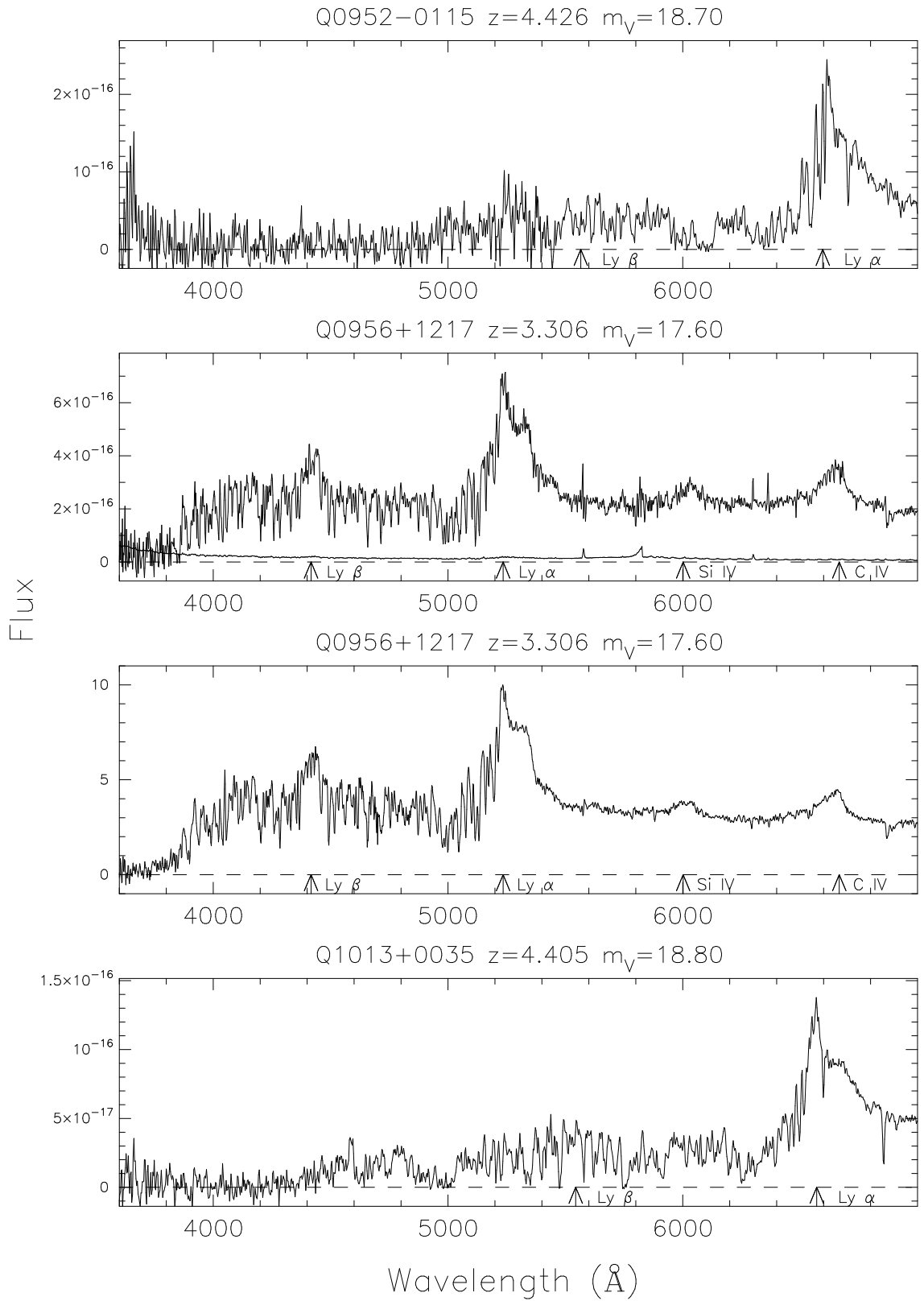
Figure 6.6 – *continued*

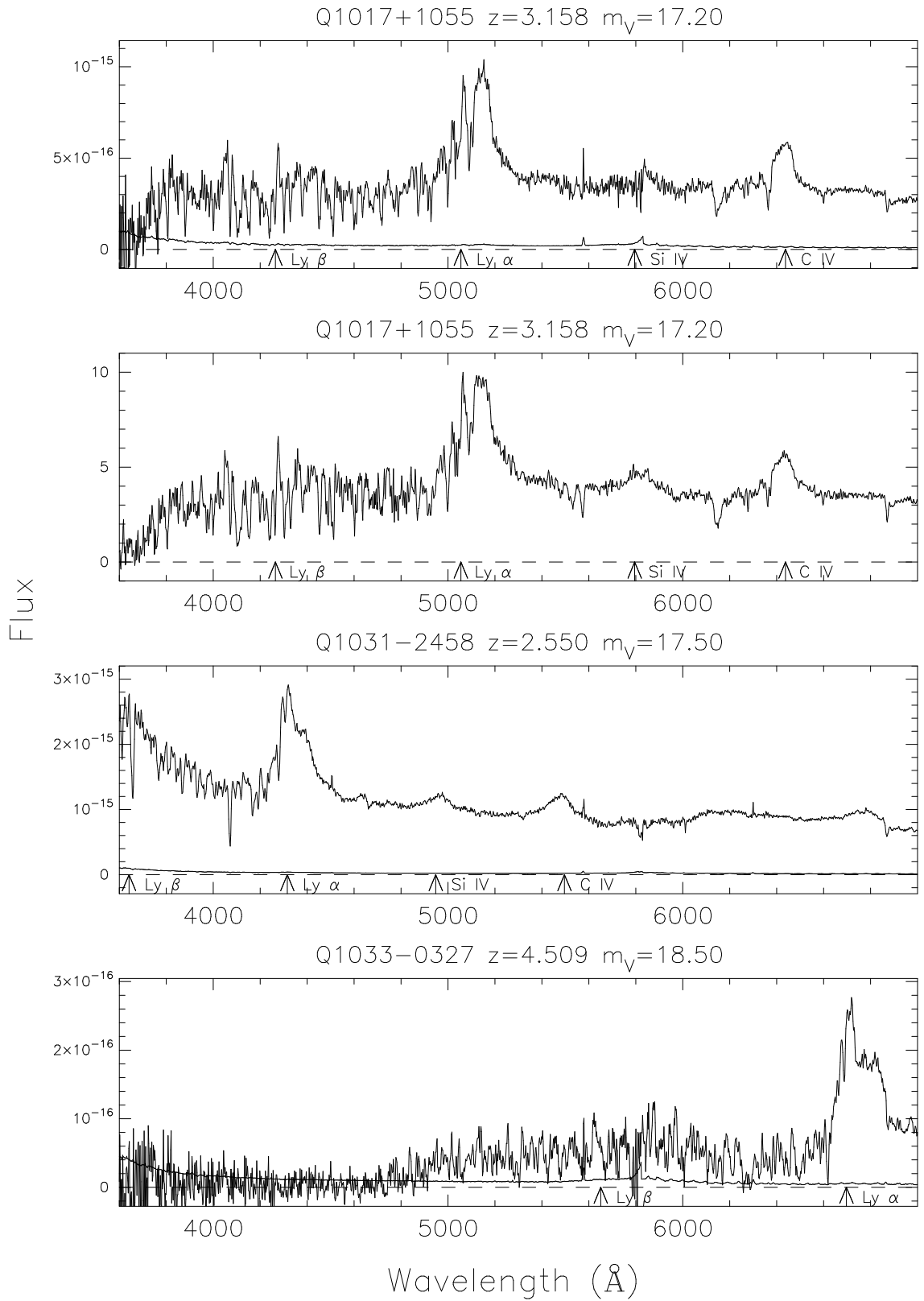
Figure 6.6 – *continued*

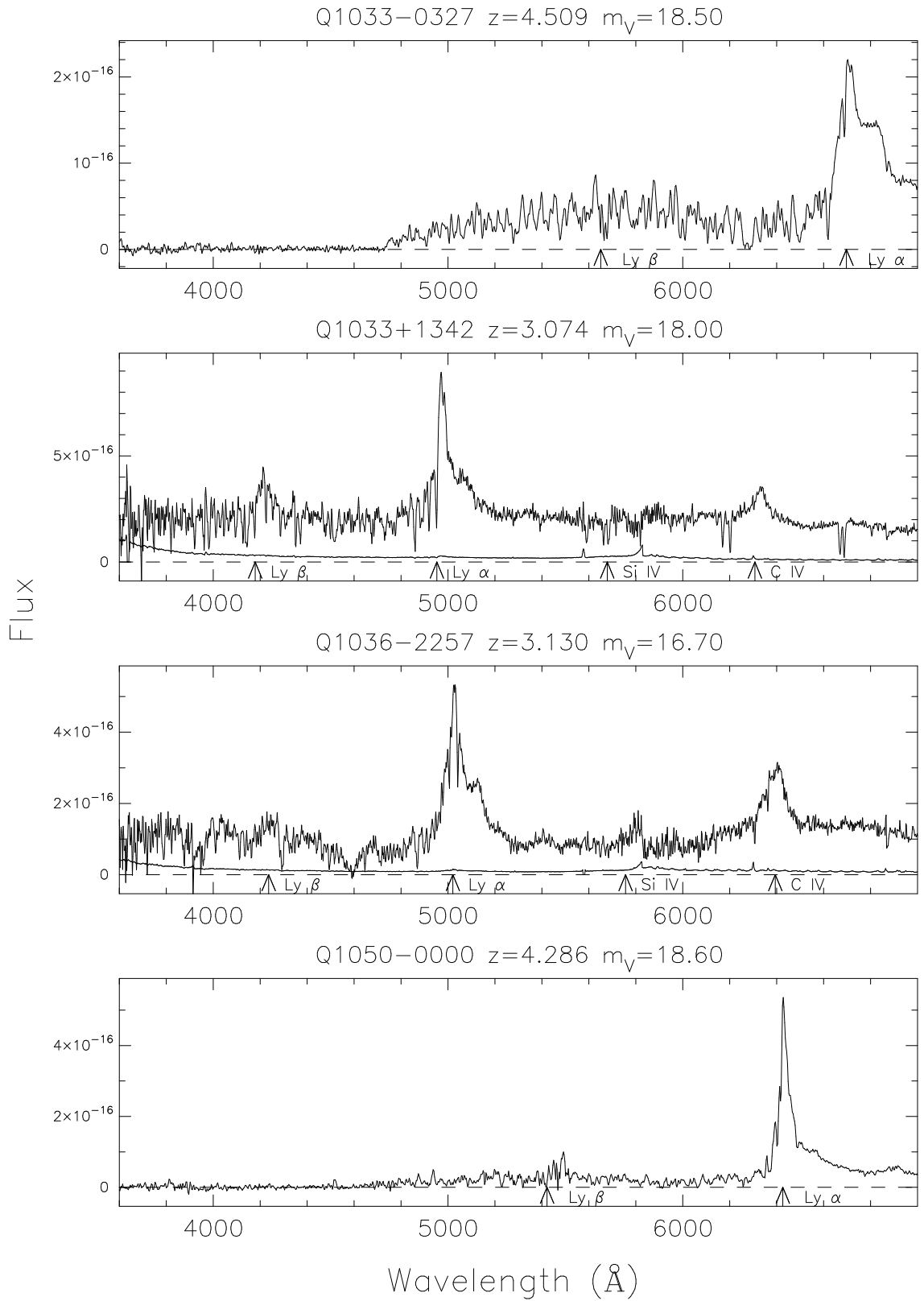
Figure 6.6 – *continued*

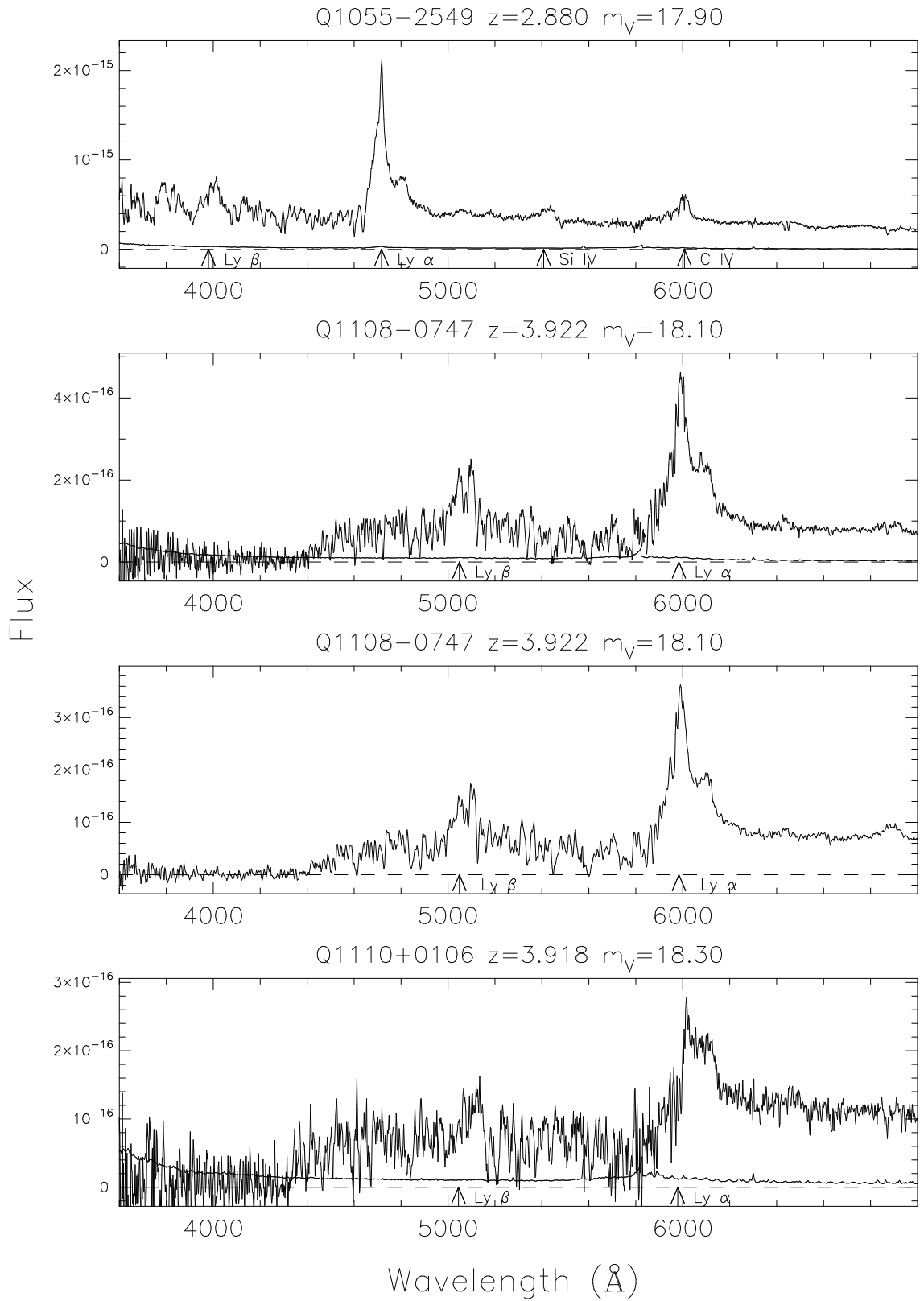
Figure 6.6 – *continued*

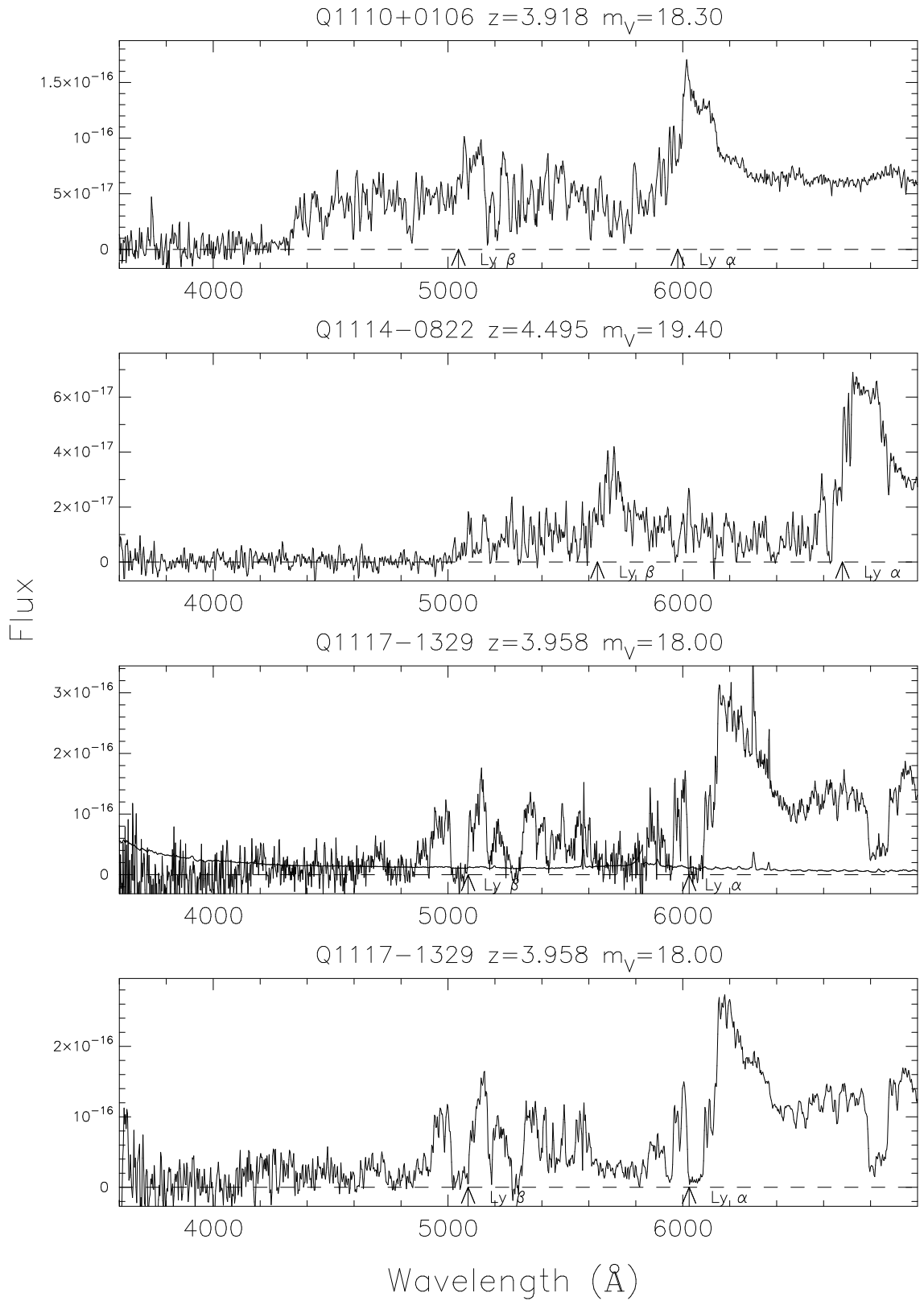
Figure 6.6 – *continued*

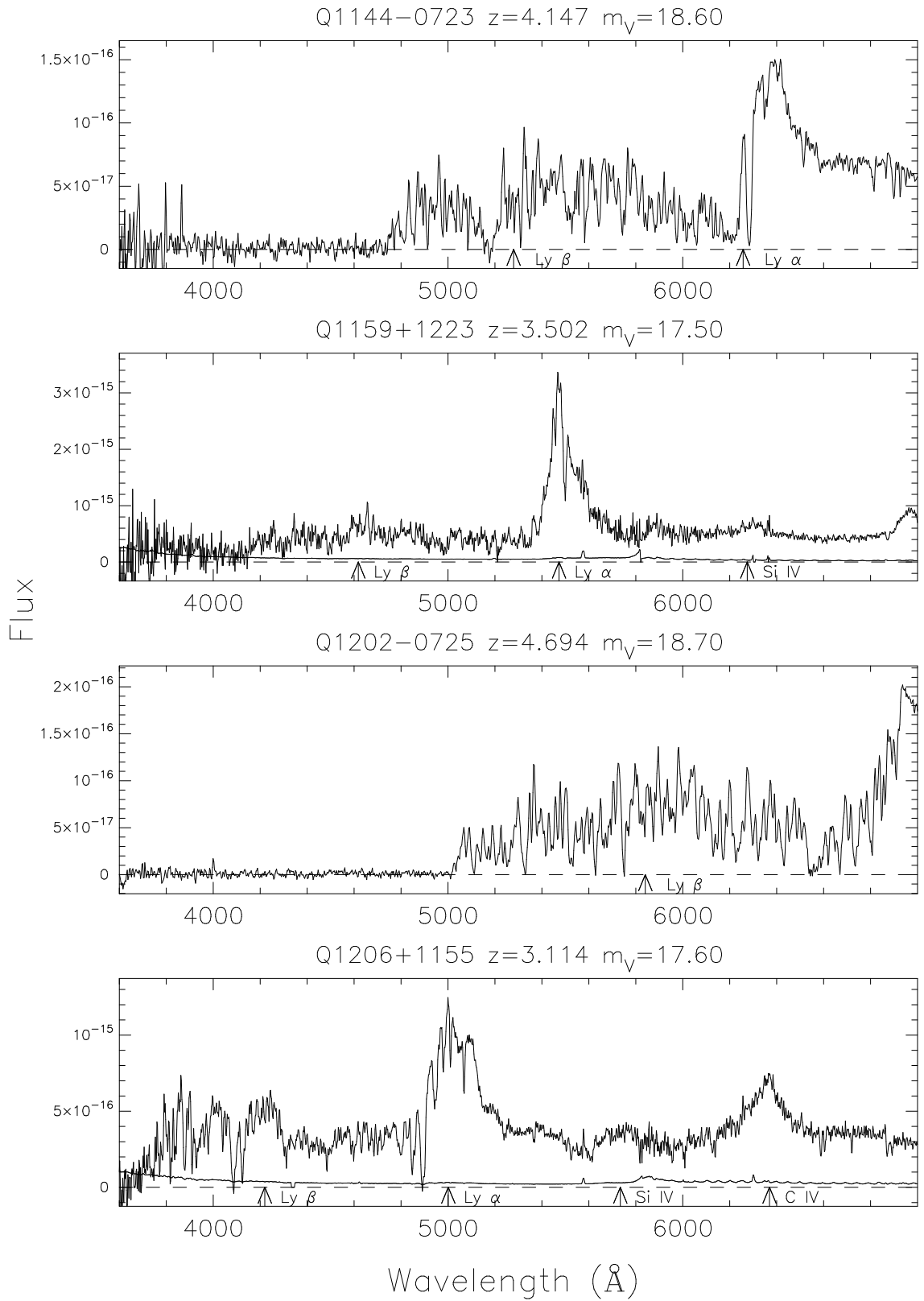
Figure 6.6 – *continued*

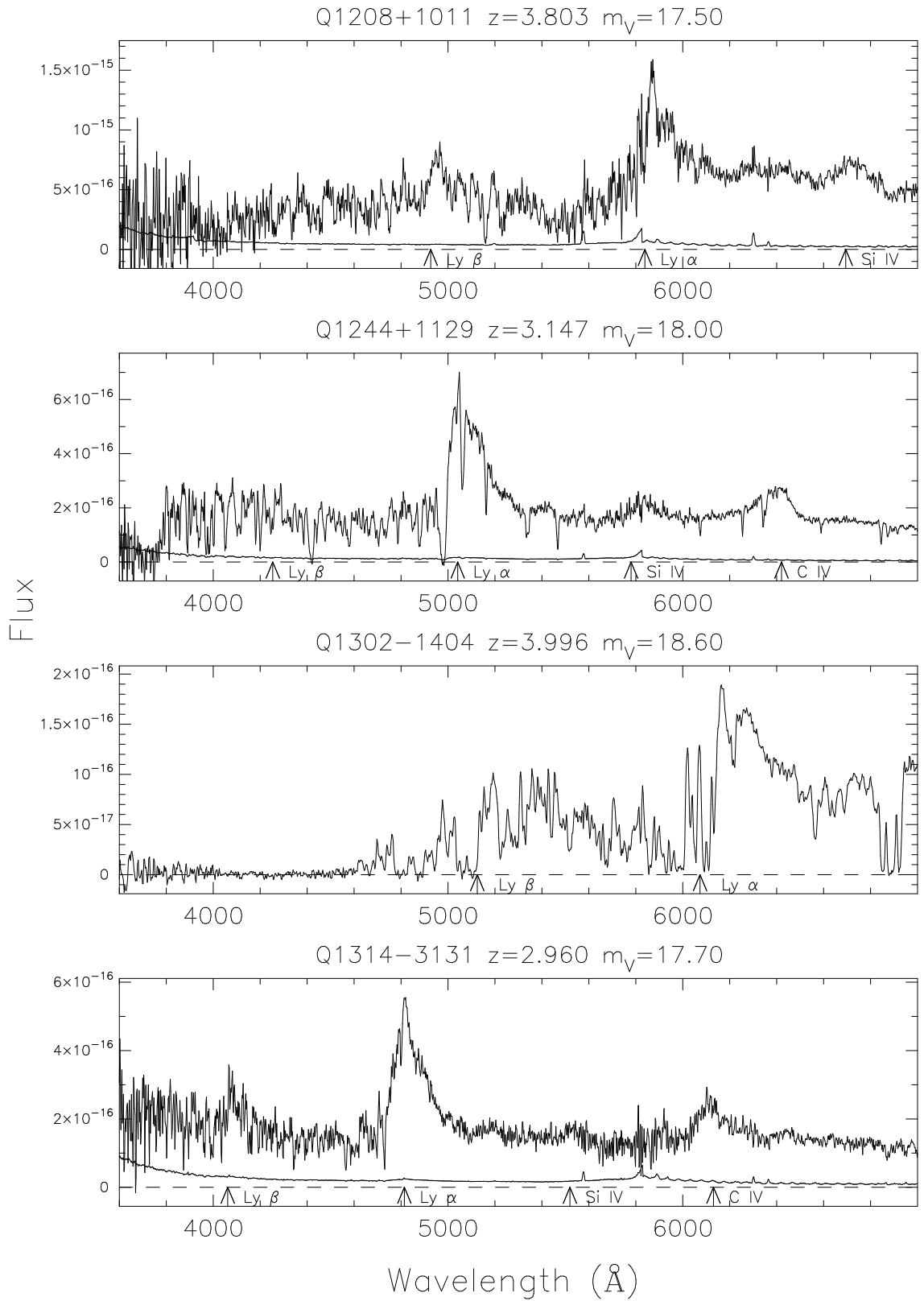
Figure 6.6 – *continued*

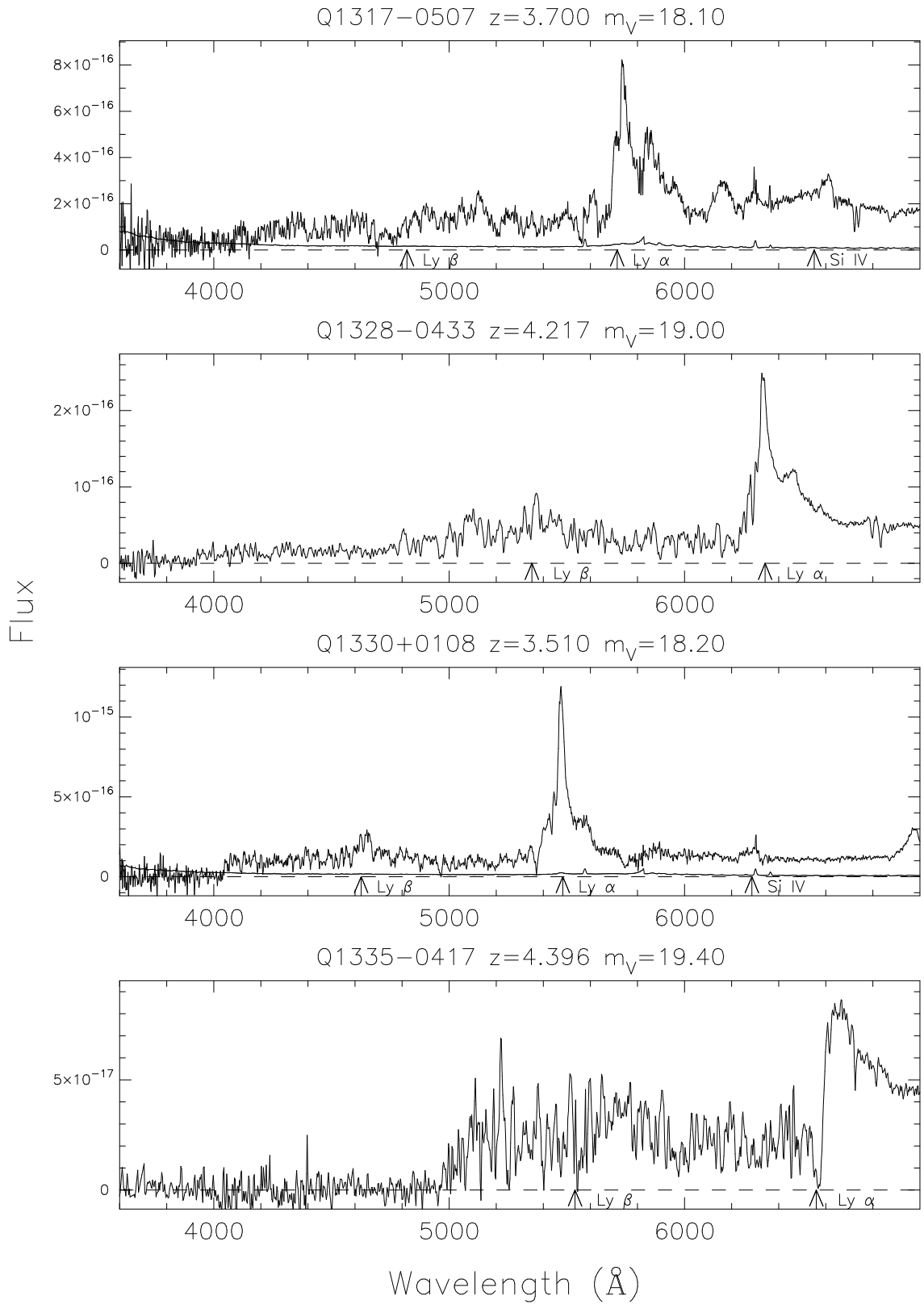
Figure 6.6 – *continued*

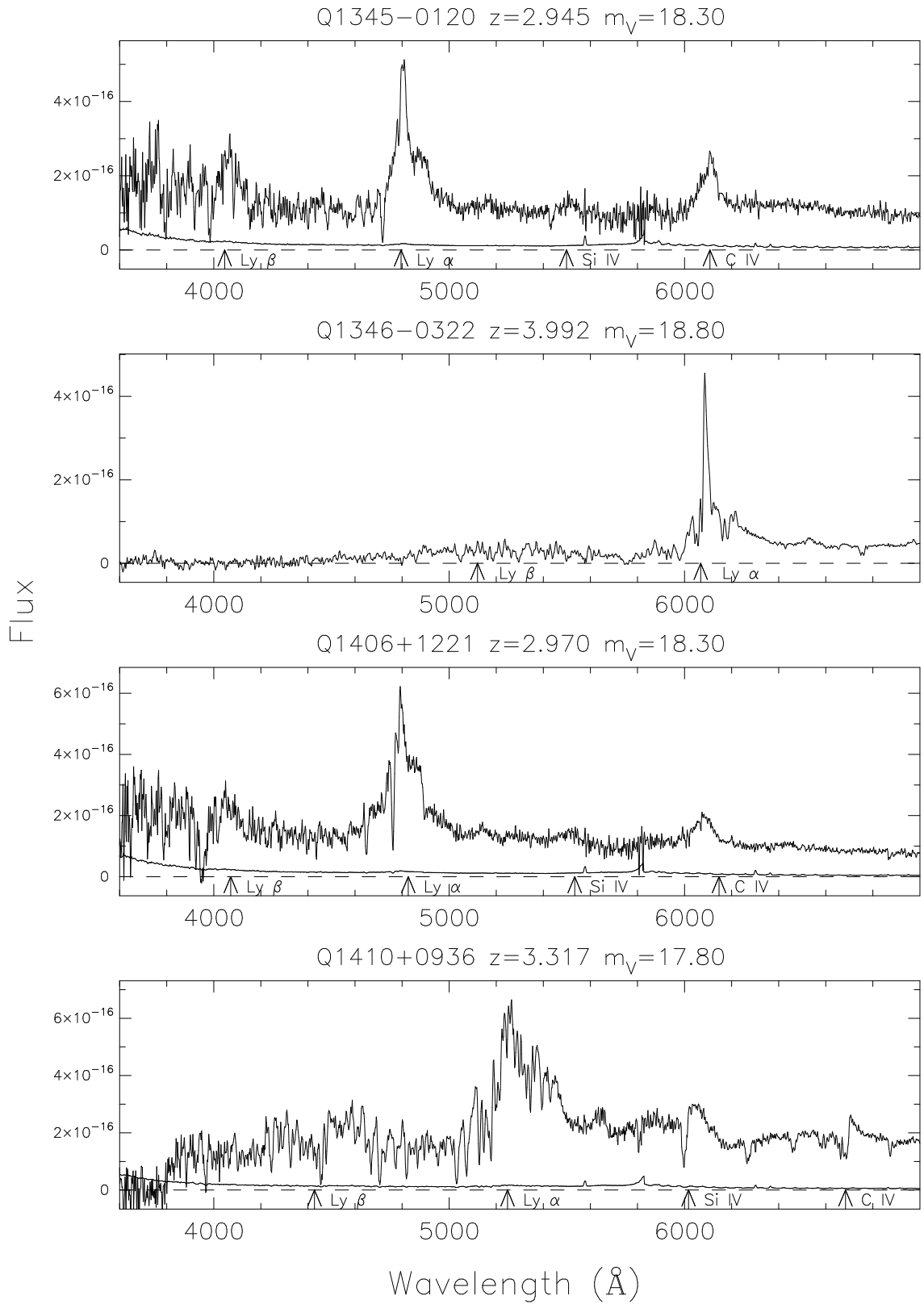
Figure 6.6 – *continued*

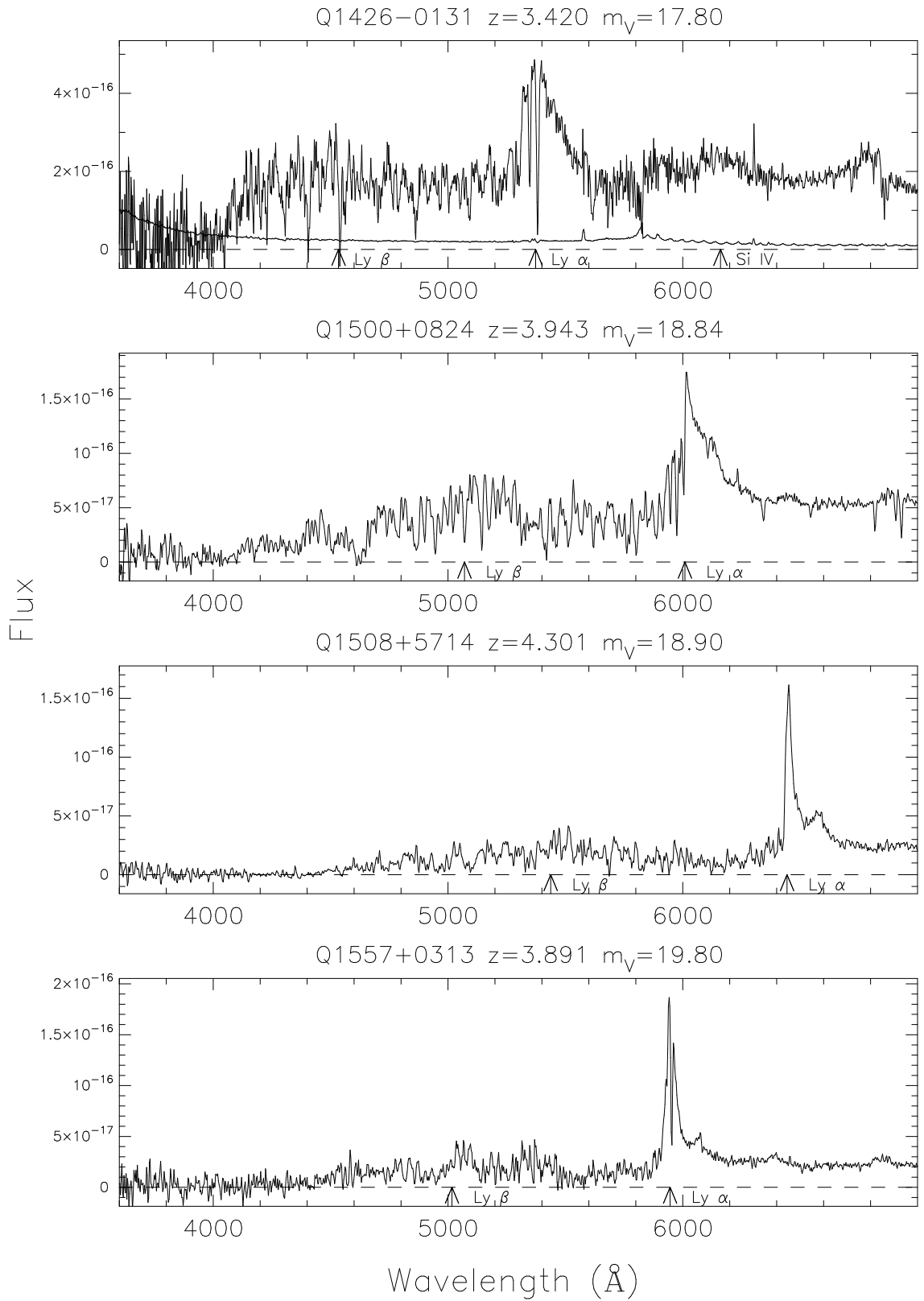
Figure 6.6 – *continued*

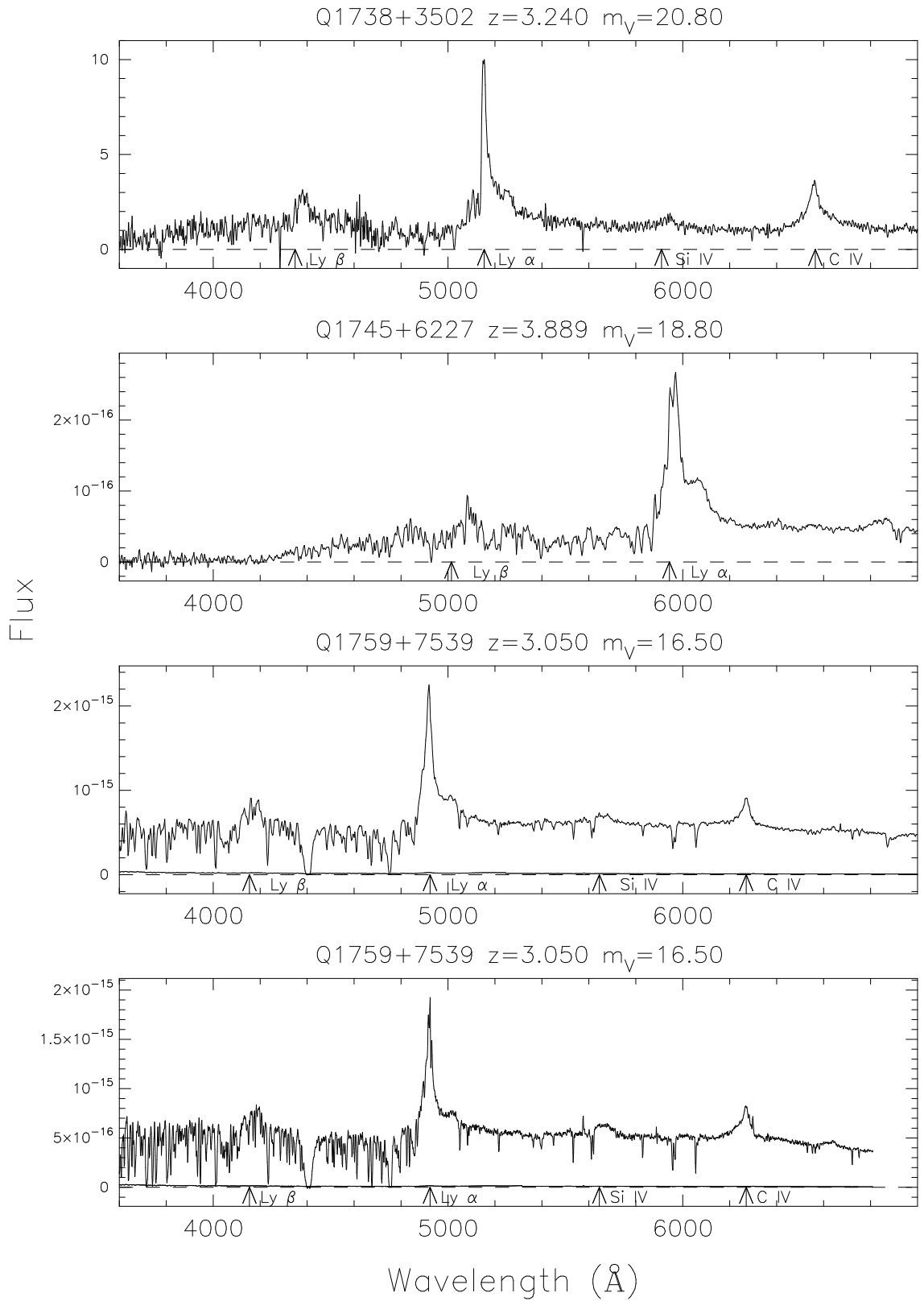
Figure 6.6 – *continued*

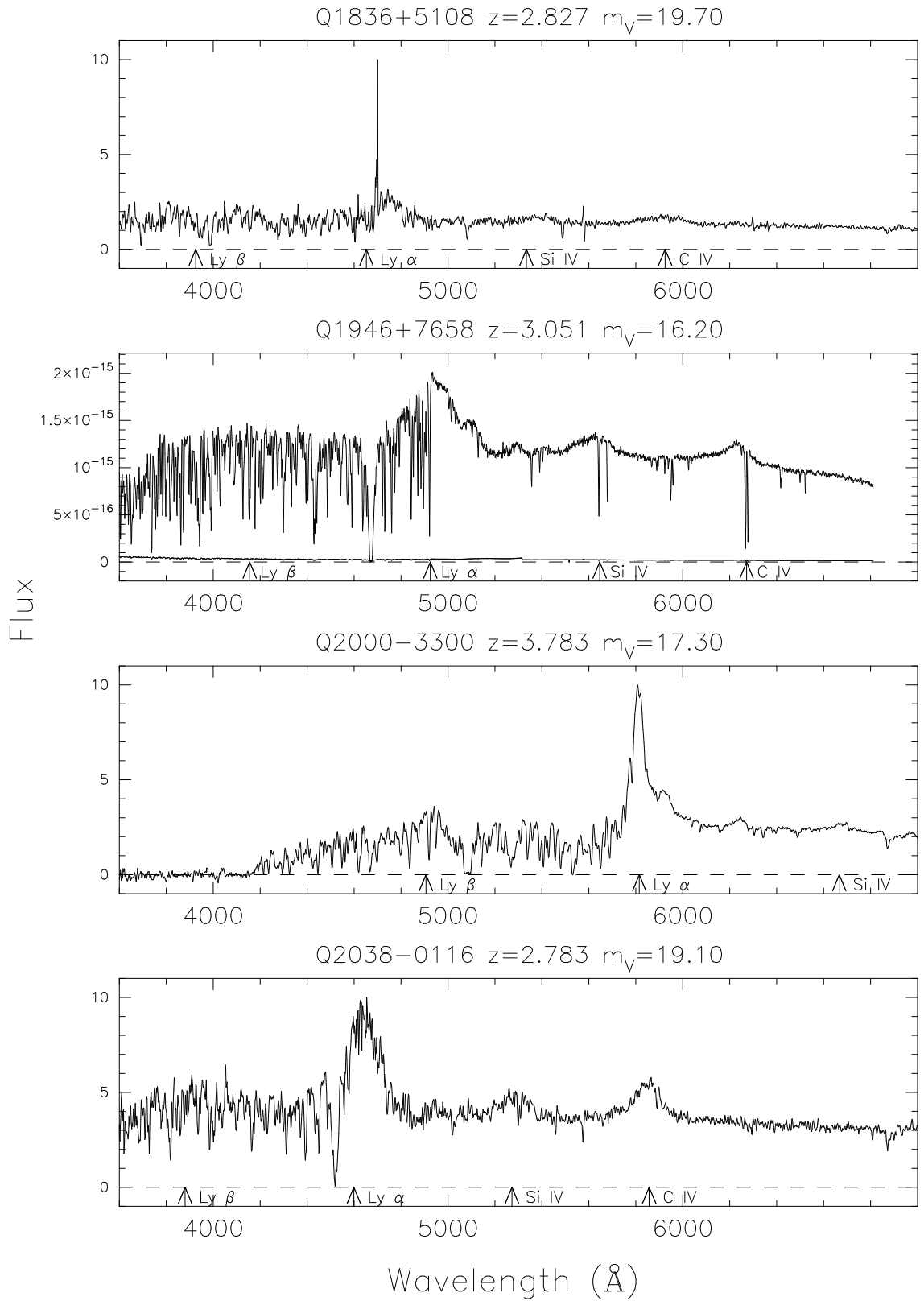
Figure 6.6 – *continued*

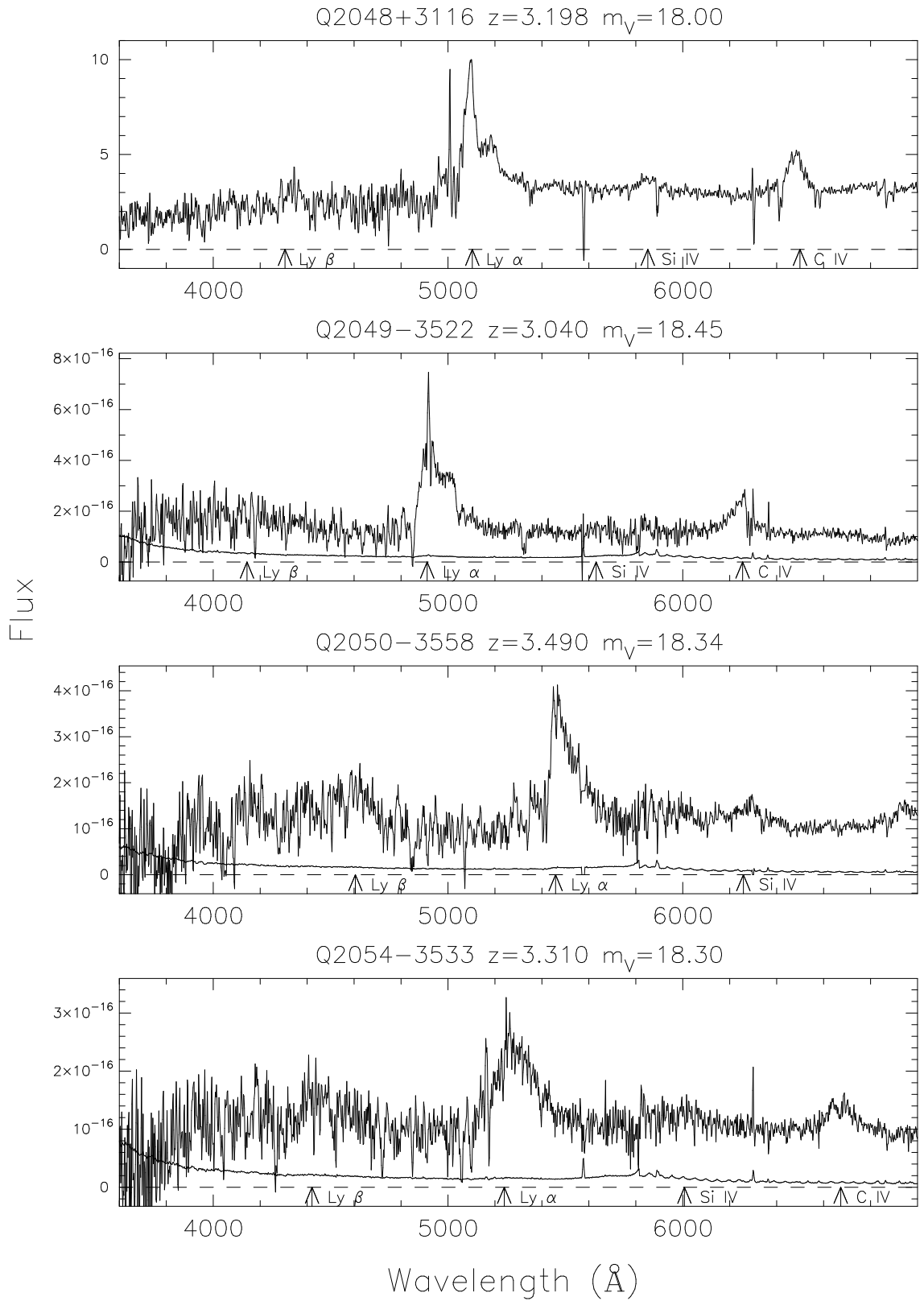
Figure 6.6 – *continued*

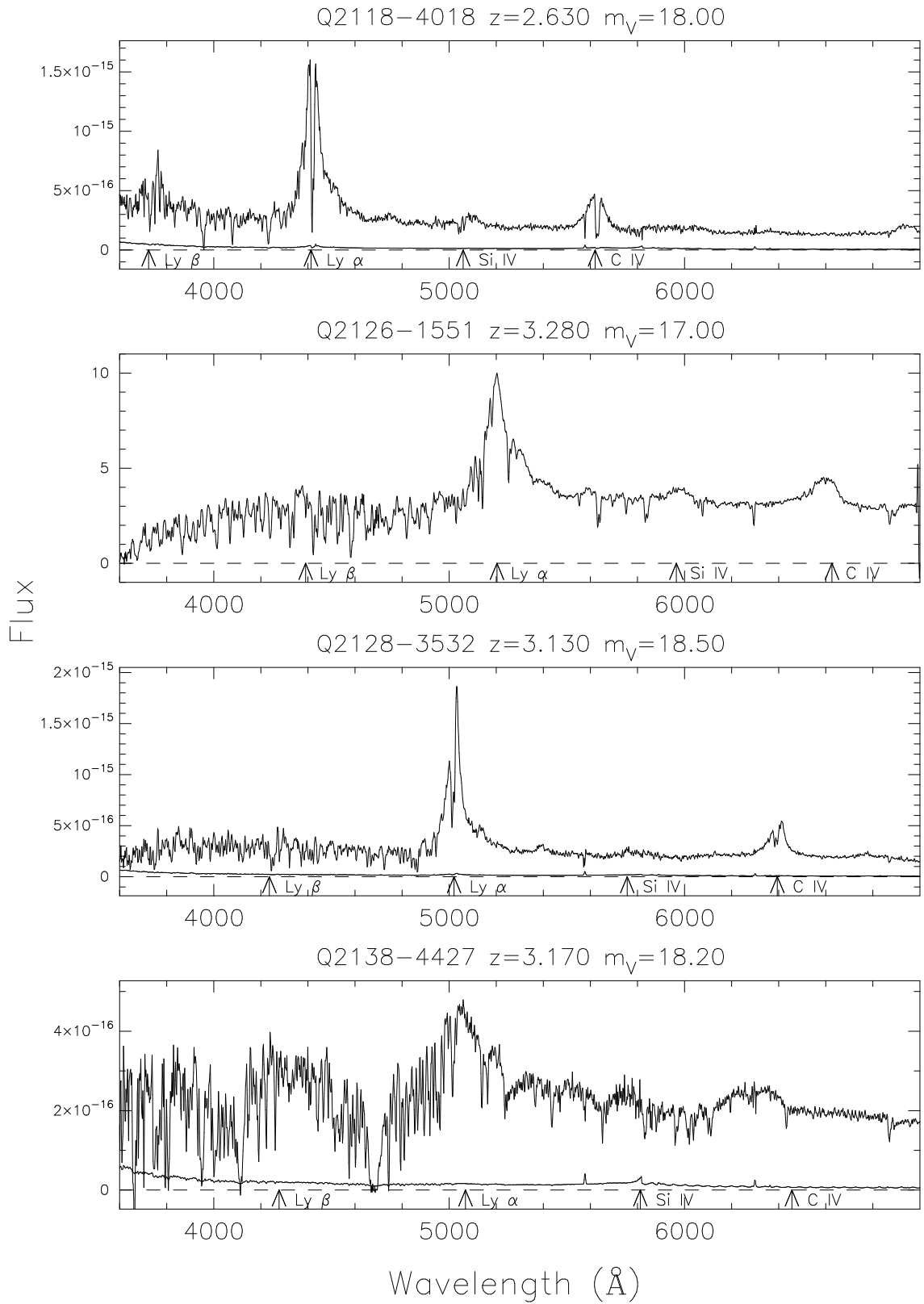
Figure 6.6 – *continued*

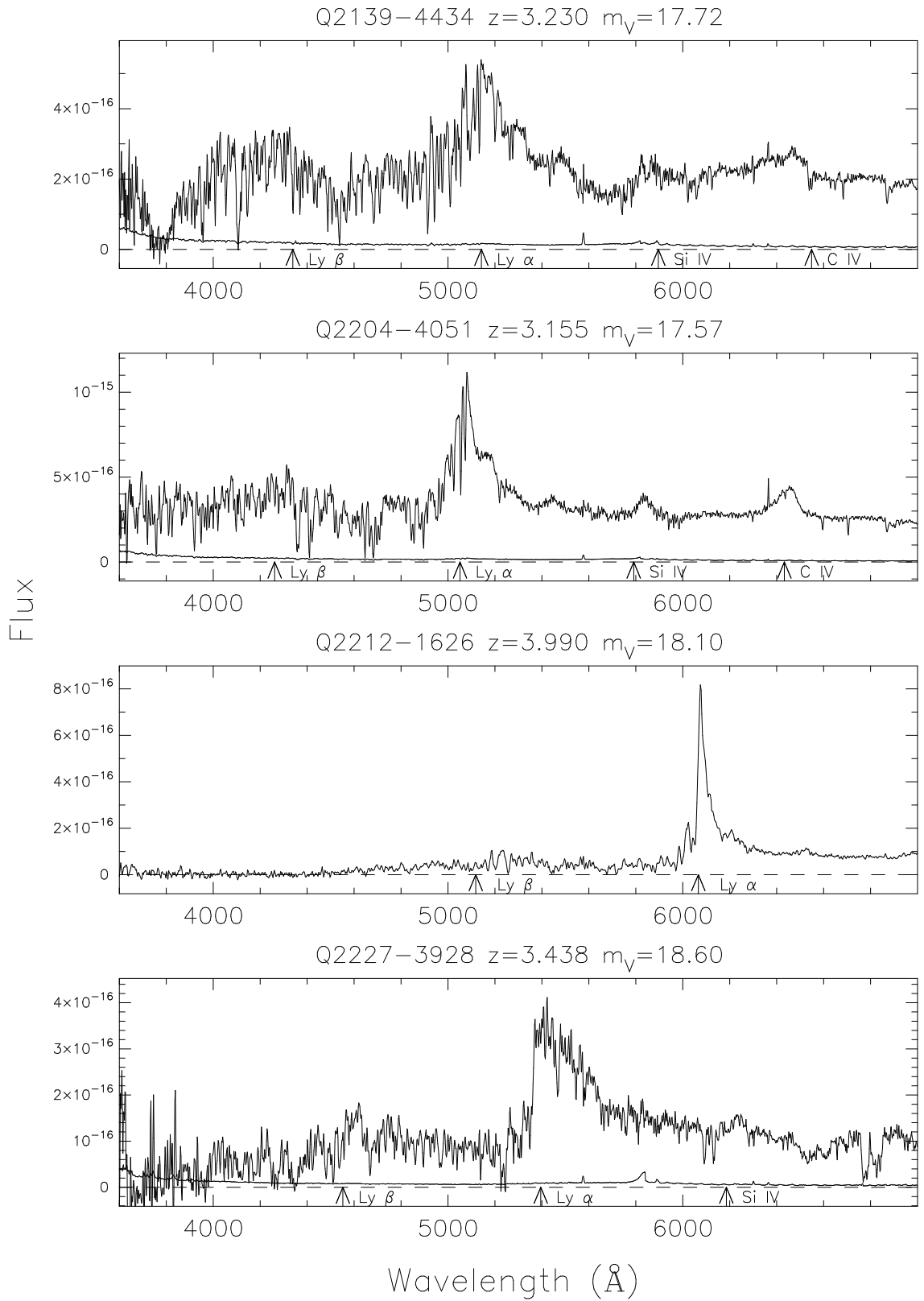
Figure 6.6 – *continued*

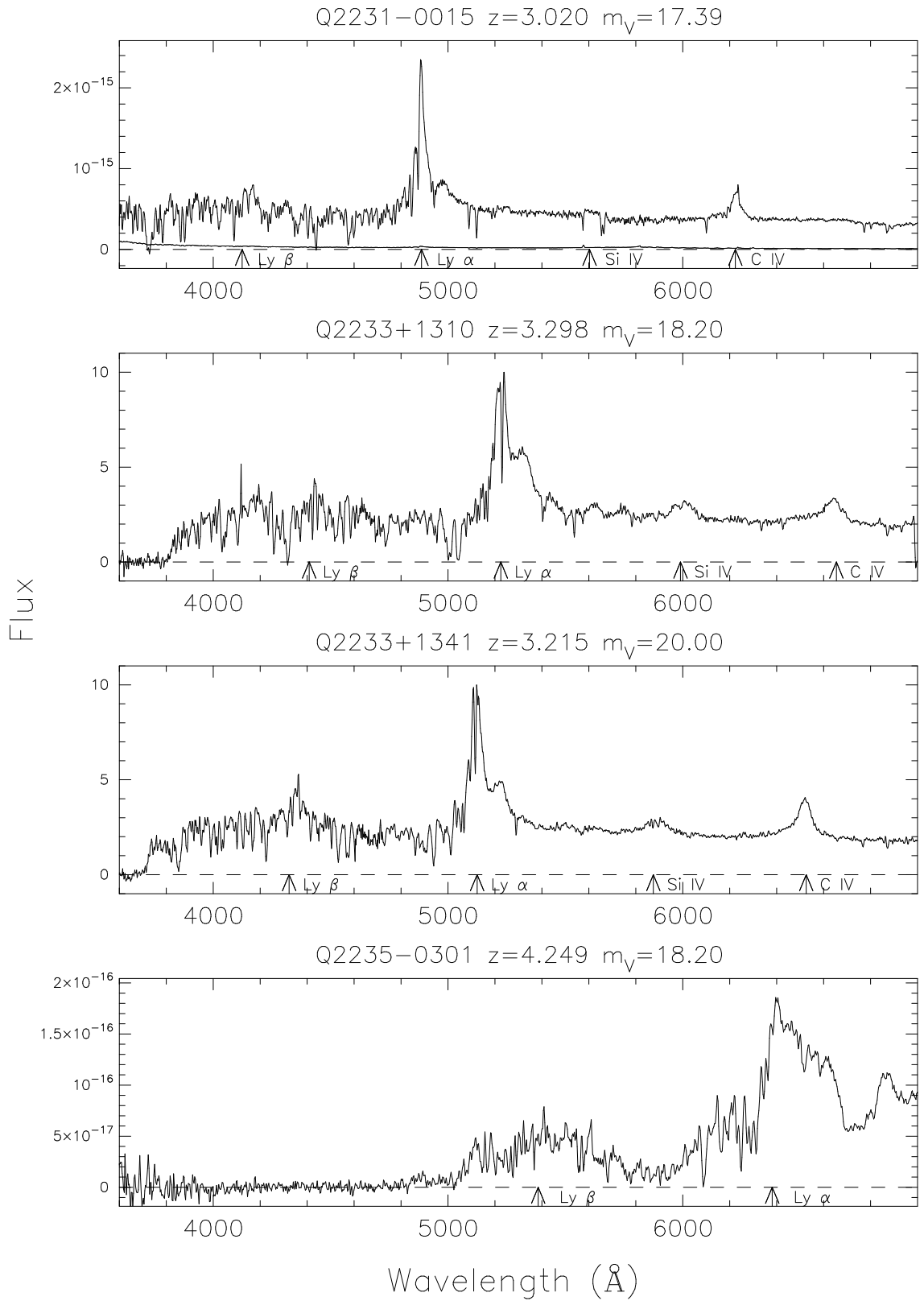
Figure 6.6 – *continued*

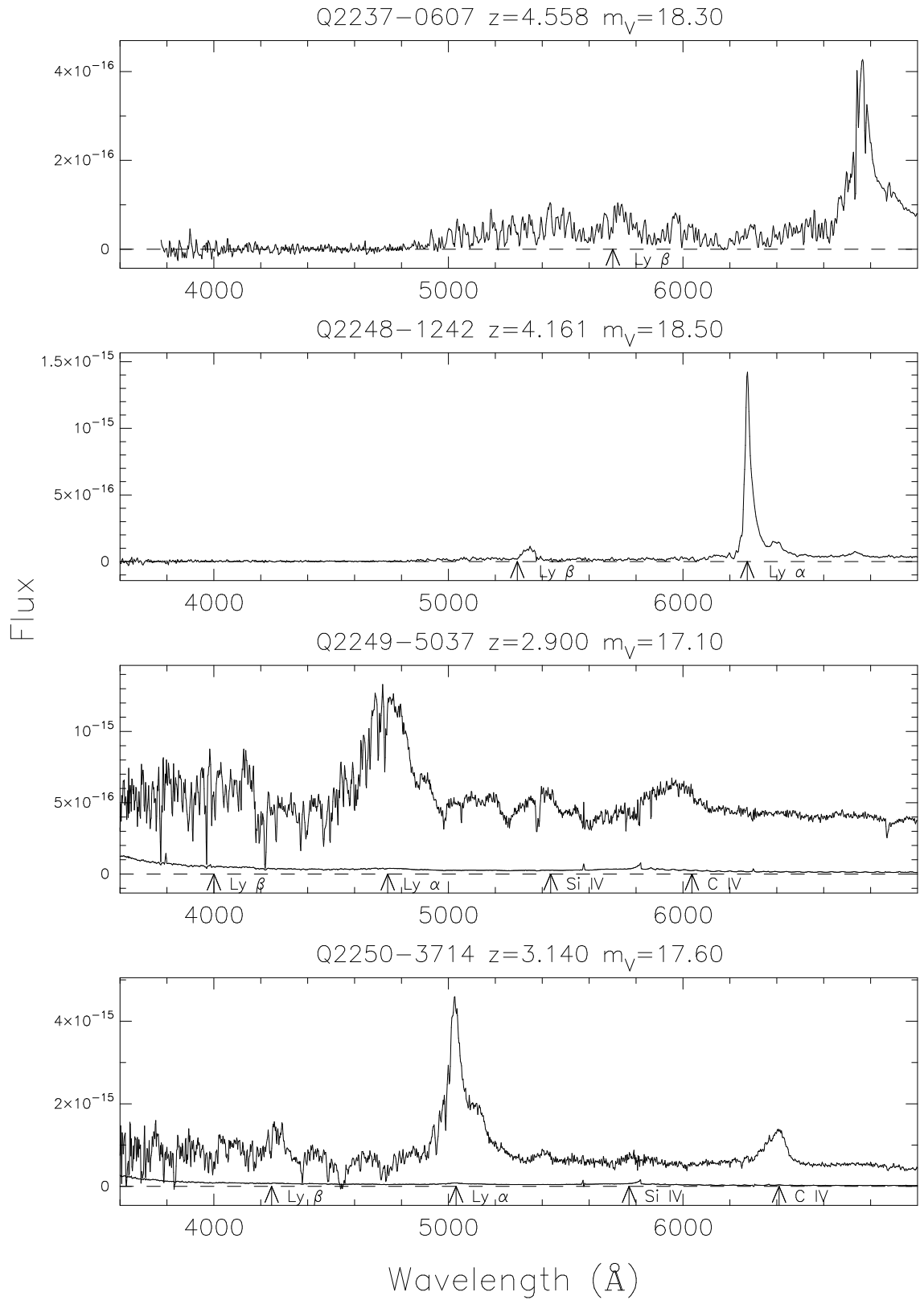
Figure 6.6 – *continued*

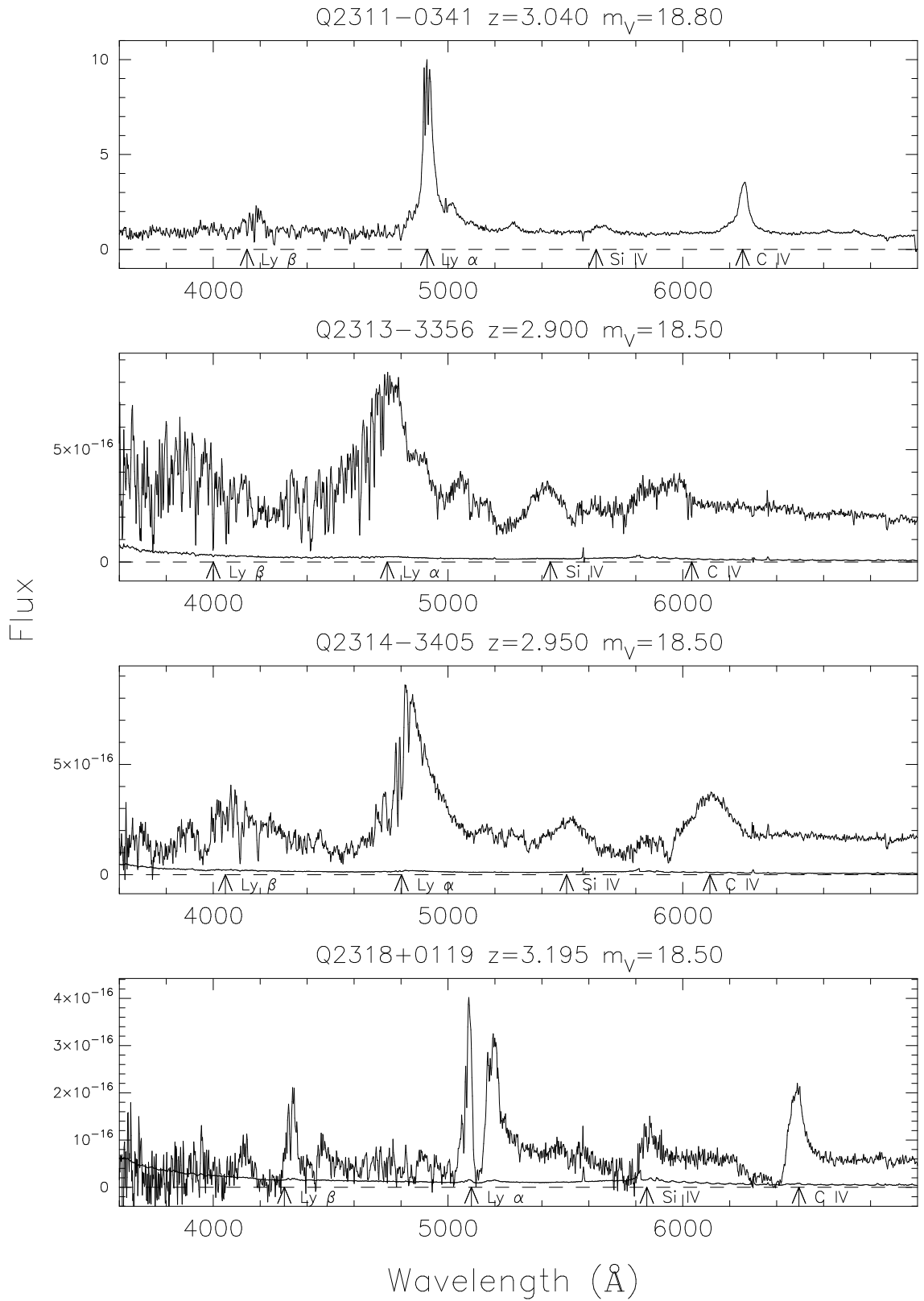
Figure 6.6 – *continued*

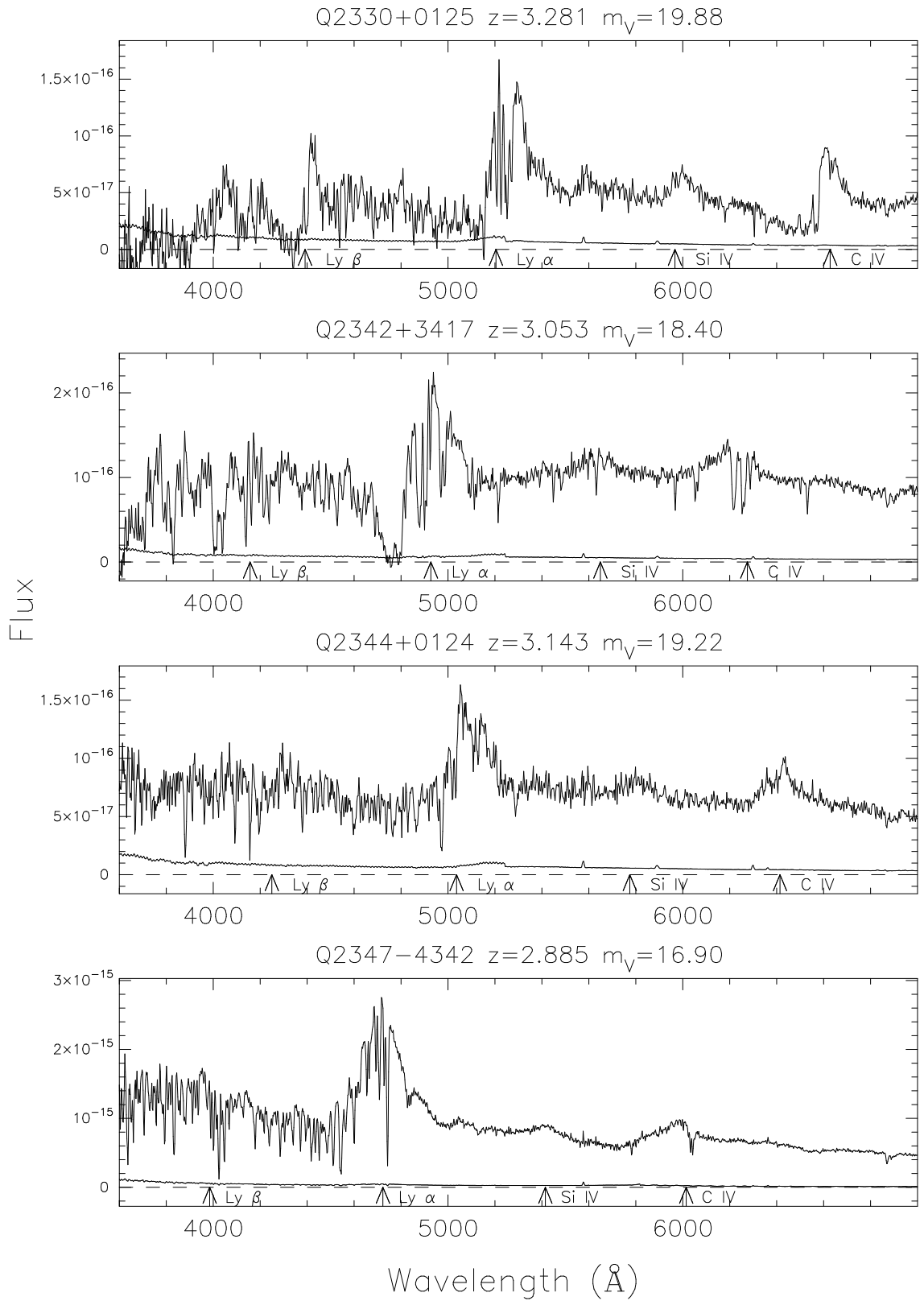
Figure 6.6 – *continued*

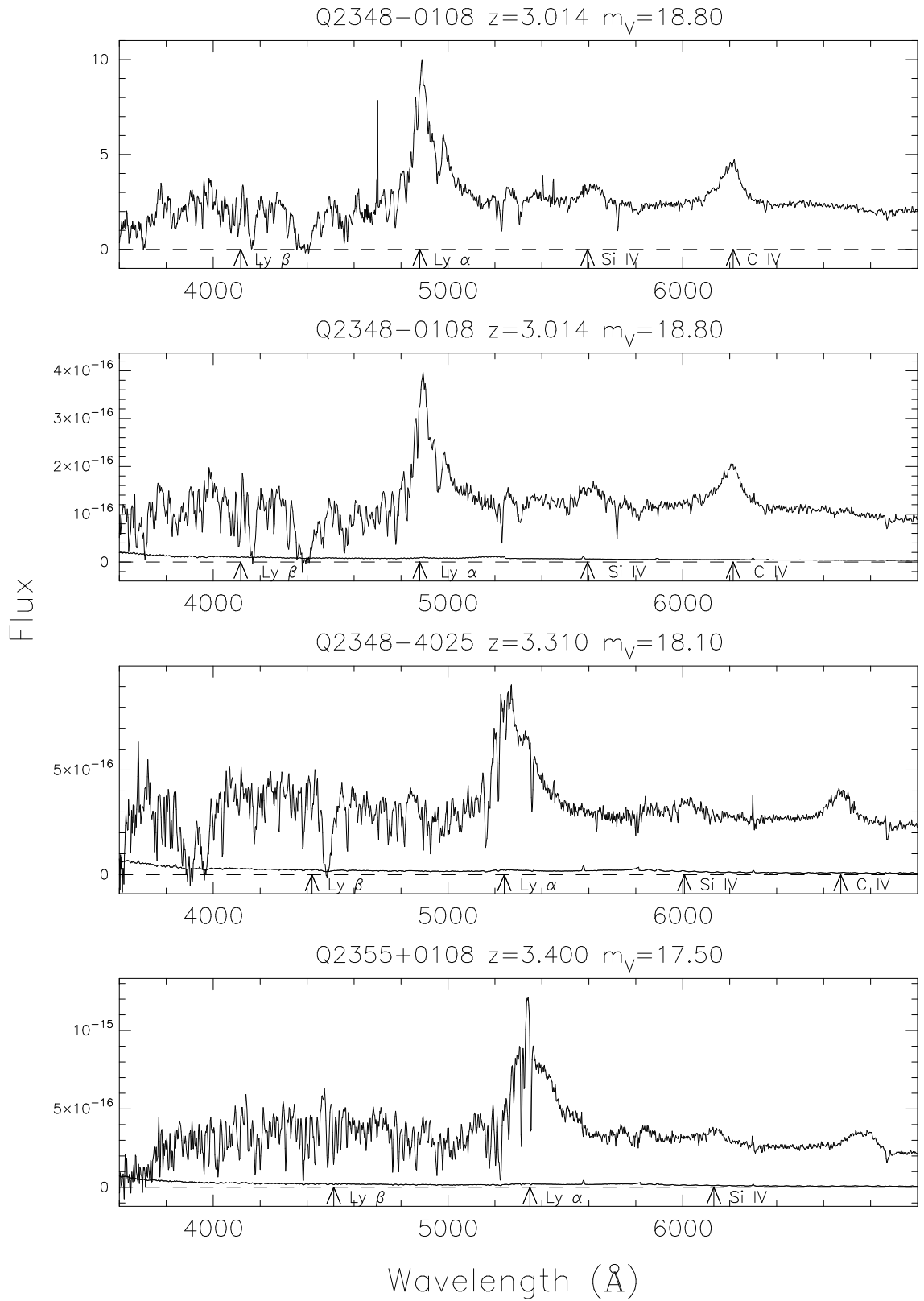
Figure 6.6 – *continued*

Figure 6.6 – *continued*

Figure 6.6 – *continued*

Figure 6.6 – *continued*

Figure 6.6 – *continued*

Figure 6.6 – *continued*

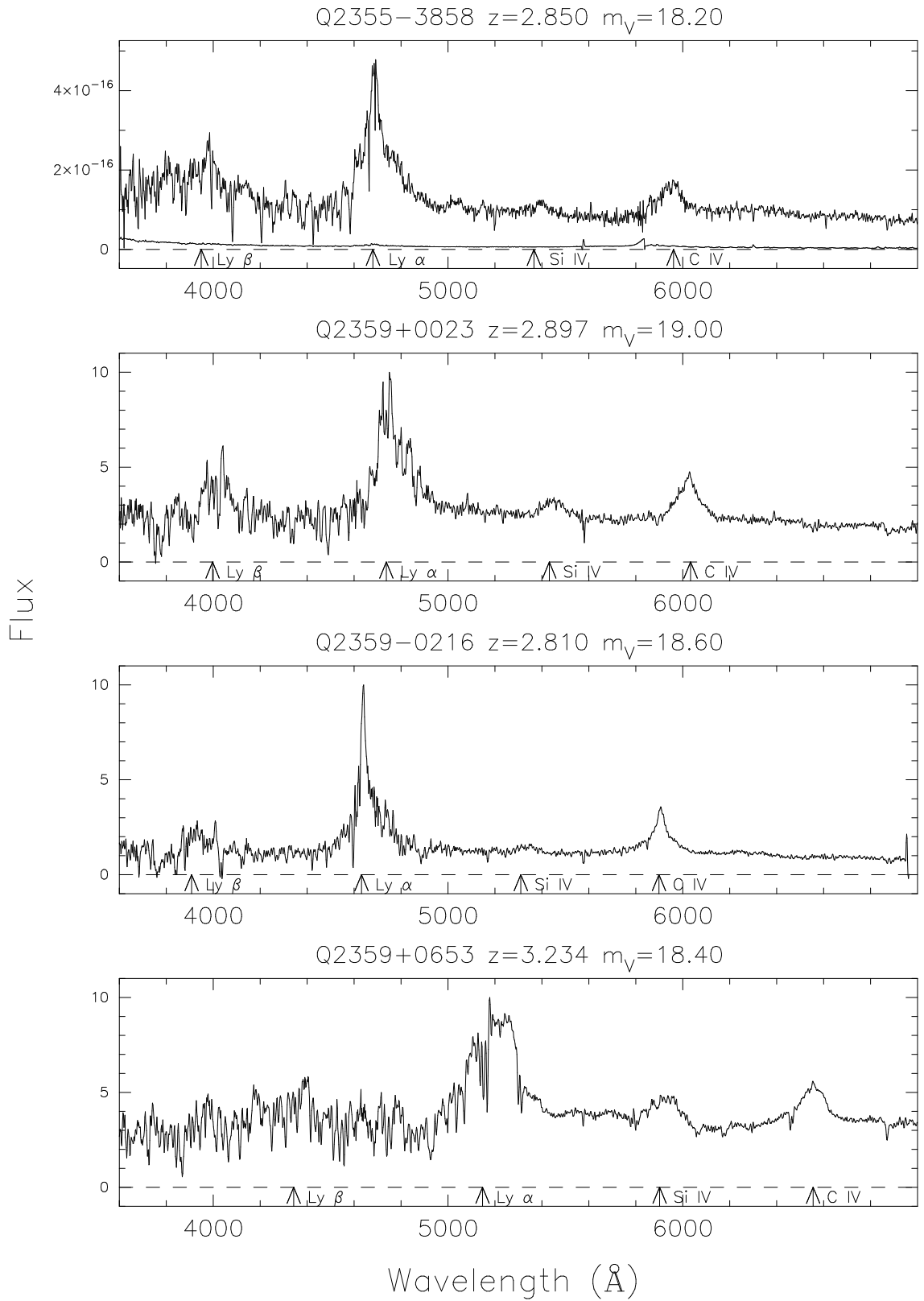
Figure 6.6 – *continued*

Table 6.2: Unidentified objects in PD2H survey.

Object	α_{J2000}			δ_{J2000}			m_V	Telescope	Date	Exposed
	h	m	s	°	'	"				
0101–2653	01	03	40.5	–26	37	23	18.40	2.3m	08/10/99	1800
0105–4238	01	07	17.9	–42	22	50	18.30	2.3m	31/10/00	3600
0143–0050	01	46	12.4	–00	35	39	17.00	2.3m	06/10/99	600
								2.3m	07/11/99	2700
								WHT	21/10/99	1200
0351–3749	03	53	08.5	–37	40	54	18.40	2.3m	06/10/99	7200
2331+0216	23	34	32.0	+02	33	21	19.98	WHT	20/10/99	600
2348–0100	23	50	55.9	–00	43	27	18.50	2.3m	28/10/00	3600

6.3.1 2.3-m observations

We have had seven observing runs at the ANU 2.3-m Telescope, totalling 30 nights, of which effectively 60 per cent were useful. All observations were performed using the Double Beam Spectrograph (DBS) with an identical instrumental setup for each run.

Observational setup and procedures

DBS is mounted at one of the telescope’s Nasmyth foci. The light from the telescope is first split into two beams by a dichroic. We used dichroic D1 which has its blue-red cross-over point at $\sim 5700 \text{ \AA}$. After splitting, the two beams are fed into two separate but essentially similar spectrographs. Each spectrograph has its own optical components and a detector optimized for the blue and red parts of the optical spectrum respectively. We dispersed the beams using the 300B and 316R gratings. The grating angles were set to give central wavelengths of 4600 \AA and 7600 \AA , covering from well below the atmospheric cutoff to $\sim 9400 \text{ \AA}$ with $\sim 600 \text{ \AA}$ overlap between the two arms. In both arms we used a SITE CCD with 1752×532 $15 \mu\text{m}$ pixels, which was windowed to give 200 pixels in the spatial direction and

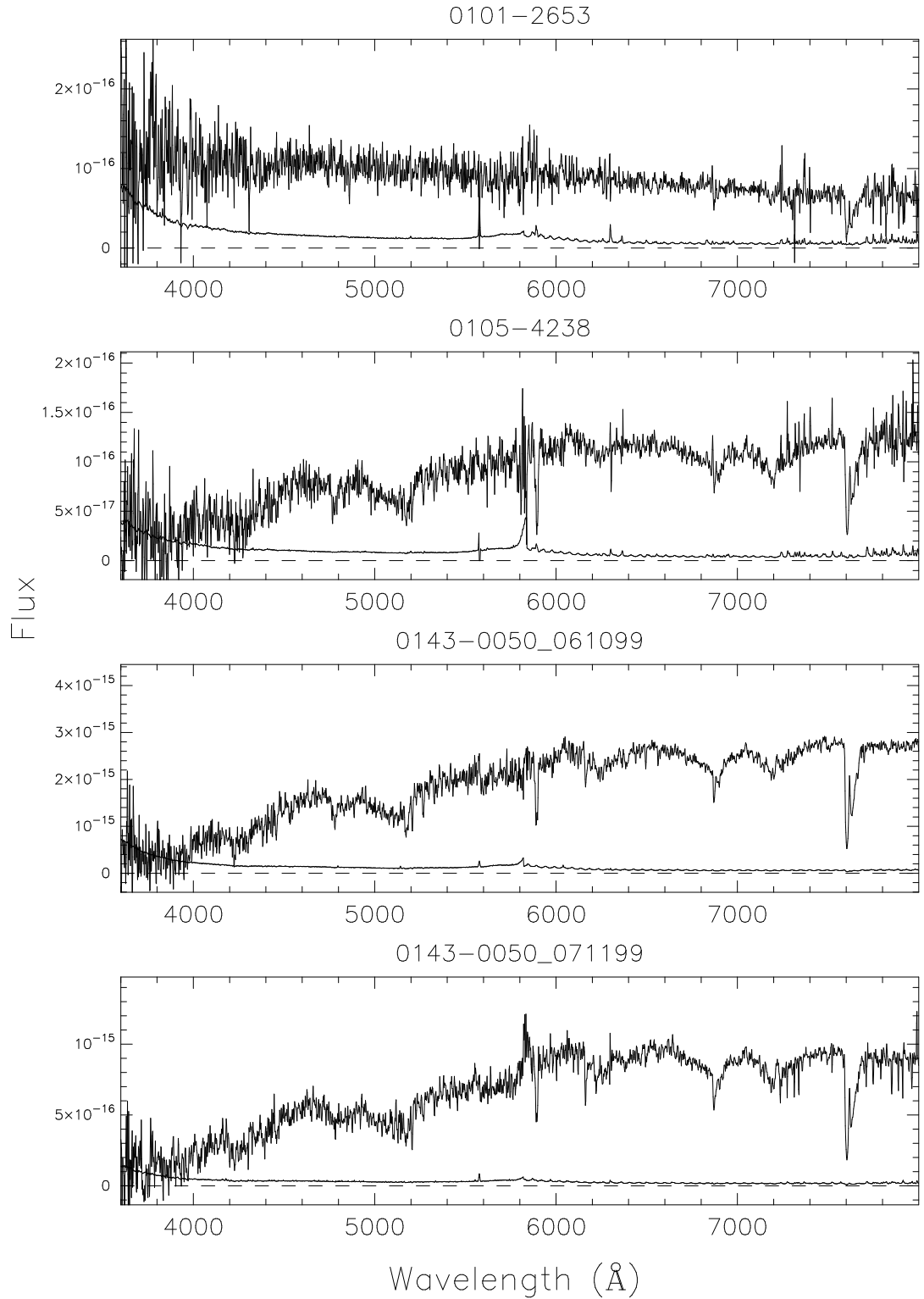
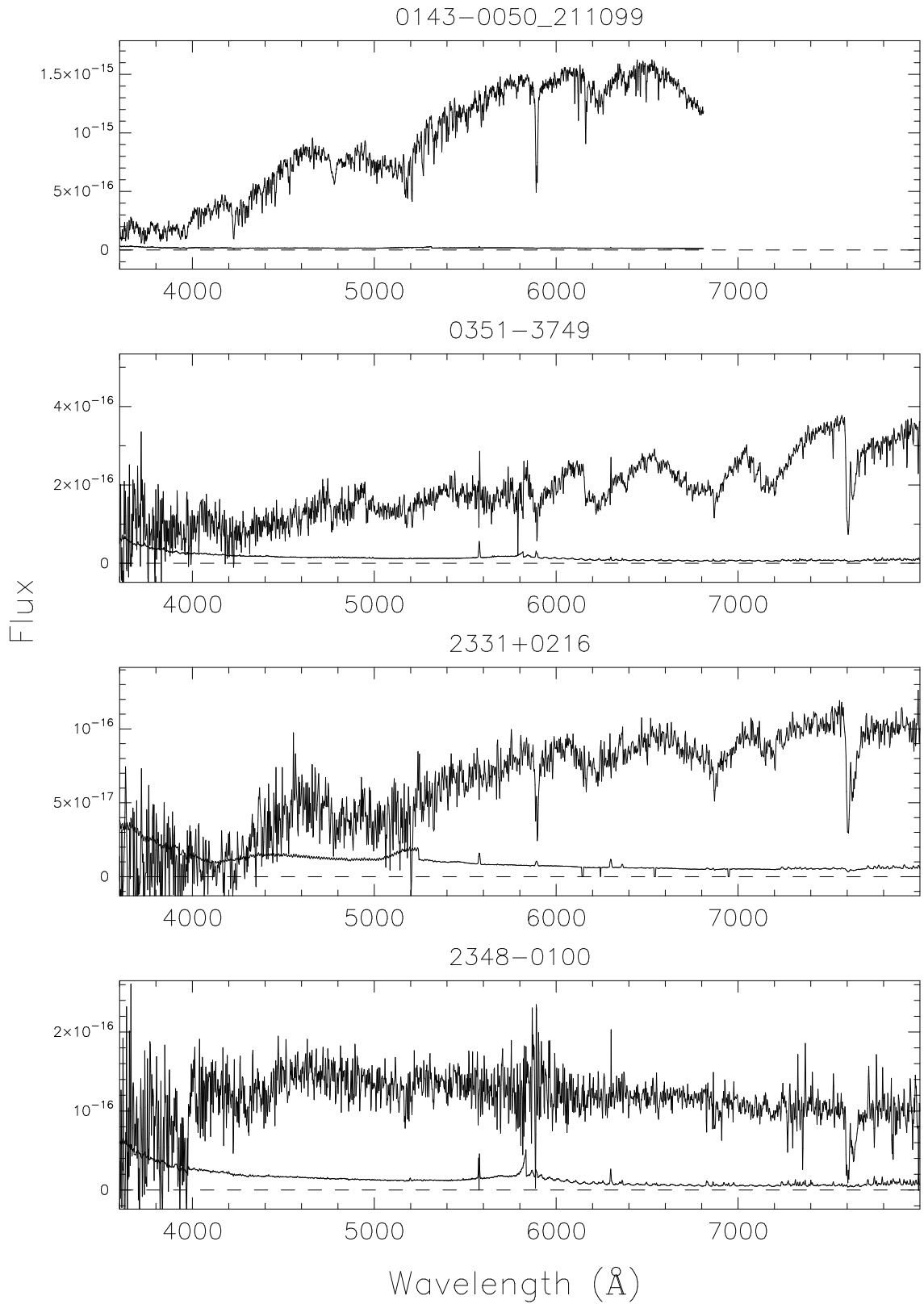


Figure 6.7: Flux calibrated spectra and 1σ error arrays of unidentified objects in PD2H (cf. Table 6.2) versus heliocentric wavelength. The flux is in units of $\text{ergs s}^{-1} \text{cm}^{-2} \text{\AA}^{-1}$.

Figure 6.7 – *continued*

100 columns overscan.

We took 11 bias frames and quartz lamp flat fields at the beginning and end of each night. CuAr comparison arc spectra were taken before and after each science exposure and 2 – 3 spectrophotometric standard stars were observed for flux calibration each night. Since we are most interested in the blue part of the spectrum (below Ly α emission) and since there is no atmospheric absorption in this part, we did not observe smooth spectrum stars. We usually found it necessary to refocus the telescope and often also the spectrograph around midnight. The slit width was typically 1.5'' to 2'', depending on the conditions. Due to the autoguiding system we were unable to observe at the parallactic angle. Instead, we set the slit angle at the beginning of each exposure so that the slit would be vertical with respect to the horizon approximately in the middle of the exposure. This procedure ensured that the slit was never more than 15–20° away from the vertical position. The exposure time of individual frames was 1800 s, with typical total integration times of 1–2 hours per QSO (cf. Table 5.1).

CCD processing

All data reduction was performed separately for the blue and red arms using standard IRAF¹ routines.

First we subtracted the overscan region. From bias frames it was apparent that there were ‘stripes’ of a few pixels across of both increased and decreased counts across the chip. These are believed to be caused by the CCD controllers. Fortunately, these ‘stripes’ were nearly parallel to the image lines and extended into the overscan region. We were thus able to more or less subtract them out by using the median of the overscan columns (rather than a functional fit). However, since the ‘stripes’ were not perfectly parallel to the image lines this procedure worked less well for columns far from the overscan region. Unfortunately, the overscan region of the

¹IRAF is distributed by the National Optical Astronomy Observatories, which are operated by the Association of Universities for Research in Astronomy, Inc., under cooperative agreement with the National Science Foundation.

blue CCD is on the red side. Thus, at the blue end of the chip, where the Ly limit region was recorded, we sometimes encountered zero-level problems (cf. Fig. 6.6).

Following overscan correction and trimming, a bad image column was ‘fixed’ by interpolating across it. Bias frames were then averaged without using the highest value in each pixel (in order to reject cosmic ray events) and the result was subtracted from each image.

Flat fields were averaged using IRAF’s cosmic ray rejection algorithm. The goal of flat-fielding at this stage is to remove pixel-to-pixel sensitivity variations. However, the resulting master flats had a strong wavelength dependence due to the throughput of the optical system. In particular, the dichroic caused strong ‘wiggles’ near the end of the respective wavelength ranges. These have to be preserved in the science frames (and thus removed from the flat fields) in order to preserve the image statistics. Cubic spline fits to the flat fields’ response functions were thus divided into the flat fields before applying them to the rest of the images. A copy of the fitted response function was kept for later use.

Individual images of the same object (from the same night) were then registered and combined, again using IRAF’s cosmic ray rejection algorithm.

Extraction and calibration of spectra

First, we extracted the standard stars. An aperture was defined by hand and traced along the chip by fitting a Legendre polynomial of order 3–5. 40 pixel regions on either side of the spectrum were used to determine the background, which was fit with a Chebyshev polynomial of order 2–3. Since the QSO spectra can be quite faint we extracted all object spectra using one of the standard stars’ trace. Although the spectra were optimally extracted (i.e. using variance weighting) we nevertheless resized all object apertures by hand (after automatically repositioning them) and checked the background regions and fits at the same time. Arc spectra were extracted using the corresponding object’s aperture. We then divided the flat field response function into the extracted spectra (objects, standards and corresponding

error arrays) in order to remove the large scale features of the dichroic which would otherwise interfere with the flux calibration process.

The emission lines of the arc spectra were identified and a pixel-to-wavelength calibration curve was found by fitting a fifth order Chebyshev polynomial. We identified > 50 lines in the blue and > 40 in the red. Typical residuals from the fits were $\sim 0.3 \text{ \AA}$. These dispersion solutions were applied to the object spectra which were rebinned to a linear wavelength scale and corrected for heliocentric motion. The spectral resolution varied from 4.1 \AA to 5.5 \AA in the red and from 4.9 \AA to 6.0 \AA in the blue.

We then used the standard star observations to derive sensitivity functions. In the blue arm the sensitivity function turned downward fairly sharply below 3400 \AA . Otherwise they were smooth, low order functions since we had already removed the effects of the dichroic. The object spectra were then flux calibrated and corrected for extinction.

In a last step, all blue and red spectra of the same object from different nights were combined by first rebinning them to a common wavelength scale, then scaling them to a common median level where they overlap and then averaging them using inverse variance weighting.

Finally, we note that the absolute flux scale of the spectra is unreliable because we observed through a narrow slit and the conditions were rarely photometric. However, the relative energy distributions should be reasonably accurate.

6.3.2 WHT observations

On the nights of 20 and 21 October 1999 we used the ISIS spectrograph on the 4.2-m WHT to observe a total of 27 QSOs. ISIS is a double-armed, medium resolution spectrograph which is mounted at the Cassegrain focal station of the WHT. The setup, observations and data reduction procedures were very similar to those described in the previous section. Here, we just list the differences.

We employed a dichroic with a blue-red cross-over at $\sim 5400 \text{ \AA}$. On the first

night we used the 158B and 158R gratings with central wavelengths of 4400 Å and 6700 Å in the blue and red arms respectively. On the second night we decided to forsake speed in favour of higher resolution and used the 300B and 316R gratings with central wavelengths of 4000 Å and 6050 Å. The detector in the blue arm was a blue sensitive EEV12 CCD with 4096×2048 $13.5 \mu\text{m}$ pixels. In the red arm we used a TEK4 CCD with 1024×1024 $24 \mu\text{m}$ pixels.

The seeing was $1.0''$ to $1.2''$ and we thus used slit widths of $1.2''$ and $1.0''$ during the first and second nights respectively. We observed at the parallactic angle at all times. Typically, we performed two 600 s integrations per QSO in the first night and a varying number of 900 s integrations in the second (cf. Table 5.1).

All data reductions were performed in the manner described in the previous section. The only difference was that we now performed the overscan correction by subtracting a third order Chebyshev polynomial fit to the overscan region, rather than the median. For the first night the spectral resolution was 7.7 \AA in the blue and 7.4 \AA in the red. For the second night we found 3.3 \AA and 3.1 \AA respectively.

6.4 D/H towards Q0940–1050

6.4.1 Selection of Q0940–1050

In Fig. 6.8 we plot the 2.3-m spectrum of the Ly α forest in Q0940–1050. As we can see it exhibits a very sharp and well-defined Ly break. This is usually an indication of simple velocity structure. We will now attempt to apply the arguments of Section 6.2 to this absorption system in order to determine whether it might yield a D/H measurement.

First, we need to fit a continuum. At the low resolution employed here, the absorption lines in the Ly α forest are heavily blended and one cannot be certain at which points the spectrum recovers to the continuum. We are thus forced to extrapolate the continuum from wavelengths longwards of the Ly α emission line. The smooth solid line in Fig. 6.8 shows a power law fit to those spectral regions

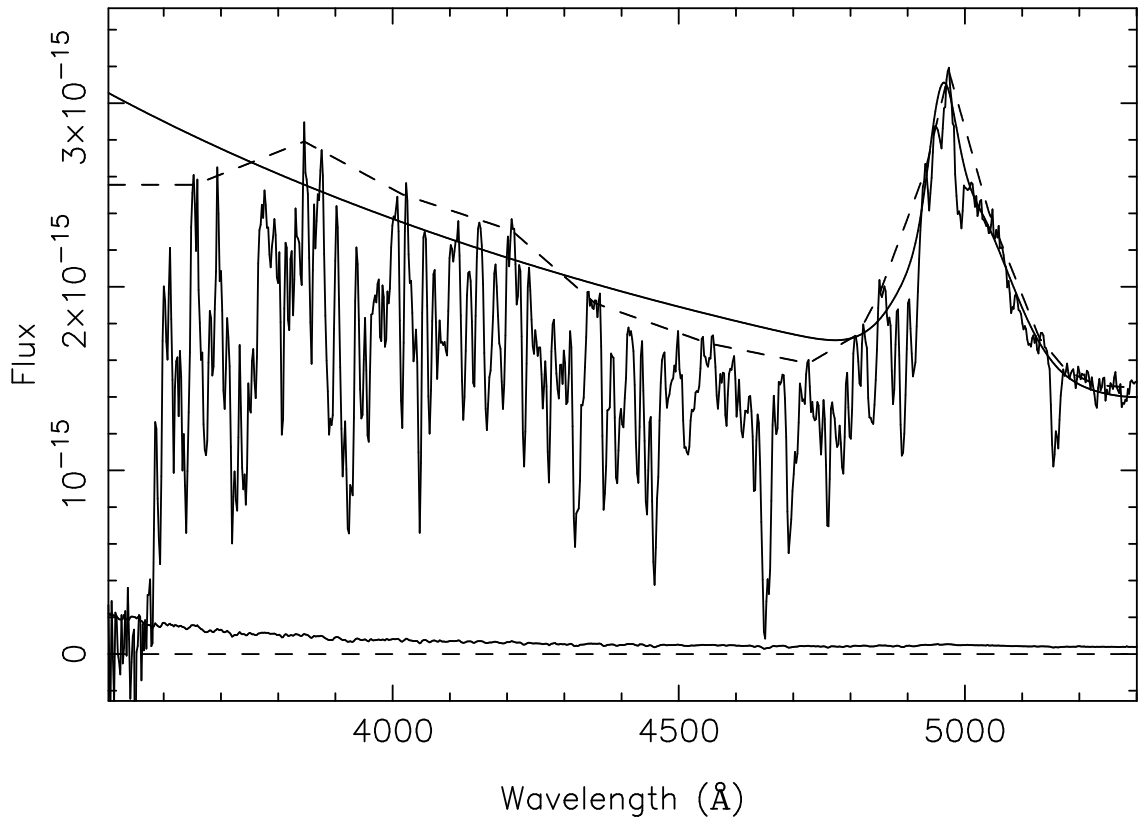


Figure 6.8: 5 \AA spectrum of the Ly α forest in Q0940-1050, taken at the ANU 2.3-m. The line near zero flux is the 1σ error array. The flux is in units of $\text{ergs s}^{-1} \text{cm}^{-2} \text{\AA}^{-1}$. The smooth solid curve is the extrapolation of a power law continuum fit longwards of Ly α emission. The blended Ly α and N v emission lines were fit with Gaussians. The dashed line is a ‘hand-drawn’ continuum consisting of straight line segments. Notice the sharp Lyman limit which is a good indication of simple velocity structure.

longwards of Ly α that are deemed free of emission (Francis et al. 1991). We have also fitted the blended Ly α and N v emission lines with two Gaussian components. In order to test how sensitive our conclusions are to the adopted continuum we have created a second continuum by connecting the upper tips of the spectrum with straight line segments. This was done by hand. This rather arbitrary continuum is shown as the dashed line in Fig. 6.8.

In Fig. 6.9 we show a detailed plot of the Ly limit absorption system at $z = 2.916$. In this plot the spectrum was normalised using the power law continuum. The first three panels show the Ly α , β and γ lines, whereas the fourth panel displays the Ly limit region up to Ly δ . The histogram is the data and the smooth solid line shows a model of the absorption. The model spectrum contains a single absorption line and was convolved with a 5 Å Gaussian. Tick marks indicate the positions of the various transitions.

A close inspection of the Ly limit region reveals that it is probably not quite black. Averaging the pixels over the 100 Å immediately below the Ly limit we find 2σ evidence that there is residual flux. This gives a reasonable constraint on the column density, $\log N(\text{H I}) = 17.8 \pm 0.1$, and leaves only the redshift and b as free parameters. The model shown in Fig. 6.9 has $b = 37 \text{ km s}^{-1}$. Clearly, Ly γ and the higher order lines are all under-absorbed which could be remedied to some extent by increasing b . However, if we increase the b -parameter the model begins to over-absorb in several other places. The Ly limit becomes less steep and absorbs the flux near 3588 Å and 3601 Å which is unphysical. Note that the absorption near 3595 Å is most certainly due to a lower redshift system. The over-absorption in the Ly limit could be avoided by moving the system to a slightly lower redshift. However, in Ly α and Ly β the model already lies at the blue edge of the absorption. Moving the system to lower redshift will cause over-absorption in the blue wings of both Ly α and Ly β . This will be exacerbated by the increased b -parameter. Thus we cannot simultaneously account for the observed absorption in Ly α , Ly β and the Ly limit if we use $b \gtrsim 40 \text{ km s}^{-1}$.

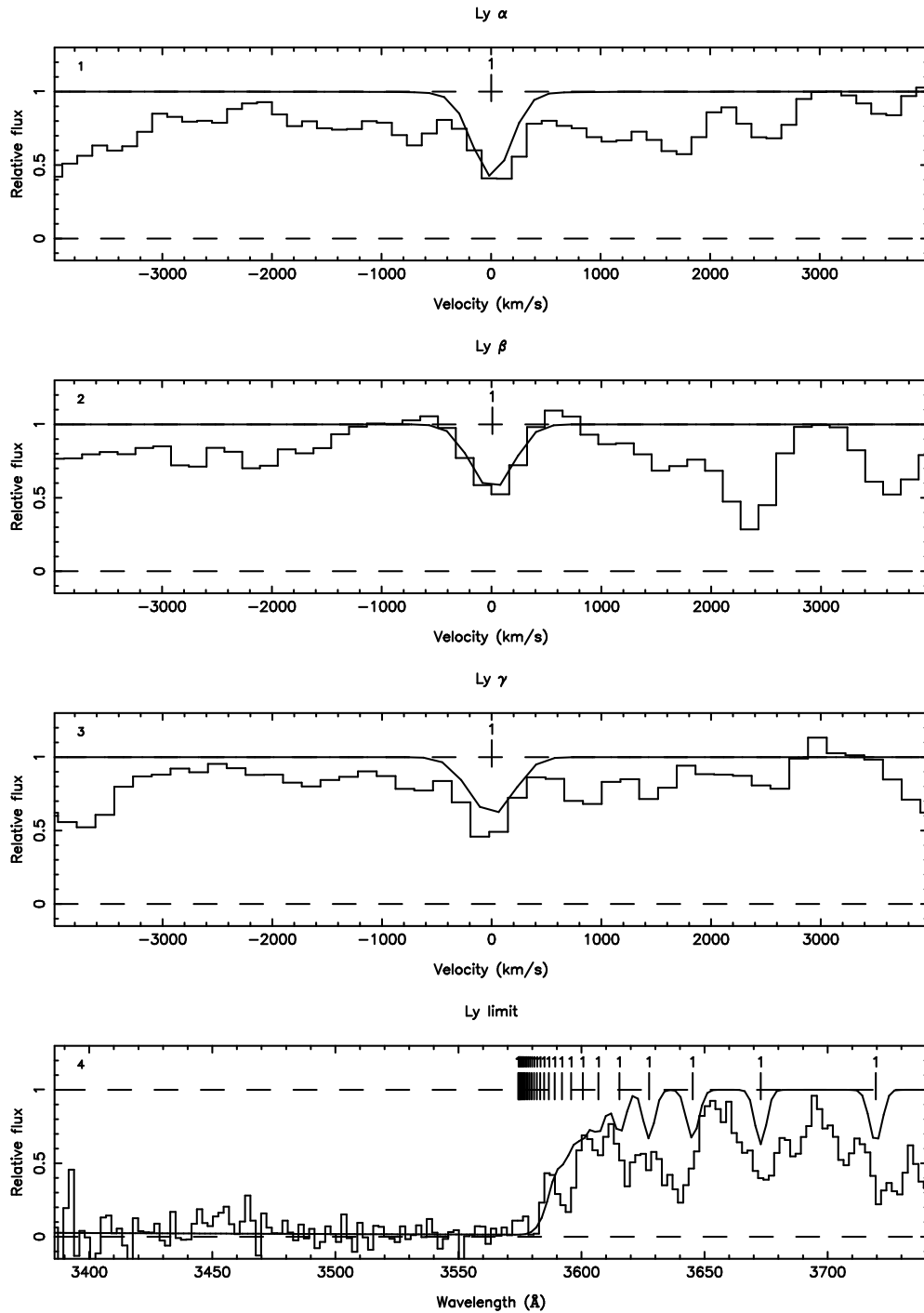


Figure 6.9: The absorption system at $z = 2.9164$. The first three panels show the Ly α to Ly γ lines respectively. The last panel shows the Ly limit region up to Ly δ . The histogram is the low resolution data. The solid line is a one component model of the absorption with $\log N(\text{HI}) = 17.83$ and $b = 37 \text{ km s}^{-1}$.

$\text{Ly}\alpha$ clearly shows the presence of additional absorption within $\pm 400 \text{ km s}^{-1}$ of the main component. However, at least on the blue side this absorption must be fairly weak because it is not seen in $\text{Ly}\beta$. In fact, the data seem to suggest that $\text{Ly}\beta$ may offer the best opportunity to measure D/H. This line looks quite ‘clean’ and from Fig. 1 of Webb et al. (1991) we can see that at $\log N(\text{HI}) = 17.8$ the blue wing of $\text{Ly}\beta$ will at least give a stringent upper limit on D/H.

We have repeated this analysis using the ‘hand-drawn’ continuum to normalise the spectrum. The outcome was nearly identical. In fact, because the continuum is lower in both the $\text{Ly}\alpha$ and Ly limit regions, the upper limit on b becomes even more stringent.

We thus conclude that this absorption system may be useful for a D/H measurement but intermediate resolution data is clearly desirable to constrain the amount of low column density absorption near the main component(s). So far, several applications to observe this and other objects at a resolution of $\sim 1 \text{ \AA}$ with the Anglo-Australian Telescope (AAT) have been unsuccessful. We were, however, successful with an application to obtain high resolution data.

6.4.2 Echelle spectroscopy

On the nights of 1–3 February 2000 we used the University College London Coudé Echelle Spectrograph (UCLES) on the AAT to obtain a high resolution spectrum of most of the Ly series lines, including the Ly limit, and the C IV and Si IV lines of the $z = 2.916$ Ly limit system in Q0940–1050.

We used a grating with 79 lines mm^{-1} . This grating has a smaller free spectral range than the other available grating but its advantage lies in its greater inter-order spacing which allows the use of a longer slit for more reliable sky subtraction. We used three different wavelength settings (one in the red and two in the blue, separated by $\sim 13 \text{ \AA}$) which enabled us to cover the entire Ly series except Ly 9, as well as the C IV $\lambda\lambda 1548, 1550$ and Si IV $\lambda\lambda 1394, 1403$ doublets. The detector was a Tektronix CCD with $1024 \times 1024 \text{ } 24 \mu\text{m}$ pixels which was binned by a factor of

2 and read out at extra-slow speed to decrease the readout noise. The CCD could accommodate 10 echelle orders for the blue wavelength settings and 16 for the red with substantial gaps in the wavelength coverage between the orders.

We took five bias frames at the beginning and end of each night, as well as five quartz lamp flat fields for each wavelength setting. ThAr comparison spectra were taken at regular intervals throughout the night. We performed one standard star observation per wavelength setting and night in order to be able to derive reliable traces for the spectra. The observing conditions were far from perfect with the seeing varying from 1.2'' to 2.5''. The slit width was kept constant at 1.3'' throughout the run. A beam rotator was used to keep the slit vertical with respect to the horizon at all times. Individual exposure times were either 1800 s or 2700 s with total integration times being 6 hours in the red and 13.9 hours in the blue.

Except for the last few steps, all data reduction was performed using standard IRAF routines. First, all images were overscan corrected by subtracting a second order Chebyshev fit to the overscan columns. The images were trimmed and a number of ‘hot’ pixels and their trails were ‘fixed’ by interpolating across them. Since the bias frames showed no evolution at all throughout the run, we combined all of them into a single master bias frame which was used for bias subtraction on all other images. The flat fields of a given night and wavelength setting were combined to a master flat which was fit with cubic splines in the wavelength direction in order to remove its wavelength dependence and to retain only the pixel-to-pixel sensitivity variations. This ‘flattened’ master flat was then divided into the appropriate object frames. All object frames of the same night and wavelength setting were scaled and weighted by their exposure times before combining them. Due to the stability of the spectrograph (which is located in the Coudé room) it was unnecessary to register the images before combining.

We used the stellar observations to trace the positions of the spectra along the chip, using third order Legendre polynomials for the fits. Apertures were defined by hand for each echelle order separately. For the blue (red) wavelength setting

there were only 4 (8) pixels available for sky determination on either side of the spectrum. We doubled this number by smoothing the background by two pixels in the wavelength direction. This procedure worsened the background subtraction near sky emission lines but these all lie far from the parts of the spectrum that we are interested in. A constant was used to fit the background regions. All spectra were extracted optimally.

After extraction the ThAr comparison arc spectra were used for wavelength calibration. Typically, we identified $\gtrsim 15$ lines per echelle order. The wavelength was fit as a function of echelle order and position along the spectrum, using fourth order Chebyshev polynomials for both. We measured a spectral resolution 8.8 km s^{-1} . The dispersion solutions were applied to the object spectra which were rebinned to a linear wavelength scale and corrected for heliocentric motion.

In principle, it would not have been necessary to flux calibrate the spectra because we are only interested in normalised spectra. However, we preferred to fit continua to the final combined spectra rather than to the spectra of the individual nights. Since we used two slightly different wavelength settings in the blue we needed to remove the blaze profiles from the spectra before we could combine them. Using the standard star observations we thus derived a sensitivity function for each order and applied it to the object spectra.

From here on we used our own software for all further processing. We next ‘cleaned’ the individual spectra by interpolating across very deviant pixels near sky emission lines, where the sky subtraction had failed. This was done purely for cosmetic purposes and has no effect on the analysis of the next section. Cleaned pixels were flagged by setting the corresponding pixels in the 1σ error array to zero.

We then combined the spectra of the same echelle order from different nights. During this process we confirmed that the flux calibration had removed the blaze profiles and that the shape of the individual spectra agreed very well. However, it also became apparent that the 1σ error arrays did not accurately reflect the actual S/N of the spectra. This was unacceptable since we wished to use an inverse

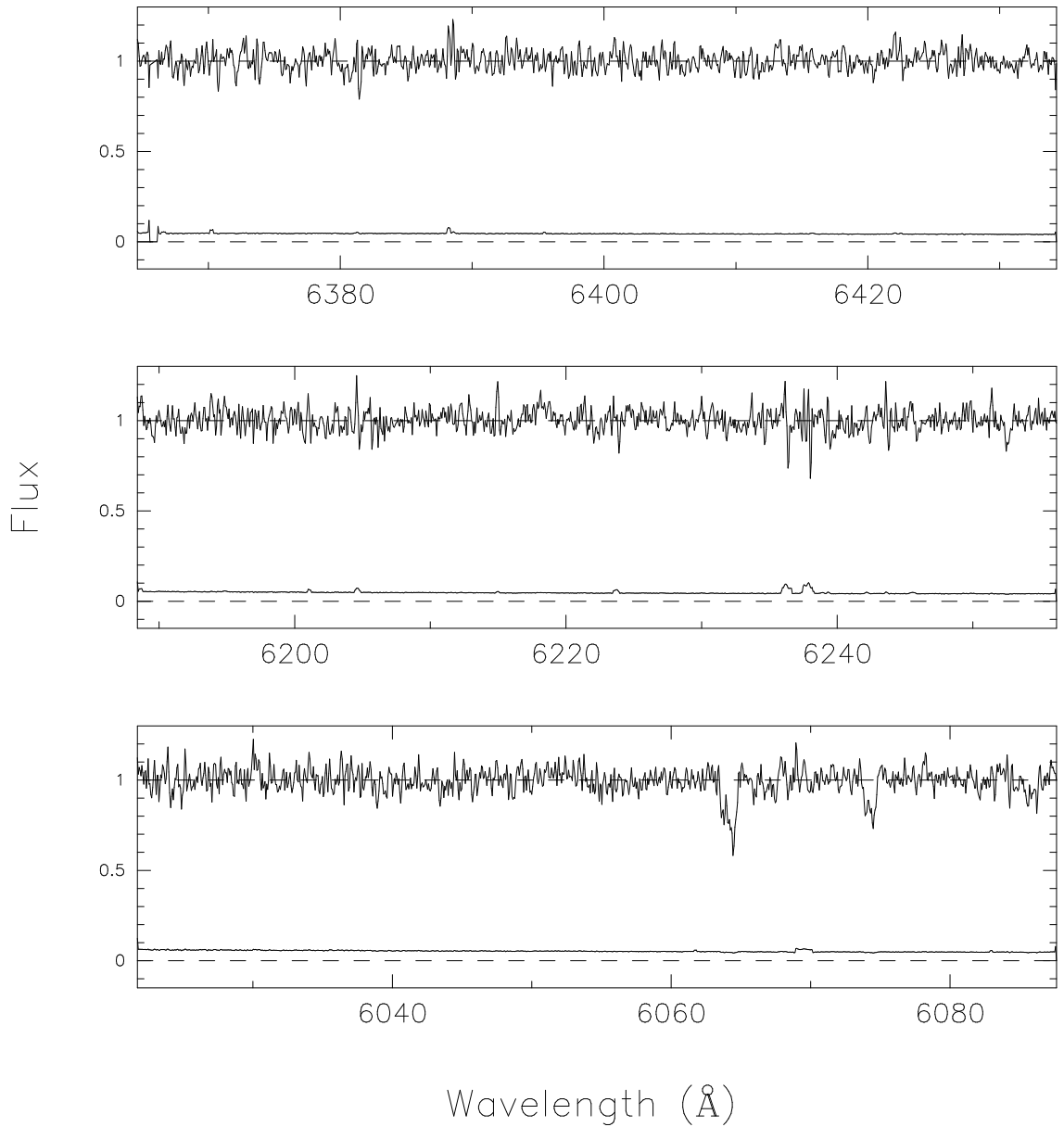
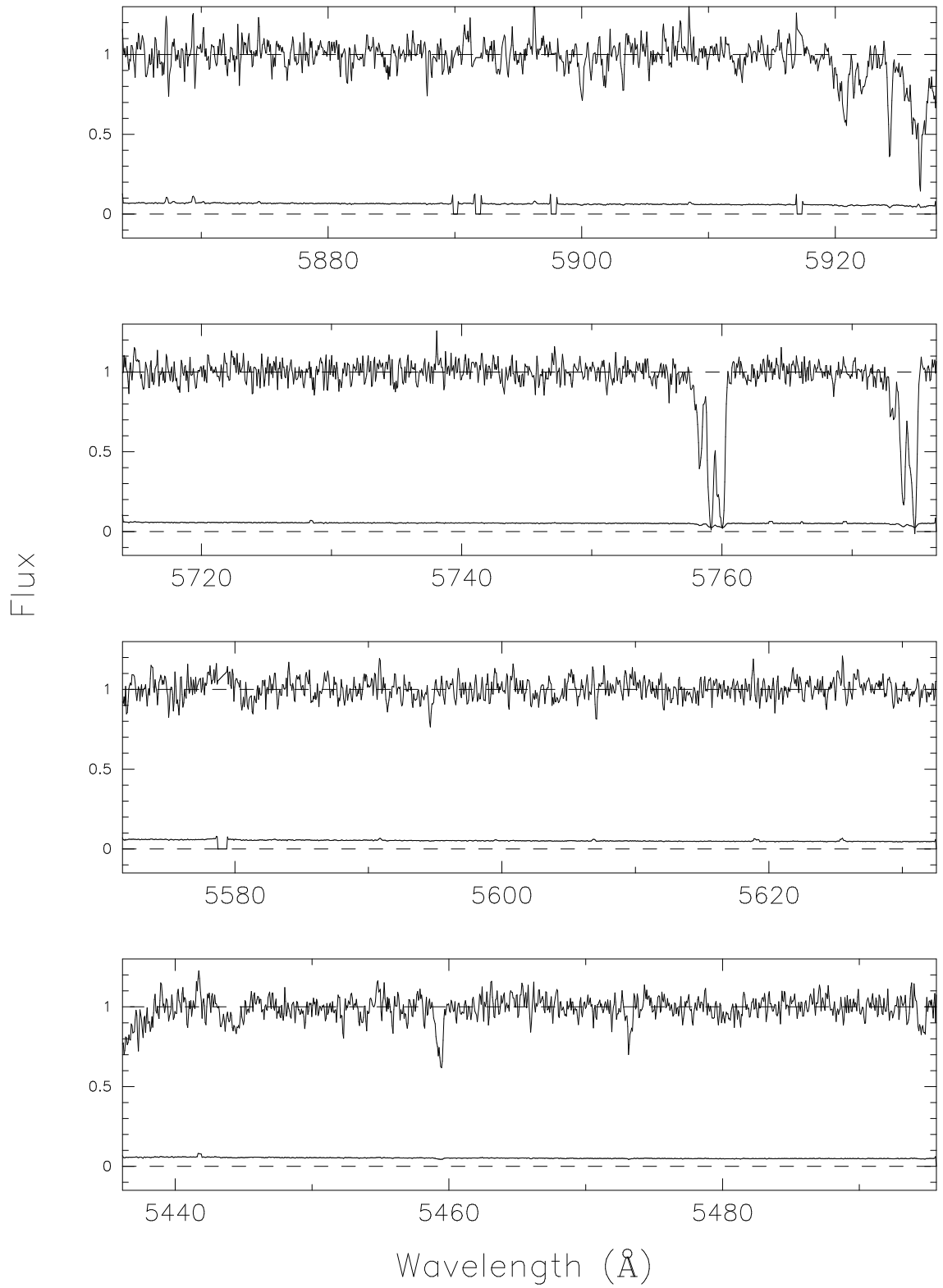
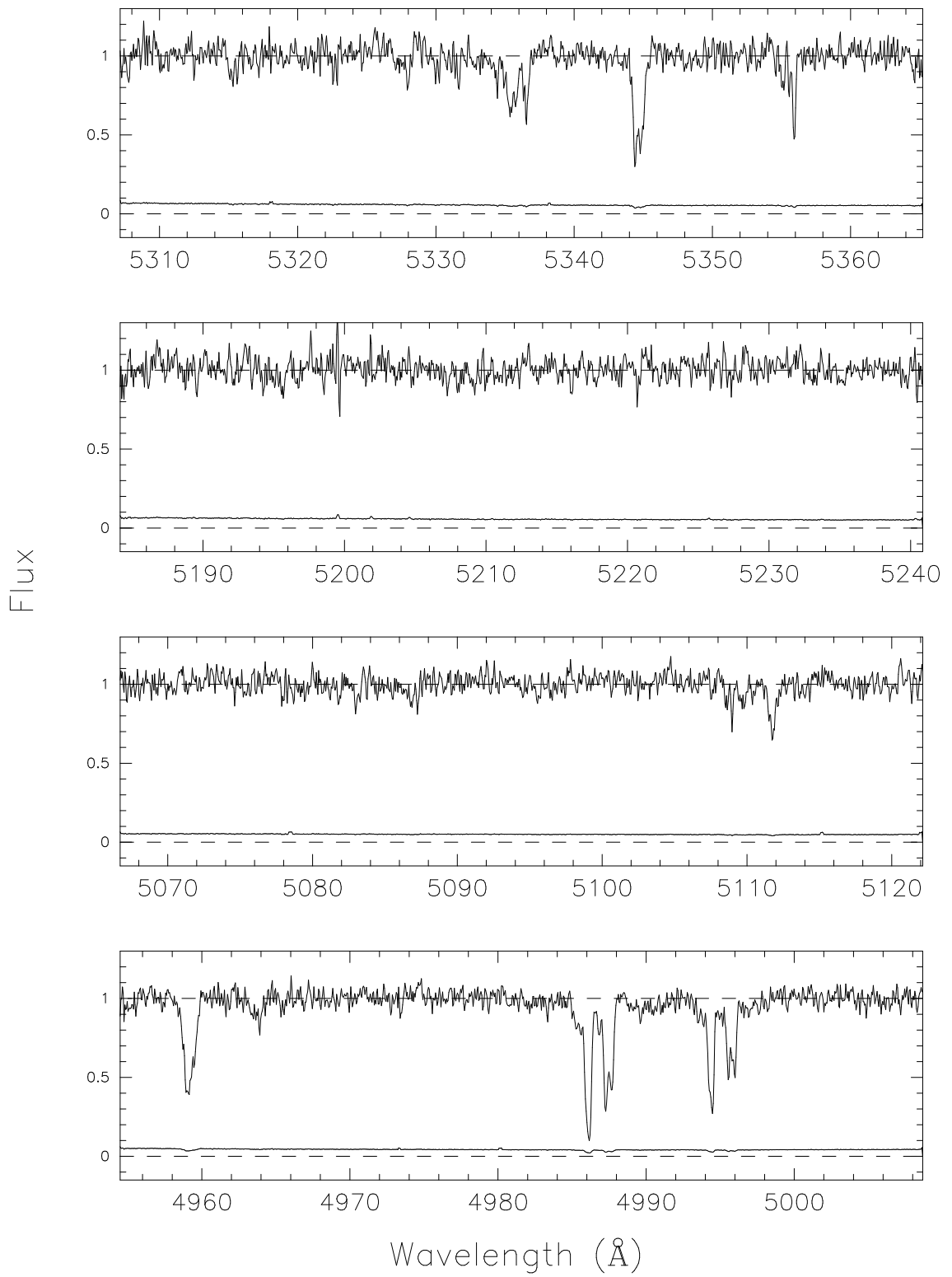
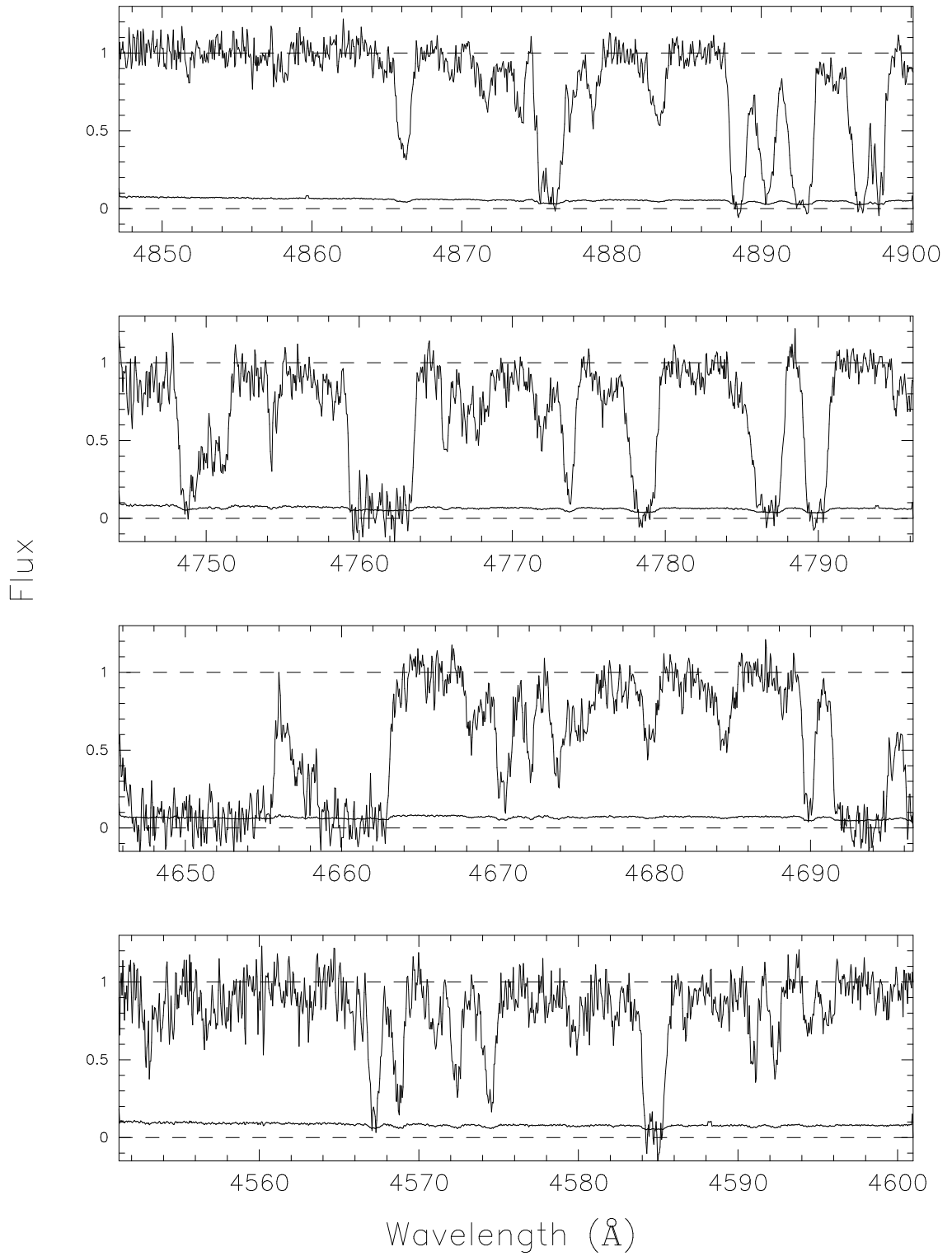
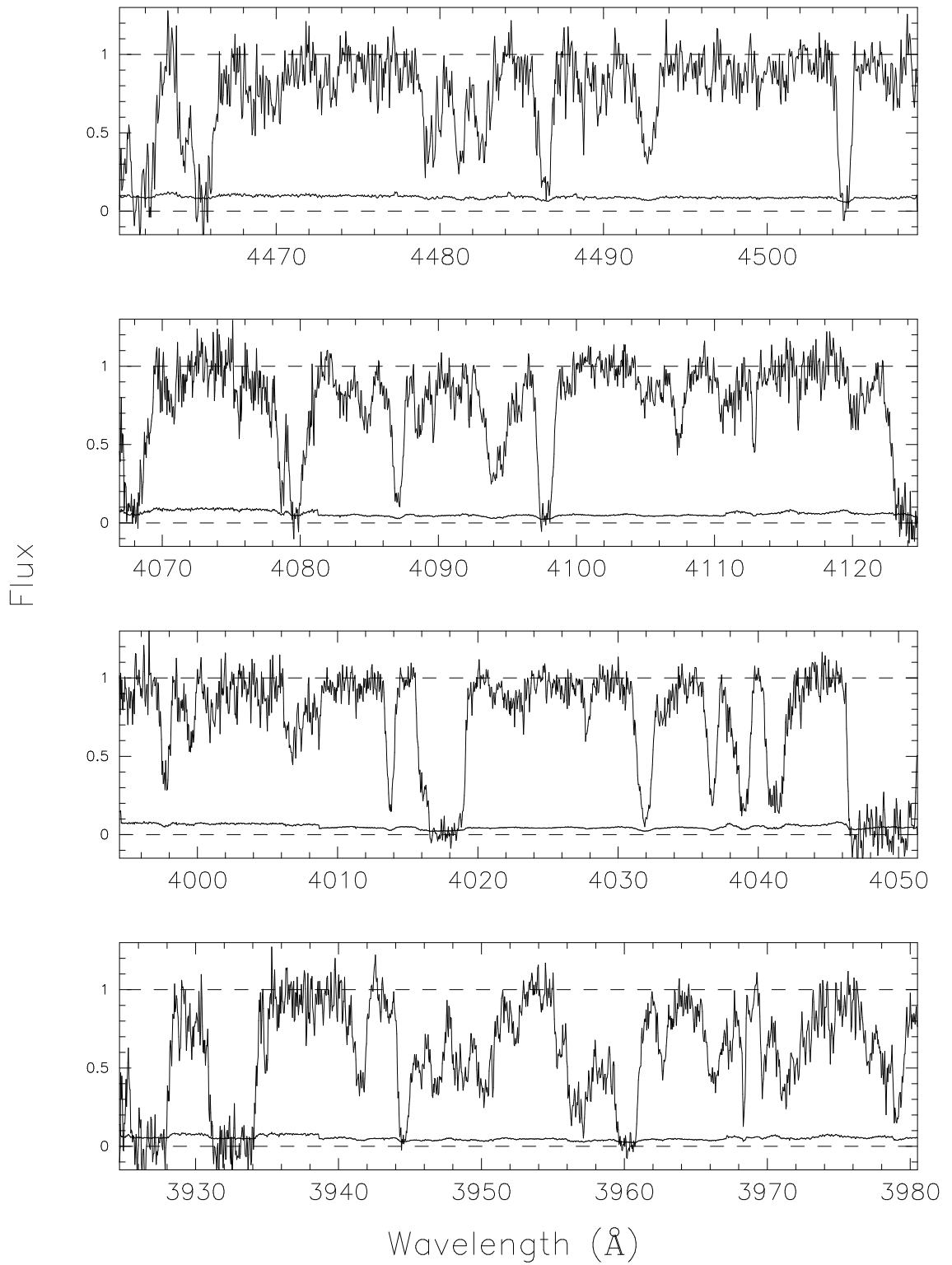


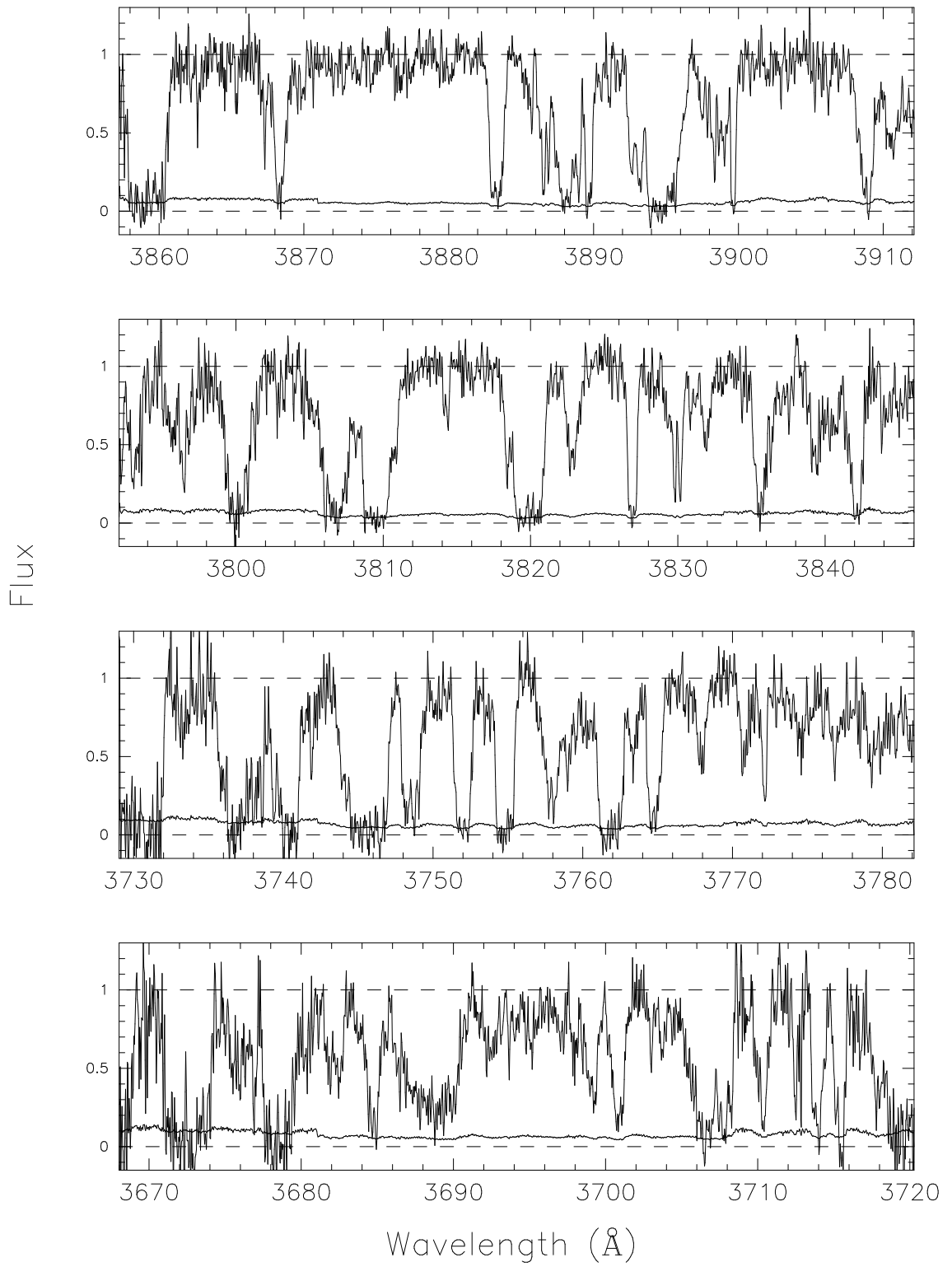
Figure 6.10: Normalised AAT echelle spectrum of Q0940–1050 versus heliocentric vacuum wavelength. The resolution of this spectrum is 8.8 km s^{-1} . The solid line near zero flux is the 1σ error array. Error values of zero indicate points that have been ‘cleaned’ (see text).

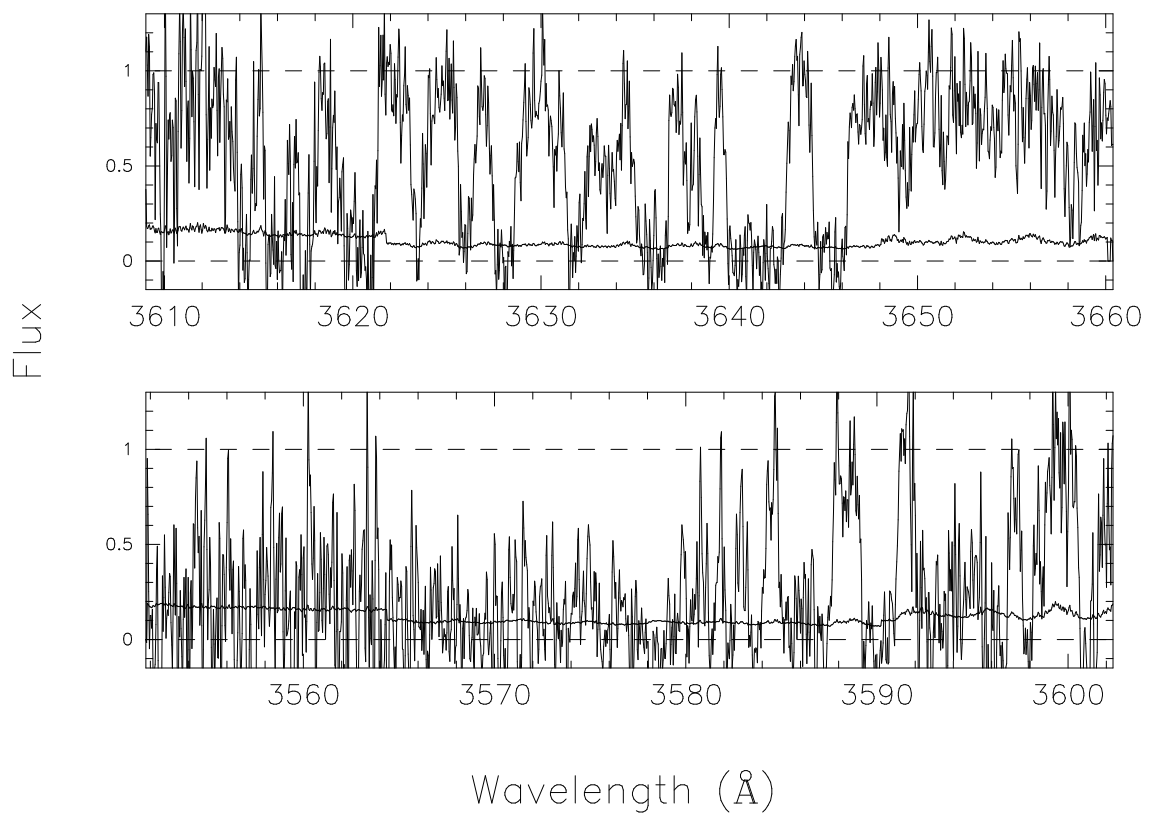
Figure 6.10 – *continued*

Figure 6.10 – *continued*

Figure 6.10 – *continued*

Figure 6.10 – *continued*

Figure 6.10 – *continued*

Figure 6.10 – *continued*

variance weighted average when combining the spectra. We have been unable to trace the source of this discrepancy. We thus resorted to the following procedure. We fitted low order Chebyshev polynomials or constants to spectral regions that were either completely free of absorption (in the red part of the spectrum) or completely absorbed (in the cores of saturated lines in the blue part of the spectrum) and forced $\chi_{\min}^2 = 1$ for the fit by applying a constant multiplicative factor to the 1σ error arrays. This factor was very similar for the different orders of a particular wavelength setting and night and it ranged from ~ 1 to ~ 1.8 . Having corrected the error arrays we then proceeded to combine the spectra from different nights by first scaling them to a common median and then applying an inverse variance weighted average.

Finally, we fit continua to the combined spectra, using Chebyshev polynomials of order 2–4. Towards the blue end of the spectrum this becomes more difficult and ambiguous as the combined density of low and high order absorption lines increases. In the bluest order, where there is virtually no flux at all, we simply used a constant. Usually, this issue is dealt with by allowing the continuum to vary during the fitting of the absorption system. As we will see in the next section, this will not be necessary in the present case.

The final normalised spectra are shown in Fig. 6.10.

6.4.3 An upper limit on D/H

Fig. 6.11 is a detailed plot of the Ly limit system at $z = 2.917$ towards Q0940–1050. The corresponding metal lines are shown in Fig. 6.12. We show all the transitions for which we have data except Ly δ and Si IV $\lambda 1403$, both of which lie at the very ends of their respective echelle orders and could not be used in the analysis.

We have fit multiple Voigt profiles to the data using VPFIT² (Webb 1987b) and its new extension VPGUESS. VPFIT uses an unconstrained non-linear least-squares optimization method to find the best-fit values of the three parameters describing

²<http://www.ast.cam.ac.uk/~rfc/vpfit.html>

each Voigt profile. VPGUESS is a new graphical interface to VPFIT which facilitates the setup of first guess values for the parameters and the display of the data. The result of the fit is shown as the smooth solid line in Figs. 6.11 and 6.12 and the individual components are listed in Table 6.3. The minimum χ^2 per degree of freedom for this fit is 1.17.

There are clearly two main components in this system as evidenced by the C IV, Si IV and H I absorption. To begin with we ‘tied’ the redshifts of these three ions for both the main components, i.e. the fit was performed under the requirement that the redshifts of these absorption lines are equal. However, this requirement resulted in a worse fit for the metal lines. It is not unusual to find slightly different redshifts for these ions. When the redshifts are allowed to vary independently we find a small difference of $< 4 \text{ km s}^{-1}$ between the three ions for the strongest component and good agreement between C IV and H I for the weaker component (cf. Table 6.3).

Lines 5 and 6 in Fig. 6.11 are the H I lines of the two main components. 7 and 8 are the corresponding D I lines. Since H I and D I have almost identical ionization energies they should trace the same gas. Their redshifts were thus tied during the fitting process. Assuming a combination of turbulent and thermal broadening we also tied their b -parameters by requiring that the two ions should have the same turbulent velocity dispersion as well as the same temperature of 10^4 K . Alternatively, we considered purely thermal broadening ($b(\text{D I}) = b(\text{H I})/\sqrt{2}$) and purely turbulent broadening ($b(\text{D I}) = b(\text{H I})$) but this had no effect on our conclusions.

We have not attempted to include in our model all the unrelated lower redshift lines that would be necessary in order to fit the entire Ly series. We have included only those lines that were required to adequately represent the system in Ly α , Ly β and Ly γ . However, notice how well the two main components reproduce the edges of the Ly 8, 10, 13, 14 and 15 transitions even though these regions were not included in the fit. The model includes two H I lines (13 and 15) with very small b -parameters (cf. Table 6.3). Line 15 is not necessarily required but its presence does improve the fit to blue edges of Ly α and Ly β . However, the absorption near -100 km s^{-1}

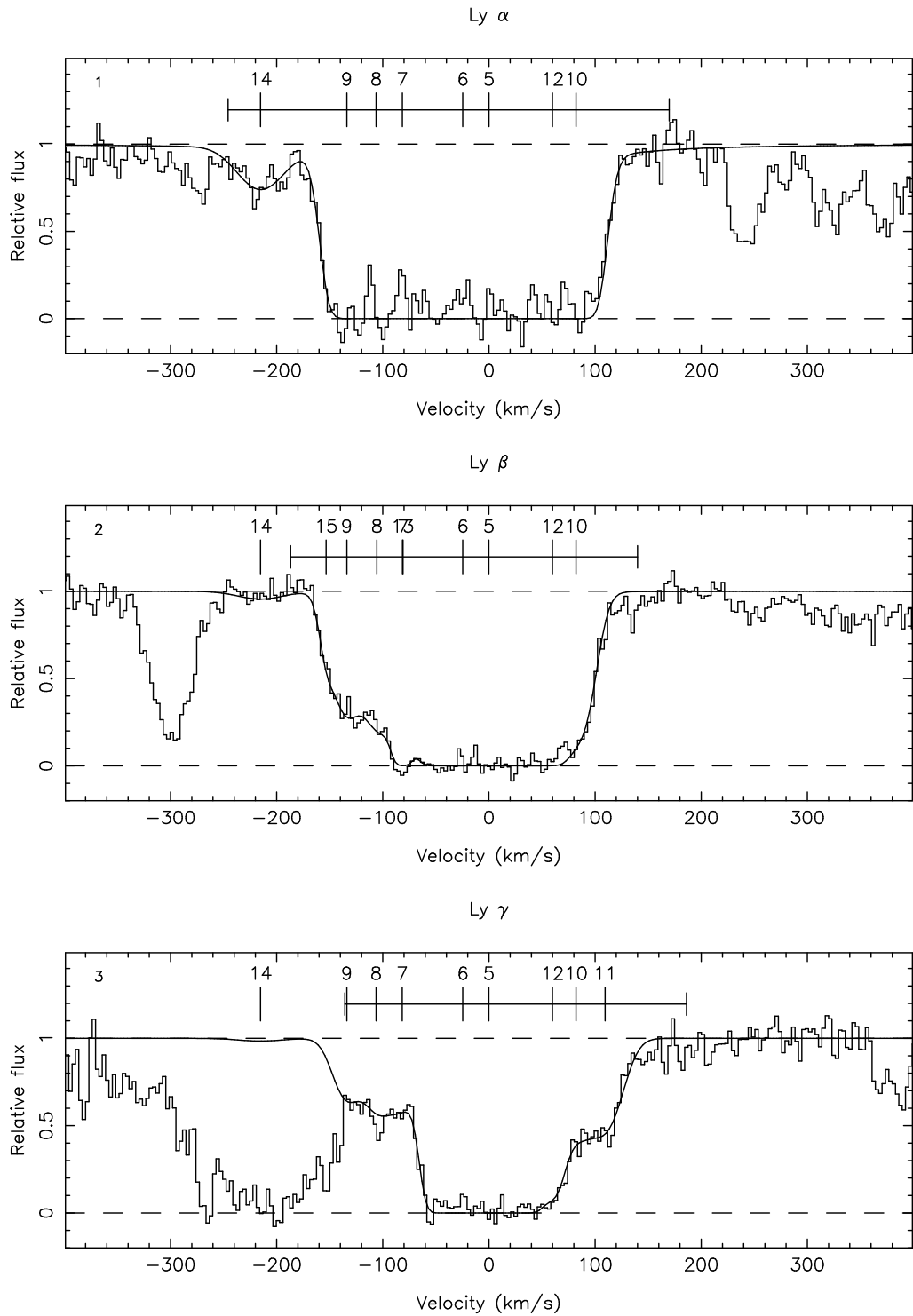
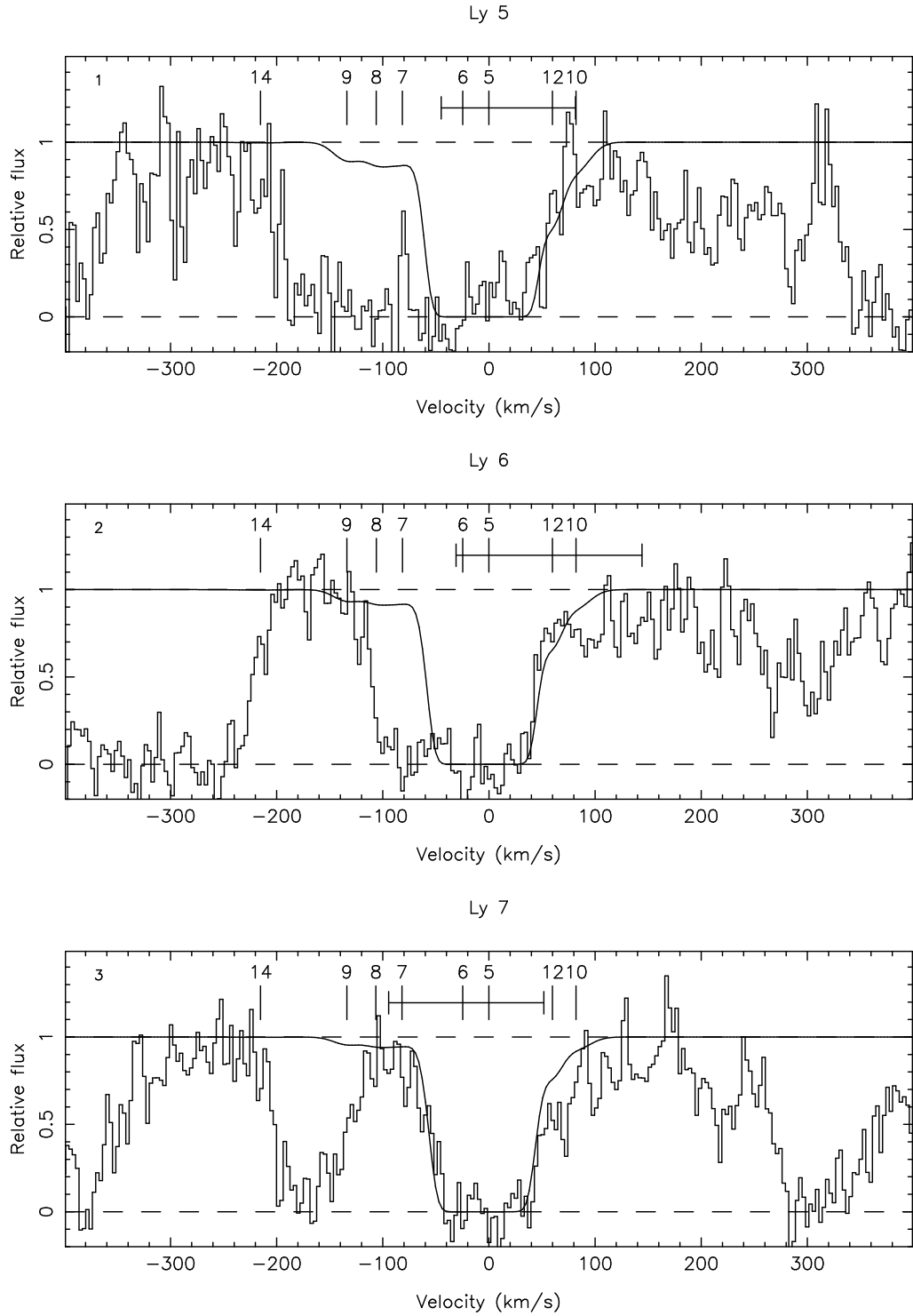


Figure 6.11: Ly limit system at $z = 2.917$ towards Q0940-1050. The histogram is the data. The smooth solid line shows our fit, the tick marks indicate the positions of the individual components of the fit. The solid horizontal lines delineate the spectral regions used for the fit. The numbers above the tick marks correspond to those in the first column of Table 6.3.

Figure 6.11 – *continued*

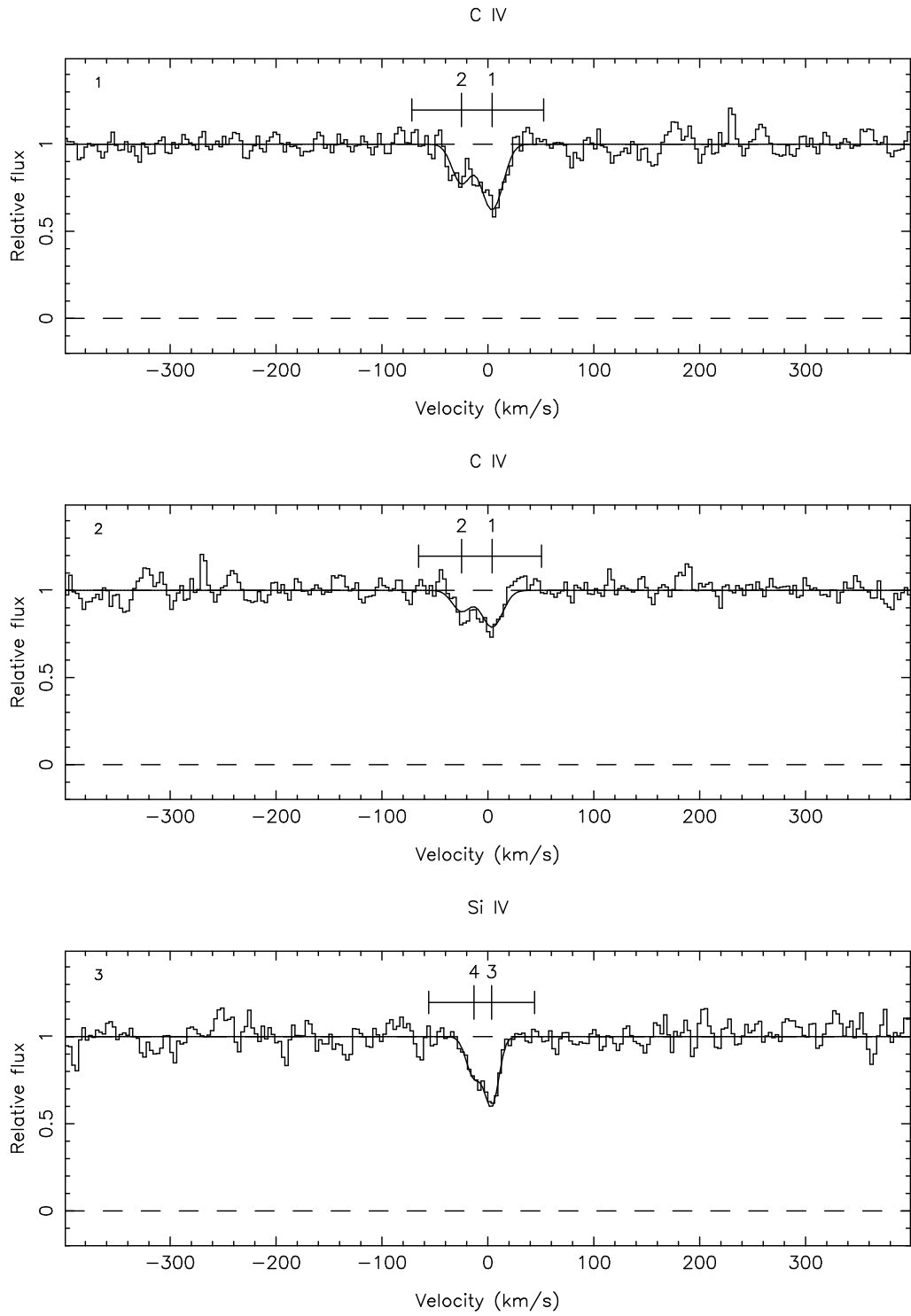


Figure 6.12: Same as Fig. 6.11 for the corresponding metal lines.

Table 6.3: Components of the of the $z = 2.917$ Ly limit system (cf. Fig 6.11).

ID	Ion	$\log N$ cm^{-2}	\pm	z	\pm	b km s^{-1}	\pm	v^a km s^{-1}
1	C IV	13.1622	0.0394	2.917080	0.000013	12.37	1.58	+4.0
2	C IV	12.8498	0.0770	2.916703	0.000022	10.87	2.55	−24.9
3	Si IV	12.6254	0.1245	2.917074	0.000025	7.20	2.55	+3.5
4	Si IV	12.3807	0.2235	2.916857	0.000051	8.31	4.47	−13.1
5	H I	17.4979	0.0726	2.917028	0.000045	21.19	2.17	0.0
6	H I	16.8187	0.2910	2.916706	0.000049	18.10	1.32	−24.6
7	D I	14.3631	0.1036	2.917028		19.17		
8	D I	14.2250	0.1096	2.916706		15.70		
9	H I	14.2432	0.0440	2.915279	0.000026	16.69	1.53	−133.9
10	H I	14.4740	0.2020	2.918100	0.000079	17.50	3.03	+82.0
11	H I	13.2968	0.0331	2.134770	0.000014	20.04	1.83	
12	H I	14.8358	0.2115	2.917810	0.000044	12.25	4.98	+59.8
13	H I	15.3055	4.0539	2.304090	0.000014	4.50	4.57	
14	H I	13.0375	0.1131	2.914216	0.000077	28.98	0.09	−215.3
15	H I	12.5166	0.1834	2.303296	0.000028	6.68	3.91	

^aVelocity relative to the redshift of the main component, $z = 2.917028$.

in Ly β and Ly γ cannot be fit by Ly β and Ly γ transitions alone. We have fit the required additional absorption in Ly β with an H I Ly α line but it is most likely a metal line at some other redshift.

The H I column density of the weaker of the main components is not very well constrained because of its proximity to the stronger one. However, the parameters of line 5 are quite well constrained. In agreement with the low resolution spectrum we find that there is some residual flux below the Ly limit, which gives $N(\text{H I})$. We will bear in mind that this estimate is subject to uncertainties due to the placement of the continuum.

From the Ly α , Ly β and Ly γ transitions we can easily see that this absorption system can accommodate a very high value of D/H. Indeed, for the strongest (and best constrained) component we find

$$D/H \lesssim 7 \times 10^{-4}.$$

Obviously, the data are consistent with much lower values of D/H. If we require that $D/H = 2 \times 10^{-5}$, then we can find an adequate model by adding one H I line with $\log N = 14.6$ between the two D I lines. Line 9 is not much affected by this.

We thus conclude that there exists an adequate model for the present Ly limit system that allows D/H as large as $\sim 7 \times 10^{-4}$. Therefore, this system does not give any useful constraints. This conclusion is very robust and will not be changed significantly by considering other absorption models, different continuum fits or better data.

The question then arises where our selection process has failed. First, we note that we have successfully identified an absorption system with very little velocity dispersion (25 km s^{-1}) among its main components which have relatively low b -parameters. However, we failed to recognize the presence of significant amounts of additional absorption on the blue side of the main components. For $D/H = 2 \times 10^{-5}$ we found above that there are two absorption lines with $\log N = 14.6$ and 14.2 (line 9) within $\sim 140 \text{ km s}^{-1}$ of the main components. Had these two lines not been present this system may well have yielded at least an interesting upper limit on

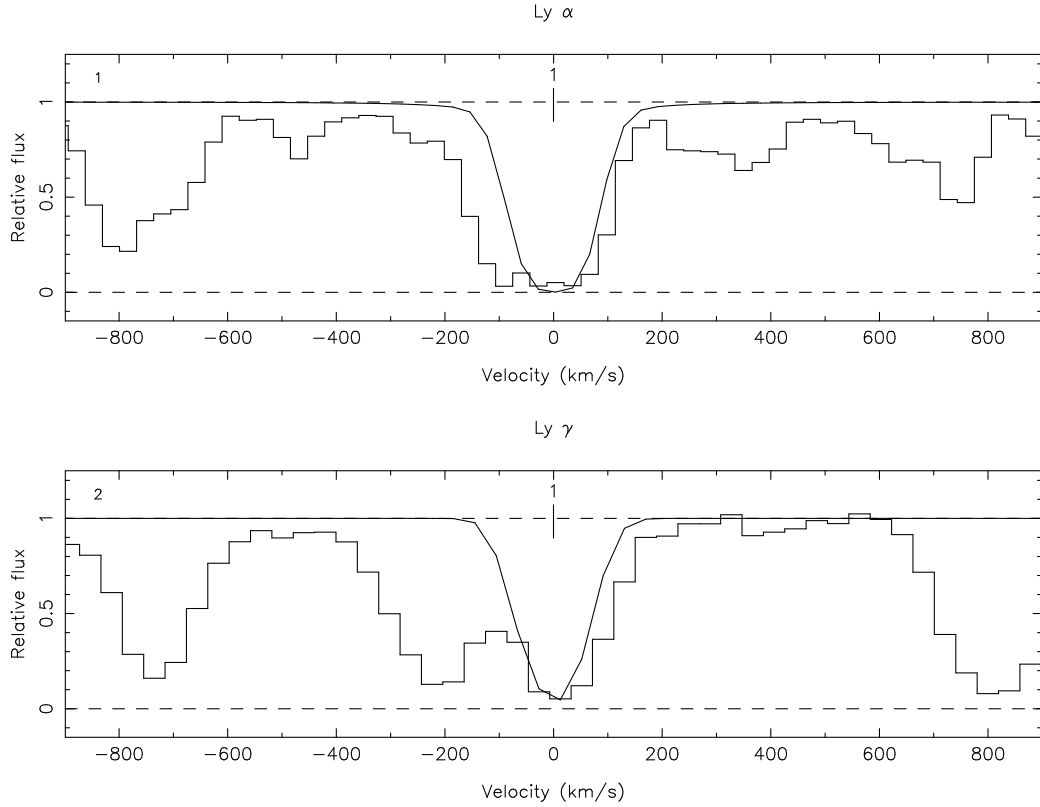


Figure 6.13: The histogram shows the degraded echelle spectra of the Ly α and Ly γ transitions of the $z = 2.917$ Ly limit system towards Q0940-1050. The original echelle spectra (cf. Figs. 6.10 and 6.11) were convolved with a 1 \AA Gaussian and rebinned to a pixel size of 0.5 \AA . Noise was added to give a S/N of 30. The smooth solid line shows a model absorption line with $\log N = 17.5$ and $b = 29 \text{ km s}^{-1}$.

D/H.

We think it unlikely that a more detailed analysis of the low resolution spectrum would have revealed these interlopers because they are simply too close to the main components (cf. Fig. 6.4). Could we have detected them using a 1 \AA spectrum? To answer this question we convolved our high resolution spectrum with a Gaussian of 1 \AA FWHM. The result was rebinned to a pixel size of 0.5 \AA and noise was added to give a S/N of 30. In Fig. 6.13 we show this intermediate resolution version of the Ly α and Ly γ transitions of the present Ly limit system. We also show as the smooth solid curve a single absorption line with $\log N(\text{HI}) = 17.5$ (determined from the Ly limit) and $b = 29 \text{ km s}^{-1}$ (determined from the requirement not to over-absorb anywhere in the spectrum). The line has been moved as far as possible towards the blue without violating the ‘bump’ of flux near -100 km s^{-1} in Ly γ . At this resolution we can unambiguously identify the additional absorption in Ly α . If we insist on moving the line all the way to the blue edge of the observed Ly α absorption then we require an unlikely low effective b -parameter of 15 km s^{-1} .

We thus conclude that we would have been able to reject this system as a D/H candidate on the basis of a 1 \AA spectrum. We further find that our argument for a two-phased selection process based on low and intermediate resolution spectra is reinforced by this specific, ‘real-world’ example.

6.5 Further work

As we have already pointed out this project is work in progress and much remains to be done. For example, we need to consider in more detail the criteria on which to base the selection process. What are the most sensitive indicators of simple velocity structure and little contamination? To what limiting column density and velocity spread can we detect interlopers? Given the constraints of existing facilities, what is the most efficient combination of observations in terms of resolution and S/N? These questions will have to be answered with a combination of detailed simulations and careful analysis of low resolution spectra of known D/H systems. This issue

is our most immediate concern because it will prove a critical factor in obtaining future telescope time.

On the observational side, the agenda is clear: we must obtain and carefully scrutinize low and intermediate resolution data of as many QSOs as possible and observe the most promising candidates at high resolution.

However, going beyond the issue of selection, we believe that the general problem of reliably measuring D/H in QSO absorption line systems has not been fully solved. A commonly adopted approach towards the various discrepant D/H values and limits discussed in Section 6.1.2 is that the higher limits are contaminated and the low values give approximately the correct value. This seems to be the only way in which all the data can be consistently accounted for without invoking more ‘exotic’ solutions such as inhomogeneous BBN. The central issue is: given a true value of D/H, what is the probability distribution of D/H *measurements*? The proponents of the above approach would argue that this probability distribution is more or less strictly one-sided, with a long tail extending towards high values of D/H. However, at present we do not really know the answer to this question and the complexity of the problem surely demands a much larger sample from which to derive an answer.

Chapter 7

Summary

In this thesis we have addressed three different cosmological topics by extracting some of the information that is encoded in the Ly α forest spectra of high redshift QSOs. We have used intermediate resolution spectra from the CTIO 4-m Telescope of a close group of ten QSOs (provided by G. M. Williger) to investigate the large-scale distribution of the Ly α forest absorption. The same dataset has been subjected to an analysis of both the classical background, as well as the foreground proximity effect. We have presented 101 new, low resolution spectra of high redshift QSOs, obtained at the ANU 2.3-m and William-Herschel Telescopes, with the goal of identifying new D/H candidate absorption systems. A promising candidate has been selected for further study and we have obtained echelle spectroscopy for this absorption system at the Anglo-Australian Telescope. We summarize our results in the following.

1. We have developed a new technique to search for large-scale structure in the Ly α forest by considering the integral properties of the absorption rather than the statistics of its constituents. Although this paradigm shift was in part motivated by recent theoretical developments we have taken a purely empirical and descriptive approach in deriving a simple model for these integral properties, while carefully accounting for instrumental effects. In equations (2.28) and (2.31) we have derived useful formulae for the mean and variance of the

transmitted flux.

2. A direct comparison of our method with a more common two-point correlation function analysis has revealed that the former is considerably more sensitive to the presence of large-scale structure in intermediate resolution data than the latter. We have shown our method to be particularly useful when applied to multiple lines of sight.
3. We have applied this technique to intermediate resolution spectra of a close group of ten QSOs. We have found evidence for large-scale structure in the distribution of Ly α forest absorption at the > 99 per cent confidence level. Along the line of sight we have identified overdense structures on scales of up to 1200 km s^{-1} .
4. We have found strong evidence for the existence of coherent absorption across neighbouring lines of sight for separations $< 3 h^{-1} \text{ Mpc}$. The cross-correlation signal was found to be much weaker for line of sight separations between 3 and $6 h^{-1} \text{ Mpc}$ and had disappeared completely for even larger separations. We have thus presented the first evidence for a dependence of the cross-correlation on sightline separation.
5. In a brief diversion from the main theme of this thesis we have considered the problem of how to calculate the distance between two cosmological objects given their redshifts and angular separation on the sky. Although of a fundamental nature, this problem lacks a detailed discussion in the literature which we have now provided. We have presented a new variant of the problem's solution and compared its results to the most commonly used approximation.
6. Using the same data and method as before we have performed a new analysis of the proximity effect. We have confirmed that the Ly α forest absorption is less dense near the background QSOs than elsewhere at the > 99 per cent confidence level. Incorporating the ionization model of Bajtlik, Duncan, & Ostriker

(1988) into our absorption model we have derived a measurement of the mean extragalactic background intensity at the Lyman limit: $J = 3.6_{-1.3}^{+3.5} \times 10^{-22}$ ergs s⁻¹ cm⁻² Hz⁻¹ sr⁻¹. This value assumes that QSO redshifts measured from high ionization lines differ from the true systemic redshifts by 800 km s⁻¹.

7. The validity of inferring J from the observed proximity effect was reinforced by the positive detection of a correlation between the strength of the proximity effect and QSO Lyman limit luminosity. This correlation was found to be entirely consistent with the expectations from the ionization model. Thus we have provided further evidence that the interpretation of the proximity effect as being due to increased ionization caused by the extra UV flux in the vicinity of QSOs is essentially correct.
8. The data have also allowed an investigation of the foreground proximity effect where the Ly α forest of a background QSO is depleted by the UV radiation from a nearby foreground QSO. For the complete sample we have found no evidence for the existence of this effect. Under the assumption of isotropic QSO emission this null-result implied that $J > 20 \times 10^{-22}$ ergs s⁻¹ cm⁻² Hz⁻¹ sr⁻¹ at 90 per cent confidence. Since this limit is inconsistent with our previous measurement we have argued that it may represent direct observational evidence for either anisotropic QSO emission or large variability on time-scales of 10⁶ years. If the former explanation is correct then QSOs emit at least a factor of 1.4 less ionizing radiation in the plane of the sky than along the line of sight to Earth.
9. However, adding to the two previously known examples we have found one case that *does* show the foreground proximity effect. The inferred value of J was found to be consistent with the measurement from the background effect. This new example is arguably the most interesting case because it involves not just one, but four lines of sight passing close to a foreground QSO.
10. We have argued for the importance and timeliness of new measurements of

the primordial deuterium abundance by pointing out that, together with the results of future CMB missions, they will provide us with a new and fundamental cosmological consistency test. We have described the necessity of pre-selecting D/H candidate absorption systems from lower resolution data and we have investigated ways in which this might be achieved. We have found that the particular H I characteristics needed for a D/H measurement are recognizable in low and intermediate resolution spectra. On the basis of these results we have proposed an observing strategy that involves two distinct phases: a $\sim 5 \text{ \AA}$ resolution survey to identify Lyman limit systems with simple velocity structure followed by $\sim 1 \text{ \AA}$ observations of preliminary candidates in order to reject systems with interlopers of $N(\text{H I}) \gtrsim 10^{14} \text{ cm}^{-2}$ near the expected D I feature.

11. Taking the first step in this selection process, we have presented 101 new $\sim 5 \text{ \AA}$ resolution spectra obtained at the ANU 2.3-m and WHT. We have combined this sample with data from the literature to form a valuable database containing 187 spectra of 171 high redshift QSOs.
12. We have described the arguments that led to the selection of Q0940–1050 for further observations. We have presented an AAT/UCLES echelle spectrum of its $z = 2.917$ Lyman limit system with a resolution of 8.8 km s^{-1} . We were able to show conclusively that it is not very useful for a D/H measurement and provides only a weak upper limit of $\text{D/H} \lesssim 7 \times 10^{-4}$. Nevertheless, based on the ‘almost’ suitability of this system and the realisation that we would have been able to reject it with the help of 1 \AA data, we have concluded that the selection process is on the right track and that we can realistically expect a result in the near future.

References

- Adams T. F., 1976, *A&A*, 50, 461
- Alcock C., Paczyński B., 1979, *Nat*, 281, 358
- Allen C. W., 1991, *Astrophysical Quantities*. The Athlone Press, London
- Alpher R. A., 1948, *Phys. Rev.*, 74, 1577
- Alpher R. A., Bethe H. A., Gamow G., 1948, *Phys. Rev.*, 73, 803
- Alpher R. A., Follin J. W., Herman R. C., 1953, *Phys. Rev.*, 92, 1347
- Antonucci R., 1993, *ARA&A*, 31, 473
- Bahcall J. N. et al., 1993, *ApJS*, 87, 1
- Bahcall J. N., Jannuzi B. T., Schneider D. P., Hartig G. F., Bohlin R., Junkkarinen V., 1991, *ApJ*, 377, L5
- Bahcall J. N., Salpeter E. E., 1965, *ApJ*, 142, 1677
- Bajtlik S., Duncan R. C., Ostriker J. P., 1988, *ApJ*, 327, 570
- Bechtold J., 1994, *ApJS*, 91, 1
- Bechtold J., Weymann R. J., Zuo L., Malkan M. A., 1987, *ApJ*, 315, 180
- Bi H., Davidsen A. F., 1997, *ApJ*, 479, 523
- Blair M., Gilmore G., 1982, *PASP*, 94, 742

- Bond J. R., Wadsley J. W., 1998, in Petitjean P., Charlot S., ed, Proceedings of the 13th IAP Colloquium “Structure and Evolution of the Intergalactic Medium from QSO Absorption Line Systems”. Editions Frontières, Paris, p. 143
- Bowen D. V., Blades J. C., Pettini M., 1996, *ApJ*, 464, 141
- Broadhurst T. J., Ellis R. S., Koo D., Szalay A. S., 1990, *Nat*, 343, 726
- Burbidge E. M., Lynds C. R., Burbidge G. R., 1966, *ApJ*, 144, 447
- Burles S., Kirkman D., Tytler D., 1999, *ApJ*, 519, 18
- Burles S., Nollett K. M., Turner M. S., 2001, *ApJ*, 552, L1
- Burles S., Tytler D., 1997, *AJ*, 114, 1330
- Burles S., Tytler D., 1998a, *ApJ*, 499, 699
- Burles S., Tytler D., 1998b, *ApJ*, 507, 732
- Cardelli J. A., Clayton G. C., Mathis J. S., 1989, *ApJ*, 345, 245
- Carswell R. F., Morton D. C., Smith M. G., Stockton A. N., Turnshek D. A., Weymann R. J., 1984, *ApJ*, 278, 486
- Carswell R. F., Rauch M., Weymann R. J., Cooke A. J., Webb J. K., 1994, *MNRAS*, 268, L1
- Carswell R. F., Webb J. K., Baldwin J. A., Atwood B., 1987, *ApJ*, 319, 709
- Carswell R. F. et al., 1996, *MNRAS*, 278, 506
- Carswell R. F., Whelan J. A. J., Smith M. G., A. B., Tytler D., 1982, *MNRAS*, 198, 91
- Cen R., Miralda-Escudé J., Ostriker J. P., Rauch M., 1994, *ApJ*, 437, L9
- Cen R., Simcoe R. A., 1997, *ApJ*, 483, 8

- Chaffee F. H., Foltz C. B., Bechtold J., Weymann R. J., 1986, *ApJ*, 301, 116
- Chaffee F. H., Foltz C. B., Röser H.-J., Weymann R. J., Latham D. W., 1985, *ApJ*, 292, 362
- Charlton J. C., Churchill C. W., Linder S. M., 1995, *ApJ*, 452, L81
- Chen H.-W., Lanzetta K. M., Webb J. K., Barcons X., 1998, *ApJ*, 498, 77
- Chernomordik V. V., 1995, *ApJ*, 440, 431
- Chernomordik V. V., Ozernoy L. M., 1993, *ApJ*, 404, L5
- Clayton G. C., Cardelli J. A., 1988, *AJ*, 96, 695
- Connolly A. J., Szalay A. S., Koo D. C., Romer A. K., Holden B., Nichol R. C., Miyaji T., 1996, *ApJ*, 473, L67
- Cooke A. J., Espey B., Carswell R. F., 1997, *MNRAS*, 284, 552
- Cowie L. L., Songaila A., Kim T.-S., Hu E. M., 1995, *AJ*, 109, 1522
- Cristiani S., D'Odorico S., D'Odorico V., Fontana A., Giallongo E., Savaglio S., 1997, *MNRAS*, 285, 209
- Cristiani S., D'Odorico S., Fontana A., Giallongo E., Savaglio S., 1995, *MNRAS*, 273, 1016
- Cristiani S., Vio R., 1990, *A&A*, 227, 385
- Croft R. A. C., Weinberg D. H., Katz N., Hernquist L., 1998, *ApJ*, 495, 44
- Croft R. A. C., Weinberg D. H., Pettini M., Hernquist L., Katz N., 1999, *ApJ*, 520, 1
- Croom S. M., Shanks T., 1996, *MNRAS*, 281, 893
- Croom S. M., Shanks T., 1999, *MNRAS*, 303, 411

- Crotts A. P. S., 1989, *ApJ*, 336, 550
- Crotts A. P. S., Fang Y., 1998, *ApJ*, 502, 16
- Dalton G. B., Croft R. A. C., Efstathiou G., Sutherland W. J., Maddox S. J., Davis M., 1994, *MNRAS*, 271, L47
- Davé R., Hellsten U., Hernquist L., Katz N., Weinberg D. H., 1998, *ApJ*, 509, 661
- Davé R., Hernquist L., Katz N., Weinberg D. H., 1999, *ApJ*, 511, 521
- Davé R., Hernquist L., Weinberg D. H., Katz N., 1997, *ApJ*, 477, 21
- Di Nella H., Couch W. J., Paturel G., Parker Q. A., 1996, *MNRAS*, 283, 367
- Dinshaw N., Foltz C. B., Impey C. D., Weyman R. J., 1998, *ApJ*, 494, 567
- Dinshaw N., Impey C. D., 1996, *ApJ*, 458, 73
- Dinshaw N., Weyman R. J., Impey C. D., Foltz C. B., Morris S. L., Ake T., 1997, *ApJ*, 491, 45
- Disney M. J., 2000, *Gen. Relativ. Gravitation*, 32, 1125
- Dobrzycki A., Bechtold J., 1991, *ApJ*, 377, L69
- D'Odorico V., Cristiani S., D'Odorico S., Fontana A., Giallongo E., Shaver P., 1998, *A&A*, 339, 678
- Drinkwater M., 1987, Ph.D. thesis, University of Cambridge
- Einasto J. et al., 1997, *Nat*, 385, 139
- Elowitz R. M., Green R. F., Impey C. D., 1995, *ApJ*, 440, 458
- Espey B. R., 1993, *ApJ*, 411, L59
- Ettori S., Guzzo L., Tarenghi M., 1997, *MNRAS*, 285, 218
- Evans A., Hart D., 1977, *A&A*, 58, 241

- Fang Y., Duncan R. C., Crofts A. P. S., Bechtold J., 1996, *ApJ*, 462, 77
- Fernández-Soto A., Barcons X., Carballo R., Webb J. K., 1995, *MNRAS*, 277, 235
- Fernández-Soto A., Lanzetta K. M., Barcons X., Carswell R. F., Webb J. K., Yahil A., 1996, *ApJ*, 460, L85
- Francis P. J., 1993, *ApJ*, 407, 519
- Francis P. J., 1996, *Proc. Astron. Soc. Aust.*, 13, 212
- Francis P. J., Hewitt P. C., Foltz C. B., Chaffee F. H., Weymann R. J., Morris S. L., 1991, *ApJ*, 373, 465
- Fukugita M., Hogan C. J., Peebles P. J. E., 1998, *ApJ*, 503, 518
- Gamow G., 1948a, *Phys. Rev.*, 74, 505
- Gamow G., 1948b, *Nat*, 162, 680
- Gaskell C. M., 1982, *ApJ*, 263, 79
- Giallongo E., Cristiani S., D'Odorico S., Fontana A., Savaglio S., 1996, *ApJ*, 466, 46
- Giallongo E., Cristiani S., Fontana A., Trevese D., 1993, *ApJ*, 416, 137
- Giavalisco M., Steidel C. C., Adelberger K. L., Dickinson M. E., Pettini M., Kellogg M., 1998, *ApJ*, 503, 543
- Giveon U., Maoz D., Kaspi S., Netzer H., Smith P. S., 1999, *MNRAS*, 306, 637
- Gnedin N. Y., 1998, *MNRAS*, 294, 407
- Gnedin N. Y., Hui L., 1998, *MNRAS*, 296, 44
- Gunn J. E., Peterson B. A., 1965, *ApJ*, 142, 1633
- Haardt F., Madau P., 1996, *ApJ*, 461, 20

- Halliday D., Resnick R., Walker J., 1993, *Fundamentals of Physics*. John Wiley & Sons, New York
- Hamana T., Martel H., Futamase T., 2000, *ApJ*, 529, 56
- Hayashi C., 1950, *Progr. Theor. Phys.*, 5, 224
- Hellsten U., Davé R., Hernquist L., Weinberg D. H., Katz N., 1997, *ApJ*, 487, 482
- Hernquist L., Katz N., Weinberg D. H., Miralda-Escudé J., 1996, *ApJ*, 457, L51
- Hewitt P. C., Foltz C. B., Chaffee F. H., 1995, *AJ*, 109, 1498
- Holz D. E., Wald R. M., 1998, *Phys. Rev. D*, 063501
- Hoyle F., Tayler R. J., 1964, *Nat*, 203, 1108
- Hu E. M., Kim T.-S., Cowie L. L., Songaila A., Rauch M., 1995, *AJ*, 110, 1526
- Hui L., 1999, *ApJ*, 516, 519
- Hui L., Gnedin N. Y., Zhang Y., 1997, *ApJ*, 486, 599
- Ikeuchi S., 1986, *ApJS*, 118, 509
- Ikeuchi S., Ostriker J. P., 1986, *ApJ*, 301, 522
- Izotov Y. I., Thuan T. X., 1998, *ApJ*, 500, 188
- Jedamzik K., 1998, in *Proceedings of "Neutrino Astrophysik"*, astro-ph/9805156
- Jedamzik K., Fuller G. M., 1997, *ApJ*, 483, 560
- Jenkins E. B., Ostriker J. P., 1991, *ApJ*, 376, 33
- Jenkins G. M., Watts D. G., 1968, *Spectral Analysis and its Applications*. Holden-Day, San Francisco
- Kaplinghat M., Turner M. S., 2001, *Phys. Rev. Lett.*, 86, 385

- Kayser R., Helbig P., Schramm T., 1997, *A&A*, 318, 680
- Khare P., Srikanand R., York D. G., Green R. F., Welty D. E., Huang K., Bechtold J., 1997, *MNRAS*, 285, 167
- Khersonsky V. K., Briggs F. H., Turnshek D. A., 1995, *PASP*, 107, 570
- Kim T.-S., Hu E. M., Cowie L. L., Songaila A., 1997, *AJ*, 114, 1
- King I. R., 1966, *AJ*, 71, 64
- Kirkman D., Tytler D., 1997, *ApJ*, 484, 672
- Kirkman D., Tytler D., Burles S., Lubin D., O'Meara J. M., 2000, *ApJ*, 529, 655
- Kolb E. W., Turner M. S., 1990, *The Early Universe*. Addison-Wesley, Redwood City, California
- Kulkarni V. P., Fall S. M., 1993, *ApJ*, 413, L63
- Kulkarni V. P., Huang K., Green R. F., Bechtold J., Welty D. E., York D. G., 1996, *MNRAS*, 279, 197
- Lanzetta K. M., Bowen D. B., Tytler D., Webb J. K., 1995, *ApJ*, 442, 538
- Lanzetta K. M., Webb J. K., Barcons X., 1996, *ApJ*, 456, L17
- Le Brun V., Bergeron J., 1998, *A&A*, 332, 814
- Le Brun V., Bergeron J., Boissé P., 1996, *A&A*, 306, 691
- Lemoine M. et al., 1999, *New Astr.*, 4, 231
- Levshakov S. A., Kegel W. H., Takahara F., 1998a, *ApJ*, 499, L1
- Levshakov S. A., Kegel W. H., Takahara F., 1998b, *A&A*, 336, L29
- Levshakov S. A., Kegel W. H., Takahara F., 2000, *A&A*, 355, L1
- Lineweaver C. H., 1999, *Sci*, 284, 1503

- Loeb A., Eisenstein D. J., 1995, *ApJ*, 448, 17
- Loveday J., Maddox S. J., Efstathiou G., Peterson B. A., 1995, *ApJ*, 442, 457
- Lu L., Sargent W. L. W., Barlow T. A., Rauch M., 1998, *AJ*, submitted, astro-ph/9802189
- Lu L., Sargent W. L. W., Womble D. S., Takada-Hidai M., 1996, *ApJ*, 472, 509
- Lu L., Wolfe A. M., Turnshek D. A., 1991, *ApJ*, 367, 19
- Lu L., Zuo L., 1994, *ApJ*, 426, 502
- Lynds R., 1971, *ApJ*, 164, L73
- Mather J. C., Fixsen D. J., Shafer R. A., Mosier C., Wilkinson D. T., 1999, *ApJ*, 512, 511
- Meiksin A., Bouchet F. R., 1996, *MNRAS*, 283, 1388
- Miralda-Escudé J., Cen R., Ostriker J. P., Rauch M., 1996, *ApJ*, 471, 582
- Miralda-Escudé J., Rees M. J., 1997, *ApJ*, 478, L57
- Misner C. W., Thorne K. S., Wheeler J. A., 1973, *Gravitation*. W. H. Freeman and Company, San Francisco
- Mo H. J., Xia X. Y., Deng Z. G., Börner G., Fang L. Z., 1992, *A&A*, 256, L23
- Molaro P., Bonifacio P., Centurion M., Vladilo G., 1999, *A&A*, 349, L13
- Møller P., Kjærgaard P., 1992, *A&A*, 258, 234
- Morris S. L., Weymann R. J., Savage B. D., Gilliland R. L., 1991, *ApJ*, 377, L21
- Mücket J. P., Petitjean P., Kates R. E., Riediger R., 1996, *A&A*, 308, 17
- Murdoch H. S., Hunstead R. W., Pettini M., Blades J. C., 1986, *ApJ*, 309, 19
- Neyman J., Scott E. L., 1952, *ApJ*, 116, 144

- Nusser A., Haehnelt M., 1999, MNRAS, 303, 179
- Nusser A., Haehnelt M., 2000, MNRAS, 313, 364
- O'Donnell J. E., 1994, ApJ, 422, 158
- Oke J. B., Korycansky D. G., 1982, ApJ, 255, 11
- Olive K. A., Steigman G., Walker T. P., 2000, Phys. Rep., 333-334, 389
- O'Meara J. M., Tytler D., Kirkman D., Suzuki N., Prochaska J. X., Lubin D., Wolfe A. M., 2001, ApJ, 552, 718
- Osmer P. S., 1981, ApJ, 247, 762
- Ostriker J. P., Bajtlik S., Duncan R. C., 1988, ApJ, 327, L35
- Ostriker J. P., Ikeuchi S., 1983, ApJ, 268, L63
- Pando J., Fang L.-Z., 1996, ApJ, 459, 1
- Pando J., Fang L.-Z., 1998, A&A, 340, 335
- Peacock J. A., 1999, *Cosmological Physics*. Cambridge University Press, Cambridge
- Peebles P. J. E., 1966, ApJ, 146, 542
- Peebles P. J. E., 1993, *Principles of Physical Cosmology*. Princeton University Press, Princeton, New Jersey
- Pei Y. C., 1995, ApJ, 440, 500
- Penzias A. A., Wilson R. W., 1965, ApJ, 142, 419
- Petitjean P., Mückel J. P., Kates R. E., 1995, A&A, 295, L9
- Petitjean P., Surdej J., Smette A., Shaver P., Mückel J., Remy M., 1998, A&A, 334, L45

- Petitjean P., Webb J. K., Rauch M., Carswell R. F., Lanzetta K. M., 1993, *MNRAS*, 262, 499
- Phillipps S., 1994, *MNRAS*, 269, 1077
- Popowski P. A., Weinberg D. H., Ryden B. S., Osmer P. S., 1998, *ApJ*, 498, 11
- Press W. H., Rybicki G. B., 1993, *ApJ*, 418, 585
- Press W. H., Rybicki G. B., Schneider D. P., 1993, *ApJ*, 414, 64
- Quashnock J. M., Vanden Berk D. E., 1998, *ApJ*, 500, 28
- Rauch M., 1998, *ARA&A*, 36, 267
- Rauch M., Haehnelt M. G., 1995, *MNRAS*, 275, 76
- Rauch M. et al., 1997, *ApJ*, 489, 7
- Rees M. J., 1986, *MNRAS*, 218, 25
- Reeves H., Audouze J., Fowler W. A., Schramm D. N., 1973, *ApJ*, 179, 909
- Riediger R., Petitjean P., Mucket J. P., 1998, *A&A*, 329, 30
- Rugers M., Hogan C. J., 1996a, *ApJ*, 459, L1
- Rugers M., Hogan C. J., 1996b, *AJ*, 111, 2135
- Ryan S. G., Beers T. C., Olive K. A., Fields B. D., Norris J. E., 2000, *ApJ*, 530, L57
- Ryan S. G., Norris J. E., Beers T. C., 1999, *ApJ*, 523, 654
- Sargent W. L. W., Steidel C. C., Boksenberg A., 1989, *ApJS*, 69, 703
- Sargent W. L. W., Young P. J., Boksenberg A., Tytler D., 1980, *ApJS*, 42, 41
- Saslaw W. C., 1989, *ApJ*, 341, 588

- Saslaw W. C., Hamilton A. J. S., 1984, *ApJ*, 276, 13
- Savaglio S., Cristiani S., D'Odorico S., Fontana A., Giallongo E., Molaro P., 1997, *A&A*, 318, 347
- Schlegel D. J., Finkbeiner D. P., Davis M., 1998, *ApJ*, 500, 525
- Schmidt M., 1963, *Nat*, 197, 1040
- Schramm D. N., Turner M. S., 1998, *Rev. Mod. Phys.*, 70, 303
- Scott J., Bechtold J., Dobrzycki A., Kulkarni V. P., 2000, *ApJS*, 130, 67
- Sheth R. K., Saslaw W. C., 1994, *ApJ*, 437, 35
- Smette A., Robertson J. G., Shaver P. A., Reimers D., Wisotzki L., Köhler T., 1995, *A&AS*, 113, 199
- Smith R. J., Boyle B. J., Maddox S. J., 2000, *MNRAS*, 313, 252
- Songaila A., Cowie L. L., 1996, *AJ*, 112, 335
- Songaila A., Cowie L. L., Hogan C. J., Rugers M., 1994, *Nat*, 368, 599
- Songaila A., Wampler E. J., Cowie L. L., 1997, *Nat*, 385, 137
- Srianand R., 1997, *ApJ*, 478, 511
- Srianand R., Khare P., 1994, *MNRAS*, 271, 81
- Srianand R., Khare P., 1996, *MNRAS*, 280, 767
- Stockton A. N., Lynds C. R., 1966, *ApJ*, 144, 451
- Storrie-Lombardi L. J., McMahon R. G., Irwin M. J., Hazard C., 1996, *ApJ*, 468, 121
- Surdej J. et al., 1993, *AJ*, 105, 2064
- Susa H., Umemura M., 2000, *ApJ*, 537, 578

- Tegmark M., Zaldarriaga M., 2000, *Phys. Rev. Lett.*, 85, 2240
- Theuns T., Leonard A., Efstathiou G., 1998, *MNRAS*, 297, L49
- Theuns T., Leonard A., Efstathiou G., Pearce F. R., Thomas P. A., 1998, *MNRAS*, 301, 478
- Tosi M., Steigman G., Matteucci F., Chiappini C., 1998, *ApJ*, 498, 226
- Tripp T. M., Lu L., Savage B. D., 1998, *ApJ*, 508, 200
- Tytler D., 1987, *ApJ*, 321, 69
- Tytler D., Burles S., Lu L., Fan X.-M., Wolfe A. M., Savage B. D., 1999, *AJ*, 117, 63
- Tytler D., Fan X.-M., 1992, *ApJS*, 79, 1
- Tytler D., Fan X.-M., Burles S., 1996, *Nat*, 381, 207
- Tytler D., O'Meara J. M., Suzuki N., Lubin D., 2000, *Phys. Scr.*, 85, 12, astro-ph/0001318
- Ulmer A., 1996, *ApJ*, 473, 110
- Vanden Berk D. E., Quashnock J. M., York D. G., 1996, *ApJ*, 469, 78
- Véron-Cetty M. P., Véron P., 2000, *ESO Sci. Rep.*, 19, 1
- Vidal-Madjar A. et al., 1998, *A&A*, 338, 694
- Wadsley J. W., Bond J. R., 1997, in *ASP Conference Series*, Vol. 123, Clarke D. A., West M. J., ed, *Proceedings of the 12th Kingston Meeting "Computational Astrophysics"*, San Francisco, p. 332, astro-ph/9612148
- Wagoner R. V., 1973, *ApJ*, 179, 343
- Wagoner R. V., Fowler W. A., Hoyle F., 1967, *ApJ*, 148, 3

- Walker T. P., Steigman G., Schramm D. N., Olive K. A., Kang H.-S., 1991, *ApJ*, 376, 51
- Wambsganss J., Cen R., Ostriker J. P., 1998, *ApJ*, 494, 29
- Wampler E. J., 1996, *Nat*, 383, 308
- Wampler E. J., Williger G. M., Baldwin J. A., Carswell R. F., Hazard C., McMahon R. G., 1996, *A&A*, 316, 33
- Warren S. J., Hewitt P. C., Irwin M. J., Osmer P. S., 1991, *ApJS*, 76, 1
- Warren S. J., Hewitt P. C., Osmer P. S., 1991, *ApJS*, 76, 23
- Webb J. K., 1987a, in Hewitt A., Burbidge G., Fang L.-Z., ed, *Proceedings of the 124th IAU Symposium "Observational Cosmology"*. Reidel, Dordrecht, p. 803
- Webb J. K., 1987b, Ph.D. thesis, University of Cambridge
- Webb J. K., Barcons X., Carswell R. F., Parnell H. C., 1992, *MNRAS*, 255, 319
- Webb J. K., Carswell R. F., Irwin M. J., Penston M. V., 1991, *MNRAS*, 250, 657
- Webb J. K., Carswell R. F., Lanzetta K. M., Ferlet R., Lemoine M., Vidal-Madjar A., Bowen D. V., 1997, *Nat*, 388, 250
- Weinberg D. H., Miralda-Escudé J., Hernquist L., Katz N., 1997, *ApJ*, 490, 564
- Weinberg S., 1972, *Gravitation and Cosmolgy*. John Wiley & Sons, New York
- Weymann R. J., Carswell R. F., Smith M. G., 1981, *ARA&A*, 19, 41
- Williger G. M., Babul A., 1992, *ApJ*, 399, 385
- Williger G. M., Baldwin J. A., Carswell R. F., Cooke A. J., Hazard C., Irwin M. J., McMahon R. G., Storrie-Lombardi L. J., 1994, *ApJ*, 428, 574
- Williger G. M., Hazard C., Baldwin J. A., McMahon R. G., 1996, *ApJS*, 104, 145

- Williger G. M., Smette A., Hazard C., Baldwin J. A., McMahon R. G., 1998, in Petitjean P., Charlot S., ed, Proceedings of the 13th IAP Colloquium “Structure and Evolution of the Intergalactic Medium from QSO Absorption Line Systems”. Editions Frontières, Paris, p. 191
- Williger G. M., Smette A., Hazard C., Baldwin J. A., McMahon R. G., 2000, *ApJ*, 532, 77
- Yang J., Turner M. S., Schramm D. N., Steigman G., Olive K. A., 1984, *ApJ*, 281, 493
- York D. G., Yanny B., Crofts A., Carilli C., Garrison E., Matheson L., 1991, *MNRAS*, 250, 24
- Yoshii Y., Peterson B. A., Takahara F., 1993, *ApJ*, 414, 431
- Zhang Y., Anninos P., Norman M. L., 1995, *ApJ*, 453, L57
- Zhang Y., Anninos P., Norman M. L., Meiksin A., 1997, *ApJ*, 485, 496
- Zhang Y., Meiksin A., Anninos P., Norman M. L., 1998, *ApJ*, 495, 63
- Zuo L., 1992, *MNRAS*, 258, 45
- Zuo L., 1993, *A&A*, 278, 343
- Zuo L., Bond J. R., 1994, *ApJ*, 423, 73
- Zuo L., Lu L., 1993, *ApJ*, 418, 601
- Zuo L., Phinney E. S., 1993, *ApJ*, 418, 28